



DOCTORAL DISSERTATION

Advances in the numerical modelling of nonlinearities in dynamic soil-structure interaction problems

Programa de Doctorado:

Tecnologías de Telecomunicación e Ingeniería Computacional

Línea de Investigación:

Ingeniería Computacional

Francisco González Pérez

Continuum Mechanics and Structures Division

Las Palmas de Gran Canaria • November 2019



UNIVERSIDAD DE LAS PALMAS
DE GRAN CANARIA



INSTITUTO UNIVERSITARIO
SIANI
INGENIERIA COMPUTACIONAL



Advances in the numerical modelling of nonlinearities in dynamic soil-structure interaction problems

Programa de doctorado:
Tecnologías de Telecomunicación e Ingeniería Computacional

Línea de Investigación:
Ingeniería Computacional

Autor:
D. Francisco González Pérez

Director:
Dr. D. Luis Alberto Padrón Hernández

Las Palmas de Gran Canaria, November 2019

Acknowledgements

First, and most especially, I am highly grateful to Luis A. Padrón, not only for all the time expended in giving me explanations and corrections, but also for his strong encouragement, patience and for always giving priority to my issues. It becomes evident, for those who have followed this work either in the university or in my personal environment, that this work would have not been possible without you. Thank you very much for taking on the challenge of supervising my Thesis.

To Juan J. Aznárez, for being the first who trusted me, and for giving me the chance of being part of such an excellent group, the Continuum Mechanics and Structures Division of the SIANI University Institute. To him and to Orlando Maeso for the continuous advises and support along these years. I would also like to thank the rest of professors and colleagues of the Research Group, and more especially to Cristina Medina, Jacob D. R. Bordón, Guillermo M. Álamo, Juan Carlos Galván, María Castro and Román Quevedo, from whom I have learned a huge amount of things just seeing how they work, and also for being always ready to solve any problem that arises to me. Many thanks to all the people involved in the SIANI Institute for providing a very nice atmosphere, and also for giving us all the needed resources.

I would like to thank Sandro Carbonari for giving me the valuable opportunity to work with him and learn from him and his research team in *Universtà Politecnica delle Marche*. I would like to extend my gratitude to Michele Morici and Graziano Leoni from University of Camerino, and to Francesca Dezi from University of San Marino. Your guidance and assistance, together with the kindness of all professors and colleagues in Ancona, made very easy the decision of doing a second research stay with you. Both research stays were also plenty of great and funny moments, especial thanks to Maria Chiara Capatti and Lucia Minnucci.

I would also like to thank Luis A. Padrón and Sandro Carbonari to all contributions and corrections made to the text of this Thesis and the derived journal articles, and to Michele Morici for providing the results needed for the comparison between models of the soil-foundation systems.

To my family, for all the time I didn't spent with them in the last years, and because of their unconditional love and support, especially to my parents Pilar and Francisco, and my sister Raquel. Also to my grandparents, aunts and uncles, and more especially to "Abuela Nieves" for the intense love I have always received from her. Many thanks for taking care of all the family, you simply are second to none. My sincere thanks to Cristina for having pushed for this goal as much as I did. Also to her family for their care, love and support.

Finally, it is fair to acknowledge the institutions that have provided the financial support to this research:

On the one hand, I have been recipient of a Ph.D. fellowship from the *Ministerio de Ciencia, Innovación y Universidades*, whose code is FPU14/06936. Also, this institution provided me with financial support for two short-term research stays at *Università Politecnica delle Marche*, one in 2017 (EST16/00392) and the other in 2018 (EST17/00370).

On the other hand, throughout the grant period, the Research Group in which I have been involved has received founding from two national research projects of the *Ministerio de Ciencia, Innovación y Universidades*, the *Agencia Estatal de Investigación* and FEDER, whose codes are BIA2014-57640-R and BIA2017-88770-R.

Contents

1	Introduction	1
1.1	Motivation and background	1
1.2	Objectives	2
1.3	Literature review	3
1.3.1	Soil-pile foundation modelling	3
1.3.2	Soil-structure interaction in the seismic response of bridges	4
1.4	Structure of the dissertation	7
1.5	Published works derived from the Ph.D. Thesis	8
1.5.1	Contribution to JCR journals	8
1.5.2	Conference contributions	8
I	Lateral dynamic analysis of pile foundations considering pile-soil interface degradation	9
2	Problem definition and system modelling	11
2.1	Introduction	11
2.2	Problem definition	12
2.3	Description of the proposed model	14
2.3.1	Pile and soil load-line discretization	15
2.3.2	Boundary element equations	16
2.3.3	Finite element equations	18
2.3.4	Model of the soil-pile interface	22
2.3.5	Assembly of the global system matrix of equations	25
3	Model calibration and results	27
3.1	Introduction	27
3.2	Multi-domain BEM reference model	27
3.3	Calibration of proportionality function F_l	28
3.4	Modelling of material damping in the degraded domain	31
3.5	Verification for a degraded domain with shape changing along pile depth	34
3.5.1	Verification in terms of impedance functions	36
3.5.2	Verification in terms of displacements	37
3.6	Influence of the soil column stiffness and inertia terms	39
3.7	Conclusions	43

II	Seismic response of bridge piers on pile groups	45
4	Problem definition, methodology and modelling	47
4.1	Introduction	47
4.2	Bridge piers seismic design procedure	50
4.3	Moment – curvature – chord rotation relationships	52
4.4	Selection of input earthquake records	54
4.5	Overview of the methodology employed for the computation of the system response	55
4.6	Models used for the computation of impedances and kinematic interaction functions	58
4.7	Modelling of the soil material damping	60
4.8	Substructuring scheme	60
4.8.1	Equations of motion	61
4.8.2	Energy balance	64
4.9	Lumped parameter models for the representation of the soil-pile foundation system	65
4.9.1	Consistent LPM	65
4.9.2	Simplified LPM	73
5	Influence of the soil damping model and the lumped parameter representations of the foundation	77
5.1	Introduction	77
5.2	Configurations under study	77
5.3	Soil properties and seismic actions	78
5.4	Error measurement	79
5.5	Influence of soil damping model on impedance and kinematic interaction functions	82
5.6	Parametric analysis	87
5.6.1	Influence of ground type on the accuracy of the responses computed using LPMs	99
5.6.2	Influence of superstructure fundamental periods on the accuracy of the responses computed using LPMs	100
5.6.3	Influence of pile foundation layouts on the accuracy of the responses computed using LPMs	102
5.6.4	Influence of pile inclination on the accuracy of the responses computed using LPMs	102
5.7	Conclusions	104
6	Benefits of inclined pile foundations in earthquake resistant design of bridges	107
6.1	Introduction	107
6.2	Soil properties and seismic actions	108
6.3	Decks design	109
6.4	Piers design	109
6.5	Pile foundations design	113
6.6	Results	114
6.6.1	Piers plastic hinge parameters	114
6.6.2	Impedance functions and kinematic interaction factors	115

6.6.3	Inelastic responses	119
6.6.4	Ductility demand	124
6.6.5	Energy	127
6.7	Conclusions	129
7	General conclusions and future research directions	133
7.1	Summary and conclusions	133
7.2	Future research directions	134
A	Kinematic interaction factors, and computed and fitted impedance functions of the soil-foundation systems used in Chapter 5	139
A.1	Kinematic interaction factors	140
A.2	Impedance functions and LPM fitting results	148
B	Summary in Spanish / Resumen en castellano	161
B.1	Motivación y antecedentes	161
B.2	Objetivos	163
B.3	Estructura del documento	163
B.4	Trabajos publicados que se derivan de esta Tesis	165
	B.4.1 Contribución a revistas JCR	165
	B.4.2 Contribución a conferencias	165
B.5	Resumen y conclusiones	166
B.6	Líneas futuras de investigación	167
	Bibliography	171

List of Figures

2.1	Generic depiction of the variation of the soil shear modulus and the soil damping ratio as a function of soil shear strain.	12
2.2	Depiction of the problem.	13
2.3	Linear equivalent modelling of an imperfect pile-soil interface through distributed springs and dashpots.	14
2.4	Discretization of pile and soil load-lines.	16
2.5	Equilibrium conditions between pile and soil load-line.	17
2.6	Example of mesh typology used in the model (only a quarter of the geometry is shown).	17
2.7	Possible distributions of the F_l and F_a proportionality functions.	23
3.1	First configuration analysed, with a degraded zone of constant diameter along the whole length of the pile.	28
3.2	Complete (a) and top zoom view (b) of a multi-domain BEM mesh for the particular degraded zone diameter ratio of $\chi = d_{dz}/d = 1.4$, and BEM-FEM mesh detail (c) with 1D elements for the piles. (Only a quarter of the geometry is meshed).	30
3.3	Comparison between stiffness and damping function obtained from the proposed BEM-FEM model and the reference multi-domain BEM model for the case depicted in Figure 3.1. $\xi_{dz} = 0$, $E_p/E_s = 1000$	30
3.4	Comparison between stiffness and damping function obtained from the proposed BEM-FEM model and the reference multi-domain BEM model for the case depicted in Figure 3.1. $\xi_{dz} = 0$, $E_p/E_s = 100$	31
3.5	Plot of the proposed proportionality function F_l for the specific values of χ and G_{dz}/G_s studied. Point values shown in Table 3.1.	32
3.6	Plot of Equation (3.3) for the interpolation of the proportionality function F_l . Point values shown in Table 3.1.	32
3.7	Plot of Equation (3.4) for different values of the soil plasticity index I_p	33
3.8	Comparison between stiffness and damping function obtained from the proposed BEM-FEM model and the reference multi-domain BEM model for the case depicted in Figure 3.1. $\xi_{dz} \neq 0$, $E_p/E_s = 1000$	34
3.9	Comparison between stiffness and damping function obtained from the proposed BEM-FEM model and the reference multi-domain BEM model for the case depicted in Figure 3.1. $\xi_{dz} \neq 0$, $E_p/E_s = 100$	35
3.10	Second configuration analysed, with an inverted truncated conical degraded zone.	36

3.11	Detail of one of the meshes generated for the multi-domain BEM analyses with the inverted conical degraded zone (only a quarter of the geometry is shown).	36
3.12	Comparison between stiffness and damping function obtained from the proposed BEM-FEM model and the reference multi-domain BEM model for the case depicted in Figure 3.10 with an inverted truncated conical degraded zone. $\xi_{dz} \neq 0$, $\chi(0) = 1.6$ and $E_p/E_s = 1000$	37
3.13	Comparison between stiffness and damping function obtained from the proposed BEM-FEM model and the reference multi-domain BEM model for the case depicted in Figure 3.10 with an inverted truncated conical degraded zone. $\xi_{dz} \neq 0$, $\chi(0) = 1.5$ and $E_p/E_s = 1000$	38
3.14	Comparison between stiffness and damping function obtained from the proposed BEM-FEM model and the reference multi-domain BEM model for the case depicted in Figure 3.10 with an inverted truncated conical degraded zone. $\xi_{dz} \neq 0$, $\chi(0) = 1.6$ and $E_p/E_s = 100$	39
3.15	Comparison between stiffness and damping function obtained from the proposed BEM-FEM model and the reference multi-domain BEM model for the case depicted in Figure 3.10 with an inverted truncated conical degraded zone. $\xi_{dz} \neq 0$, $\chi(0) = 1.5$ and $E_p/E_s = 100$	40
3.16	Pile and soil load-line displacements for the case of an inverted truncated conical zone with $E_p/E_s = 1000$, $\chi(0) = 1.6$ and $h_{dz}/d = 6.0$ and for different degraded zone degradation levels. Comparison between BEM-FEM and reference multi-domain BEM models.	41
3.17	Influence of the consideration of the soil column inertia and stiffness in the FEM equations. Absolute value of the horizontal impedance function of a single pile foundation for different representative values of the F_l proportionality function.	43
4.1	Viaduct of Rodén, Spain (courtesy of Miguel Ángel Tremps).	47
4.2	Soil – piles foundation – superstructure system and foundation layouts.	48
4.3	Girders installation. Visit to the ongoing works in the road between Perugia and Ancona, Italy.	49
4.4	(a) Viaduct longitudinal view and restraint conditions of the deck under (b) dynamic and (c) static loading.	50
4.5	Fundamentals of the displacement-based seismic design of structures [111]. (a) Plastic hinges at the pier base. (b) Takeda’s hysteretic cyclic rule [112]. (c) Effective stiffness and hysteretic area for equivalent damping calculation. (d) Design displacement spectra.	51
4.6	Mander constitutive law for the confined and unconfined concrete [115], and the King law [116] for rebars.	53
4.7	Curvature – chord rotation relationships [111, 113, 117, 118].	54
4.8	Scheme of the substructuring methodology for computing the nonlinear response of piled bridge piers.	56
4.9	Example of a 3×3 pile group BEM-FEM discretization (only a quarter of the geometry is shown) [23].	59
4.10	Schematic model of the pile group embedded in the Winkler-type medium and connected by a rigid cap [9].	59
4.11	\mathcal{M} values assuming $\xi = 0.1$ for the hysteretic and Biot’s damping models.	61

4.12	CB and FB substructuring models of the in-plane dynamic response of the soil-foundation-pier systems.	62
4.13	Adopted scheme for the second-order discrete-element model [99,142,143].	68
4.14	Proposed scheme for the consistent LPM.	70
4.15	Scheme of the simplified LPM [133].	74
5.1	Time histories of the selected records for ground type D (see Table 5.3). .	80
5.2	Time histories of the selected records for ground type C (see Table 5.4). .	81
5.3	Mean response spectrum of the resulting sets of accelerograms scaled for each superstructure and ground type (Ground type D in continuous line and Ground type C in dashed line).	83
5.4	Illustration of the computed and fitted impedance functions for one of the configurations analyzed (vertical 2×2 , $s = 7$ m foundation layout in ground type D). Continuous and dashed black lines represent impedance functions assuming hysteretic and Biot's damping models, respectively; blue and green lines represent fitted functions using consistent LPM with orders $N = 2$ and $N = 4$, respectively; red lines represent fitted functions using simplified LPM; and Ψ represents the weight functions used by the LPM approaches (defined in Equations (5.3a) and (5.3b)).	84
5.5	Illustration of the computed kinematic interaction factors for 2×2 , $s = 7$ m foundation layout in ground type D with vertical and inclined piles. Continuous and dashed black lines represent kinematic interaction factors assuming hysteretic and Biot's damping models, respectively; the gray line represents normalized mean Fourier amplitude spectrum of the ground motion, scaled for superstructure 3 ($T_n = 1.0$ s).	85
5.6	Time history of 429–111 earthquake acceleration (Table 5.3), scaled for superstructure 3 ($T_n = 1.0$ s); and FIM derived from soil-foundation kinematic interaction analysis. Vertical 2×2 , $s = 7$ m foundation layout in ground type D.	86
5.7	Time history of superstructure and pile cap degrees of freedom. Particular case of vertical 2×2 , $s = 7$ m foundation layout in ground type D (impedance functions and kinematic interaction factors shown in Figures 5.4 and 5.5 respectively) using superstructure 3 ($T_n = 1.0$ s) and earthquake 429–111 (Table 5.3).	88
5.8	Contribution of the different degrees of freedom to the mean maximum lateral displacement of the bridge deck u_D (H: hysteretic damping model and B: Biot's damping model).	96
5.9	Comparison between the mean maximum magnitudes of foundation rotation and superstructure relative rotation using frequency domain approach (H: hysteretic damping model and B: Biot's damping model).	97
5.10	Contribution of the different degrees of freedom to the mean maximum lateral displacement of the bridge deck u_D considering inclined piles of 2×2 cases (H: hysteretic damping model and B: Biot's damping model).	98
5.11	Differences due to the use of hysteretic or Biot's soil damping model, and errors due to the use of LPM approaches. Influence of ground type.	100
5.12	Differences due to the use of hysteretic or Biot's soil damping model, and errors due to the use of LPM approaches. Influence of superstructure fundamental periods (ground type D).	101

5.13	Differences due to the use of hysteretic or Biot's soil damping model, and errors due to the use of LPM approaches. Influence of superstructure fundamental periods (ground type C).	101
5.14	Differences due to the use of hysteretic or Biot's soil damping model, and errors due to the use of LPM approaches. Influence of foundation layouts (ground type D).	103
5.15	Differences due to the use of hysteretic or Biot's soil damping model, and errors due to the use of LPM approaches. Influence of foundation layouts (ground type C).	103
5.16	Differences due to the use of hysteretic or Biot's soil damping model, and errors due to the use of LPM approaches. Influence of pile inclination in 2×2 pile groups (ground type D).	105
5.17	Differences due to the use of hysteretic or Biot's soil damping model, and errors due to the use of LPM approaches. Influence of pile inclination in 2×2 pile groups (ground type C).	105
6.1	Time histories of the selected records (see Table 6.2).	110
6.2	Elastic response spectrum of the selected earthquakes (see Table 6.2), in terms of accelerations (top) and displacements (bottom).	111
6.3	(a) Decks cross-section (values in meters), (b) girders plates thicknesses and dimensions (values in Table 6.3).	112
6.4	Moment-curvature relationships of piers cross sections [114].	115
6.5	Hysteretic cyclic rules adopted to model the nonlinear response of the plastic hinge.	116
6.6	Example of BEM discretization for the computation of impedance functions and kinematic interaction factors (only a quarter of the geometry is shown).	117
6.7	Computed impedance functions for vertical foundation layouts comparing BEM-FEM and Winkler-type models.	118
6.8	Computed kinematic interaction factors for vertical foundation layouts comparing BEM-FEM and Winkler-type models (the gray line represents normalized mean Fourier amplitude spectrum of the selected ground motions).	119
6.9	Computed and fitted impedance functions for all foundations layouts. Impedance functions computed through the BEM-FEM.	120
6.10	Computed and fitted impedance functions for all foundations layouts. Impedance functions computed through the Winkler model.	121
6.11	Computed kinematic interaction factors of pile foundations (the gray line represents normalized mean Fourier amplitude spectrum of the selected ground motions). Kinematic interaction factors computed through the BEM-FEM.	122
6.12	Computed kinematic interaction factors of pile foundations (the gray line represents normalized mean Fourier amplitude spectrum of the selected ground motions). Kinematic interaction factors computed through the Winkler model.	122
6.13	Hysteresis cycles and pier bending moment time histories for the H15L50 case (Table 6.5) with input motion E7 (Table 6.2).	123

6.14	Comparison between the ductility demands, computed through the equal displacement rule in the frequency domain, and using the BEM-FEM or the Winkler-type model for obtaining impedances and kinematic interaction factors. Vertical piles cases.	123
6.15	Comparison between the ductility demands, computed through the equal displacement rule, obtained in the frequency domain using the original impedance functions, and in the time domain using the LPM approximations. Vertical piles cases.	124
6.16	Ductility demand of all simulated cases. (a) Piers designed according to [111,113].	125
6.17	Ductility demand of all simulated cases. Piers designed according to [111] relaxing the restraints over minimum content of reinforcement and stability index [113].	126
6.18	Time history of the energy terms for the H15L50 case with input motion E7.	129
6.19	Mean over the 7 accelerograms of the energy balances at the end of the time history analyses for all structural cases. L: linear, T: Takeda's constitutive law, B: bilinear constitutive law.	130
A.1	Kinematic interaction factors of the vertical 2×2 , $s = 3$ m foundation layout in ground type D.	140
A.2	Kinematic interaction factors of the vertical 2×2 , $s = 5$ m foundation layout in ground type D.	140
A.3	Kinematic interaction factors of the vertical 2×2 , $s = 7$ m foundation layout in ground type D.	141
A.4	Kinematic interaction factors of the vertical 3×3 , $s = 3$ m foundation layout in ground type D.	141
A.5	Kinematic interaction factors of the vertical 3×3 , $s = 5$ m foundation layout in ground type D.	141
A.6	Kinematic interaction factors of the vertical 3×3 , $s = 7$ m foundation layout in ground type D.	142
A.7	Kinematic interaction factors of the $\theta = 5^\circ$ inclined 2×2 , $s = 3$ m foundation layout in ground type D.	142
A.8	Kinematic interaction factors of the $\theta = 5^\circ$ inclined 2×2 , $s = 5$ m foundation layout in ground type D.	142
A.9	Kinematic interaction factors of the $\theta = 5^\circ$ inclined 2×2 , $s = 7$ m foundation layout in ground type D.	143
A.10	Kinematic interaction factors of the $\theta = 10^\circ$ inclined 2×2 , $s = 3$ m foundation layout in ground type D.	143
A.11	Kinematic interaction factors of the $\theta = 10^\circ$ inclined 2×2 , $s = 5$ m foundation layout in ground type D.	143
A.12	Kinematic interaction factors of the $\theta = 10^\circ$ inclined 2×2 , $s = 7$ m foundation layout in ground type D.	144
A.13	Kinematic interaction factors of the vertical 2×2 , $s = 3$ m foundation layout in ground type C.	144
A.14	Kinematic interaction factors of the vertical 2×2 , $s = 5$ m foundation layout in ground type C.	144

A.15 Kinematic interaction factors of the vertical 2×2 , $s = 7$ m foundation layout in ground type C.	145
A.16 Kinematic interaction factors of the vertical 3×3 , $s = 3$ m foundation layout in ground type C.	145
A.17 Kinematic interaction factors of the vertical 3×3 , $s = 5$ m foundation layout in ground type C.	145
A.18 Kinematic interaction factors of the vertical 3×3 , $s = 7$ m foundation layout in ground type C.	146
A.19 Kinematic interaction factors of the $\theta = 5^\circ$ inclined 2×2 , $s = 3$ m foundation layout in ground type C.	146
A.20 Kinematic interaction factors of the $\theta = 5^\circ$ inclined 2×2 , $s = 5$ m foundation layout in ground type C.	146
A.21 Kinematic interaction factors of the $\theta = 5^\circ$ inclined 2×2 , $s = 7$ m foundation layout in ground type C.	147
A.22 Kinematic interaction factors of the $\theta = 10^\circ$ inclined 2×2 , $s = 3$ m foundation layout in ground type C.	147
A.23 Kinematic interaction factors of the $\theta = 10^\circ$ inclined 2×2 , $s = 5$ m foundation layout in ground type C.	147
A.24 Kinematic interaction factors of the $\theta = 10^\circ$ inclined 2×2 , $s = 7$ m foundation layout in ground type C.	148
A.25 Computed and fitted impedance functions of the vertical 2×2 , $s = 3$ m foundation layout in ground type D.	148
A.26 Computed and fitted impedance functions of the vertical 2×2 , $s = 5$ m foundation layout in ground type D.	149
A.27 Computed and fitted impedance functions of the vertical 2×2 , $s = 7$ m foundation layout in ground type D.	149
A.28 Computed and fitted impedance functions of the vertical 3×3 , $s = 3$ m foundation layout in ground type D.	150
A.29 Computed and fitted impedance functions of the vertical 3×3 , $s = 5$ m foundation layout in ground type D.	150
A.30 Computed and fitted impedance functions of the vertical 3×3 , $s = 7$ m foundation layout in ground type D.	151
A.31 Computed and fitted impedance functions of the $\theta = 5^\circ$ inclined 2×2 , $s = 3$ m foundation layout in ground type D.	151
A.32 Computed and fitted impedance functions of the $\theta = 5^\circ$ inclined 2×2 , $s = 5$ m foundation layout in ground type D.	152
A.33 Computed and fitted impedance functions of the $\theta = 5^\circ$ inclined 2×2 , $s = 7$ m foundation layout in ground type D.	152
A.34 Computed and fitted impedance functions of the $\theta = 10^\circ$ inclined 2×2 , $s = 3$ m foundation layout in ground type D.	153
A.35 Computed and fitted impedance functions of the $\theta = 10^\circ$ inclined 2×2 , $s = 5$ m foundation layout in ground type D.	153
A.36 Computed and fitted impedance functions of the $\theta = 10^\circ$ inclined 2×2 , $s = 7$ m foundation layout in ground type D.	154
A.37 Computed and fitted impedance functions of the vertical 2×2 , $s = 3$ m foundation layout in ground type C.	154
A.38 Computed and fitted impedance functions of the vertical 2×2 , $s = 5$ m foundation layout in ground type C.	155

A.39	Computed and fitted impedance functions of the vertical 2×2 , $s = 7$ m foundation layout in ground type C.	155
A.40	Computed and fitted impedance functions of the vertical 3×3 , $s = 3$ m foundation layout in ground type C.	156
A.41	Computed and fitted impedance functions of the vertical 3×3 , $s = 5$ m foundation layout in ground type C.	156
A.42	Computed and fitted impedance functions of the vertical 3×3 , $s = 7$ m foundation layout in ground type C.	157
A.43	Computed and fitted impedance functions of the $\theta = 5^\circ$ inclined 2×2 , $s = 3$ m foundation layout in ground type C.	157
A.44	Computed and fitted impedance functions of the $\theta = 5^\circ$ inclined 2×2 , $s = 5$ m foundation layout in ground type C.	158
A.45	Computed and fitted impedance functions of the $\theta = 5^\circ$ inclined 2×2 , $s = 7$ m foundation layout in ground type C.	158
A.46	Computed and fitted impedance functions of the $\theta = 10^\circ$ inclined 2×2 , $s = 3$ m foundation layout in ground type C.	159
A.47	Computed and fitted impedance functions of the $\theta = 10^\circ$ inclined 2×2 , $s = 5$ m foundation layout in ground type C.	159
A.48	Computed and fitted impedance functions of the $\theta = 10^\circ$ inclined 2×2 , $s = 7$ m foundation layout in ground type C.	160

List of Tables

3.1	Proposed values of the proportionality function F_l	32
3.2	Damping ratios of the degraded zone based on the expression proposed by Ishibashi and Zang [103] for different levels of degradation.	33
5.1	Superstructures parameters.	78
5.2	Pile cap properties depending on foundation layout for CB model.	78
5.3	Selected records for ground type D (WC: Waveform Code and EC: Earthquake Code) [119,123].	79
5.4	Selected records for ground type C (WC: Waveform Code and EC: Earthquake Code) [119].	82
5.5	Differences between damping models and errors committed by using the different LPM approaches in the results shown in Figure 5.7.	87
5.6	Resulting parameter values from the fitting with the consistent LPM with $N = 2$. Horizontal impedance component. Particular case of vertical 2×2 , $s = 7$ m foundation layout in ground type D (impedance functions shown in Figure 5.4).	89
5.7	Resulting parameter values from the fitting with the consistent LPM with $N = 2$. Rocking impedance component. Particular case of vertical 2×2 , $s = 7$ m foundation layout in ground type D (impedance functions shown in Figure 5.4).	90
5.8	Resulting parameter values from the fitting with the consistent LPM with $N = 2$. Cross-coupled horizontal-rocking impedance component. Particular case of vertical 2×2 , $s = 7$ m foundation layout in ground type D (impedance functions shown in Figure 5.4).	90
5.9	Resulting parameter values from the fitting with the consistent LPM with $N = 4$. Horizontal impedance component. Particular case of vertical 2×2 , $s = 7$ m foundation layout in ground type D (impedance functions shown in Figure 5.4).	91
5.10	Resulting parameter values from the fitting with the consistent LPM with $N = 4$. Rocking impedance component. Particular case of vertical 2×2 , $s = 7$ m foundation layout in ground type D (impedance functions shown in Figure 5.4).	92
5.11	Resulting parameter values from the fitting with the consistent LPM with $N = 4$. Cross-coupled horizontal-rocking impedance component. Particular case of vertical 2×2 , $s = 7$ m foundation layout in ground type D (impedance functions shown in Figure 5.4).	93

5.12	Resulting parameter values from the fitting with the simplified LPM. Particular case of vertical 2×2 , $s = 7$ m foundation layout in ground type D (impedance functions shown in Figure 5.4).	94
6.1	Soil profile and lithotypes.	108
6.2	Selected records for input motion (WC: Waveform Code, EC: Earthquake Code, Δ : epicentral distance and PGA: Peak Ground Acceleration.) [122].	109
6.3	Bending moments due to self weights, and girders plates thicknesses and dimensions (scheme in Figure 6.3b).	112
6.4	Analysis of deck permanent loads due to self weights.	112
6.5	Definition of cases of studies, case labels and pier properties.	113
6.6	Design action effects at the foundation level and pile foundations dimensions.	114
6.7	Set of parameters defining the different FB and CB systems (see Figure 4.12) used to model the superstructure considered for each case of analysis.	114
6.8	Parameters for the plastic hinge modelling. Data within parenthesis refers to analyses disregarding code provisions concerning reinforcement detailing and stability issues.	116
6.9	Degrees of freedom contribution (in percentage) to the total displacement at the deck ($h_S = h_d + h_c + h_p$, $h_F = h_d + h_c + h_p + h_f$), according to Eurocode 8–Part 2 [113].	128

Chapter 1

Introduction

1.1 Motivation and background

While it is true that nowadays there is considerable knowledge in seismic engineering, the fact is that earthquakes keep on killing at least thousands of people annually, even tens of thousands in specific years [1]. To make matters worse, the damage to urban areas, cities and civil infrastructures becomes completely devastating. As in any type of catastrophic situation, not all regions of the planet have the capacity to recover in the same way. That is why it is completely necessary and essential to develop new and cheaper techniques for the design and calculation of earthquake-resistant structures.

To do so, it is very common in engineering the resolution of dynamic problems involving the propagation of mechanical waves through continuous media. The analysis of the response of structures or mechanical parts to variable loads over time, as an earthquake, requires high levels of precision in the search for more optimized and safe designs. It has become a common problem and no longer constitutes a closed shop typical of large studios and engineering companies.

The way in which the soil properties and motion influences the response of the structure and, in turn, the motion of the structure interacts with the soil response is usually called as Soil-Structure Interaction (SSI). This concept refers to both static and dynamic phenomena mediated by a compliant soil and a stiffer superstructure. Frequently, structural calculations neglect SSI which often leads to over-conservative designs. However, as will be shown, SSI can also convey detrimental effects in the system response for some particular cases. The literature collects a multitude of evidences about the existence of scenarios where the SSI must be taken into account. When a structure is partially embedded into the ground, and also when the site class is constituted by soft soil, SSI becomes decisive. The proper design on the foundation plays a significant role, and mitigate the detrimental effects.

This thesis focuses on the particular case of pile foundations, and tackles different problems involving the dynamic and seismic response of piles and piled structures taking into account dynamic SSI effects and nonlinear phenomena developed either on the pile-soil system or in the superstructure. More precisely, one part of the dissertation proposes a linear equivalent boundary element – finite element coupled model (BEM-FEM) for the analysis of the dynamic response of pile foundations considering degradation along the pile-soil interface. The other part of the dissertation studies different ways of building a numerical model for the analysis of the seismic response of piled viaducts, and uses such a model to analyse the influence of many different aspects, including for instance, the

benefits of employing inclined elements in the pile foundations.

The developed codes for the soil-foundation analysis are verified obtaining results for some basic problems already known, or for other problems, in general of unknown solution, which are solved with the programs available in the research group. A careful calibration of the model parameters is necessary to guarantee stability and accuracy in the results. The corresponding parametric studies are carried out depending on the characteristics of the structure, the type of solicitation and the nonlinear nature of the problem.

The Ph.D. Candidate has been attached to the University Institute of Intelligent Systems and Numeric Applications in Engineering (SIANI from its Spanish initials: *Sistemas Inteligentes y Aplicaciones Numéricas en Ingeniería*), specifically to the Continuum Mechanics and Structures Division. The SIANI Institute has been active for two decades and has appropriate facilities, including a high performance data processing center that houses a general purpose calculation cluster, located at the central building of the Science and Technology Park of the *Universidad de Las Palmas de Gran Canaria*.

The Group in which the Ph.D. Candidate is integrated has worked for more than thirty years in the development of FEM, BEM and BEM-FEM models for the dynamic analysis of structural mechanics problems where the effects related with SSI phenomena are crucial, although only in the linear range of their behaviour. Thus, in recent years, the contributions made in the form of models and software in this field are considerable, as well as the deep study of specific problems of interest: seismic response of dams, buried structures and building structures founded on piles.

1.2 Objectives

Linear analysis may be adequate in many cases. In others, however, it is necessary to use models that are able to incorporate also nonlinear phenomena. The objective of this Thesis is to advance in the numerical modelling of nonlinearities in dynamic SSI problems, and has aimed to advance the development of the Research Group's software including formulations that allow addressing problems with nonlinear behaviour in the field of dynamic SSI. The resulting models allow a more realistic analysis of practical problems.

The thesis has, as its first objective, the formulation and implementation of a coupled model of finite elements and boundary elements for the dynamic analysis of pile foundations that exhibit a nonlinear behaviour in the contact between the pile and the soil. It takes into account, through an equivalent linear model, the soil degradation around the piles.

The second objective is the development of a tool for the analysis of the nonlinear behaviour of structures taking into account the dynamic SSI and the frequency-dependent reaction forces of the soil-foundation system.

To achieve these general objectives, a sequence of partial objectives has been accomplished:

- Development of an equivalent linear BEM-FEM model for the approximate analysis of the time harmonic lateral response of piles considering soil degradation along the soil-pile interface.
- Study of the theoretical bases of the Lumped Parameter Models (LPMs), and

implementation of linear step-by-step schemes for the study of structures founded on piles.

- Study of the selection criteria and treatment of seismic signals.
- Analysis of the influence on the superstructure response of the type of damping modelling for the soil domain.
- Analysis of the influence on the superstructure response of the type of lumped parameter representation of the soil-foundation system.
- Implementation of the nonlinear behaviour laws associated to the superstructures included in this study, i.e. bridge piers. Development of substructuring schemes for their response analyses.
- Analysis of the influence of SSI effects on the nonlinear dynamic response of piled bridges and viaducts.
- Evaluation of the damage reduction in viaduct superstructures when inclined piles are used in the foundation.

1.3 Literature review

1.3.1 Soil-pile foundation modelling

The dynamic and seismic response of piles under linear-elastic assumptions constitutes a topic that has received significant attention. The time-harmonic dynamic response of pile foundations, whose knowledge allows the use of substructuring approaches for the analysis of piled structures, has been studied through a number of approaches: analytical solutions (see e.g. [2–4]); simplified semi-analytical procedures, including Winkler-type models (see e.g. [5–11]); and through different numerical techniques such as the FEM (see e.g. [12–14]), the BEM (see e.g. [15–17]), or BEM-FEM schemes assuming Green's functions or BEM formulations for the soil, and structural monodimensional elements for the piles (see e.g. [18–26]).

Each one of the different approaches to the problem has advantages and disadvantages. Rigorous analytical solutions are usually oriented to a specific problem, lacking versatility and generality. On the other hand, they accurately reproduce the physics of the problem with very low computing efforts. Winkler-type models consume low computational resources and their simplicity makes them easy to handle, but are not always able to incorporate aspects such as pile-to-pile interaction, radiation damping or the effects derived from the three-dimensional character of the problem. FEM models can be very versatile and flexible, being the difficulty in modelling unbounded regions (such as the soil) one of their major disadvantages. BEM models require meshing only the boundaries and interfaces of the problem, with the corresponding reduction in numbers of nodes and elements. At the same time, allows to obtain results of high accuracy not only in displacements but also, for instance, in tractions. In any case, one of the biggest advantages is the implicit treatment of unbounded domains. On the contrary, the models are limited by the available fundamental solutions, and the resulting matrices (which are generally non-sparse) and the effort needed to evaluate the fundamental solution, may increase the computational cost.

The dynamic response of pile foundations taking different types of nonlinearities into account has also received a significant amount of attention. Thanks to empirical tests that provide information about the different mechanisms and aspects involved, numerical methods of analysis for this problem have been proposed in the literature. The nonlinear effects in soil-pile foundation systems studied by empirical dynamic analyses cover full-scale systems, e.g. [27–31], scaled 1g experimental models, e.g. [14, 32–35], and centrifuge tests, e.g. [36–40]. Among all developed numerical methods, they include Beam on Nonlinear Winkler Foundation (BNWF) approaches, finite element formulations, and models that consider a weak zone in the soil around the pile. It has been a hard task for researchers to propose reliable and complete models that account for different types of dynamic nonlinearities involved in the problem.

BNWF models (see e.g. [41–48]) are popular due to the possibility of implementing all kinds of geometrical and material behaviour laws with limited complexity, which makes them versatile and computationally not very costly. However, modelling the soil medium through a series of one-dimensional springs, usually uncoupled among them, constitutes an approach with limitations when it comes to taking into account the three-dimensionality of the problem, and specially in stratified or anisotropic soils. At the same time, the characterization of the laws of the nonlinear springs is not a trivial task, and involves a significant amount of uncertainty. For instance, Rhamani et al. [49] found recently that BNWF models fail to predict accurately the response of soil-pile systems under dynamic or seismic loads even if they incorporate API p-y curves or more specific p-y curves derived from continuum models. Consequently, they recommended the use of continuum models.

Gerolymos et al. [46] found a good agreement between results of a BNWF model and those of a nonlinear FEM for the dynamic analysis of piles including soil and interface nonlinearities. In fact, models based on finite element formulations are also very popular (see e.g. [50–52]). They can be advanced, and can incorporate a significant amount of detail and complexity, but are therefore complicated to set up and verify properly, and can be computationally expensive. A significant source of uncertainty lies in the calibration of the different parameters involved, specially those related to the nonlinear constitutive laws. Mesh and boundary conditions imposed at the edges where the soil mesh is truncated, are additional sources of uncertainty.

A different approach is based on approximately incorporating to the model the effects of degradation and lack of bond by including a cylindrical soil zone around the pile whose shear modulus and material damping differ from those of the outer medium [53–56].

In fact, linear equivalent models can be very appealing if they are able to incorporate the most significant features influencing the dynamic response of the soil-pile system. They are computationally very efficient and can be used in substructuring analysis, in optimization algorithms and in parametric studies. However, traditional equivalent linear soil models could underestimate the structural acceleration response under seismic action, as stated recently by Luo et al. [57].

1.3.2 Soil-structure interaction in the seismic response of bridges

Dynamic SSI has been known, for a long time [58, 59], to be a factor that can affect significantly the seismic response of structures, being bridges [60–63] a case of particular interest. When this is the case, the structural model used in the analyses should be

able to take into account, as rigorously as possible, the complex dynamic response of foundations such as the pile group. Such response can be efficiently characterized in the frequency domain when the soil–foundation system is assumed to remain in the linear–elastic range. However, if non–linear phenomena need to be considered in the bridge superstructure, the analyses should be carried out in the time–domain. In this case, if the response of the soil–foundation system is assumed to remain in linear–elastic range, stiffness and damping functions obtained in the frequency domain to characterize the response of the foundations can still be incorporated into the analysis, for instance, by approximating them by pertinent LPMs that can subsequently be used to represent the response of the soil–foundation system in a substructuring scheme [61, 63–66].

Such LPMs are simple systems, with relatively few degrees of freedom, tuned to approximate the dynamic response of a different system (for instance, a foundation) both in the frequency and the time domains. Their application to SSI problems gained momentum with the seminal papers by Wolf [67, 68] proposing the consistent approach, although other simple schemes had already been previously used [64, 69–71]. Thus, there exist now different possible LPMs, with different levels of complexity and accuracy, that can be adopted. However, it is still unclear whether it is justified to use complex LPMs when the aim of the study is analysing the response of the superstructure, and taking into account the simplifying assumptions and the uncertainty associated to all elements in the model built to represent the whole system.

Part of such uncertainty resides in the model adopted to represent the behaviour of the soil. The absence of non–linear response in the foundation is a common simplifying hypothesis, justified by the fact that, in general, foundations must be designed and detailed to avoid substantial permanent deformations [72] and because of the complexity of dealing with the frequency–dependent non–linear nature of soil. Another assumption is related to the model of energy dissipation in the soil. In this regard, classical frequency–independent material damping (labelled as “hysteretic damping” by Bishop [73] in 1955) is the most common choice when the analysis is performed in the frequency domain [74], partly due to its simplicity. This is the case even though it is well known that it gives rise to non–causal and unrealizable structural models. Besides, the adoption of this damping model leads to frequency–response functions with non–zero imaginary parts at zero frequency, which lacks of physical meaning. However, there exist alternative damping models that also show a frequency–independent (or quasi–independent) hysteretic damping but are, at the same time, causal, though rarely used in structural analysis. For such damping models to be causal, it is condition both necessary and sufficient to satisfy the equations of Kramers–Kronig [75], which relates the real and the imaginary parts of the mathematical model. The first hysteretic damping model both causal and with a damping rate almost frequency–independent was proposed by Biot [76] in 1958, with real and imaginary parts both variable with frequency. Later, Makris [77] proposed a model whose initial premise was the invariability of the damping rate with frequency, giving rise to a function whose real part is bounded for all frequencies except for the static value, point at which it tends to $-\infty$. For this reason, the use of Biot’s model is preferred in this research, even if both are causal models suitable for frequency–domain SSI analysis, and both provide very close results for low and medium frequencies. In this respect, and despite the time since its publication, the magnitude of the influence of the use of Biot’s or the classical hysteretic damping model on the seismic response of the superstructure is still unclear

The earthquake resistance of civil structures is based on the concept of energy dis-

sipation, since it would be economically unfeasible to guarantee an elastic response of structures for severe actions. In the case of bridges, namely for strategic structures characterised by high costs of construction, the task of reducing the seismic damage, and hence repair costs after an earthquake, is of paramount importance to assure a good resilience to the society.

Besides the well-known approaches based on seismic passive protection systems, which foresee the use of isolators (such as elastomeric bearings, lead rubber bearings, single or double concave friction pendulums) with or without supplementary dissipative devices (such as viscous dampers) [78–82], the research is also focusing on innovative solutions that take advantage of the inelastic dissipative capabilities of piers, as demonstrated by recent numerical and experimental investigations presented in [83–86].

With reference to bridges developing ductile inelastic mechanisms in the piers under earthquake loading, the role of SSI in the inelastic behaviour has been investigated in the literature mainly focusing on the effects induced by surface or vertical pile foundations.

SSI effects on inelastic bridge response were studied by Ciampoli and Pinto in 1995 [87] by considering a spread footing foundation. They found that, for the analysed set of foundation layouts, SSI effects were not significant, as the inelastic demand remained unaffected. One year later, Elnashai and McClure [88] studied the case of bridge piers on pile foundations, finding that SSI plays a significant role in the response of the system and thus should be included in the seismic assessment, being ductility demand significantly affected by the inclusion of piles. Later, Mylonakis and Gazetas [89] found, through parametric analyses, that SSI in inelastic bridge piers supported on deformable soil may cause significant increases in the ductility demand of the piers, depending on the characteristics of the motion and the structure. The work of Jeremić et al. [90], studying the influence of SSI in the I-880 viaduct, supported this idea and showed that detrimental effects of SSI can be observed depending on the soil properties and on the characteristics of the ground motion [89, 90]. Looking more deeply into this issue, the role of SSI on the collapse of the Hanshin Expressway was analysed by Mylonakis et al. [91]. The bridge consisted of single circular concrete piers monolithically connected to a concrete deck with 18 spans in total, founded on groups of 17 piles in layers of loose to dense sands and moderate to stiff clays. They found that the compliance of the foundation increased the participation of the fundamental mode of the structure, inducing a stronger response. It was shown that the increase in inelastic seismic demand in the piers had exceeded 100% in comparison with piers fixed at the base.

The analysis of previous observations concerning the seismic damage in bridge piers reveals that the characteristics of the induced Foundation Input Motions (FIMs) may play an important role on the bridge response. In this framework, peculiarities of the filtering effects exerted by inclined piles, mainly consisting in an overall reduction of the input motion to the system, are worth of investigation. One of the most important mechanisms, which characterise the kinematic response of inclined pile foundations, is constituted by foundation rotations which are responsible of anti-phase displacements and accelerations of the superstructures, with respect to those induced by the horizontal components of the seismic action. Cap rotation and horizontal free-field ground motion become out of phase when inclining piles parallel to the direction of excitation. This effect depends on the rake angle, as well as on the pile-soil Young's modulus ratio [92]. Beneficial effects were found in idealised linear systems, e.g. [93–95], but as far as the author knows, the effects on the ductility demand of bridge piers have not been studied yet.

1.4 Structure of the dissertation

As will be seen, the SSI phenomena at hand can be tackled by adopting a substructuring scheme. It allows to study the soil-foundation system and the superstructure separately. Traditionally, nonlinear effects relevant to the system response have been structured in three categories, nonlinear material behaviour, geometrical nonlinearities mainly due to large deformations, and nonlinear boundary conditions. The nonlinear behaviour could arise either in the soil-foundation system and/or in the superstructure. The thesis document has been structured in two parts, one focused on the development of an equivalent linear model for the soil-foundation system, and the other focused on the nonlinear response of superstructures taking into account SSI effects.

Attending to the soil-foundation system, in the Part I of the dissertation a numerical model is developed for reproducing the dynamic mechanical behaviour of pile foundations. The model aims to include nonlinear effects due to contact failures and soil yielding at the soil-pile interface through equivalent linear considerations. First, in Chapter 2, the problem at hand is defined, and then, the coupled BEM-FEM model is described. The BEM equations that governs the soil domain behaviour are outlined at the beginning, just after describing the discretization adopted for the soil boundaries and interfaces, and for the piles. The FEM equations that govern the piles dynamic behaviour are then described in detail. Finally, the system modelling section conclude with the implementations of the equivalent linear coupling equations that link the piles into the soil.

In the second chapter of Part I, i.e. Chapter 3, the model is calibrated for the different soil degradation levels for its lateral behaviour. For doing so, a multi-domain BEM is used where the degraded domain is explicitly included in the simulations. The basis of the multi-domain BEM are briefly presented at the beginning of the section. After the BEM-FEM calibration is done through horizontal impedance functions of the soil-foundations systems, verifications of degraded domain damping and varying degraded domain shape implementations are stated. A significant portion of the content of the Part I is included in a manuscript already submitted for publication [96].

Part II of the dissertation focuses on the seismic response of bridge piers on pile groups. This part begins, in the Chapter 4, with the problem definition, the description of the basis of the adopted design procedure for the bridge piers, and the methodology description for the computation of the system response. Then, the chapter continues with the description of the adopted substructuring scheme and the models used for characterizing the soil-foundation behaviour. Then, the nonlinear modelling assumptions of the bridge piers are stated, together with the description of the two adopted LPMs, i.e. the here called “*consistent*” and “*simplified*”.

The influence on the computed seismic response of bridge piers on pile groups depending on the model assumed for the material damping of the soil is presented in Chapter 5. Also, the type of LPM adopted for reproducing the complex dynamic behaviour of the soil-pile foundation resistant forces, necessary for time-domain analyses, is analysed in terms of the bridge pier response. A wide parametric study involving different soil profiles and superstructures is carried out in order to be able to draw general conclusions. The analysis is done into a linear-elastic framework so that the conclusions of the study provide an informed starting point for the study of the more involved nonlinear case.

Following the conclusions generated through the analyses in the linear range, the analysis of the nonlinear response of the bridge piers is explained in Chapter 6. Mainly, the beneficial effects of the use of inclined pile foundations in terms of the damage

reduction at the bridge piers are shown. Results are presented in terms of ductility demand and energy dissipated by damping or by yielding. A significant portion of the content of the Part II has already been published [97], or is part of a manuscript already accepted for publication [98].

Finally, a summary of the most outstanding achievements and conclusions that can be drawn from this work is given in Chapter 7. The dissertation finishes discussing future research directions and developments that could shortly follow this work.

1.5 Published works derived from the Ph.D. Thesis

The work carried out during the realization of the present Ph.D. Thesis have contributed to different publications and communications. Those are detailed in the following.

1.5.1 Contribution to JCR journals

- F González, LA Padrón, S Carbonari, M Morici, JJ Aznárez, F Dezi, and G Leoni. Seismic response of bridge piers on pile groups for different soil damping models and lumped parameter representations of the foundation. *Earthquake Engineering & Structural Dynamics*, 48(3):306–327, 2019. [97]
- F González, S Carbonari, LA Padrón, M Morici, JJ Aznárez, F Dezi, O Maeso, and G Leoni. Benefits of inclined pile foundations in earthquake resistant design of bridges. Submitted to *Engineering Structures*, accepted. [98]
- F González, LA Padrón, JJ Aznárez and O Maeso. Equivalent linear model for the lateral dynamic analysis of pile foundations considering pile-soil interface degradation. Submitted to *Engineering Analysis with Boundary Elements*, under review. [96]

1.5.2 Conference contributions

- F. González, L. A. Padrón, J. J. Aznárez, and O. Maeso. Implementation of the consistent lumped-parameter model for the computation of the seismic response of nonlinear piled structures. In *Proceedings of the 10th International Conference on Structural Dynamics (EURODYN 2017)*. Rome, Italy, 10–13 September 2017. [99]
- F. González, M. Morici, S. Carbonari, F. Dezi, M. C. Capatti, G. Leoni, L. A. Padrón, J. J. Aznárez, and O. Maeso. Lumped Parameter Models for time domain Soil-Structure Interaction analysis: consistent vs. simplified formulations and effects on the superstructure response. In *Proceedings of the 5th International Workshop on Dynamic Interaction of Soil and Structure (DISS_17)*. Rome, Italy, 19–20 October 2017. [100]

Part I

Lateral dynamic analysis of pile foundations considering pile-soil interface degradation

Chapter 2

Problem definition and system modelling

2.1 Introduction

When piles are subjected to significant dynamic loads, such as those caused by machine vibration, wind over the superstructure, or seismic actions, high levels of stress and strain are likely to develop along the pile-soil interface (more probably in the upper parts of the pile) and induce effects such as soil degradation in the soil region immediately adjacent to the pile. Separation (gapping) can also occur close to the soil surface due to the low confinement pressure. These phenomena lead to damaged or imperfect pile-soil interfaces that should be taken into account in the process of design of pile foundations and piled structures subjected to dynamic loads.

This Part I of the dissertation aims at proposing a new equivalent linear numerical model for the approximate analysis of pile-soil systems with degraded or damaged pile-soil interfaces. The model assumes that the soil immediately adjacent to the pile shaft develops a certain level of degradation, which is usually a function of depth. It is well-known that soils that have undergone high levels of strain, experience a process of reduction of its shear modulus and an increase of its material damping ratio (see e.g. [101–103]). This is depicted in Figure 2.1, where the representative shape of the curves of evolution of shear modulus and damping ratio with shear strain are shown. Depending on the stiffness and type of soil (sand, normal- or over-consolidated clay), and also on the depth of the water table or soil properties such as the plasticity index, the variation in the soil shear modulus and material damping ratio as a function of shear strain is different. Eurocode-8 [72], within its fifth part, Section 4.2.3, states that, in such cases, the differences between small-strain values of the shear wave velocity and those compatible with the strain levels induced by the design earthquake should be taken into account, and provides indications on damping ratios and shear modulus reduction factors as a function of ground acceleration ratio.

The proposal is based on a coupled BEM-FEM approach, uniting the advantages of both methods: the piles are modelled as beam with finite elements; the degraded or imperfect pile-soil interface is represented by distributed springs and dashpots whose properties vary with depth; and the soil beyond the degraded interface is modelled by boundary elements. The starting point of this model is another previous one developed by Padrón et al. [23]. That model is based on the idea of a previous static approach (Mendonça and Paiva [104]) where it is assumed that the continuity of the soil is not

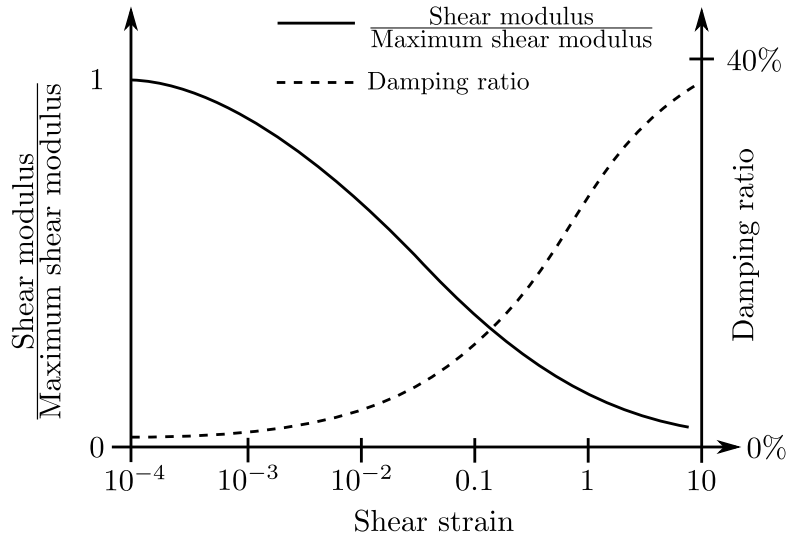


Figure 2.1: Generic depiction of the variation of the soil shear modulus and the soil damping ratio as a function of soil shear strain.

altered by the presence of the piles and where the tractions in the pile-soil interface are considered as a load-line applied within the half-space in the boundary integral representation of the soil. It allows to simplify the formulation of the model without significant loss of accuracy in the problems treated. The perfectly bonded compatibility conditions between pile and soil assumed in that work is generalized in the present to soil-pile equilibrium equations accounting for contact effects through the inclusion of the mentioned distributed springs and dashpots between pile and soil load-line. The formulation can rigorously take into account layered soils and can be generalized to take into account groups of piles and inclined elements. The parameters that define the distributed springs and dashpots along the pile-soil interface can later be calibrated against numerical and empirical results, and can be used in efficient parametric analysis by substructuring or direct methodologies in the frequency domain.

To this end, the developed numerical tool is defined in Section 2.3, and the reference and more rigorous tool used for comparison purposes is defined in Section 3.2. Calibration results are presented in Sections 3.3 in terms of horizontal impedance functions of single pile foundations. Then, the inclusion of the degradation damping, which has been shown to be an essential phenomena involved in the system, is validated in Section 3.4. Also, varying soil degradation through the pile depth is analysed and validated in terms of horizontal impedance functions in Section 3.5.1, and in terms of displacements along the pile length in Section 3.5.2. The new formulation is computationally more efficient and flexible, easing the study of more complex problems. It and can be extended to study pile groups and generalized to rake piles. On the other hand, the possibility for incorporating more genuine and complex models of soil degradation is completely open.

2.2 Problem definition

The problem under consideration is depicted in Figure 2.2. A pile is embedded in a homogeneous or horizontally stratified soil, and is subjected to time harmonic loads (horizontal, vertical or rocking) applied at the pile head. The pile, of length L and di-

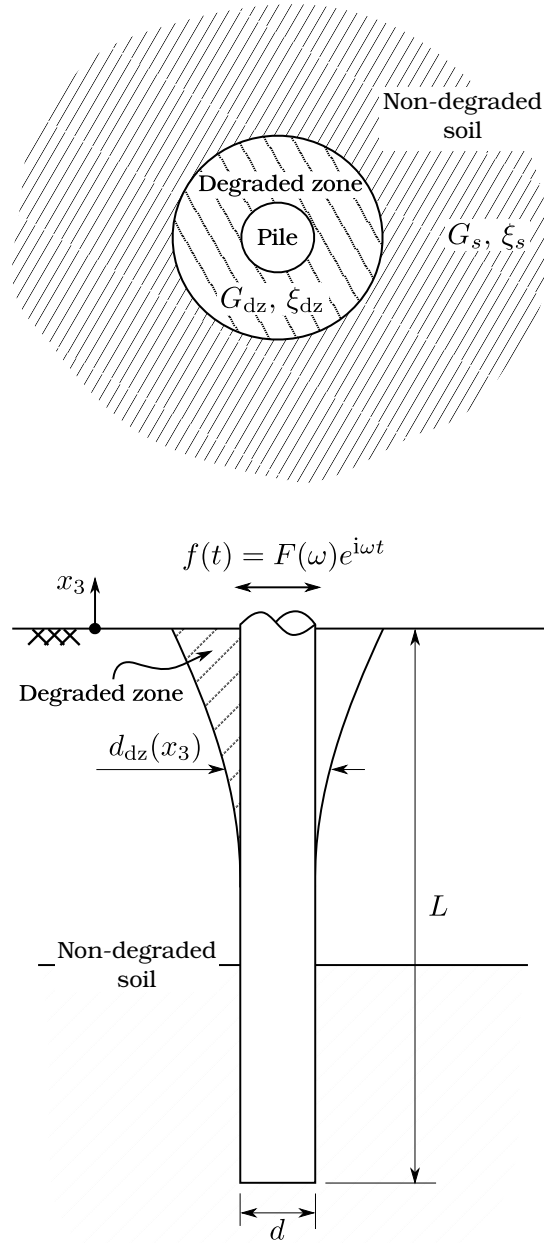


Figure 2.2: Depiction of the problem.

diameter d , is assumed to respond as a linear elastic beam with Young's modulus E_p , area and mass moment of inertia A_p and I_p , and material density ρ_p , and will be modelled with Euler-Bernoulli beam finite elements. The mass moments of inertia with respect to both principal axes of inertia of the pile section have been assumed to be identical. Zero material damping is considered for the pile. The non-degraded soil around the foundation is assumed to respond as a horizontally layered isotropic homogeneous viscoelastic medium with Young's modulus E_{s_i} and density ρ_{s_i} , and will be modelled with boundary elements. The material damping of the soil medium is considered by assuming frequency-independent hysteretic damping through complex valued soil modulus of the type $E_{s_i} = \text{Re}[E_{s_i}](1 + i\xi_{s_i})$, where ξ_{s_i} is the damping coefficient in layer i .

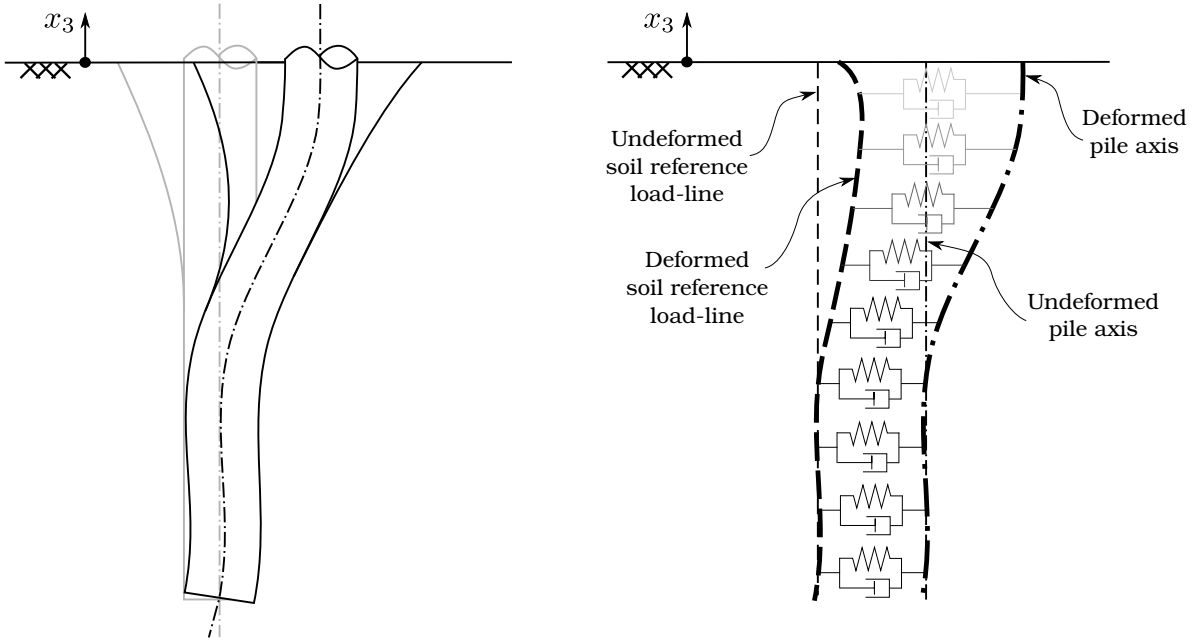


Figure 2.3: Linear equivalent modelling of an imperfect pile-soil interface through distributed springs and dashpots.

2.3 Description of the proposed model

Most models of this kind assume perfectly bonded contact conditions between pile and soil, which would imply imposing compatibility conditions between pile and soil displacements. The model proposed herein for the computation of the dynamic response of piles, on the contrary, seeks to take into account, through an equivalent linear approach, the influence of a damaged pile-soil interface representing soil degradation around the pile, together with possible contact effects such as lack of bond. This imperfect pile-soil interface can be visualized as a degraded soil domain surrounding the piles whose mechanical properties differ from those of the undisturbed soil beyond. Besides, damage at the pile-soil interface will usually be a function of depth, as the largest displacements will usually be experienced near the pile head, coinciding with the lowest soil confinement pressures. For this reason, the diameter $d_{dz}(x_3)$ and shear modulus $G_{dz}(x_3)$ of such degraded domain are assumed to be also a function of depth. The size of this domain in relation to the pile diameter will be denoted by the dimensionless parameter $\chi(x_3) = d_{dz}(x_3)/d$.

As depicted in Figure 2.3, such damaged pile-soil interface is modelled by relating displacements along FEM piles and within BEM soil through distributed springs and dashpots whose properties vary along the pile and that represent the varying stiffness and energy dissipation properties of the pile-soil interface with different levels of degradation at different depths.

The next subsections describe the discretization scheme adopted for pile and soil load-line and, afterwards, the boundary element equations and the beam finite element equations used to describe the dynamic response of non-degraded soil and pile, respectively. The following subsection introduces the equations used to model the imperfect pile-soil interface described above and couple both formulations through distributed springs and dashpots that relate pile and soil displacements and whose properties can change along the pile length. Finally, all involved equations are assembled into a global system matrix

of equations.

2.3.1 Pile and soil load-line discretization

Piles are discretized using three-nodded Euler-Bernoulli beam finite elements with axial deformation, with thirteen degrees of freedom defined in each element: one vertical and two lateral displacements at each node, and two rotations at each one of the extreme nodes, one around each lateral axis of the pile (i.e., torsion excluded). Figure 2.4 depicts the element, axes and the symbols used to refer to each one of the variables involved. ξ is the elemental dimensionless coordinate varying from $\xi = -1$ to $\xi = 1$. The lateral displacements u_1^p and u_2^p along the pile element are approximated by a set of fourth degree shape functions, while vertical displacements u_3^p are approximated by the three Lagrangian polynomials of second order, so that one can write

$$u_i^p(\xi) = \varphi_1 u_{k_i}^p + \varphi_2 \theta_{k_i}^p + \varphi_3 u_{l_i}^p + \varphi_4 u_{m_i}^p + \varphi_5 \theta_{m_i}^p; \quad i = 1, 2 \quad (2.1a)$$

$$u_3^p(\xi) = \phi_1 u_{k_3}^p + \phi_2 u_{l_3}^p + \phi_3 u_{m_3}^p \quad (2.1b)$$

where

$$\varphi_1(\xi) = \xi \left(-\frac{3}{4} + \xi + \frac{1}{4}\xi^2 - \frac{1}{2}\xi^3 \right) \quad (2.2a)$$

$$\varphi_2(\xi) = \frac{L_e}{8} \xi (-1 + \xi + \xi^2 - \xi^3) \quad (2.2b)$$

$$\varphi_3(\xi) = 1 - 2\xi^2 + \xi^4 \quad (2.2c)$$

$$\varphi_4(\xi) = \xi \left(\frac{3}{4} + \xi - \frac{1}{4}\xi^2 - \frac{1}{2}\xi^3 \right) \quad (2.2d)$$

$$\varphi_5(\xi) = \frac{L_e}{8} \xi (-1 - \xi + \xi^2 + \xi^3) \quad (2.2e)$$

and

$$\phi_1(\xi) = \frac{1}{2} \xi (\xi - 1) \quad (2.3a)$$

$$\phi_2(\xi) = 1 - \xi^2 \quad (2.3b)$$

$$\phi_3(\xi) = \frac{1}{2} \xi (\xi + 1) \quad (2.3c)$$

This last set of functions is also used to interpolate within each element the pile-soil contact interaction forces \mathbf{q}^p acting over the pile as

$$q_i^p(\xi) = \phi_1 q_{k_i}^p + \phi_2 q_{l_i}^p + \phi_3 q_{m_i}^p; \quad i = 1, 2, 3 \quad (2.4)$$

Similarly, the displacements along the load-lines within the soil are interpolated, also within the element defined before, through an equivalent scheme

$$u_i^{\text{int}} = \phi_1 u_{k_i}^{\text{int}} + \phi_2 u_{l_i}^{\text{int}} + \phi_3 u_{m_i}^{\text{int}}; \quad i = 1, 2, 3 \quad (2.5)$$

where $u_{(\cdot)_i}^{\text{int}}$ are the unknown displacements at internal soil BEM points coinciding with the beam finite element nodes (see Figure 2.4).

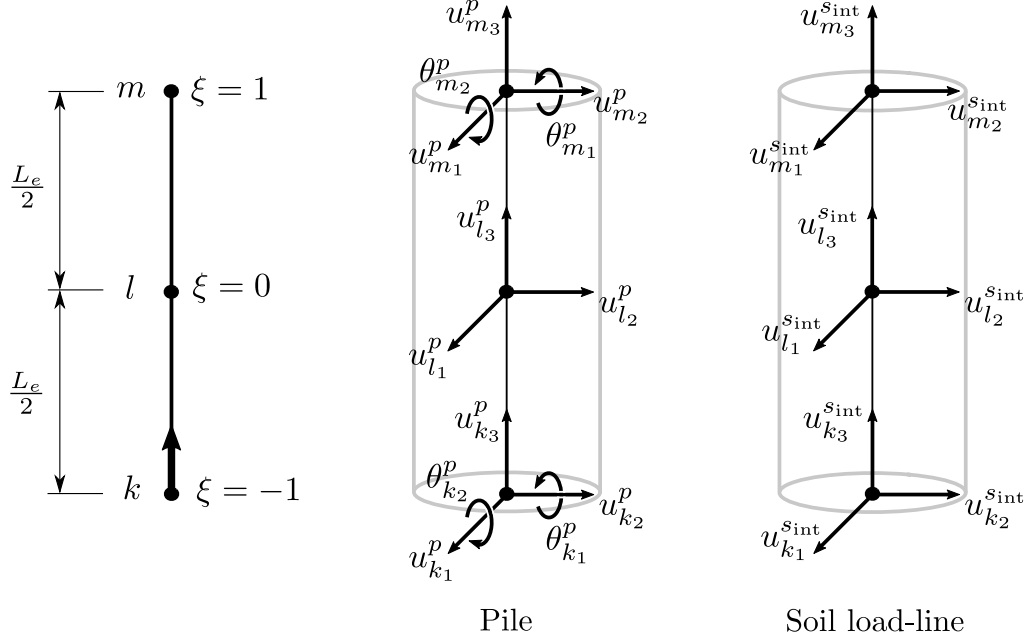


Figure 2.4: Discretization of pile and soil load-lines.

2.3.2 Boundary element equations

As mentioned before, each stratum of the layered non-degraded soil domain is modelled by BEM. The boundary integral equation for a time-harmonic elastodynamic state defined in a domain Ω_m with boundary Γ^m can be written in a condensed and general form as

$$\mathbf{c}^t \mathbf{u}^t + \int_{\Gamma^m} \mathbf{p}^* \mathbf{u} d\Gamma = \int_{\Gamma^m} \mathbf{u}^* \mathbf{p} d\Gamma + \int_{\Omega_m} \mathbf{u}^* \mathbf{X} d\Gamma \quad (2.6)$$

where \mathbf{c}^t is the local free term matrix at collocation point \mathbf{x}^t , \mathbf{X} are the body forces in the domain Ω_m , \mathbf{u} and \mathbf{p} are the displacement and traction over the boundaries, and \mathbf{u}^* and \mathbf{p}^* are the elastodynamic fundamental solution tensors corresponding to the complete space (Cruse and Rizzo [105]).

From the point of view of this formulation for the dynamic behaviour of the soil medium, it is assumed that the soil continuity is not altered by the presence of the piles or by the degraded zone around them. In turn, the effects of the pile-soil interaction are introduced through internal distributed forces located along a load-line within the soil medium. This distributed forces, that will depend on the relationship mentioned above between displacements along the pile and within the soil medium, are treated as body forces, and being the sole body forces involved in the problem, Equation (2.6) can be written as

$$\mathbf{c}^t \mathbf{u}^t + \int_{\Gamma^m} \mathbf{p}^* \mathbf{u} d\Gamma = \int_{\Gamma^m} \mathbf{u}^* \mathbf{p} d\Gamma + \int_{\Gamma_l^m} \mathbf{u}^* \mathbf{q}_s d\Gamma_l \quad (2.7)$$

where Γ_l^m is the soil load-line within the domain Ω_m and \mathbf{q}_s are the pile-soil contact interaction forces induced within the soil domain (see Figure 2.5a).

These tractions along the soil load-line will also be interpolated in terms of the nodal pile-soil contact interaction forces \mathbf{q}^s defined at internal points coinciding with the nodes

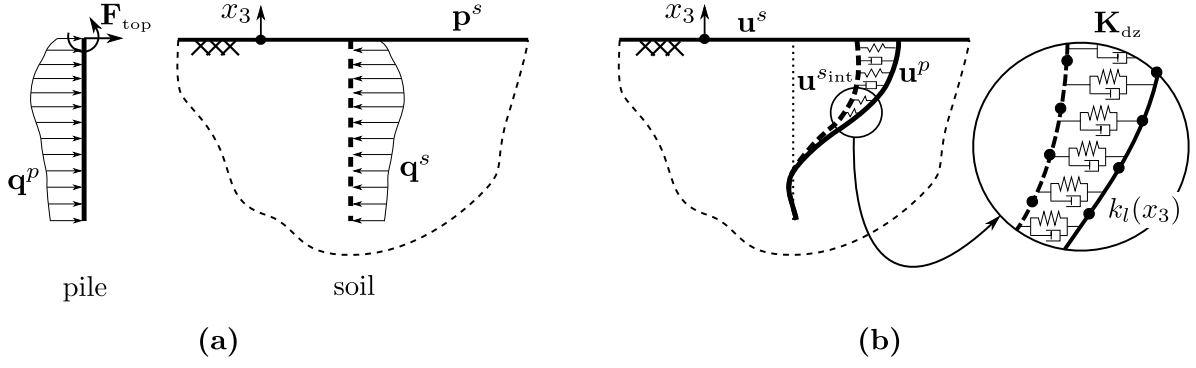


Figure 2.5: Equilibrium conditions between pile and soil load-line.

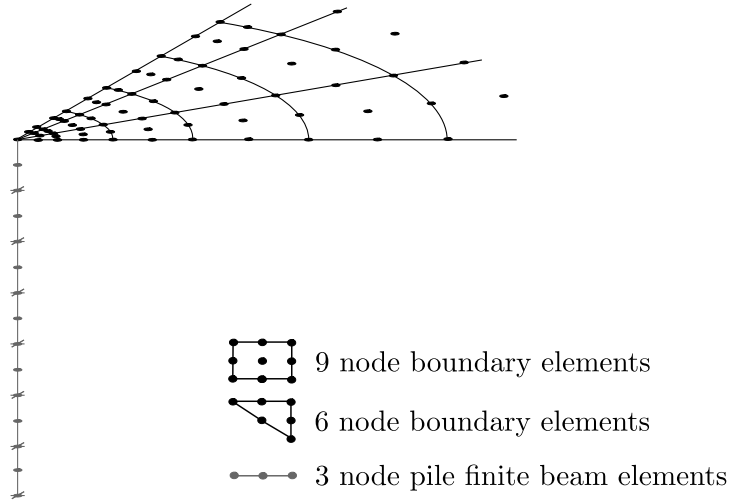


Figure 2.6: Example of mesh typology used in the model (only a quarter of the geometry is shown).

of the beam pile finite elements defined before as

$$q_i^s(\xi) = \phi_1 q_{k_i}^s + \phi_2 q_{l_i}^s + \phi_3 q_{m_i}^s; \quad i = 1, 2, 3 \quad (2.8)$$

As shown in Figure 2.6, the boundaries Γ^m are discretized into quadratic elements of triangular and quadrilateral shapes with six and nine nodes, respectively. Once all boundaries have been discretized, for each region Ω_m , Equation (2.7) can be written in all nodes on Γ^m in order to obtain a matrix equation of the type

$$\mathbf{H}^{ss} \mathbf{u}^s - \mathbf{G}^{sl} \mathbf{q}^s = \mathbf{G}^{ss} \mathbf{p}^s \quad (2.9)$$

where \mathbf{u}^s and \mathbf{p}^s are, respectively, the vectors of nodal displacements and tractions on the boundary elements, \mathbf{H}^{ss} and \mathbf{G}^{ss} are coefficient matrices obtained by integration over the boundary elements of the fundamental solution times the corresponding shape functions, and \mathbf{G}^{sl} is the coefficient matrix obtained by numerical integration over the soil load-line of the fundamental solution times the interpolation functions shown in Equation (2.3), when the unit load is applied on Γ^m .

Furthermore, Equation (2.7) must be also applied on the internal nodes of the soil load-line leading to

$$\mathbf{H}^{ls} \mathbf{u}^s - \mathbf{G}^{ll} \mathbf{q}^s + \mathbf{C} \mathbf{u}^{s_{\text{int}}} = \mathbf{G}^{ls} \mathbf{p}^s \quad (2.10)$$

where \mathbf{H}^{ls} and \mathbf{G}^{ls} are coefficient matrices obtained by numerical integration over the boundary elements of the fundamental solution times the corresponding shape functions, \mathbf{G}^{ll} is the coefficient matrix obtained by numerical integration over the soil load-line of the fundamental solution times the interpolation functions shown in Equation (2.3) when the unit load is applied on the soil load-line, and $\mathbf{u}^{s_{\text{int}}}$ is the vector of nodal displacements along the soil load-line, which is multiplied by the diagonal matrix \mathbf{C} , whose non-zero terms are valued 1/2 in positions corresponding to pile nodes placed on a smooth surface, as e.g. pile heads, and unity at the internal points.

2.3.3 Finite element equations

The time-harmonic dynamic response of the piles, discretized using the linear elastic beam finite elements described in Section 2.3.1, can be described, in the finite element sense, by the matrix equation

$$(\mathbf{K}^p - \omega^2 \mathbf{M}^p) \mathbf{u}^p - (\mathbf{K}^s - \omega^2 \mathbf{M}^s) \mathbf{u}^{s_{\text{int}}} = \mathbf{F}_{\text{top}} + \mathbf{Q} \mathbf{q}^p \quad (2.11)$$

where \mathbf{M}^p and \mathbf{K}^p are the global mass and stiffness global matrices of the pile, \mathbf{u}^p is the vector of nodal displacements along the pile, \mathbf{F}_{top} are the forces at the top of the pile, \mathbf{Q} is the global matrix that transforms tractions along the pile to equivalent nodal forces and moments, and ω is the circular frequency of the excitation.

In the case of models where welded contact conditions between pile and soil are assumed, the equation of motion presented in Equation (2.11) does normally not include the second term in brackets multiplied by the vector of nodal displacements along the soil load-line $\mathbf{u}^{s_{\text{int}}}$, where \mathbf{M}^s and \mathbf{K}^s are the global mass and stiffness matrices of the soil column occupied by the pile shaft. The soil continuity, from the point of view of the BEM model for the soil, is not altered by the presence of the pile. This fact entails that the model would initially overestimate the inertia and stiffness of the pile by taking also into account those of the mentioned soil column. This effect is well known and, given that the inertial effect is very significant, and much more important than the effect of the additional stiffness, it has usually been corrected by subtracting the material soil density from the pile density (see for instance [2, 18, 19, 23]).

On the other hand, displacements along pile and soil load-line are, in the present model, related but not rigidly linked, which prevents from following the simpler strategy mentioned in the previous paragraph and forces to subtract those additional inertia and stiffness proportionally to the displacements of the soil, and not to the displacements of the pile.

These two aspects justify the introduction of the $-(\mathbf{K}^s - \omega^2 \mathbf{M}^s) \mathbf{u}^{s_{\text{int}}}$ term, where the mass and stiffness matrices of the soil column have been computed assuming the shear beam model. Section 3.6 presents an example where the influence of each term is illustrated.

Taking into account the discretization described above, and the corresponding shape functions, the element stiffness sub-matrices corresponding to the lateral and axial behaviour (denoted by l and a , respectively) of the pile can be obtained by using the principle of virtual displacements (see e.g. [106]):

$$k_{ij}^{pi} = \int_{L_e} \varphi_i'' \cdot E_p I_p \cdot \varphi_j'' dx_3; \quad i, j = 1, 2, 3, 4, 5 \quad (2.12)$$

and

$$k_{ij}^{pa} = \int_{L_e} \phi_i' \cdot E_p A_p \cdot \phi_j' dx_3; \quad i, j = 1, 2, 3 \quad (2.13)$$

where primes denote derivative with respect to x_3 . These expressions yield the following sub-matrices

$$\mathbf{K}^{pi} = \frac{E_p I_p}{15L_e} \begin{bmatrix} \frac{316}{L_e^2} & \frac{94}{L_e} & \frac{-512}{L_e^2} & \frac{196}{L_e^2} & \frac{-34}{L_e} \\ \frac{94}{L_e} & 36 & \frac{-128}{L_e} & \frac{34}{L_e} & -6 \\ \frac{-512}{L_e^2} & \frac{-128}{L_e} & \frac{1024}{L_e^2} & \frac{-512}{L_e^2} & \frac{128}{L_e} \\ \frac{196}{L_e^2} & \frac{34}{L_e} & \frac{-512}{L_e^2} & \frac{316}{L_e^2} & \frac{-94}{L_e} \\ \frac{-34}{L_e} & -6 & \frac{128}{L_e} & \frac{-94}{L_e} & 36 \end{bmatrix} \quad (2.14)$$

and

$$\mathbf{K}^{pa} = \frac{E_p A_p}{3L_e} \begin{bmatrix} 7 & -8 & 1 \\ -8 & 16 & -8 \\ 1 & -8 & 7 \end{bmatrix} \quad (2.15)$$

Similarly, the element stiffness sub-matrices corresponding to the lateral and axial behaviour of the soil column are obtained as

$$k_{ij}^{si} = \int_{L_e} \varphi_i' \cdot G_s A_p \cdot \varphi_j' dx_3; \quad i = 1, 2, 3, 4, 5; j = 1, 2, 3 \quad (2.16)$$

and

$$k_{ij}^{sa} = \int_{L_e} \phi_i' \cdot E_s A_p \cdot \phi_j' dx_3; \quad i, j = 1, 2, 3 \quad (2.17)$$

leading to the following sub-matrices

$$\mathbf{K}^{si} = \frac{G_s A_p}{15L_e} \begin{bmatrix} 31 & -32 & 1 \\ -L_e & 2L_e & -L_e \\ -32 & 64 & -32 \\ 1 & -32 & 31 \\ L_e & -2L_e & L_e \end{bmatrix} \quad (2.18)$$

and

$$\mathbf{K}^{sa} = \frac{E_s A_p}{3L_e} \begin{bmatrix} 7 & -8 & 1 \\ -8 & 16 & -8 \\ 1 & -8 & 7 \end{bmatrix} \quad (2.19)$$

Concerning the mass influence coefficients for a pile element, that represents the inertia force opposing the acceleration experimented by a certain degree of freedom, can be evaluated by a similar procedure as

$$m_{ij}^{pl} = \int_{L_e} \varphi_i \cdot \bar{m}^p \cdot \varphi_j dx_3; \quad i, j = 1, 2, 3, 4, 5 \quad (2.20)$$

and

$$m_{ij}^{pa} = \int_{L_e} \phi_i \cdot \bar{m}^p \cdot \phi_j dx_3; \quad i, j = 1, 2, 3 \quad (2.21)$$

Thus, considering a beam with uniformly distributed mass $\bar{m}^p = \rho_p \pi d/4$, the consistent mass matrices obtained for the lateral and axial behaviours are, respectively

$$\mathbf{M}^{pl} = \bar{m}^p L_e \begin{bmatrix} \frac{13}{63} & \frac{L_e}{63} & \frac{4}{63} & \frac{-23}{630} & \frac{L_e}{180} \\ \frac{L_e}{63} & \frac{L_e^2}{630} & \frac{2L_e}{315} & \frac{-L_e}{180} & \frac{L_e^2}{1260} \\ \frac{4}{63} & \frac{2L_e}{315} & \frac{128}{315} & \frac{4}{63} & \frac{-2L_e}{315} \\ \frac{-23}{630} & \frac{-L_e}{180} & \frac{4}{63} & \frac{13}{63} & \frac{-L_e}{63} \\ \frac{L_e}{180} & \frac{L_e^2}{1260} & \frac{-2L_e}{315} & \frac{-L_e}{63} & \frac{L_e^2}{630} \end{bmatrix} \quad (2.22)$$

and

$$\mathbf{M}^{pa} = \frac{\bar{m}^p L_e}{30} \begin{bmatrix} 4 & 2 & -1 \\ 2 & 16 & 2 \\ -1 & 2 & 4 \end{bmatrix} \quad (2.23)$$

Similarly, mass element sub-matrices coefficients of the soil column can be obtained as

$$m_{ij}^{sl} = \int_{L_e} \varphi_i \cdot \bar{m}^s \cdot \phi_j dx_3; \quad i = 1, 2, 3, 4, 5; j = 1, 2, 3 \quad (2.24)$$

and

$$m_{ij}^{sa} = \int_{L_e} \phi_i \cdot \bar{m}^s \cdot \phi_j \, dx_3; \quad i, j = 1, 2, 3 \quad (2.25)$$

yielding

$$\mathbf{M}^{sl} = \bar{m}^s L_e \begin{bmatrix} \frac{23}{140} & \frac{11}{105} & \frac{-1}{28} \\ \frac{L_e}{84} & \frac{L_e}{105} & \frac{-L_e}{210} \\ \frac{4}{105} & \frac{16}{35} & \frac{4}{105} \\ \frac{-1}{28} & \frac{11}{105} & \frac{23}{140} \\ \frac{L_e}{210} & \frac{-L_e}{105} & \frac{-L_e}{84} \end{bmatrix} \quad (2.26)$$

and

$$\mathbf{M}^{sa} = \frac{\bar{m}^s L_e}{30} \begin{bmatrix} 4 & 2 & -1 \\ 2 & 16 & 2 \\ -1 & 2 & 4 \end{bmatrix} \quad (2.27)$$

where $\bar{m}^s = \rho_s \pi d/4$ is the distributed mass of the soil column.

Again, using the principle of the virtual displacements, the coefficients of matrix \mathbf{Q} for lateral forces can be obtained as

$$q_{ij}^l = \int_{L_e} \varphi_i \phi_j \, dx_3; \quad i = 1, 2, 3, 4, 5; \quad j = 1, 2, 3 \quad (2.28)$$

and the ones for axial forces as

$$q_{ij}^a = \int_{L_e} \phi_i \phi_j \, dx_3; \quad i, j = 1, 2, 3 \quad (2.29)$$

from which the following matrices for lateral and axial equivalent nodal forces, respectively, can be derived

$$\mathbf{Q}^l = L_e \begin{bmatrix} \frac{23}{140} & \frac{11}{105} & \frac{-1}{28} \\ \frac{L_e}{84} & \frac{L_e}{105} & \frac{-L_e}{210} \\ \frac{4}{105} & \frac{16}{35} & \frac{4}{105} \\ \frac{-1}{28} & \frac{11}{105} & \frac{23}{140} \\ \frac{L_e}{210} & \frac{-L_e}{105} & \frac{-L_e}{84} \end{bmatrix} \quad (2.30)$$

$$\mathbf{Q}^a = \frac{L_e}{30} \begin{bmatrix} 4 & 2 & -1 \\ 2 & 16 & 2 \\ -1 & 2 & 4 \end{bmatrix} \quad (2.31)$$

2.3.4 Model of the soil-pile interface

The relative displacements between pile and soil load-line $\mathbf{u}^p - \mathbf{u}^{s_{\text{int}}}$ are related to the pile-soil contact interaction distributed forces (see Figure 2.5). Therefore, for an infinitesimal section at a certain depth x_3 , one can write:

$$k_l (u_i^p - u_i^{s_{\text{int}}}) = q_i^p; \quad i = 1, 2 \quad (2.32a)$$

$$k_a (u_3^p - u_3^{s_{\text{int}}}) = q_3^p \quad (2.32b)$$

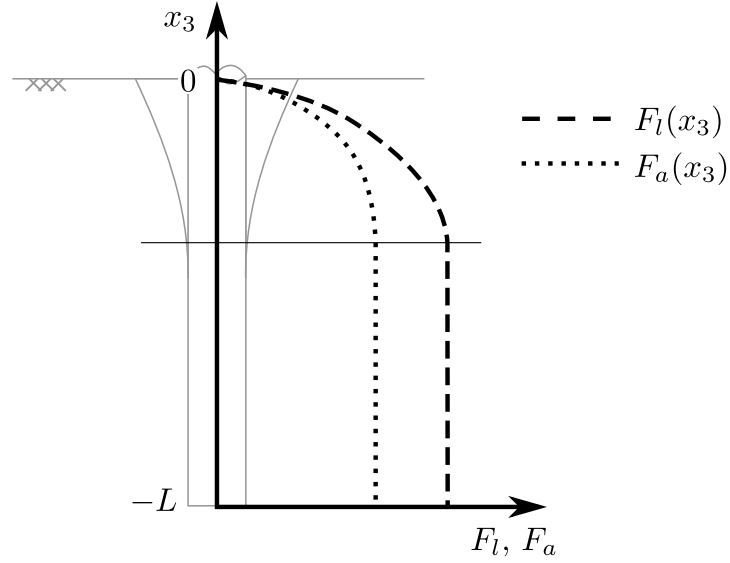
where $k_l = k_l(\chi, G_{\text{dz}}/G_s)$ and $k_a = k_a(\chi, G_{\text{dz}}/G_s)$ are the lateral and axial distributed impedances, respectively, that represent the stiffness and damping properties of the degraded pile-soil interface. In both cases, material damping is introduced assuming a frequency-independent hysteretic damping model through complex valued coefficients of the form $k_{(\cdot)} = \text{Re}[k_{(\cdot)}](1 + 2i\xi_{\text{dz}})$, where ξ_{dz} is the soil-pile contact damping coefficient. These distributed impedances can be written as

$$k_l(\chi, G_{\text{dz}}/G_s) = F_l(\chi, G_{\text{dz}}/G_s) \cdot E_s \quad (2.33a)$$

$$k_a(\chi, G_{\text{dz}}/G_s) = F_a(\chi, G_{\text{dz}}/G_s) \cdot G_s \quad (2.33b)$$

where $F_l(\chi, G_{\text{dz}}/G_s)$ and $F_a(\chi, G_{\text{dz}}/G_s)$ are proportionality functions that determine the strength of the bond between the pile and the soil. Taking into account that both the diameter and the shear modulus of the degraded zone will, in general, be functions of depth ($\chi = \chi(x_3)$ and $G_{\text{dz}} = G_{\text{dz}}(x_3)$), the distributed impedances and the proportionality functions will, in turn, be also x_3 -dependent. Possible distributions of these $F_l(x_3)$ and $F_a(x_3)$ functions are shown in Figure 2.7. Usually, deficient contact effects will be concentrated close to the ground surface, which is represented by lower values of the proportionality functions in that region than in deeper zones. Later, different values of F_l and F_a will be proposed depending on the level of degradation in the damaged pile-soil interface. It is worth noting here that Equation (2.33) is similar to the one provided by Guin and Banerjee [22]. In that case, however, the proportionality functions appear divided by the pile diameter d , leading to pile diameter dependent functions.

Taking into account the discretization proposed in Section 2.3.1 for the displacements along pile and soil load-line (Equations (2.1) and (2.5)) and the corresponding sets of shape functions (Equations (2.2) and (2.3)), element stiffness sub-matrices can be computed by premultiplying Equation (2.32) by the shape functions in Equation (2.3) and integrating along each element. Those element stiffness sub-matrices are labelled as $\mathbf{K}_{\text{dz}}^{pl}$, $\mathbf{K}_{\text{dz}}^{pa}$, $\mathbf{K}_{\text{dz}}^{sl}$ and $\mathbf{K}_{\text{dz}}^{sa}$, where the indices l and a stand for lateral and axial, respectively, and p and s refer to pile and soil load-line. Then, the entries of the element stiffness sub-matrices can be computed as


 Figure 2.7: Possible distributions of the F_l and F_a proportionality functions.

$$k_{dzij}^{pl} = \int_{L_e} \phi_i \cdot k_l(x_3) \cdot \phi_j dx_3; \quad i = 1, 2, 3; j = 1, 2, 3, 4, 5 \quad (2.34)$$

$$k_{dzij}^{sl} = \int_{L_e} \phi_i \cdot k_l(x_3) \cdot \phi_j dx_3; \quad i, j = 1, 2, 3 \quad (2.35)$$

$$k_{dzij}^{pa} = k_{dzij}^{sa} = \int_{L_e} \phi_i \cdot k_a(x_3) \cdot \phi_j dx_3; \quad i, j = 1, 2, 3 \quad (2.36)$$

For reference, if F_l and F_a are assumed to be constant over the element length, and hence independent of x_3 , the degraded zone element stiffness sub-matrices for the lateral and axial behaviour can be written as

$$\mathbf{K}_{dz}^{pl} = \frac{L_e K_l}{2} \begin{bmatrix} \frac{23}{70} & \frac{L_e}{42} & \frac{8}{105} & \frac{-1}{14} & \frac{L_e}{105} \\ \frac{22}{105} & \frac{2L_e}{105} & \frac{32}{35} & \frac{22}{105} & \frac{-2L_e}{105} \\ \frac{-1}{14} & \frac{-L_e}{105} & \frac{8}{105} & \frac{23}{70} & \frac{-L_e}{42} \end{bmatrix} \quad (2.37)$$

$$\mathbf{K}_{dz}^{sl} = \frac{L_e K_l}{30} \begin{bmatrix} 4 & 2 & -1 \\ 2 & 16 & 2 \\ -1 & 2 & 4 \end{bmatrix} \quad (2.38)$$

$$\mathbf{K}_{dz}^{pa} = \mathbf{K}_{dz}^{sa} = \frac{L_e K_a}{30} \begin{bmatrix} 4 & 2 & -1 \\ 2 & 16 & 2 \\ -1 & 2 & 4 \end{bmatrix} \quad (2.39)$$

However, as $F_l(x_3)$ and $F_a(x_3)$ will usually vary with depth, these matrices will, in general, be evaluated numerically or semi-analytically for each specific case. For example, if a second order approximation of the F_l and F_a values over the element length can be adopted, i.e. $F_l = a_l \xi^2 + b_l \xi + c_l$ and $F_a = a_a \xi^2 + b_a \xi + c_a$, being a_l , a_a , b_l , b_a , c_l and c_a constant values resulting from the approximation, the degraded zone element stiffness sub-matrices for the lateral and axial behaviour can be written as

$$\mathbf{K}_{dz}^{pl} = \frac{L_e K_l}{1260} \begin{bmatrix} 207c_l - 153b_l + & (15c_l - 9b_l + & 48c_l - 48b_l + & -45c_l - 9b_l - & (6c_l + 2a_l)L_e \\ +127a_l & +7a_l)L_e & +16a_l & -17a_l & \\ 132c_l - 108b_l + & (12c_l - 12b_l + & 576c_l + 64a_l & 132c_l + 108b_l + & (-12c_l - 12b_l - \\ +52a_l & +4a_l)L_e & & +52a_l & -4a_l)L_e \\ -45c_l + 9b_l - & (-6c_l - 2a_l)L_e & 48c_l + 48b_l + & 207c_l + 153b_l + & (-15c_l - 9b_l - \\ -17a_l & & +16a_l & +127a_l & -7a_l)L_e \end{bmatrix} \quad (2.40)$$

$$\mathbf{K}_{dz}^{sl} = \frac{L_e K_l}{210} \begin{bmatrix} 28c_l - 21b_l + 18a_l & 14c_l - 14b_l + 6a_l & -7c_l - 3a_l \\ 14c_l - 14b_l + 6a_l & 112c_l + 16a_l & 14c_l + 14b_l + 6a_l \\ -7c_l - 3a_l & 14c_l + 14b_l + 6a_l & 28c_l + 21b_l + 18a_l \end{bmatrix} \quad (2.41)$$

$$\mathbf{K}_{dz}^{pa} = \mathbf{K}_{dz}^{sa} = \frac{L_e K_a}{210} \begin{bmatrix} 28c_a - 21b_a + 18a_a & 14c_a - 14b_a + 6a_a & -7c_a - 3a_a \\ 14c_a - 14b_a + 6a_a & 112c_a + 16a_a & 14c_a + 14b_a + 6a_a \\ -7c_a - 3a_a & 14c_a + 14b_a + 6a_a & 28c_a + 21b_a + 18a_a \end{bmatrix} \quad (2.42)$$

Here, as $F_l = F_l\left(\chi(x_3), \frac{G_{dz}(x_3)}{G_s}\right)$ and $F_a = F_a\left(\chi(x_3), \frac{G_{dz}(x_3)}{G_s}\right)$, the order of F_l and F_a will depend on the chosen x_3 -dependent expressions for the $\chi = \chi(x_3)$ and $G_{dz} = G_{dz}(x_3)$ representations.

Similarly, the entries of the element sub-matrices \mathbf{Q}_{dz}^l and \mathbf{Q}_{dz}^a that transforms tractions along the soil load-line to equivalent nodal forces, are computed as

$$q_{dz_{ij}}^l = q_{dz_{ij}}^a = \int_{L_e} \phi_i \phi_j dx_3; \quad i, j = 1, 2, 3 \quad (2.43)$$

leading to the following terms

$$\mathbf{Q}_{dz}^l = \mathbf{Q}_{dz}^a = \frac{L_e}{30} \begin{bmatrix} 4 & 2 & -1 \\ 2 & 16 & 2 \\ -1 & 2 & 4 \end{bmatrix} \quad (2.44)$$

Finally, after the assembly of the global matrices, Equation (2.32) can be expressed in matrix form as

$$\mathbf{K}_{dz}^p \mathbf{u}^p - \mathbf{K}_{dz}^s \mathbf{u}^{sint} = \mathbf{Q}_{dz} \mathbf{q}^p \quad (2.45)$$

where \mathbf{K}_{dz}^p and \mathbf{K}_{dz}^s are the resulting global stiffness complex matrices for the degraded zone.

2.3.5 Assembly of the global system matrix of equations

Grouping Equations (2.9), (2.10), (2.11) and (2.45), assuming compatibility conditions between strata interfaces and equilibrium along the pile-soil interface ($\mathbf{q}^s = -\mathbf{q}^p$), and considering that acting forces at the top of the pile (\mathbf{F}_{top}) are known together with the tractions at the free surface (usually $\mathbf{p}^s = 0$), the dynamic behaviour of the soil-pile foundation system with a degraded soil zone surrounding the pile is defined by the following system matrix of equations:

$$\begin{bmatrix} \mathbf{H}^{ss} & -\mathbf{G}^{sl} & 0 & 0 \\ \mathbf{H}^{ls} & -\mathbf{G}^{ll} & 0 & \mathbf{C} \\ 0 & \mathbf{Q} & (\mathbf{K}^p - \omega^2 \mathbf{M}^p) & -(\mathbf{K}^s - \omega^2 \mathbf{M}^s) \\ 0 & -\mathbf{Q}_{dz} & -\mathbf{K}_{dz}^p & \mathbf{K}_{dz}^s \end{bmatrix} \begin{bmatrix} \mathbf{u}^s \\ \mathbf{q}^s \\ \mathbf{u}^p \\ \mathbf{u}^{sint} \end{bmatrix} = \begin{bmatrix} \mathbf{G}^{ss} \mathbf{p}^s \\ \mathbf{G}^{ls} \mathbf{p}^s \\ \mathbf{F}_{top} \\ 0 \end{bmatrix} \quad (2.46)$$

Equation (2.46) coincides with that provided by Padrón et al. [23] when $k_l, k_a \rightarrow \infty$, situation in which $\mathbf{u}^{sint} = \mathbf{u}^p$.

Chapter 3

Model calibration and results

3.1 Introduction

The object of this chapter is twofold: (i) to verify that the proposed simplified coupled BEM-FEM model can really be used to study the problem initially described of lateral vibration of a pile with degraded pile-soil interface, and (ii) to calibrate the proportionality function $F_l(\chi, G_{dz}/G_s)$ for such a problem.

To do so, results obtained with the BEM-FEM model proposed herein are going to be compared against the ones obtained from a more rigorous three-dimensional multi-domain BEM approach for three different configurations.

The first configuration is characterized by a degraded zone with constant diameter, extending along the whole pile and with $\xi_{dz} = 0$, and will serve the purpose of obtaining an expression for function $F_l(\chi, G_{dz}/G_s)$. The second configuration will incorporate material damping in the degraded zone as a function of damage, and will be useful to calibrate the damping parameter of the pile-soil interface in the simplified model. Finally, the third configuration will be less simplified, with an inverted truncated conical damaged zone only along the upper part of the pile, and will show that the proposed model and proportionality function is adequate to reproduce also more complex configurations such as this one.

3.2 Multi-domain BEM reference model

The multi-domain BEM model taken as reference for verification and calibration of the coupled BEM-FEM model developed here, is the one developed and implemented by Maeso et al. [17]. Through this model, a rigorous continuum mechanics solution of the problem is obtained. A linear system of equations derives from the singular boundary integral equation for elastodynamics [107]. This way, the unknown boundary displacements and tractions are obtained.

Each of the domains that constitute the soil-foundation system, i.e. pile, half-space and degraded zone, are governed by the integral equation

$$\mathbf{c}'\mathbf{u}' + \int_{\Gamma^m} \mathbf{p}^*\mathbf{u} \, d\Gamma = \int_{\Gamma^m} \mathbf{u}^*\mathbf{p} \, d\Gamma \quad (3.1)$$

corresponding to a continuum, finite or semi-infinite, isotropic, homogeneous, linear, viscoelastic medium. All boundaries are discretized into quadratic elements of triangular and quadrilateral shapes with six and nine nodes, respectively. Then, for each region Ω_m ,

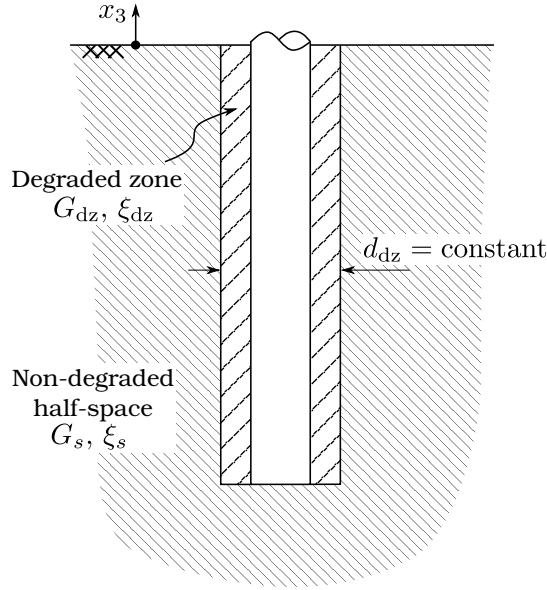


Figure 3.1: First configuration analysed, with a degraded zone of constant diameter along the whole length of the pile.

Equation (3.1) can be written in all nodes on Γ_m in order to obtain a matrix equation of the type

$$\mathbf{H}^{ss} \mathbf{u}^s = \mathbf{G}^{ss} \mathbf{p}^s \quad (3.2)$$

The application of boundary conditions, in terms of tractions or displacements, and compatibility between the different interfaces of the three domains, allows to write the final matrix system of equation that represents the dynamic response of the problem. Hence, three domains are build and meshed for each configuration: one corresponding to the soil half-space (G_s , ν_s , ρ_s and ξ_s), one corresponding to the pile (E_p , ν_p and ρ_p), and the degraded zone domain (G_{dz} , ν_{dz} , ρ_{dz} and ξ_{dz}).

3.3 Calibration of proportionality function F_l

Figure 3.1 illustrates the first configuration of the study, characterized by a degraded zone of constant diameter and extending along the whole length of the pile, which is embedded in a homogeneous half-space. Three different values are adopted for the ratio between the diameters of degraded zone and pile: $\chi = d_{dz}/d = 1.2, 1.4$ and 1.6 . Another five values are considered for the ratio between the shear modulus of degraded zone and half-space, representing different levels of degradation: $G_{dz}/G_s = 1.00, 0.75, 0.50, 0.25$ and 0.10 .

Two soil types are assumed, stiff and soft, with Young's modulus ratios of $E_p/E_s = 100$ and $E_p/E_s = 1000$, respectively, being E_p the pile Young's modulus. In both soil cases, $\xi_s = 0.01$, $\nu_s = 0.4$, being ν_s the soil Poisson's ratio, and the ratio between densities is $\rho_s/\rho_p = 0.7$. The pile aspect ratio is $L/d = 15$. In this calibration procedure no damping in the degraded zone domain is assumed, but as it is considered to be a crucial aspect, mainly in highly degraded soils, its incorporation to the BEM-FEM formulation is verified below.

Results are presented in terms of horizontal impedance functions normalized by pile diameter and soil Young's modulus. Those impedances are frequency dependent complex functions representing the horizontal resistant force of the foundation when the pile tip is horizontally and harmonically displaced a unit length. In the current formulation: $K_{hh} = k_{hh} + ia_0c_{hh}$, in which k_{hh} represents the horizontal foundation stiffness and c_{hh} the horizontal foundation damping, being a_0 the dimensionless frequency defined as $a_0 = \omega d/c_s$, where c_s is the soil shear wave velocity of the undisturbed half-space.

Figures 3.2a and 3.2b show an example of the kind of meshes generated for the reference multi-domain BEM analyses, being (a) and (b) the complete and a pile top zoom view of the multi-domain BEM mesh for the particular degraded zone diameter ratio of $\chi = d_{dz}/d = 1.4$. Figure 3.2c shows a pile top zoom view of the mesh used by the BEM-FEM simulations. It only includes the free surface boundary elements and the pile finite beam elements. It is important to notice the high reduction not only in the mesh complexity, but also in the quantity of elements and nodes, leading to considerable computing time reductions. Having the same free surface discretization, the multi-domain BEM mesh for the specific case mentioned above is composed by 10730 nodes and 4183 elements, while the BEM-FEM mesh includes only 3866 nodes and 960 elements, which represents a reduction of 61% in the number of nodes and of 77% in the number of elements.

The impedance functions obtained from the reference multi-domain BEM model for the different cases specified above are shown in continuous lines in Figures 3.3 and 3.4 for soft and stiff soils, respectively. The calibration of the values of the proportionality function F_l for each of the configurations was achieved by performing a sweep of simulations with the simplified BEM-FEM model and finding the values of F_l that minimize the difference between the impedance functions provided by both models. The resulting values of F_l , offering the better matching to the multi-domain BEM simulation results, are summarized in Table 3.1, and their associated horizontal impedance functions are shown in Figures 3.3 and 3.4 for soft and stiff soils, respectively. A very good agreement is found between the impedance functions provided by both models. The dynamic behaviour of the system is reproduced adequately in all the frequency range with a constant value of F_l through all the pile depth. As expected, the stiffness and damping of the soil-pile foundation system tend to decrease when the G_{dz}/G_s ratio decreases and also when the size of the degraded zone increases. Another relevant aspect is the independence of the F_l parameter on the Young's modulus of the pile E_p , the Young's modulus of the soil E_s , and hence, the Young's modulus ratio of the soil-pile foundation system E_p/E_s . A perfectly bonded behaviour of the pile-soil interface is obtained for $F_l = 25$, used when the soil around the pile is not degraded $G_{dz}/G_s = 1$. The function F_l is also presented in Figure 3.5 to show qualitatively how it changes with χ and G_{dz}/G_s .

The data presented in Table 3.1 has been fitted, by the least-squares technique, to the following polynomial function that can be used for interpolation:

$$\begin{aligned}
F_l = & 6.114 - 8.560\chi + 258.7\frac{G_{dz}}{G_s} + 3.013\chi^2 - 298.8\chi\frac{G_{dz}}{G_s} - 223.3\left(\frac{G_{dz}}{G_s}\right)^2 + \\
& + 90.29\chi^2\frac{G_{dz}}{G_s} + 286.0\chi\left(\frac{G_{dz}}{G_s}\right)^2 - 11.23\left(\frac{G_{dz}}{G_s}\right)^3 - 95.40\chi^2\left(\frac{G_{dz}}{G_s}\right)^2 + \\
& + 27.25\chi\left(\frac{G_{dz}}{G_s}\right)^3 - 9.345\left(\frac{G_{dz}}{G_s}\right)^4
\end{aligned} \tag{3.3}$$

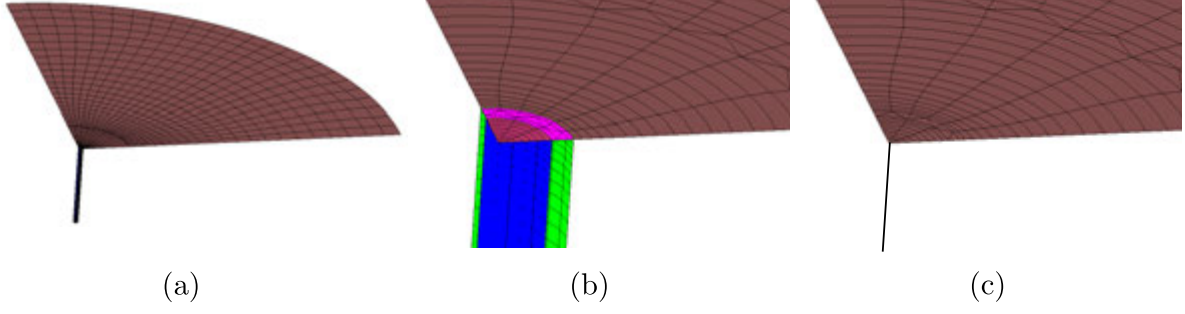


Figure 3.2: Complete (a) and top zoom view (b) of a multi-domain BEM mesh for the particular degraded zone diameter ratio of $\chi = d_{dz}/d = 1.4$, and BEM-FEM mesh detail (c) with 1D elements for the piles. (Only a quarter of the geometry is meshed).

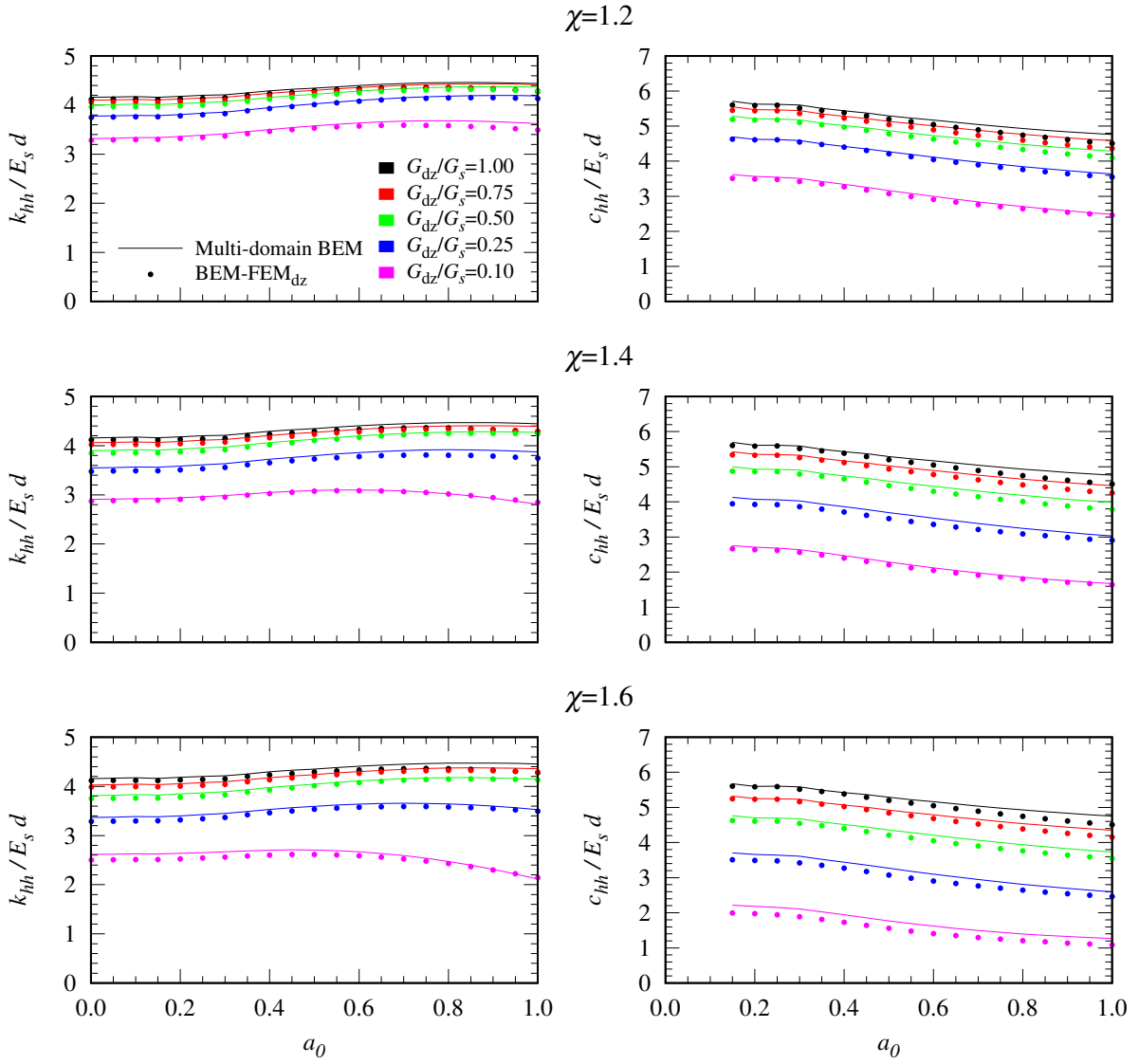


Figure 3.3: Comparison between stiffness and damping function obtained from the proposed BEM-FEM model and the reference multi-domain BEM model for the case depicted in Figure 3.1. $\xi_{dz} = 0$, $E_p/E_s = 1000$.

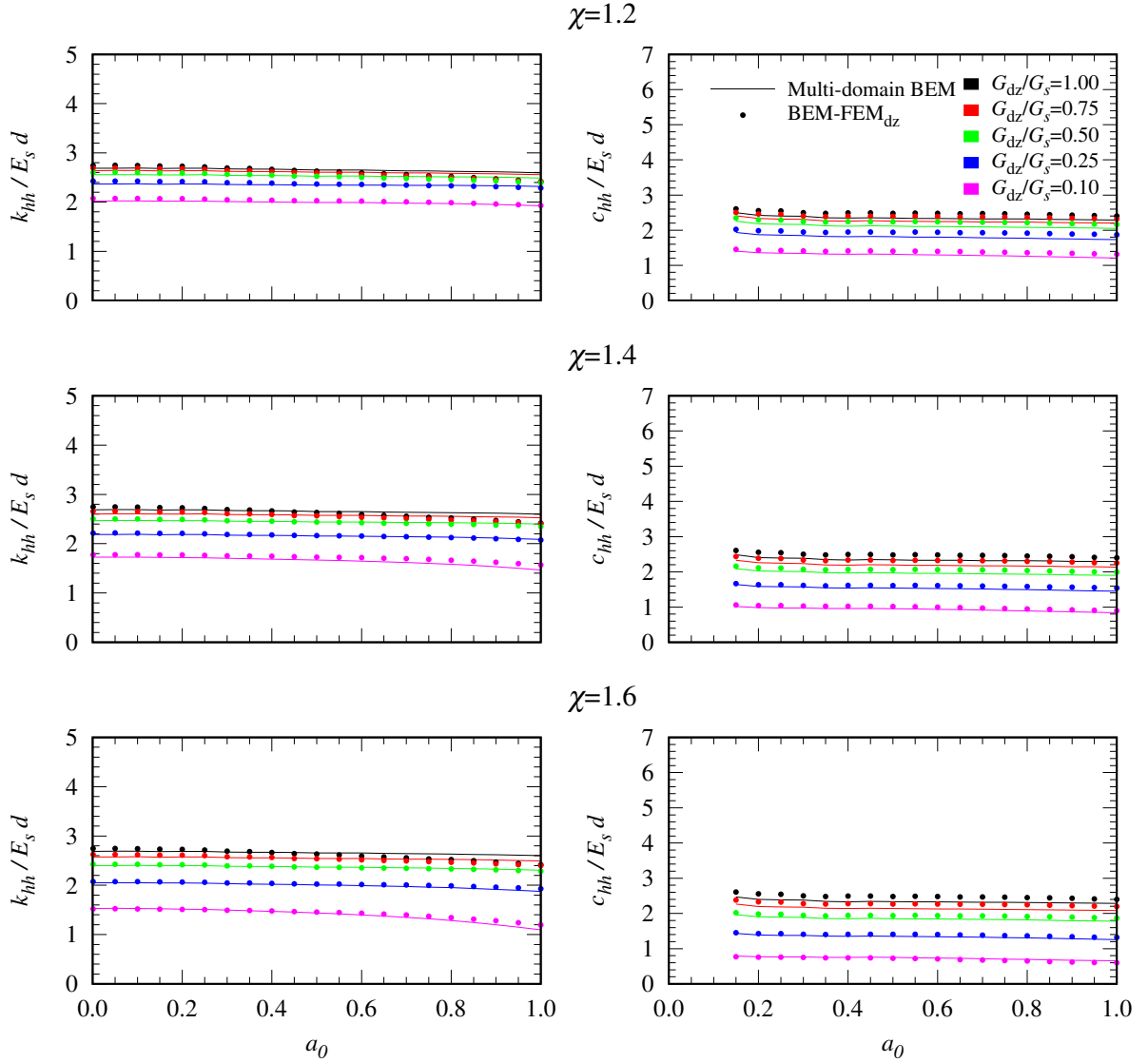


Figure 3.4: Comparison between stiffness and damping function obtained from the proposed BEM-FEM model and the reference multi-domain BEM model for the case depicted in Figure 3.1. $\xi_{dz} = 0$, $E_p/E_s = 100$.

This expression, whose range of application is for $\chi \in [1.2, 1.6]$ and $G_{dz}/G_s \in [0.10, 1.00]$, is plotted in Figure 3.6, where it is shown that it is a smooth surface that contains all the original data present in Table 3.1 (shown in red points).

3.4 Modelling of material damping in the degraded domain

In the previous section, no material damping was initially considered for the degraded zone. However, and as already mentioned in the introduction, the value of the damping ratio increases significantly with the shear strain and the damage in the soil, and must therefore be adequately incorporated into the model. For highly degraded soils, damping ratios can exceed 20%, which can induce significant variations in the dynamic behaviour

		G_{dz}/G_s				
		1.00	0.75	0.50	0.25	0.10
χ	1.2	25.0	19.0	13.0	7.0	3.0
	1.4	25.0	16.0	9.0	4.0	1.8
	1.6	25.0	14.0	7.0	3.0	1.2

Table 3.1: Proposed values of the proportionality function F_l .

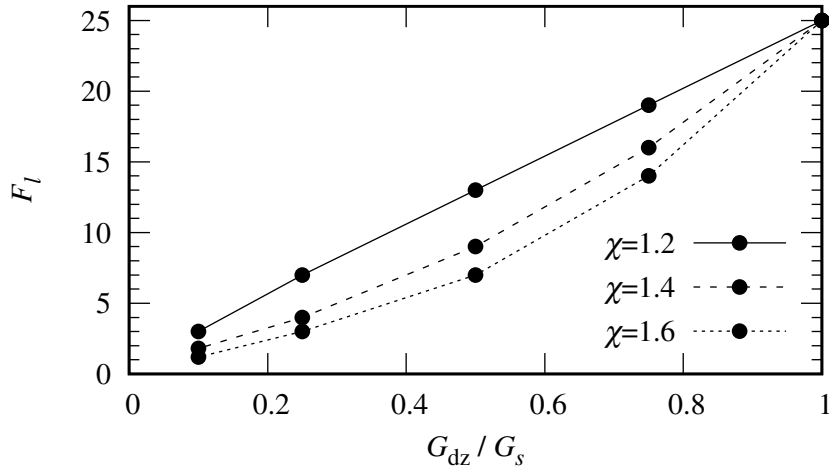


Figure 3.5: Plot of the proposed proportionality function F_l for the specific values of χ and G_{dz}/G_s studied. Point values shown in Table 3.1.

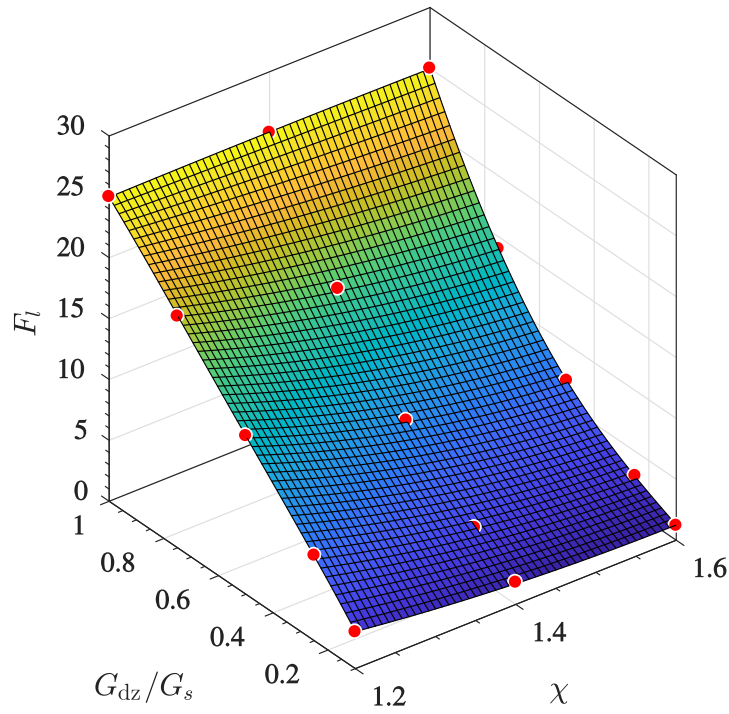


Figure 3.6: Plot of Equation (3.3) for the interpolation of the proportionality function F_l . Point values shown in Table 3.1.

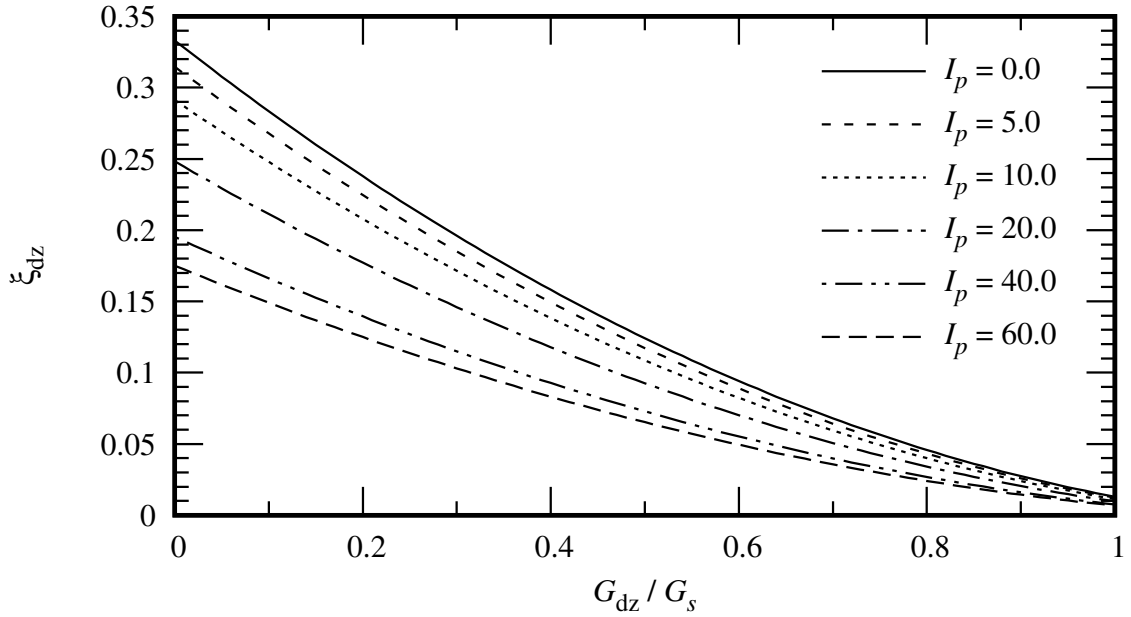


Figure 3.7: Plot of Equation (3.4) for different values of the soil plasticity index I_p .

G_{dz}/G_s	1.00	0.75	0.50	0.25	0.10
ξ_{dz}	0.010	0.043	0.096	0.166	0.218

Table 3.2: Damping ratios of the degraded zone based on the expression proposed by Ishibashi and Zang [103] for different levels of degradation.

of the soil-foundations systems, taking into account that the degraded zone surrounds the vibrating pile.

The expression proposed by Ishibashi and Zang [103] for the degraded soil damping ratios ξ_{dz} , based on experimental tests, is adopted in this section, although other options could also be used. Such expression depends on the plasticity index of the soil I_p and the ratio between the equivalent shear soil modulus and the maximum shear soil modulus G_{dz}/G_{max} :

$$\xi_{dz} = \frac{0.333 \left(1 + e^{-0.0145I_p^{1.3}}\right)}{2} \left[0.586 \left(\frac{G_{dz}}{G_{max}}\right)^2 - 1.547 \left(\frac{G_{dz}}{G_{max}}\right) + 1\right] \quad (3.4)$$

and is shown in Figure 3.7.

Assuming a medium plasticity index ($I_p = 18.0$) and considering that the maximum shear modulus of the soil is the one of the undisturbed half-space domain ($G_{max} = G_s$), the damping ratios shown in Table 3.2 are obtained for the different soil degradation levels adopted herein.

Adopting these damping ratios in the definition of the degraded zones for both in the multi-domain BEM and in the proposed BEM-FEM model, the horizontal impedance functions shown in Figure 3.8 for soft soil and in Figure 3.9 for stiff soil are obtained. The damping coefficients of the impedance functions strongly change if compared with the ones with $\xi_{dz} = 0$ (Figures 3.3 and 3.4 vs. Figures 3.8 and 3.9, respectively). Stiffness functions also vary slightly with the inclusion of the degraded zone damping. The

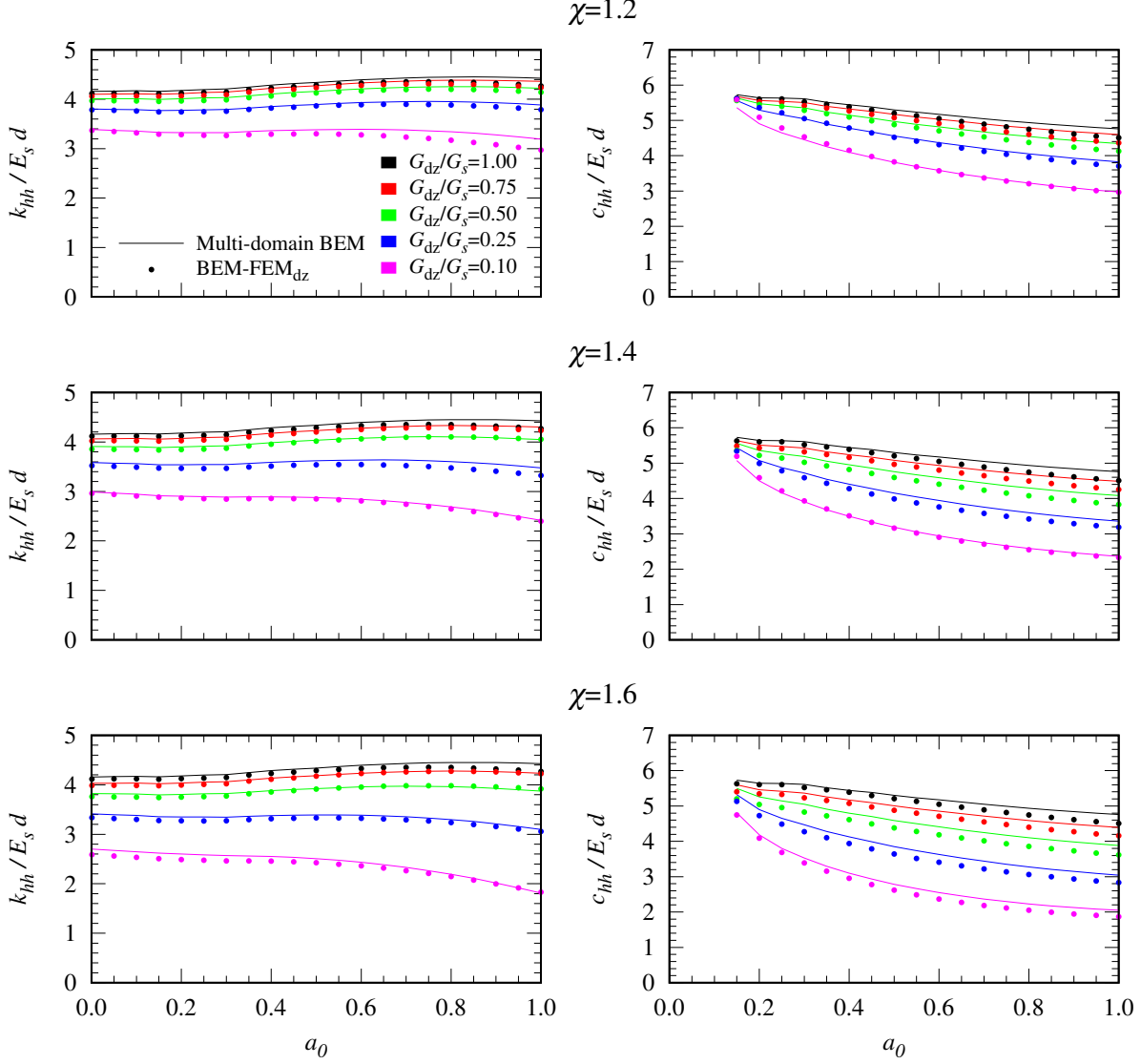


Figure 3.8: Comparison between stiffness and damping function obtained from the proposed BEM-FEM model and the reference multi-domain BEM model for the case depicted in Figure 3.1. $\xi_{dz} \neq 0$, $E_p/E_s = 1000$.

good agreement with the results provided by the reference model is maintained. It is demonstrated that the material damping in the degraded domain is perfectly captured by the simpler BEM-FEM model.

3.5 Verification for a degraded domain with shape changing along pile depth

The utility of the developed tool lies mainly in the possibility of considering a degraded zone whose properties and geometry vary with depth. Usually, the maximum stresses and maximum strains within the soil are located in the surroundings of the piles and close to the surface. Therefore, soil degradation will generally be concentrated in the upper parts of the foundation, and will not be regularly distributed along the pile, as in

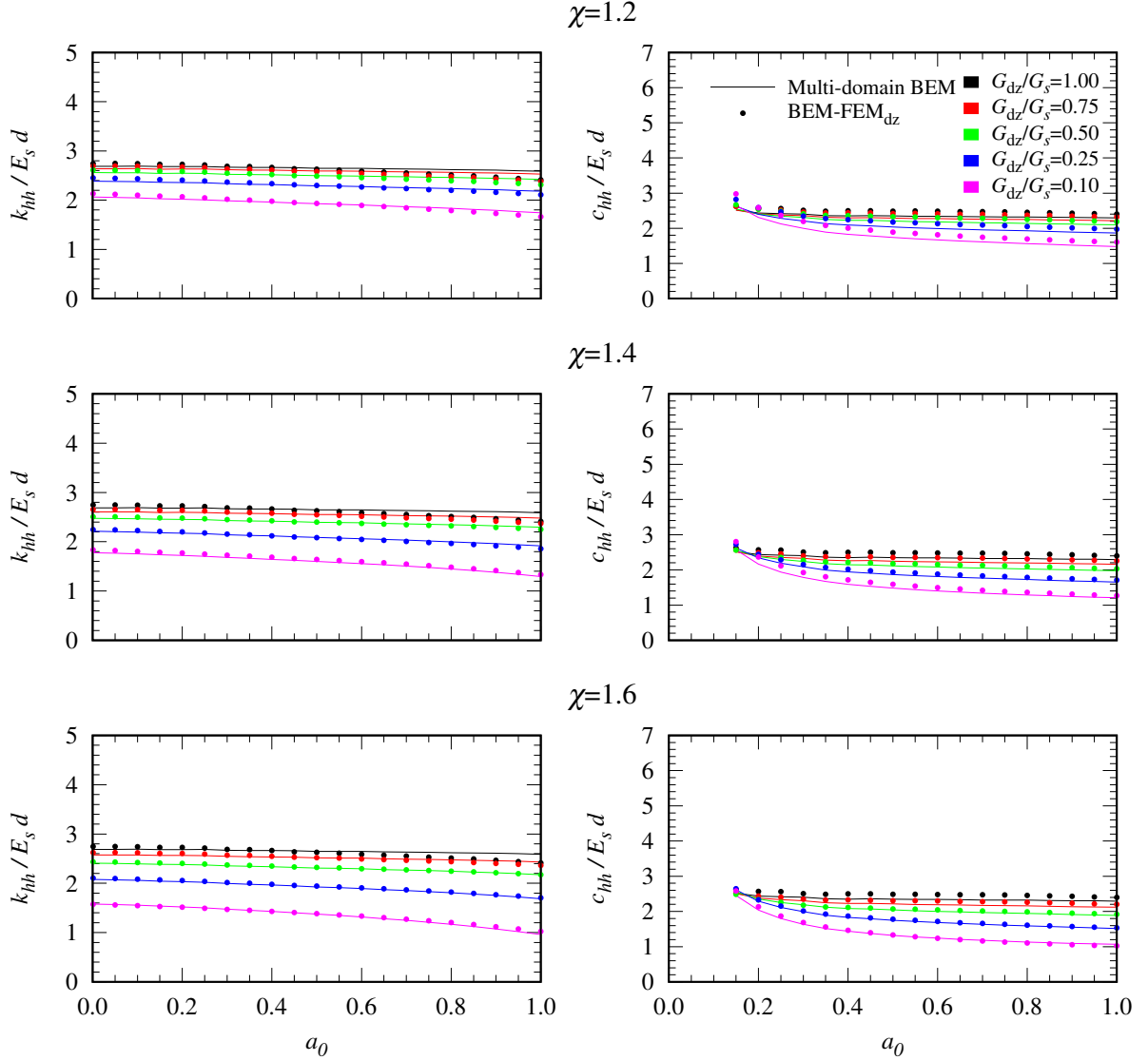


Figure 3.9: Comparison between stiffness and damping function obtained from the proposed BEM-FEM model and the reference multi-domain BEM model for the case depicted in Figure 3.1. $\xi_{dz} \neq 0$, $E_p/E_s = 100$.

the first example studied above. Thus, the aim of this section is checking whether the proportionality function proposed in the previous section can also be applied to more general configurations.

To do this, the configuration represented in Figure 3.10, with an inverted truncated conical degraded zone with $\chi(0) = 1.5$ or 1.6 , $\chi(-h_{dz}) = 1.2$, and $h_{dz}/d = 3.0$ and 6.0 , is considered in this section, being h_{dz} the depth of the degraded zone. Results are presented in terms of impedance functions for $G_{dz}/G_s = 1.00, 0.75, 0.50, 0.25$ and 0.10 , as in the previous section. The configurations are studied with both models. In the case of the proposed BEM-FEM formulation, the proportionality functions found in the previous section are implemented, and the degraded zone damping ratio is obtained from Equation (3.4). On the other hand, Figure 3.11 shows one of the meshes built for the analyses carried out with the reference multi-domain BEM code.

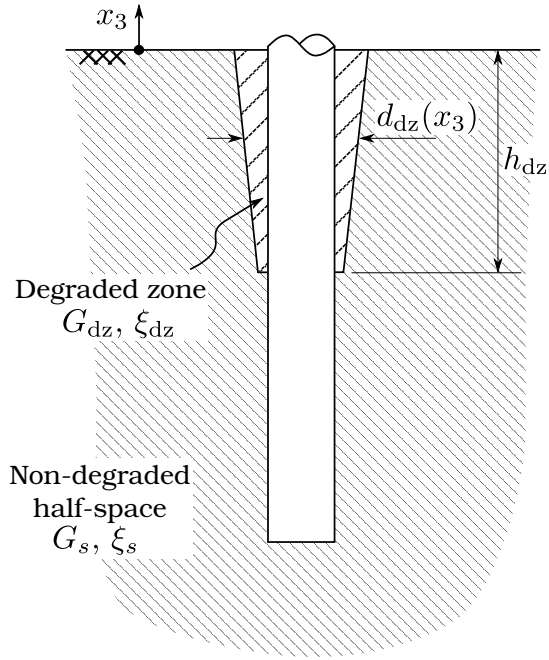


Figure 3.10: Second configuration analysed, with an inverted truncated conical degraded zone.

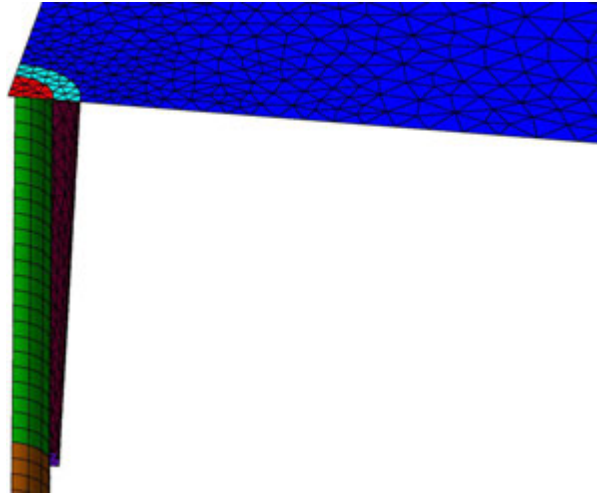


Figure 3.11: Detail of one of the meshes generated for the multi-domain BEM analyses with the inverted conical degraded zone (only a quarter of the geometry is shown).

3.5.1 Verification in terms of impedance functions

Impedance functions corresponding to $E_p/E_s = 1000$, and $\chi(0) = 1.6$ and 1.5 are presented in Figures 3.12 and 3.13, respectively, for different depths of the degraded zone domain ($h_{dz}/d = 3.0, 4.5$ and 6.0). Also, impedance functions corresponding to $E_p/E_s = 100$, and $\chi(0) = 1.6$ and 1.5 are presented in Figures 3.14 and 3.15, respectively, for $h_{dz}/d = 3.0, 4.5$ and 6.0 . It is shown that the proposed model is able to reproduce, with high accuracy, both the stiffness and damping functions provided by the reference multi-domain BEM code, which also means that expression proposed in

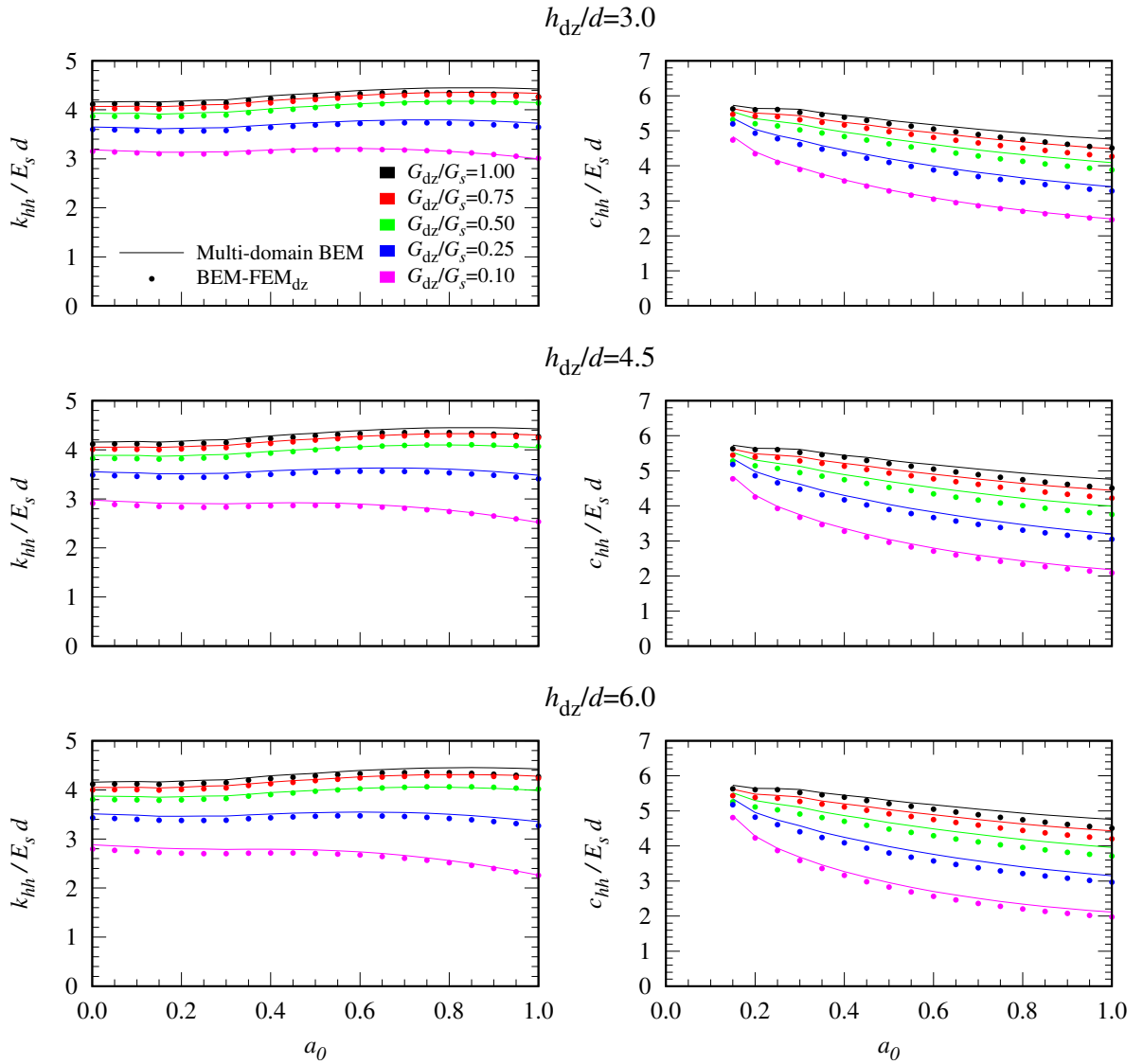


Figure 3.12: Comparison between stiffness and damping function obtained from the proposed BEM-FEM model and the reference multi-domain BEM model for the case depicted in Figure 3.10 with an inverted truncated conical degraded zone. $\xi_{dz} \neq 0$, $\chi(0) = 1.6$ and $E_p/E_s = 1000$.

Equation (3.3) for the proportionality function F_l can be applied to configurations such as the one studied here.

3.5.2 Verification in terms of displacements

Apart from these impedance functions, related to the horizontal displacements at pile head, it is also interesting to explore whether the simplified proposed model is also able to reproduce adequately the response of the pile along its length. To this end, Figure 3.16 presents the distributions of lateral displacements along the pile provided by the proposed BEM-FEM model and the reference multi-domain BEM model for the configuration with $E_p/E_s = 1000$, $\chi(0) = 1.6$ and $h_{dz}/d = 6.0$. The results are presented for the five relative shear moduli considered for the degraded soil ($G_{dz}/G_s = 1.00, 0.75, 0.50, 0.25$ and 0.10)

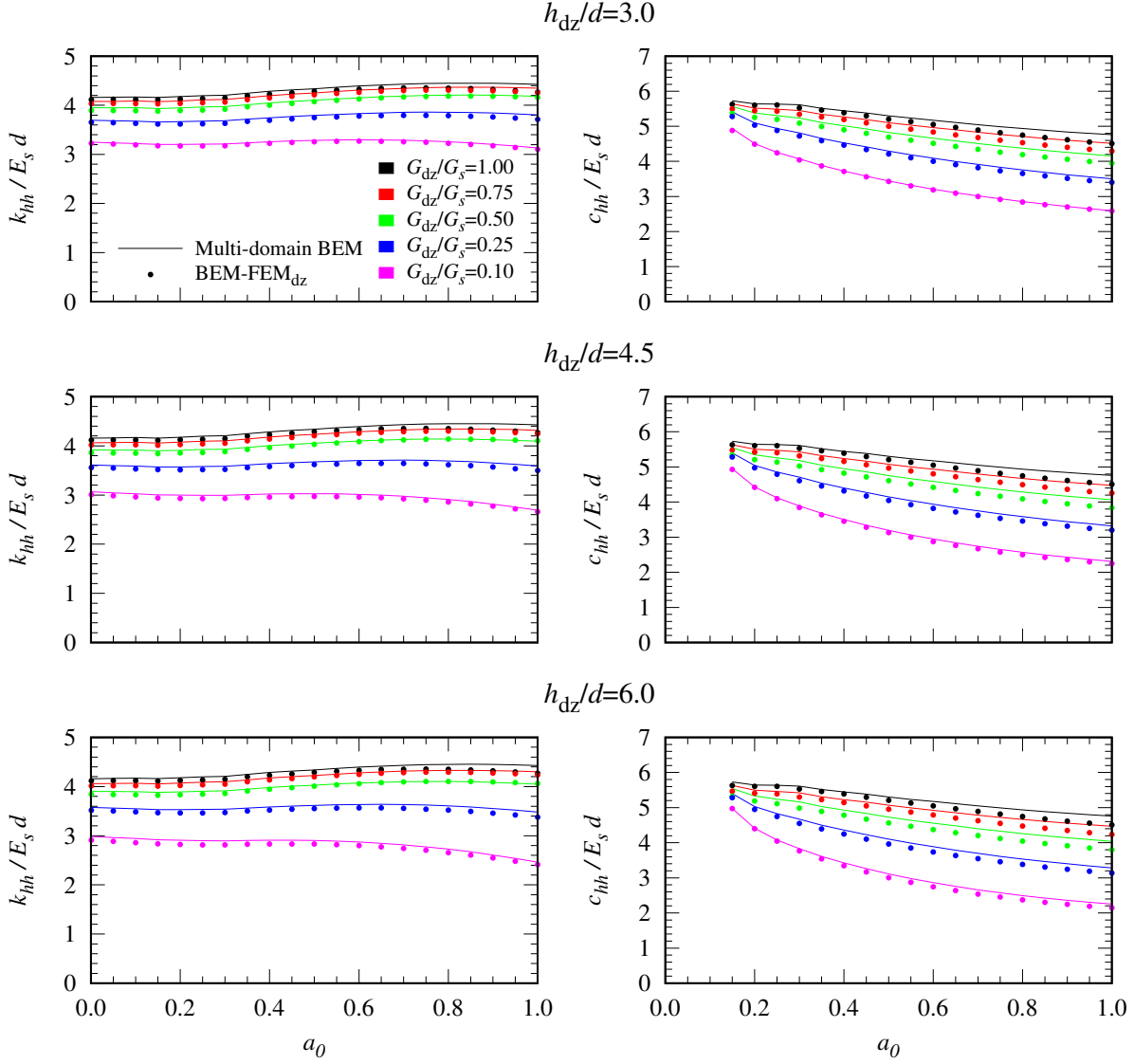


Figure 3.13: Comparison between stiffness and damping function obtained from the proposed BEM-FEM model and the reference multi-domain BEM model for the case depicted in Figure 3.10 with an inverted truncated conical degraded zone. $\xi_{dz} \neq 0$, $\chi(0) = 1.5$ and $E_p/E_s = 1000$.

and for three different dimensionless frequencies: $a_0 = 0.0, 0.5$ and 1.0 . The figure also displays the displacements obtained for the soil load-line in the coupled BEM-FEM model and the displacements obtained along the interface between degraded zone and non-degraded half-space, in the case of the multi-domain BEM reference model. The deformed shapes are normalized by the pile head displacement, and are plotted taking into account the corresponding shape functions (Equations (2.2) or (2.3)).

It can be seen that the agreement between the pile deformed shape obtained from the BEM-FEM model and the reference multi-domain BEM model is very high. It can also be seen that the deformation of the soil load-line follows very accurately that of the degraded zone-half space interface, which means that the term $u^p - u^{s\text{int}}$ is representative of the deformation of the degraded zone.

As expected, the stiffer the degraded zone (from $x_3/d = 0$ to $x_3/d = -h_{dz}/d = -6$,

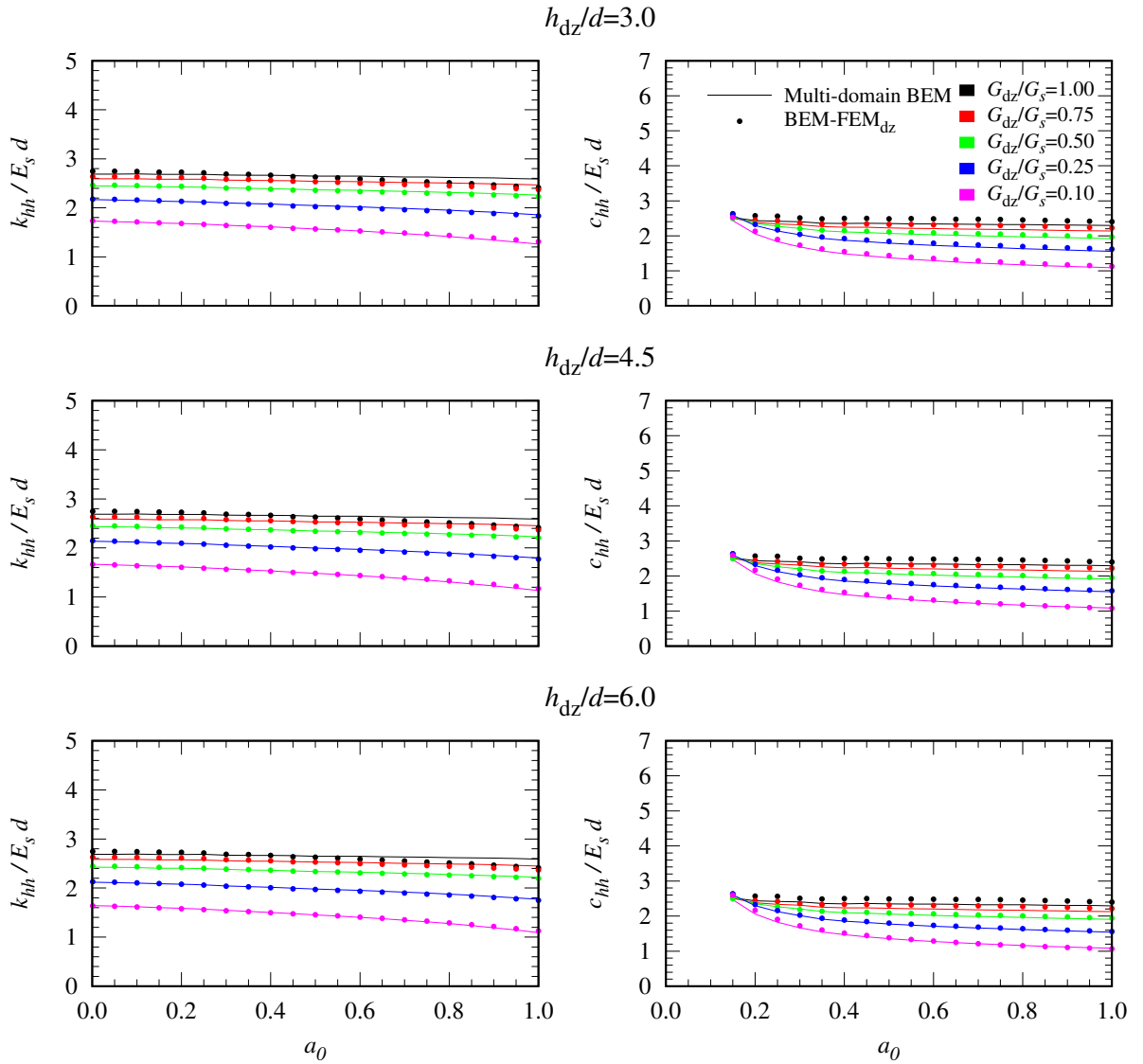


Figure 3.14: Comparison between stiffness and damping function obtained from the proposed BEM-FEM model and the reference multi-domain BEM model for the case depicted in Figure 3.10 with an inverted truncated conical degraded zone. $\xi_{dz} \neq 0$, $\chi(0) = 1.6$ and $E_p/E_s = 100$.

in this case), the smaller is the separation between pile and soil load-line. Below $x_3/d = -h_{dz}/d$, where the contact between pile and soil is no longer considered as damaged, the deformed shapes of pile and soil load-line coincide.

3.6 Influence of the soil column stiffness and inertia terms

As stated in Section 2.3.3, the soil continuity, from the point of view of the soil boundary element equations, is not altered by the presence of the pile. Thus, in order not to be considered twice, the stiffness and inertia of the soil column superimposed to the pile volume needs to be removed from the system. Here, and being the displacements of pile

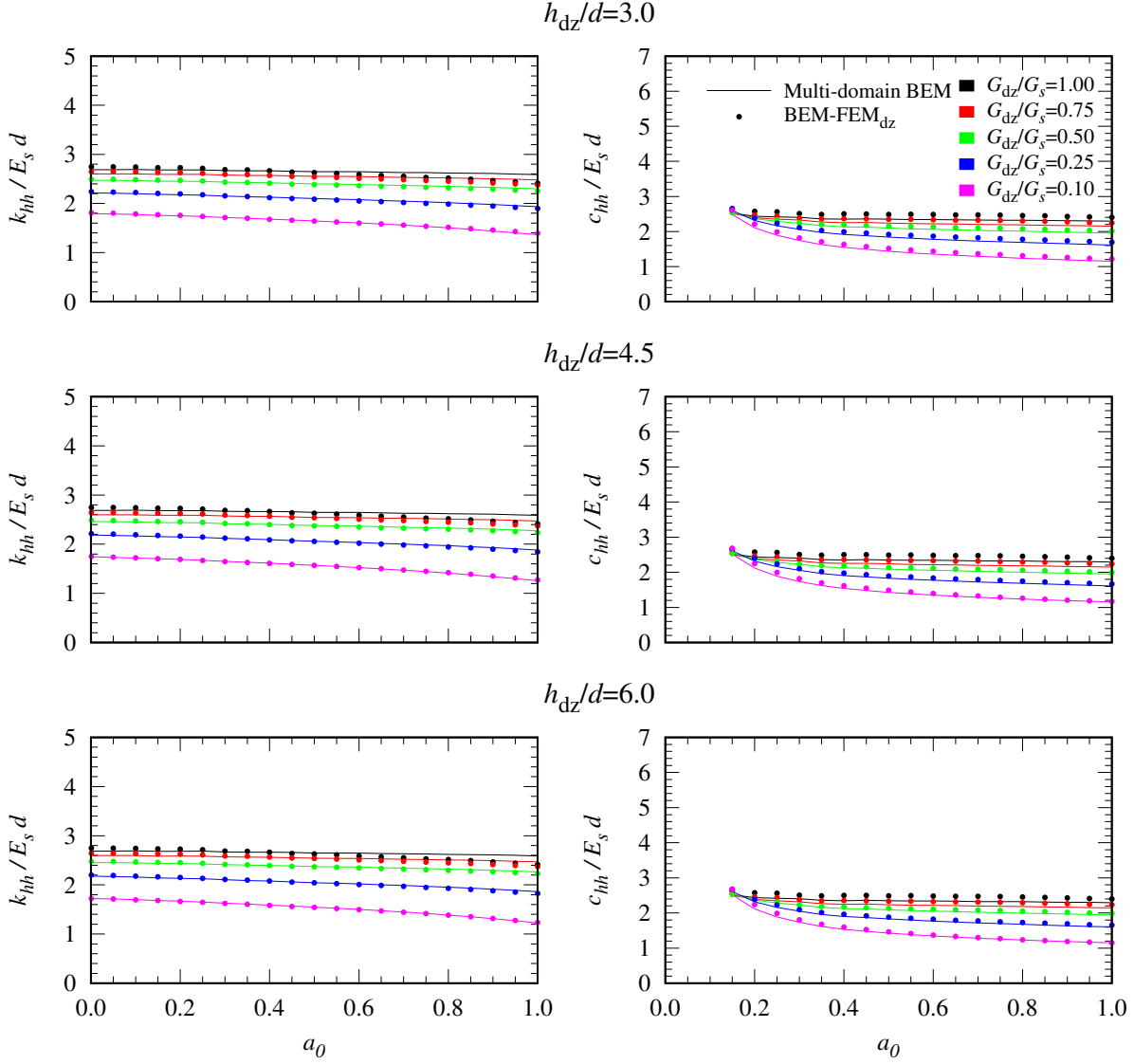


Figure 3.15: Comparison between stiffness and damping function obtained from the proposed BEM-FEM model and the reference multi-domain BEM model for the case depicted in Figure 3.10 with an inverted truncated conical degraded zone. $\xi_{dz} \neq 0$, $\chi(0) = 1.5$ and $E_p/E_s = 100$.

and soil load line not rigidly linked, this is done by subtracting the term $(\mathbf{K}^s - \omega^2 \mathbf{M}^s) \mathbf{u}^{s_{int}}$ in the left hand side of Equation (2.11).

The aim of this section is illustrating the influence of these stiffness and inertia terms. To do so, the dynamic response of the system presented in Section 3.3 is studied using five variations on Equation (2.11):

- Neglecting both additional inertia and stiffness of the soil column:

$$(\mathbf{K}^p - \omega^2 \mathbf{M}^p) \mathbf{u}^p = \mathbf{F}_{top} + \mathbf{Q} \mathbf{q}^p \quad (3.5)$$

- Following the common approach in welded models and subtracting the soil density from the pile density, but keeping the inertia term proportional to pile displacements (see for instance [2, 18, 19, 23]):

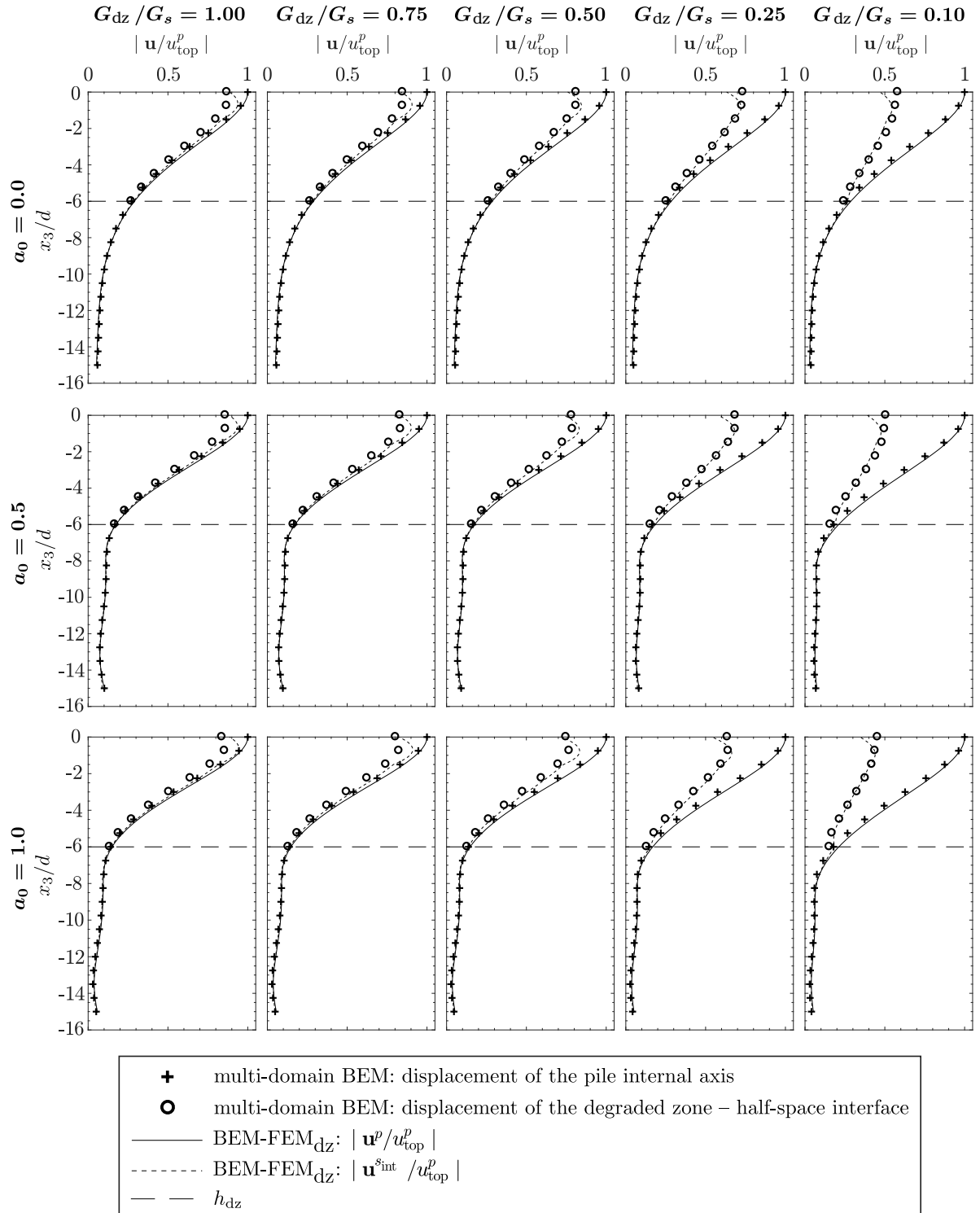


Figure 3.16: Pile and soil load-line displacements for the case of an inverted truncated conical zone with $E_p/E_s = 1000$, $\chi(0) = 1.6$ and $h_{dz}/d = 6.0$ and for different degraded zone degradation levels. Comparison between BEM-FEM and reference multi-domain BEM models.

$$\left(\mathbf{K}^p - \omega^2 \mathbf{M}^p \frac{\rho_p - \rho_s}{\rho_p} \right) \mathbf{u}^p = \mathbf{F}_{\text{top}} + \mathbf{Q}\mathbf{q}^p \quad (3.6)$$

- In parallel to the previous case, subtracting the soil column mass but keeping the inertia term proportional to the soil load-line displacements instead to the pile displacements:

$$(\mathbf{K}^p - \omega^2 \mathbf{M}^p) \mathbf{u}^p + \omega^2 \mathbf{M}^s \mathbf{u}^{s_{\text{int}}} = \mathbf{F}_{\text{top}} + \mathbf{Q}\mathbf{q}^p \quad (3.7)$$

- Subtracting the soil column stiffness from the pile stiffness, but neglecting the inertia term of the soil column:

$$(\mathbf{K}^p - \omega^2 \mathbf{M}^p) \mathbf{u}^p - \mathbf{K}^s \mathbf{u}^{s_{\text{int}}} = \mathbf{F}_{\text{top}} + \mathbf{Q}\mathbf{q}^p \quad (3.8)$$

- Finally, subtracting the soil column stiffness and inertia terms, keeping both terms proportional to the soil load-line displacements (these are the final implemented FEM equations in the current model, see Section 2.3.3):

$$(\mathbf{K}^p - \omega^2 \mathbf{M}^p) \mathbf{u}^p - (\mathbf{K}^s - \omega^2 \mathbf{M}^s) \mathbf{u}^{s_{\text{int}}} = \mathbf{F}_{\text{top}} + \mathbf{Q}\mathbf{q}^p \quad (3.9)$$

Comparison results between the previous stated five variations for the FEM equations are presented in Figure 3.17 in terms of normalized absolute value of the impedance function. Impedances are shown for both soil-pile stiffness ratios ($E_p/E_s = 1000$ and 100) and two limiting cases: a) welded soil-pile interface ($F_l \rightarrow \infty$) and b) a pile that is completely loose from the soil ($F_l \rightarrow 0$) and, therefore, behaves as a free cantilever beam; also an intermediate case is presented ($F_l = 2.0$).

When a perfectly bonded soil-pile interface is considered ($F_l(x_3) \rightarrow \infty$), the displacement fields of the pile and the soil load-line coincides, no matter if the soil column inertia term is linked to the pile or to the soil load-line, and hence the case corresponding to the blue line condense to the case represented by the green line. If this is the case, it is perfectly valid the traditional assumption [2, 18, 19, 23] of subtracting the soil density from the pile density, but keeping the inertia term proportional to pile displacements. As higher is the excitation frequency, higher is the impedance when the soil column mass is removed, i.e. passing from black line to green or light blue lines.

On the other hand, if the soil column stiffness is subtracted to the pile stiffness, dark blue line vs. black line or red line vs. light blue line, a reduction in the impedance function values are only noticeable in the stiff soil case (a reduction of 1.7% for the soft soil case ($E_p/E_s = 1000$) and a reduction of 3.0% in the stiff soil case ($E_p/E_s = 100$) are obtained).

Bringing the model to the limit when $F_l(x_3) \rightarrow 0$, i.e. when the soil-pile interface is completely degraded, it makes the soil column displacements field and the tractions along the soil-pile interface to vanish, $\mathbf{u}^{s_{\text{int}}} \rightarrow 0$ and $\mathbf{q}^p \rightarrow 0$. If the traditional assumption of subtracting the soil density to the pile density is assumed also in the current model, i.e. the green line case, the pile oscillates as a cantilever beam with its not realistic natural frequencies. This is the reason why the soil column mass and stiffness is decoupled from the pile displacements field and linked to the soil load-line displacements field. All the remaining cases, represented by red, light blue and dark blue lines, condense to the case represented by the black line due to $\mathbf{u}^{s_{\text{int}}} \rightarrow 0$, being all lines superimposed. It makes the pile to oscillates at its actual natural frequencies.

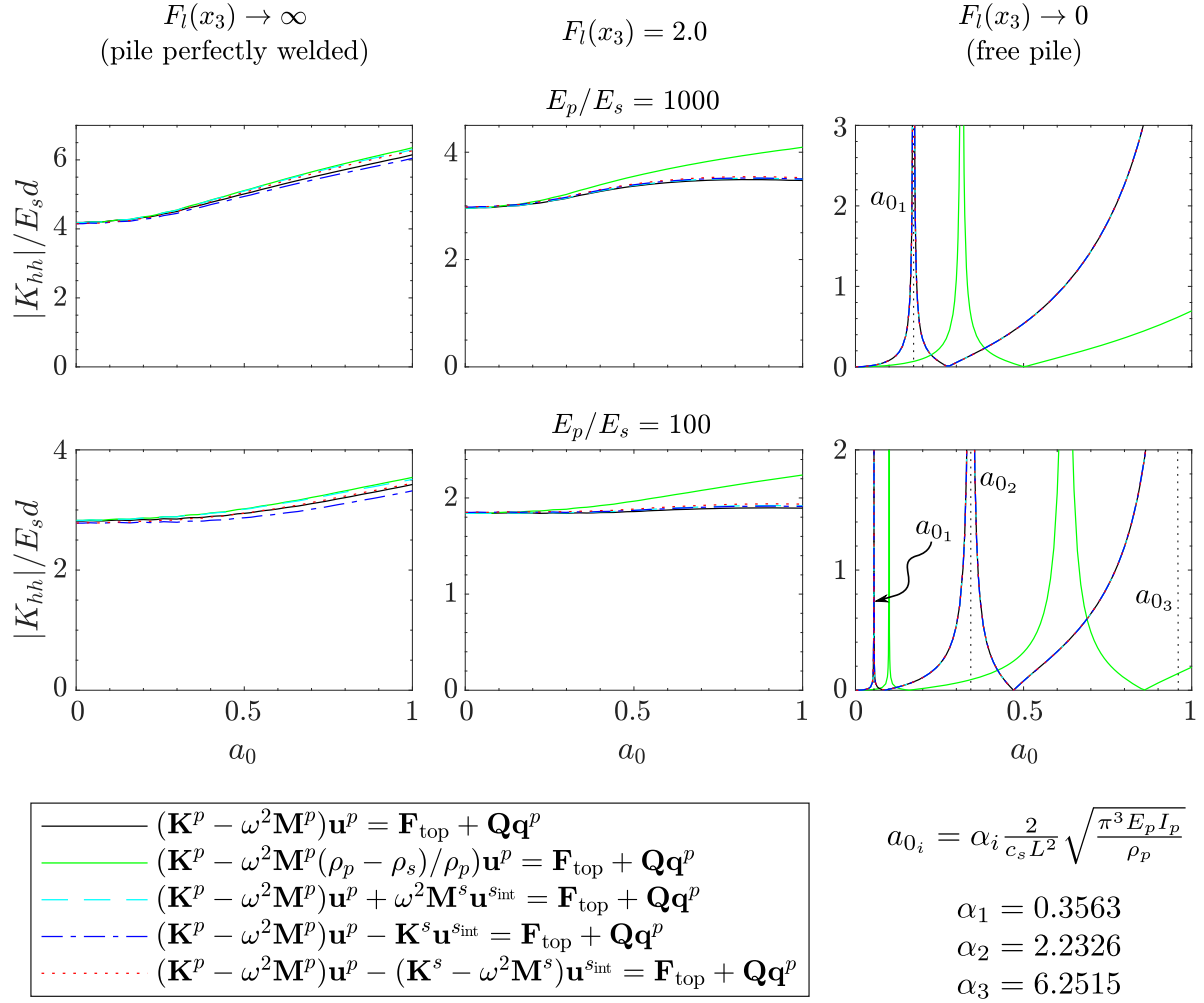


Figure 3.17: Influence of the consideration of the soil column inertia and stiffness in the FEM equations. Absolute value of the horizontal impedance function of a single pile foundation for different representative values of the F_l proportionality function.

3.7 Conclusions

An equivalent linear model for estimating the dynamic horizontal response of piles considering soil degradation along the soil-pile interface has been presented, implemented and calibrated. Taking as a starting point a previous boundary element-finite element coupled model proposed by Padrón et al. [23], the formulation proposed herein incorporates the possibility of modelling an imperfect or damaged soil-pile interface along which bounded contact conditions no longer apply. The proportionality functions used to define the distributed springs and dashpots that relate pile and soil displacements have been calibrated for a specific set of configurations by comparison against results of a multi-domain three-dimensional boundary element code. The formulation proposed herein has been shown to be able to reproduce the impedance functions and displacements provided by the more rigorous and computationally costly reference multi-domain BEM model. The proposed coupled BEM-FEM formulation is not only computationally more efficient (it is 7.5 times faster than the multi-domain BEM for the single pile case tackled here) but is also more versatile, and requires much less work in mesh generation,

which will now allow to study more complex problems. Notice that the speed-up in the computation and the savings in time for the mesh generation will increase as the complexity of the system increases, e.g. simulation with group of piles and/or using pile inclination. The efficiency of the model will also allow to perform parametric analyses or be incorporated in processes that require a large number of evaluations, such as in many optimization techniques.

The formulation can now be extended to model pile groups, as the boundary element approach used to model the soil allows to take rigorously into account pile-soil-pile interaction effects. It can also be generalized to raked piles. Also, the model can be used to obtain results for substructuring analyses, or can incorporate the superstructure or other elements for direct analyses of complete soil-foundation-superstructure systems.

The properties of the pile-soil interface can now be calibrated for different configurations. Here, the comparison against empirical results for specific cases of interest will play a crucial role. At the same time, the definition of those properties of distributed stiffness and damping along the interface could also incorporate more complex models of soil degradation depending for instance on shear strain levels, such as those cited in the literature review (Section 1.3.1).

Part II

Seismic response of bridge piers on pile groups

Chapter 4

Problem definition, methodology and modelling

4.1 Introduction

A multi-span roadway viaduct is a bridge typology that saves a valley or a ravine in its entirety. Viaducts carry the road traffic and the railway above, and usually connect two points at approximately the same height (see Figure 4.1). The deck is supported by equally spaced single piers. In many occasions, and depending on the soil properties, groups of piles are used in the pier foundation. At the base of each pier, a pile cap is embedded into the soil connecting all pile heads. The pile cap collects all the efforts of the superstructure, coming from both the static and dynamic loads, and transmits them to the heads of the piles. Then, those loads are properly passed on to the soil along the piles length.



Figure 4.1: Viaduct of Rodén, Spain (courtesy of Miguel Ángel Tremps).

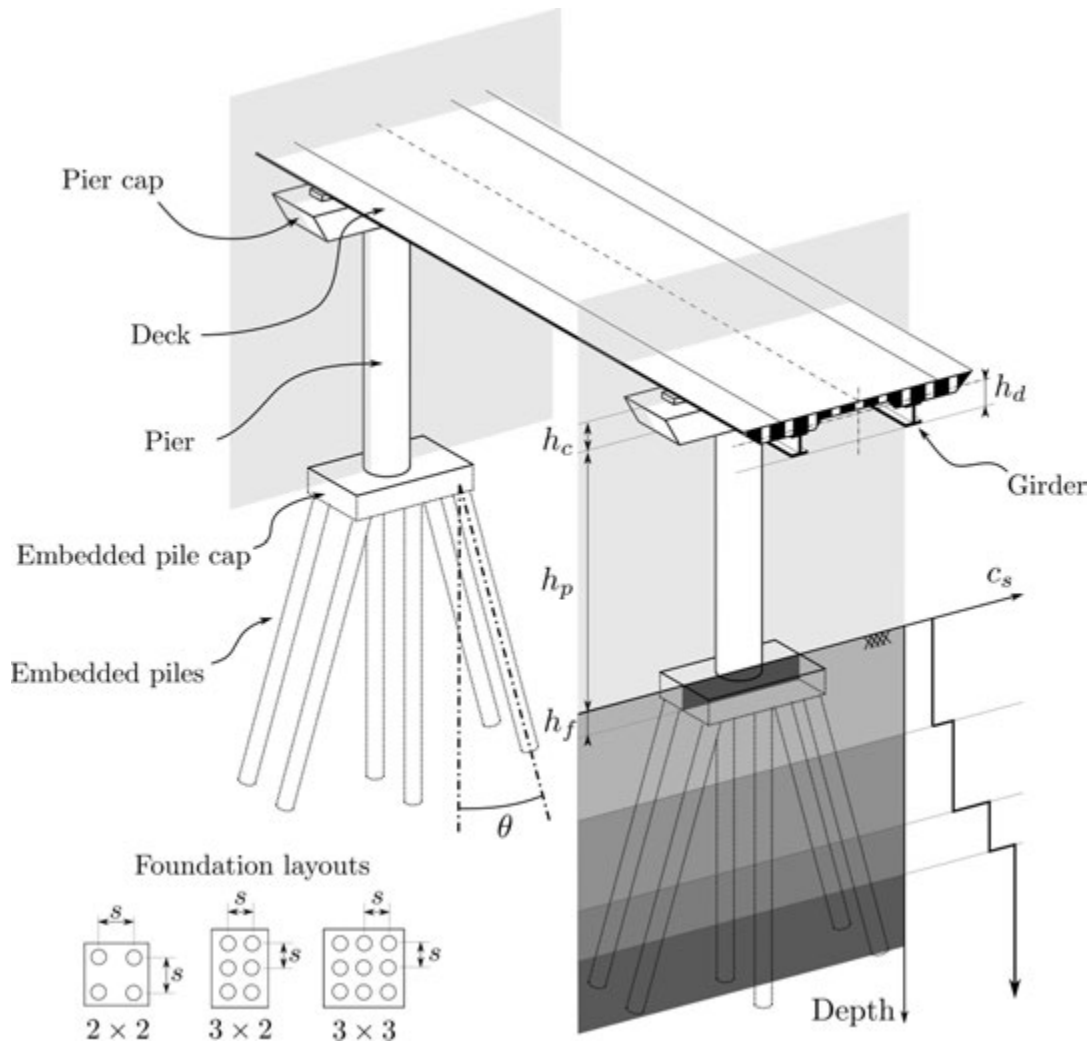


Figure 4.2: Soil – piles foundation – superstructure system and foundation layouts.

At first, masonry structural typology were used for viaducts. It is not until the early years of the past century when the reinforced concrete technology was used for elevated railways. Reinforce concrete is used in almost all the different structural members that constitute the viaduct, i.e. deck, piers, pier caps, piles, pile caps, abutments, etc. (see Figure 4.2). However, the continuous girders introduced beneath the deck, as the means of supporting it, are usually manufactured from steel. Girder sections are typically made from truss network that increases their resistance to load (see Figure 4.3).

In earthquake prone areas, and attending to the properties of the soil deposit, the design of the pile foundation system is crucial. It is not only designed to withstand superstructure static loads, also the loads induced by the earthquake must be taken into account. In the event of an earthquake, the dynamic interaction between the superstructure and the soil-foundation system play a significant role, and may lead to the collapse of the viaduct or to important repair costs. Depending on the properties and dimensions of all the structural members, and also depending on the features, properties and stratigraphy of the soil, different layouts for the pile foundations are required. The pile foundation must be properly designed in order to reduce the interaction between the soil and the structure, or even to increase it if needed for some particular cases as



Figure 4.3: Girders installation. Visit to the ongoing works in the road between Perugia and Ancona, Italy.

will be shown. Also, piles modify the input motion to the structure, so using the proper layout of the piles that compose the pile group foundation, the input energy induced by the earthquake can be reduced to a great extent.

Part II of this document will focus on the transverse seismic response of multi-span roadway viaducts characterised by identical pier heights and constant span lengths, with the exception of the edge ones, which are reduced to the 80% to optimise distribution of positive bending moments due to moving loads (Figure 4.4a). At dynamic conditions, the deck is rigidly connected to all piers both in the longitudinal and transverse directions (Figure 4.4b), through the use of shock transmitters that allow free elongations of the deck due to thermal actions at static conditions (Figure 4.4c). Finally, the deck is disconnected at the abutments in the longitudinal and transverse directions through the use of multi sliding bearings, to avoid the development of dual load path mechanisms resisting the seismic actions.

By assuming a synchronous seismic motion at all supports, above assumptions assure that the deck transverse deflections due to the out-of-phase seismic transverse response of piers are negligible [108] and the seismic response of the bridge can be studied through a single degree of freedom system representative of a single pier with its tributary deck mass. Thus, bridge decks are designed for vertical actions, including moving loads, while piers are designed to withstand the seismic actions.

The seismic action is defined according to the EC8-1 [109], avoiding the need of a specific site selection, and is represented by the elastic displacement response spectrum S_d for the life safety limit state.

The seismic transverse behaviour of bridges is studied exploiting advantages deriving from the deck restraints at dynamic conditions (see Figure 4.4b). Single bridge piers, with the tributary deck masses, are considered and suitably modelled to account for both

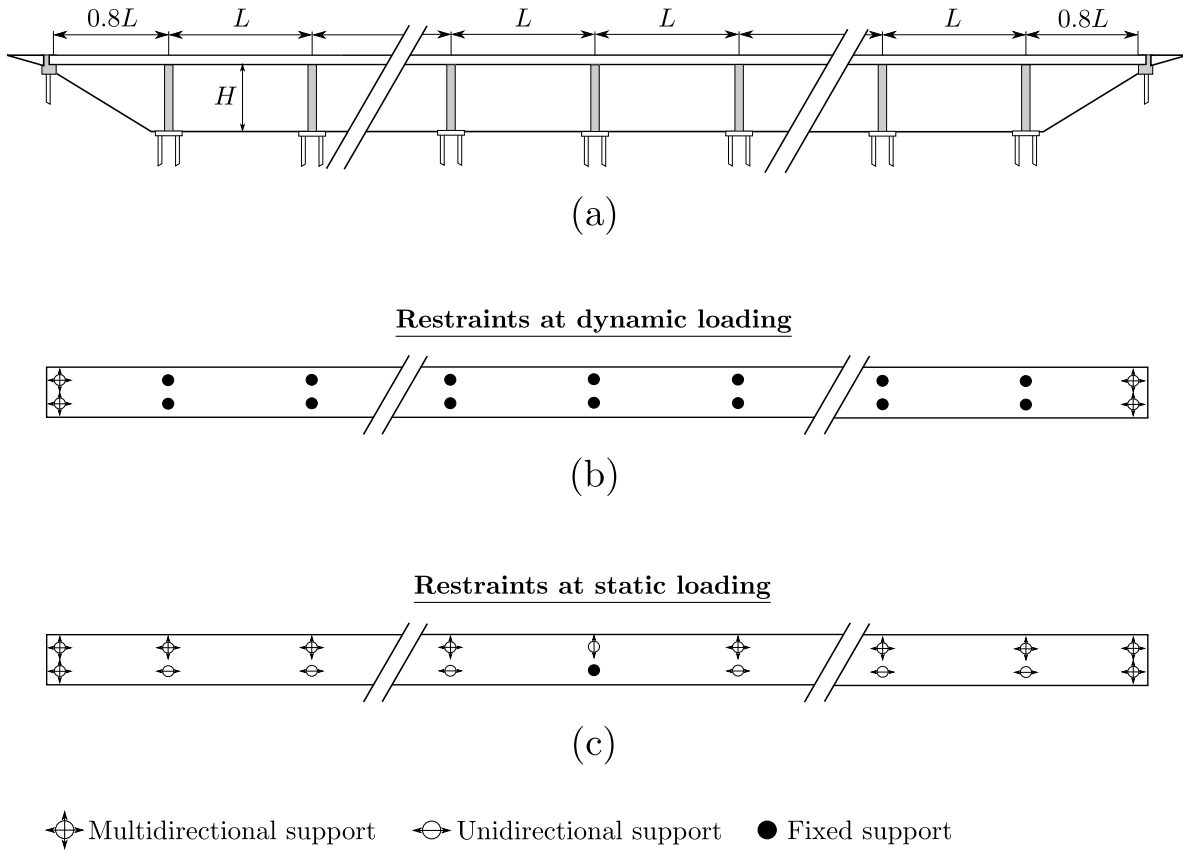


Figure 4.4: (a) Viaduct longitudinal view and restraint conditions of the deck under (b) dynamic and (c) static loading.

the nonlinear mechanical behaviour and the SSI. The response of the soil-foundation-pier system can be considered representative of the overall behaviour of inner piers of the viaducts, slightly affected by boundary effects at the abutments. The pile cap and the bent cap are assumed to be rigid, while the nonlinear elastic and damping properties of the pier are modelled through a lumped rotational spring and dashpot at the base of the pier.

Thus, SSI analyses are performed through the substructure approach both in the frequency and time domains, and the compliance of the soil-foundation system is represented by its frequency-dependent impedance matrix. Also, the pier is subjected to the FIM [110], namely the motion experienced by the foundation as a consequence of the seismic waves propagating into the soil, and obtained through a kinematic interaction analysis of the soil-foundation system.

4.2 Bridge piers seismic design procedure

Taking advantage of the decks restraints at dynamic conditions, which foresees all piers of the viaducts subjected to similar inertia forces deriving from the relevant masses of the deck and of the pier itself, a single inner pier of the bridge is considered in the design, neglecting local boundary effects and assuming a Fixed Base (FB) scheme.

Non-ductile piers are designed to remain in the elastic range while ductile piers are designed to develop dissipative plastic hinges at the base (see Figure 4.5a), charac-

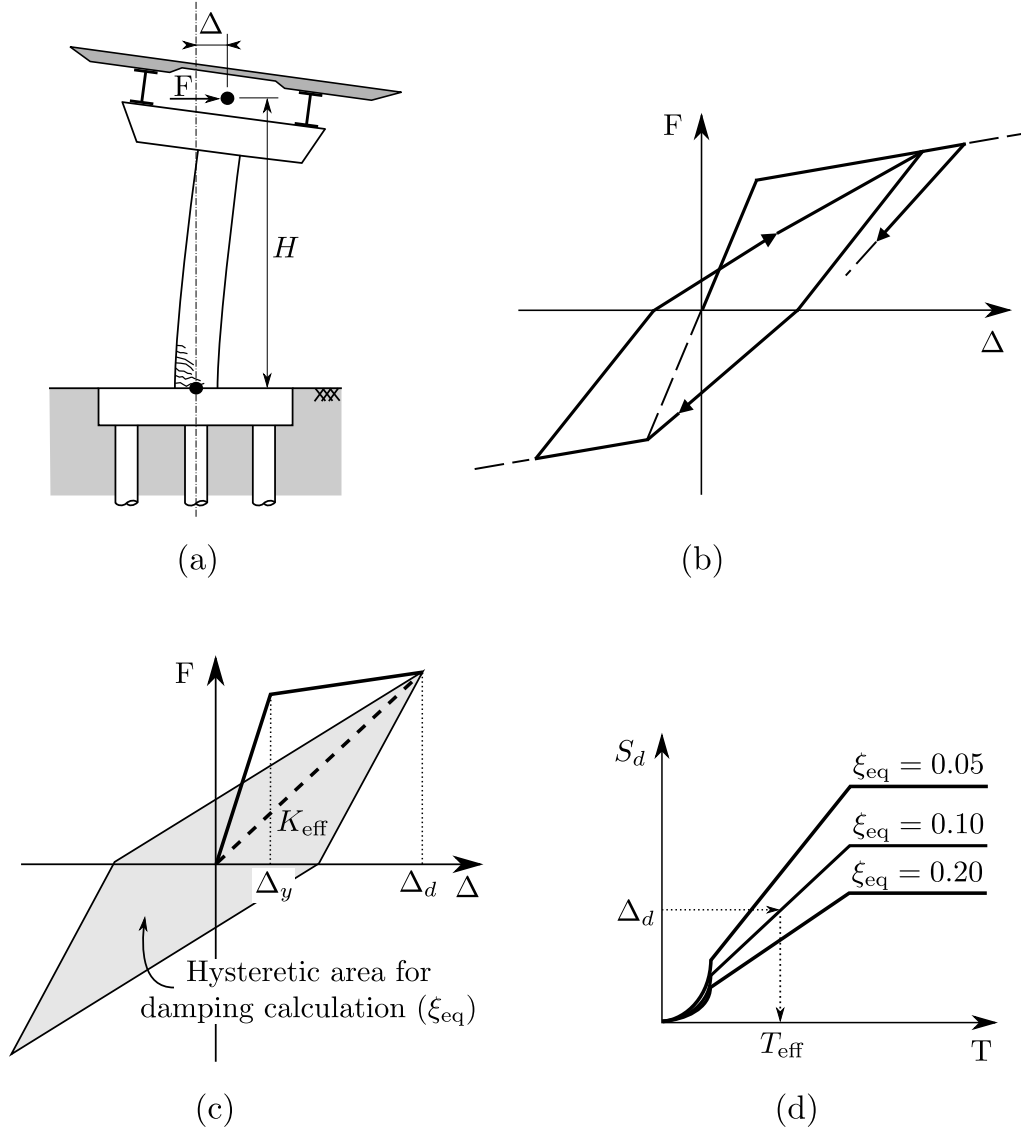


Figure 4.5: Fundamentals of the displacement-based seismic design of structures [111]. (a) Plastic hinges at the pier base. (b) Takeda's hysteretic cyclic rule [112]. (c) Effective stiffness and hysteretic area for equivalent damping calculation. (d) Design displacement spectra.

terised by a suitable plastic rotation capacity. The displacement-based design approach is adopted to design systems with established ductile performances, in terms of expected piers displacement ductility demand μ (or expected plastic rotation of hinges at the piers base) [111]. As well known, the displacement-based design approach is based on the design of an equivalent single degree of freedom system for which the secant stiffness and equivalent viscous damping properties (depending on the ductility developed by the structural system) are defined, starting from the desired displacement (or ductility) that the system should exhibit when subjected to the design seismic action (see Figure 4.5c).

The contribution to the pier transverse stiffness is essentially produced by the concrete, with the yield curvature ϕ_y essentially independent of reinforcement content and axial load level. So, based on moment-curvature analyses reported in [111], ϕ_y is a function of the yield strain of longitudinal reinforcement ε_y and section diame-

ter D , $\phi_y = 2.25\varepsilon_y/D$. Thus, the pier lateral displacement at yielding is evaluated as $\Delta_y = \phi_y(H + L_{SP})^2/3$, being L_{SP} the length of the strain penetration [113]. Then, starting from the elastic displacement Δ_y , the expected displacement demand Δ_d is defined to obtain the desired elastic or ductile behaviours, and hence, the target ductility demand is defined as $\mu = \Delta_d/\Delta_y$ (see Figure 4.5c). The reinforcement content, in terms of number and dimensions of rebars, is what is calculated through this procedure in order to withstand bending moments and shear forces at the most stressed section located at the pier base.

Being the displacement-based design method a linear-equivalent design approach, an equivalent viscous damping ratio ξ_{eq} needs to be defined to take into consideration the energy dissipation by the pier yielding. Knowing that the Takeda's hysteretic cyclic rule [112] is characteristic of the reinforced concrete column structures, which accounts for the stiffness degradation (see Figure 4.5b), and assuming a proportional to tangent stiffness damping coefficient, whose related ratio in the elastic range is 5% for all cases studied herein ($\xi_{el}=0.05$), the following expression has been adopted for the equivalent damping ratio [111]:

$$\xi_{eq} = 0.05 + 0.444 \frac{\mu - 1.0}{\mu\pi} \quad (4.1)$$

Taking into account the displacement response spectrum S_d , suitably reduced on the basis of the equivalent viscous damping ratio ξ_{eq} , the effective (i.e. inelastic) period of the pier T_{eff} is determined (see Figure 4.5d). With it, the secant stiffness K_{eff} is defined, and hence, the required bending moment at the pier base too, $M_b = K_{eff}\Delta_d H$. The required bending moment must be overestimated as $M_{Sd} = 1.044M_b$ to account for the amplification of stress resultants due to the bi-directional seismic input. Determining the longitudinal reinforcement content, the resistant bending moment of the final reinforced concrete section M_{Rd} must be higher than the required bending moment M_{Sd} . The shear resistance of the pier is ensured with the correct transverse reinforcement. The spacing between stirrups is defined according to the required shear force $V_{Sd} = \gamma_o M_{Rd}(H + h_c)$, where $\gamma_o = 1.25$ is the overstrength factor [113].

The adopted procedure comply with EC8-2 [113] requirements in terms of reinforcement detailing, stability conditions and hierarchy principles.

4.3 Moment – curvature – chord rotation relationships

For obtaining the nonlinear backbone curve that relates the pier bending moment with the chord rotation φ_S of the lumped spring at the base where plastic hinges develop, firstly the nonlinear relationship between moment and curvature of the pier cross-section must be calculated. As previously stated in Section 4.2, cross section is composed by confined concrete at the inner part, whose confinement grade depends on the longitudinal rebars content and stirrups spacing, the steel of rebars and the concrete cover.

The moment-curvature constitutive relationship is obtained through the CUMBIA software [114] adopting the Mander constitutive law for the confined and unconfined concrete [115] and King law [116] for rebars (see Figure 4.6).

In details, the unconfined concrete constitutive law is evaluated following indications of EC8-2 [113] assuming the strain at maximum strength ε_{co} and the maximum strain

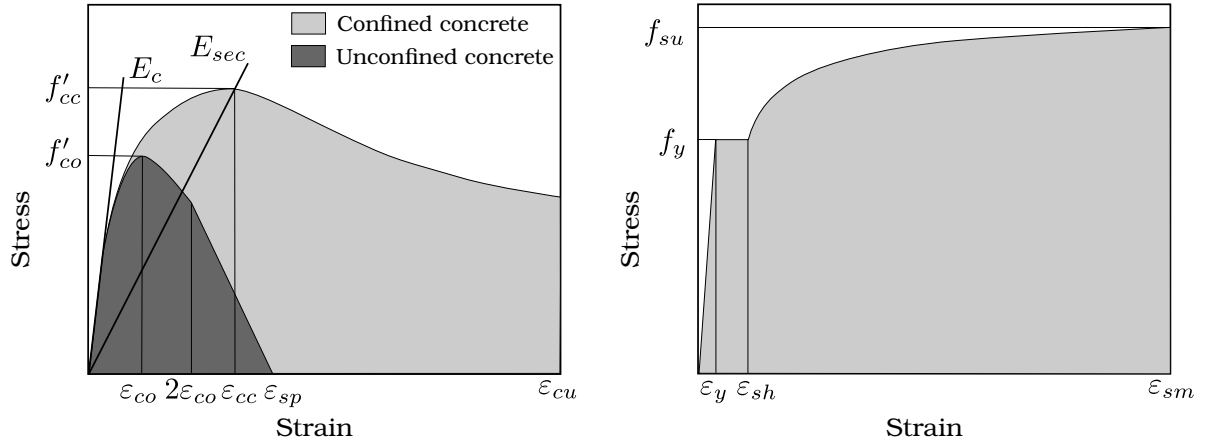


Figure 4.6: Mander constitutive law for the confined and unconfined concrete [115], and the King law [116] for rebars.

ϵ_{sp} equal to 0.002 and 0.0067, respectively. As for the maximum cylindrical compressive strength f'_{co} , the mean expected value for the concrete grade C35/45 is used, corresponding to 45.5 MPa, according to [111]. Furthermore, an initial elastic modulus E_c equal to 33.73 GPa is assumed. Constitutive laws representative of the confined concrete of piers are determined taking into account the relevant contributions provided by stirrups [115, 117]. Expected mean yielding stresses of longitudinal f_{yl} and transverse f_{yt} reinforcements of grade B450C are assumed to be 495.0 MPa and 450.0 MPa, respectively, according to indications provided in [111]; for both, considering the King's model, the strain hardening ϵ_{sh} and the ultimate strain ϵ_{sm} are assumed to be equal to 0.008 and 0.12, respectively (Figure 4.6). Finally, the mean maximum tensile strength f_{su} is assumed equal to 668.0 MPa while the Young's modulus E_s is assumed to be 210.0 GPa.

Moment – chord rotation relationships are defined starting from moment – curvature relationships (see Figure 4.7). The real curvature profile is the sum of the elastic and the real plastic contributions. Standard considerations assume a simpler and equivalent curvature profile of the plastic contribution than the real one. The plastic hinge modelling is based on the integration of a constant plastic curvature profile for being able to predict the flexural deformations of the pier [111, 113, 117, 118]. At the same time, it accounts for the stress penetration effects into the pile cap. The length of this constant distribution of plastic curvatures L_p differ from the real length at the base of the pier where plastic hinges develop L'_p . Finally, the equivalent curvature profile is constituted by the elastic contribution and a equivalent and constant plastic contribution in a fixed length (L_p) at the base of the pier, while above the plastic hinge, only elastic deformations are assumed to occur.

At the top of the pier, the lateral displacement just before yielding u_e is integrated leading to Equation (4.2a), being ϕ_y the section curvature at yielding. As the equivalent system of the pier is constituted by a rigid link with a lumped spring at the base, its equivalent rotation at yielding φ_{Sy} is given by Equation (4.2b). When the base of the pier reaches the ultimate curvature ϕ_u , the lateral displacement at the top of the pier is the summation of two contributions: the elastic lateral displacement before yielding u_e , and the plastic component u_p . The integration of the plastic curvature $\phi_u - \phi_y$ is discontinuous over the pier length, giving rise to the rotations profile φ_p shown in Figure 4.7. Integrating again, it results in the plastic contribution to the lateral displacements u_p , which value

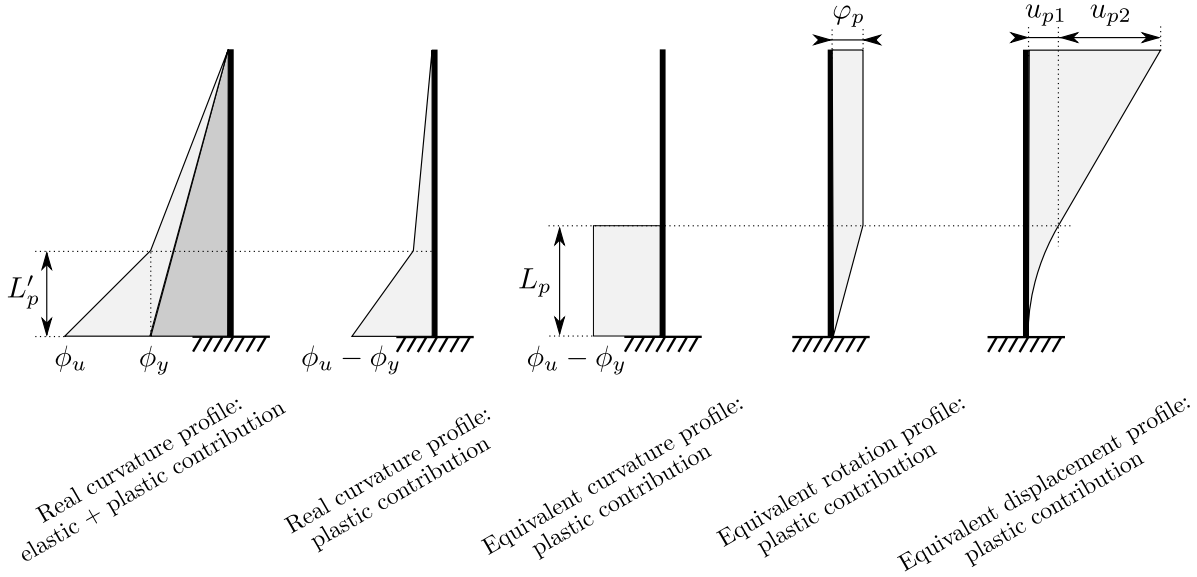


Figure 4.7: Curvature – chord rotation relationships [111, 113, 117, 118].

at the top of the pier is the sum of u_{p1} and u_{p2} calculated through Equations (4.2d) and (4.2e), respectively. Finally, the ultimate rotation of the lumped spring at the base of the pier φ_{Su} is given by Equations (4.2f).

$$u_e = \phi_y H^2 / 3 \quad (4.2a)$$

$$\varphi_{Sy} = u_e / H \quad (4.2b)$$

$$\varphi_p = (\phi_u - \phi_y) L_p \quad (4.2c)$$

$$u_{p1} = \varphi_p L_p / 2 \quad (4.2d)$$

$$u_{p2} = \varphi_p (H - L_p) \quad (4.2e)$$

$$\varphi_{Su} = (u_e + u_{p1} + u_{p2}) / H \quad (4.2f)$$

4.4 Selection of input earthquake records

Two alternatives are open for the record selection. On the one hand, an accelerogram recorded on a site where the geological conditions and the fault type are equivalent to the site of interest, or on the other hand, the acceleration signal can be modified attending to its response spectrum. If the last is the case, the response spectrum of the signal must match the design response spectrum of the standard for the particular site class. The use of modified ground motions is the preferred choice in the records selection for the present research due to two closely related reasons: (i) the limited number of accelerograms recorded on each specific geological conditions and fault type, and (ii) the savings in time when looking for the particular site class selection along the available databases, e.g. [119–124].

Also, there is software dedicated to generate artificial accelerograms by combining different Fourier amplitudes and phases spectrum in the frequency domain. It follows an iterative procedure until its response spectrum is consistent with the design response spectrum. By adopting this procedure, the final synthetic signal would not looks like an

actual earthquake ground motion, leading to high uncertainties on its adequacy to the analyses. This is the great disadvantage of using synthetic signals.

Nowadays, the earthquake records selection and scaling for nonlinear analyses constitutes by itself a significant research line, see e.g. [125–128]. Regardless of the selection approach, ground motions are often scaled by factors for the matching of its response spectrum to the design response spectrum defined by the standards. Some researchers have argued that there is no need to limit the scale factors and that scaling does not cause bias in the demands. On the other hand, some have found that scaling may induce bias, depending on how ground motions were selected. Moreover, other researchers have suggested that the value of the results from scaling is questionable [129]. As bias could be introduced in the structural response, and despite there exist different recommendations in the literature about the use of scale factors, here, as a more conservative option, a limited use of them has been assumed.

4.5 Overview of the methodology employed for the computation of the system response

The first sections of this chapter have presented the main features of the problem under study. The aim of this section is providing an overview of the methodologies employed to address the problem at hand and compute the response of the system. The approach, that includes both frequency domain and time domain analyses, is sketched in Figure 4.8. Each one of the aspects represented in Figure 4.8 will be discussed along this section with the aim of presenting a general picture of the methodology. Then, the next sections will develop in detail the different aspects involved.

Through a substructuring scheme as the one used in this Part II of the dissertation, the advantages of both time domain and frequency domain approaches are combined. In viaducts and bridges, nonlinearities are usually concentrated in the piers base, where plastic hinges develop when an earthquake occurs. Regarding the soil-foundation system, the assumption of linearity is generally adopted due to standard constraints, that states that foundations must be designed to remain in the elastic range, while for the piers, a certain damage grade would be assumed. Therefore, nothing prevents from addressing the analysis of the soil-foundation system in the frequency domain, and then including the foundation resistant forces, i.e. the impedance functions, into the substructuring system through an LPM. Then, the simulations can be performed in the time domain allowing the implicit analysis of the plastic hinges at the piers base, and hence addressing its nonlinear behaviour.

The substructuring scheme used herein (see Section 4.8) takes into account the main features of the structure of the bridge and the soil-foundation-structure dynamic interaction phenomena, including kinematic interaction (see Section 4.6). In this substructuring model, the soil medium and the foundation are represented by a boundary condition linking the degrees of freedom associated with the nodes on the interaction interface between soil-foundation and superstructure systems. This boundary condition will be formulated, in the frequency domain, based on dynamic impedances relating the displacement of the nodes in the interface to the corresponding forces. The input signal to the system is the seismic signal recorded at the soil free-field multiplied by the kinematic interaction factors. For the analysis of the soil-pile foundation systems, BEM-FEM and Winkler type formulations have been used (see Section 4.6). Those models allow the compu-

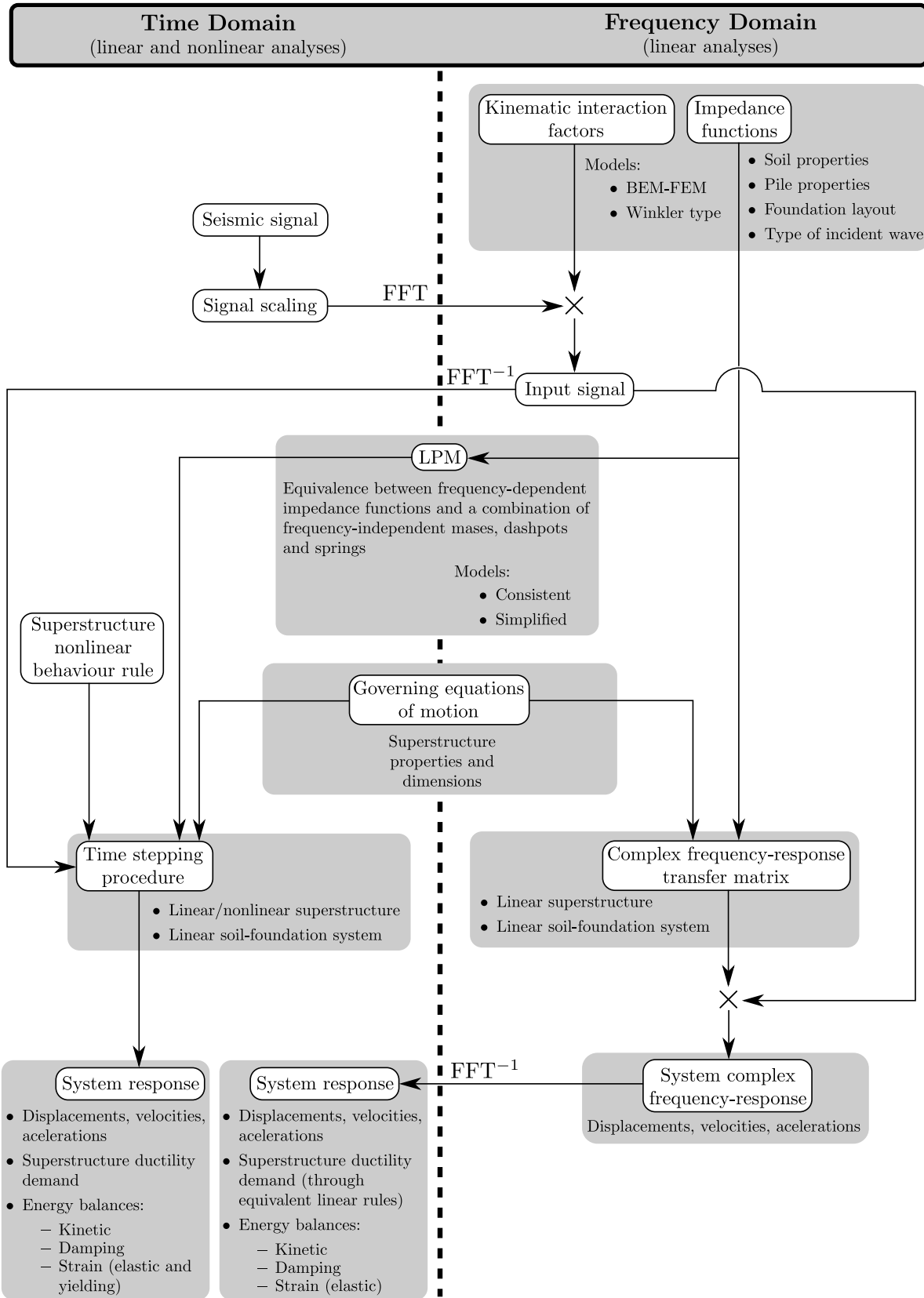


Figure 4.8: Scheme of the substructuring methodology for computing the nonlinear response of piled bridge piers.

tation of both the impedance functions and the kinematic interaction factors of linear soil-foundation systems. Additionally, two different soil material damping models have been taken into account: (a) the classical non-causal frequency-independent hysteretic damping model, and (b) the causal Biot's damping model (see Section 4.7).

For analyses in the time domain of the substructuring scheme, the obtained frequency-dependent impedances are fitted by using LPMs with frequency-independent masses, springs and dampers that reproduce the dynamic behaviour of the soil-foundation system (see, e.g., [130]). The use of these models leads to some loss of precision, but it allows the analysis of nonlinear behaviours of the structure. Also, LPMs can be straightforwardly incorporated into dedicated software for structural analysis that usually works in time domain. Two different LPMs having different complexity and possibilities are used in this study (see Section 4.9).

The numerical evaluation of the governing equations of motion of a linear substructuring system when it is subjected to an earthquake acceleration are calculated both in the time domain and in the frequency domain. Therefore, the governing equations are formulated for a time-stepping procedure or in time-harmonic form (see Section 4.8.1). If any nonlinearity is involved into the superstructure, of whatever type, i.e. contact, material or geometric, the analysis is carried out in the time domain.

There exist many numerical time-stepping methods in the literature for the integration of the system differential equations. The most common and extended are the Newmark's family methods, published in 1959 [131], or the unconditionally stable Wilson's method [132]. However, simpler methods based on a finite difference approximation of the time derivatives of displacements, velocities and accelerations are suitable for substructuring schemes with a few degrees of freedom. Here, the Newmark's linear acceleration method is used in the time domain linear simulations carried out in Chapter 5, while the central difference method formulated in terms of absolute values of displacements, velocities and accelerations is used for the computation of the nonlinear systems tackled in Chapter 6 (see, e.g., [74]).

On the other hand, for the computation of the response analysis of linear systems to excitations varying arbitrarily with time through the frequency domain method, it is necessary to define the complex frequency-response transfer matrix, which defines the harmonic response of the system (see [106]). The complex frequency-response transfer matrix is represented by the equations of motion constituting an algebraic system in the frequency domain, and it is obtained by inverting the dynamic stiffness matrix of the system. This matrix, together with the complex form of the Fourier series of the input signal, provides the response of the system to an earthquake acceleration. The Fourier series of the excitation is obtained through the Fast Fourier Transform (FFT) of the earthquake record. The product of this transform and the complex frequency-response transfer matrix yields the complex frequency-response of the system to that particular input signal. Then, applying the inverse Fast Fourier Transform (FFT^{-1}) to the complex frequency-response of the system, the system response is obtained as a function of time.

The methodology described here is used for obtaining the results discussed in Chapter 5. The system linear response is studied attending to two different aspects in the soil-foundation modelling. On the one hand, the material damping model assumed for the soil domain, and on the other hand, the type of LPM used for replacement of the frequency-dependent impedance functions. Concerning the soil material damping, two models are compared, the classical frequency-independent and non-causal hysteretic damping model and Biot's damping model [76] which is causal and with a damping rate almost

frequency-independent. And about the LPM used, two different schemes are compared, the consistent of Wolf [67, 68] and the one proposed by Carbonari et al. [133]. As will be shown, both LPMs have different complexity and possibilities, and their sensitivity in the superstructure response is evaluated.

Finally, the results discussed in Chapter 6 show the damage reduction in bridge piers when using inclined piles foundations. For carrying out the simulations, it is necessary to compute the analyses in the time domain by using the proper nonlinear rules for the piers behaviour. Also the response is analysed in the frequency domain by using equivalent linear rules for verification and comparison purposes. The response of the system is evaluated in terms of pier ductility demand and energy balances between kinetic energy, radiation and material damping energies, superstructure viscous damping energy, recoverable strain energy and superstructure yielding energy dissipation along the execution time.

4.6 Models used for the computation of impedances and kinematic interaction functions

In this work, impedance functions and kinematic interaction factors of piles foundations are computed through two different approaches.

On the one hand, a three-dimensional model for the time-harmonic dynamic analysis of piles and pile groups embedded in homogeneous isotropic viscoelastic soils was used. Piles are modelled using FEM as beams according to the Bernoulli hypothesis, while the soil is modelled using BEM as a continuum, semi-infinite, isotropic, homogeneous, linear, viscoelastic medium (see Figure 4.9). In the coupling between the pile and the soil, welded boundary contact condition at the pile-soil interfaces are assumed. It is also assumed that the soil continuity is not altered by the presence of the piles, and the tractions at the pile-soil interface are considered as a body load applied within the half-space. The formulation allows the analysis of problems including soil strata, rigid rocky beds and any topography for the soil surface. If compared with a multi-domain pure BEM in which the pile domain must be discretized, the number of degrees of freedom, and hence the computation cost, is drastically reduced by assuming one-dimensional beam FEM elements instead of the pile BEM domain. Taking advantage of the particular characteristics of each one of the methods, accurate results are obtained through this more efficient and still rigorous tool for the time harmonic dynamic analysis of piles and pile groups. More details can be found in [23, 134–136].

On the other hand, the Winkler-type model developed by Dezi et al. [9, 137] for the dynamic analysis of pile foundations is also used. In this model, piles are discretized by assuming one-dimensional beam FEM elements and the soil by assuming a Winkler-type medium, i.e., mutually independent layers of soil giving a calibrated stiffness to the pile elements displacement (see Figure 4.10). The disadvantage of the Winkler-type medium is the lack of continuity between soil layers. Both the piles and soil are considered to behave linearly. The pile-soil-pile interaction is taken into account considering the elastodynamic Green's functions. Using this fundamental solution is possible to express the mutual interactions between all the piles of the group and the radiation problem consistently without using the stepped analysis generally adopted in the technical literature.

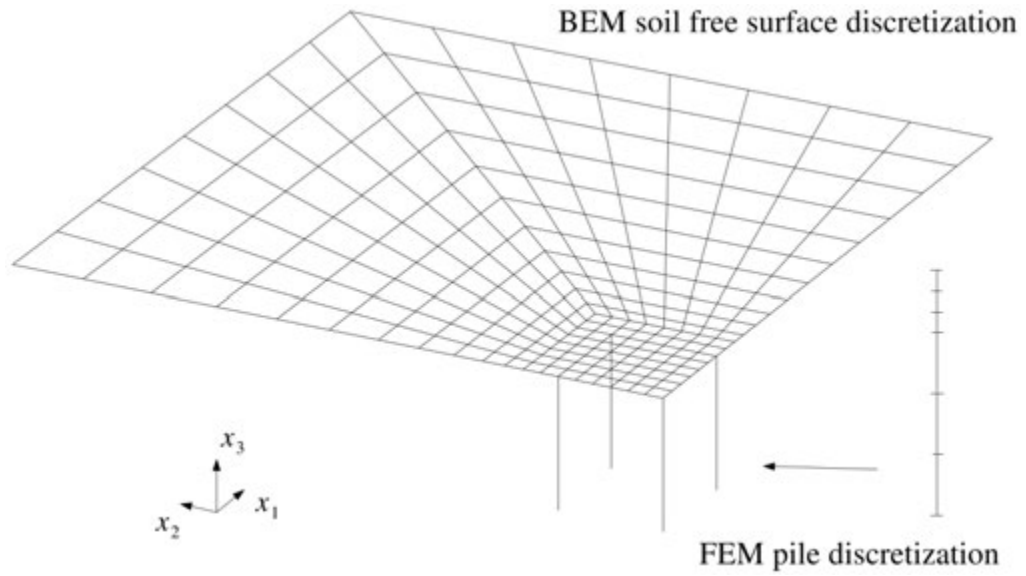


Figure 4.9: Example of a 3×3 pile group BEM-FEM discretization (only a quarter of the geometry is shown) [23].

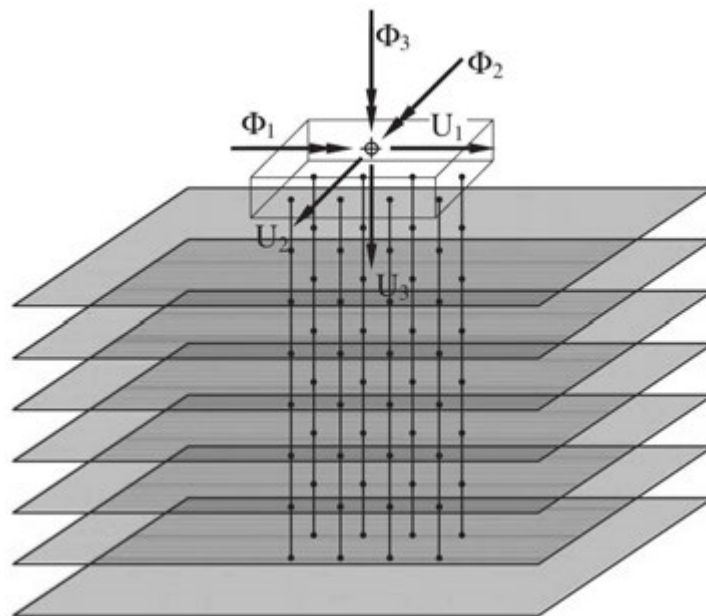


Figure 4.10: Schematic model of the pile group embedded in the Winkler-type medium and connected by a rigid cap [9].

4.7 Modelling of the soil material damping

The dissipation of energy in the soil medium is usually modelled through frequency-independent hysteretic damping of the type

$$\mathcal{M} = \text{Re}[\mathcal{M}](1 + i\xi) \quad (4.3)$$

where ξ is the damping coefficient and \mathcal{M} is a material property (shear or Young's modulus, for example). The use of this model is generally justified by the independence between the excitation frequency and the amount of energy dissipated in each cycle for some materials [138, 139], and it is massively used due to its convenience in harmonic analysis. However, its use in the analysis of non-stationary (transient) vibrations, either through Fourier analysis or directly in the time domain, is problematic for various reasons [140]. The first feature of this model that can be seen as incongruous is the non-zero imaginary component of the response in $\omega = 0$. Further analyses show that its use leads to non-causal models, which implies that a material that responds to a law of the type of the Equation (4.3) is physically impossible, i.e. in no case can this model respond to reality. Hereafter, this classical hysteretic damping model is labelled as ‘‘hysteretic’’.

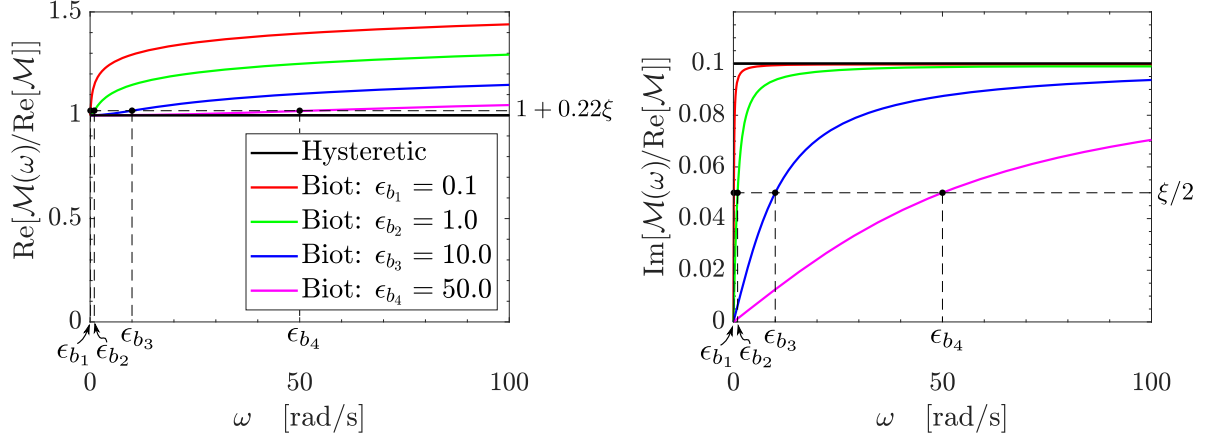
The first hysteretic model, both causal and with a damping rate almost independent of frequency, was proposed by Biot in 1958 [76]:

$$\mathcal{M}(\omega) = \text{Re}[\mathcal{M}] \left(1 + \frac{2}{\pi} \xi \ln \sqrt{1 + \left(\frac{\omega}{\epsilon_b} \right)^2} + i \frac{2}{\pi} \xi \text{atan} \left(\frac{\omega}{\epsilon_b} \right) \right) \quad (4.4)$$

where both real and imaginary parts vary with frequency but, at $\omega = 0$, imaginary part vanishes ($\mathcal{M}(\omega = 0) \rightarrow \text{Re}[\mathcal{M}]$). Here, ϵ_b is a real and positive number with the same units than ω , and can be seen as a reference frequency that defines the function variation and for which the material property acquires the value $\mathcal{M}(\omega = \epsilon_b) = \text{Re}[\mathcal{M}](1 + 0.22\xi + i\xi/2)$. The parameter ϵ_b controls how wide is the detachment to the response computed with the classical hysteretic damping model (Equation (4.3)). In order to illustrate this aspect, Figure 4.11 shows the real and imaginary parts of \mathcal{M} for both damping models and, in the case of the damping model of Biot, for different values of ϵ_b . Concerning soil-foundation impedance functions, the differences that arise from the comparison between the two damping models for the soil material are produced mainly at the lower frequency range for damping coefficients and at higher frequencies for spring coefficients (see for instance Figure 5.4).

4.8 Substructuring scheme

By considering the in-plane response of the soil-foundation-pier system, the whole problem is described as the three degree-of-freedom system depicted in Figure 4.12, with u_F and φ_F being the translation and rotation of the foundation, φ_S the relative rotation of the pier with respect to the foundation, and u_g and φ_g the translational and rotational FIM. It is worth noting that, by assuming pile layouts characterised by two symmetry axes and by referring the impedance matrix of the soil-foundation systems to the centroids of the pile configuration at the level of the pile head, the vertical degree-of-freedom is uncoupled from the horizontal and rotational ones and is not included in the formulation. Thus, the significant components of the soil-foundation impedance matrix


 Figure 4.11: \mathcal{M} values assuming $\xi = 0.1$ for the hysteretic and Biot's damping models.

are the horizontal, rotational and coupled roto-translational terms, represented in the Compliant Base (CB) model of the pier in Figure 4.12 through linear frequency dependent visco-elastic Kelvin-Voigt's models at the foundation-superstructure interface. FB models will be also considered, whose results will be used to address and discuss the significance of the SSI effects.

In Figure 4.12, m_d and m_c are the masses of bridge deck portion belonging to the generic pier, and of the pier bent cap, respectively. Furthermore, m_p and m_f are the masses of the pier and the pile cap, and I_d , I_c and I_f are the mass moments of inertia of the deck and the bent cap, and of the pile cap, respectively. Lumped at the pier base, the plastic hinge behaviour of the pier is represented by the nonlinear spring K_ϕ and the nonlinear dashpot C_ϕ . Finally, h_d , h_c , h_p and h_f are dimensions necessary to account for the position of the mass centroids of the deck, the bent cap and the pile cap.

4.8.1 Equations of motion

As seen in Section 4.5, by assuming a linear elastic behaviour for the pier and neglecting second-order effects (i.e. making the hypothesis of small displacements), the system can be solved directly in frequency domain using the complex frequency dependent soil-foundation impedances. The equations of motion of the CB system shown in Figure 4.12 may be conveniently written in the frequency domain as

$$\left\{ \begin{array}{l} \left[\begin{array}{ccc} K_\phi & 0 & 0 \\ 0 & k_{hh}(\omega) & k_{hr}(\omega) \\ 0 & k_{hr}(\omega) & k_{rr}(\omega) \end{array} \right] - \omega^2 \left[\begin{array}{ccc} m_{11} & m_{12} & m_{13} \\ m_{12} & m_{22} & m_{23} \\ m_{13} & m_{23} & m_{33} \end{array} \right] + \\ + i\omega \left[\begin{array}{ccc} C_\phi & 0 & 0 \\ 0 & c_{hh}(\omega) & c_{hr}(\omega) \\ 0 & c_{hr}(\omega) & c_{rr}(\omega) \end{array} \right] \end{array} \right\} \begin{bmatrix} \Phi_S \\ U_F \\ \Phi_F \end{bmatrix} = \omega^2 \begin{bmatrix} m_{11} & m_{12} & m_{13} \\ m_{12} & m_{22} & m_{23} \\ m_{13} & m_{23} & m_{33} \end{bmatrix} \begin{bmatrix} 0 & 0 \\ 1 & 0 \\ 0 & 1 \end{bmatrix} \begin{bmatrix} U_g \\ \Phi_g \end{bmatrix} \quad (4.5)$$

where mass matrix coefficients are

$$m_{11} = (h_p + h_c + h_d)^2 m_d + I_d + \left(h_p + \frac{h_c}{2} \right)^2 m_c + I_c + h_p^2 \frac{m_p}{2} \quad (4.6a)$$

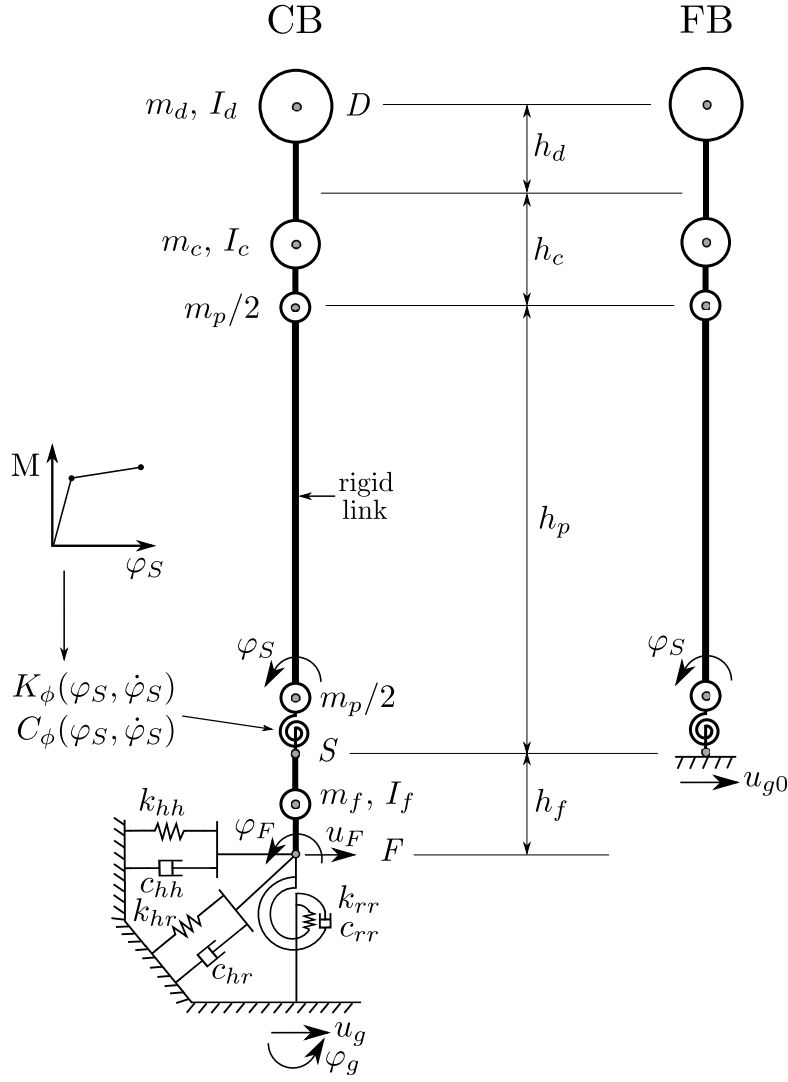


Figure 4.12: CB and FB substructuring models of the in-plane dynamic response of the soil-foundation-pier systems.

$$m_{12} = (h_p + h_c + h_d)m_d + \left(h_p + \frac{h_c}{2}\right)m_c + h_p \frac{m_p}{2} \quad (4.6b)$$

$$m_{13} = (h_p + h_c + h_d)(h_f + h_p + h_c + h_d)m_d + I_d + \left(h_p + \frac{h_c}{2}\right)\left(h_f + h_p + \frac{h_c}{2}\right)m_c + I_c + h_p(h_f + h_p)\frac{m_p}{2} \quad (4.6c)$$

$$m_{22} = m_d + m_c + m_p + m_f \quad (4.6d)$$

$$m_{23} = (h_f + h_p + h_c + h_d)m_d + \left(h_f + h_p + \frac{h_c}{2}\right)m_c + (h_f + h_p)\frac{m_p}{2} + h_f\frac{m_p}{2} + \frac{h_f}{2}m_f \quad (4.6e)$$

$$m_{33} = (h_f + h_p + h_c + h_d)^2 m_d + I_d + \left(h_f + h_p + \frac{h_c}{2}\right)^2 m_c + I_c + (h_f + h_p)^2 \frac{m_p}{2} + h_f^2 \frac{m_p}{2} + \left(\frac{h_f}{2}\right)^2 m_f + I_f \quad (4.6f)$$

being ω the frequency of excitation and “ i ” the imaginary unit. Stiffness and damping coefficients shown in Equation (4.5) are obtained from the complex-valued frequency-dependent impedance functions $Z_{hh}(\omega) = k_{hh}(\omega) + i\omega c_{hh}(\omega)$, $Z_{rr}(\omega) = k_{rr}(\omega) + i\omega c_{rr}(\omega)$ and $Z_{hr}(\omega) = k_{hr}(\omega) + i\omega c_{hr}(\omega)$, representing the stiffness and damping of the foundation in the horizontal, rocking and cross-coupled horizontal-rocking vibration modes respectively.

In Equation (4.5), Φ_S , U_F and Φ_F are the superstructure and foundation generalised relative displacements in the frequency domain (φ_S , u_F and φ_F will represent these magnitudes in the time domain), while U_g and Φ_g are the generalised displacements constituting the FIM derived from the kinematic interaction analysis of the pile foundation in the frequency domain (u_g and φ_g will represent these magnitude in the time domain). The three equations of motion describe the moment equilibrium of the pier, the horizontal force and moment equilibrium of the superstructure-foundation system, respectively.

To account for the superstructure nonlinearity it is mandatory to carry out the analyses in the time domain. In this case, a time-stepping approach, as the well known Newmark’s method, can be adopted to obtain the problem solution. The problem formulation in the time domain requires a suitable strategy to account for the frequency-dependent behaviour of the soil-foundation system. Usually, LPM yields impedances that approximate those of the soil-foundation system in a selected frequency range of interest [130] (see Section 4.9). From a general point of view, Equation (4.5) can be written in the time domain as

$$\begin{aligned}
 & \begin{bmatrix} m_{11} & m_{12} & m_{13} & \mathbf{0} \\ m_{12} & m_{22} + \bar{m}_{hh} & m_{23} + \bar{m}_{hr} & \mathbf{0} \\ m_{13} & m_{23} + \bar{m}_{hr} & m_{33} + \bar{m}_{rr} & \mathbf{0} \\ \mathbf{0} & \mathbf{0} & \mathbf{0} & \bar{\mathbf{M}}_{ll} \end{bmatrix} \begin{bmatrix} \dot{\varphi}_S \\ \dot{u}_F \\ \dot{\varphi}_F \\ \dot{\mathbf{u}}_l \end{bmatrix} + \begin{bmatrix} 0 & 0 & 0 & \mathbf{0} \\ 0 & \bar{c}_{hh} & \bar{c}_{hr} & \bar{c}_{hl} \\ 0 & \bar{c}_{hr} & \bar{c}_{rr} & \bar{c}_{rl} \\ \mathbf{0} & \bar{\mathbf{c}}_{hl}^T & \bar{\mathbf{c}}_{rl}^T & \bar{\mathbf{C}}_{ll} \end{bmatrix} \begin{bmatrix} \dot{\varphi}_S \\ \dot{u}_F \\ \dot{\varphi}_F \\ \dot{\mathbf{u}}_l \end{bmatrix} + \\
 & + \begin{bmatrix} 0 & 0 & 0 & \mathbf{0} \\ 0 & \bar{k}_{hh} & \bar{k}_{hr} & \bar{k}_{hl} \\ 0 & \bar{k}_{hr} & \bar{k}_{rr} & \bar{k}_{rl} \\ \mathbf{0} & \bar{\mathbf{k}}_{hl}^T & \bar{\mathbf{k}}_{rl}^T & \bar{\mathbf{K}}_{ll} \end{bmatrix} \begin{bmatrix} \varphi_S \\ u_F \\ \varphi_F \\ \mathbf{u}_l \end{bmatrix} + \begin{bmatrix} C_\phi & K_\phi \\ 0 & 0 \\ 0 & 0 \\ \mathbf{0} & \mathbf{0} \end{bmatrix} \begin{bmatrix} \dot{\varphi}_S \\ \varphi_S \end{bmatrix} = \\
 & = - \begin{bmatrix} m_{11} & m_{12} & m_{13} & \mathbf{0} \\ m_{12} & m_{22} & m_{23} & \mathbf{0} \\ m_{13} & m_{23} & m_{33} & \mathbf{0} \\ \mathbf{0} & \mathbf{0} & \mathbf{0} & \mathbf{0} \end{bmatrix} \begin{bmatrix} 0 & 0 \\ 1 & 0 \\ 0 & 1 \\ \mathbf{0} & \mathbf{0} \end{bmatrix} \begin{bmatrix} \ddot{u}_g \\ \ddot{\varphi}_g \end{bmatrix} \quad (4.7)
 \end{aligned}$$

where the symbol $\bar{\square}$ denotes the frequency independent stiffness, damping and mass matrices and vectors derived from the LPM parameters, which are developed in detail in Section 4.9. On the other hand, $\dot{\square}$ denotes the time derivative. Depending on the LPM complexity, hidden degrees of freedom (l) may be included in the equilibrium equations.

Notice that terms C_ϕ and K_ϕ , that account for the system nonlinearities, have been suitably decoupled from the linear contributions in Equation (4.7) to allow for an easy implementation and control of the solution in the time-stepping integration method.

The FB model is a one degree-of-freedom system, expressed in terms of the pier relative rotation φ_S . Its governing equation is the moment equilibrium, i.e. the first equation of the system presented in Equation (4.5) for frequency domain analyses, and in Equation (4.7) for time domain analyses. In FB models, no kinematic interaction is

considered, i.e. the input signal coincides with the scaled horizontal free-field ground motion (u_{g0}) as shown in Figure 4.12. Then, resulting equation for frequency domain analyses is

$$(K_\phi - \omega^2 m_{11} + i\omega C_\phi)\Phi_S = \omega^2 m_{12} U_{g0} \quad (4.8)$$

being U_{g0} the FFT of the scaled horizontal free-field ground motion (u_{g0}), and the resulting equation for time domain analyses is

$$m_{11}\ddot{\phi}_S + C_\phi\dot{\phi}_S + K_\phi\phi_S = -m_{12}\ddot{u}_{g0} \quad (4.9)$$

4.8.2 Energy balance

The input energy to the system is dissipated through different mechanisms. If the system is computed assuming FB hypothesis and the pier doesn't yields, all the input energy is dissipated by viscous damping in the superstructure. On the contrary, if the bridge is considered to be founded on an elastic foundation (CB model) and the pier yields, part of the input energy is dissipated by viscous damping in superstructure and foundation, and part is dissipated by the hysteretic cycles of the plastic hinge.

The contribution of each mechanism to the energy dissipation for a specific configuration provides useful information to understand the capability of the system to withstand the earthquake excitation.

The energy balance is computed pre-multiplying Equation (4.7) by the system velocity and integrating over the time [74, 141]. The right-hand side of the resulting equation is the input energy to the system:

$$E_{in} = - \int_0^t [\dot{\phi}_S \quad \dot{u}_F \quad \dot{\phi}_F] \begin{bmatrix} m_{11} & m_{12} & m_{13} \\ m_{12} & m_{22} & m_{23} \\ m_{13} & m_{23} & m_{33} \end{bmatrix} \begin{bmatrix} 0 & 0 \\ 1 & 0 \\ 0 & 1 \end{bmatrix} \begin{bmatrix} \ddot{u}_g \\ \ddot{\phi}_g \end{bmatrix} dt \quad (4.10)$$

The input energy is balanced during the motion by the kinetic energy (E_I) due to the inertial forces, the energy dissipated by viscous damping in foundation ($E_{D_{\text{foundd}}}$) and superstructure ($E_{D_{\text{super}}}$), the recoverable strain energy in the foundation ($E_{K_{\text{foundd}}}$) and the strain energy in the superstructure ($E_{K_{\text{super}}}$) which includes both yielding and elastic components. All energy contributions are expressed in Equation (4.11).

$$E_I = \int_0^t [\dot{\phi}_S \quad \dot{u}_F \quad \dot{\phi}_F \quad \dot{\mathbf{u}}_l^T] \begin{bmatrix} m_{11} & m_{12} & m_{13} & \mathbf{0} \\ m_{12} & m_{22} + \overline{m}_{hh} & m_{23} + \overline{m}_{hr} & \mathbf{0} \\ m_{13} & m_{23} + \overline{m}_{hr} & m_{33} + \overline{m}_{rr} & \mathbf{0} \\ \mathbf{0} & \mathbf{0} & \mathbf{0} & \overline{\mathbf{M}}_{ll} \end{bmatrix} \begin{bmatrix} \ddot{\phi}_S \\ \ddot{u}_F \\ \ddot{\phi}_F \\ \ddot{\mathbf{u}}_l \end{bmatrix} dt \quad (4.11a)$$

$$E_{D_{\text{foundd}}} = \int_0^t [\dot{u}_F \quad \dot{\phi}_F \quad \dot{\mathbf{u}}_l^T] \begin{bmatrix} \overline{c}_{hh} & \overline{c}_{hr} & \overline{c}_{hl} \\ \overline{c}_{hr} & \overline{c}_{rr} & \overline{c}_{rl} \\ \overline{c}_{hl}^T & \overline{c}_{rl}^T & \overline{c}_{ll} \end{bmatrix} \begin{bmatrix} \dot{u}_F \\ \dot{\phi}_F \\ \dot{\mathbf{u}}_l \end{bmatrix} dt \quad (4.11b)$$

$$E_{K_{\text{foundd}}} = \int_0^t [\dot{u}_F \quad \dot{\phi}_F \quad \dot{\mathbf{u}}_l^T] \begin{bmatrix} \overline{k}_{hh} & \overline{k}_{hr} & \overline{k}_{hl} \\ \overline{k}_{hr} & \overline{k}_{rr} & \overline{k}_{rl} \\ \overline{k}_{hl}^T & \overline{k}_{rl}^T & \overline{k}_{ll} \end{bmatrix} \begin{bmatrix} u_F \\ \phi_F \\ \mathbf{u}_l \end{bmatrix} dt \quad (4.11c)$$

$$E_{D_{\text{super}}} = \int_0^t \dot{\varphi}_S C_\phi \dot{\varphi}_S dt \quad (4.11d)$$

$$E_{K_{\text{super}}} = \int_0^t \dot{\varphi}_S K_\phi \varphi_S dt \quad (4.11e)$$

After the earthquake has finished, and the system has damped out completely, the kinetic energy and the recoverable strain energy vanish, being all the input energy dissipated by viscous damping and by yielding in the pier.

Considering FB systems, the energy balance is computed pre-multiplying Equation (4.9) by the pier rotation velocity $\dot{\varphi}_S$ and integrating over the time. The different quantities are computed as follows:

$$E_{in} = - \int_0^t \dot{\varphi}_S m_{12} \ddot{u}_{g0} dt \quad (4.12a)$$

$$E_I = \int_0^t \dot{\varphi}_S m_{11} \ddot{\varphi}_S dt \quad (4.12b)$$

$$E_{D_{\text{super}}} = \int_0^t \dot{\varphi}_S C_\phi \dot{\varphi}_S dt \quad (4.12c)$$

$$E_{K_{\text{super}}} = \int_0^t \dot{\varphi}_S K_\phi \varphi_S dt \quad (4.12d)$$

4.9 Lumped parameter models for the representation of the soil-pile foundation system

The accuracy of an LPM in reproducing the dynamic behaviour of the soil-foundation system depends on its configuration and degrees of freedom. Use of LPMs leads to some loss of precision, but this is compensated by the possibility of performing nonlinear analyses in time domain. To this end, it is necessary to replace of the soil-pile foundation frequency-dependent impedances by an equivalent scheme constituted by a configuration of springs, dampers and masses with real and constant values that reproduce the impedances of the soil-pile foundation system, i.e. $Z_{hh}(\omega) \approx \hat{Z}_{hh}(\omega)$, $Z_{hr}(\omega) \approx \hat{Z}_{hr}(\omega)$ and $Z_{rr}(\omega) \approx \hat{Z}_{rr}(\omega)$. The two alternative LPMs used in this study to compute the seismic response of superstructures in the time domain are presented in this section. On the one hand, a consistent LPM, as described for instance by Wolf [67, 68] or Andersen [142, 143] is used. On the other hand, an alternative simplified LPM, based on the work by Carbonari, Dezi and Leoni [133], is also evaluated. Details above both studied schemes are explained in the following.

4.9.1 Consistent LPM

Each impedance component can be expressed as $S_{hh}(a_0) = Z_{hh}(a_0)/Z_{hh}^0$, $S_{hr}(a_0) = Z_{hr}(a_0)/Z_{hr}^0$ and $S_{rr}(a_0) = Z_{rr}(a_0)/Z_{rr}^0$ where Z_{hh}^0 , Z_{hr}^0 and Z_{rr}^0 denote the static stiffness of each impedance term $Z_{hh}(0)$, $Z_{hr}(0)$ and $Z_{rr}(0)$, and a_0 denotes the dimensionless frequency, typically $a_0 = \omega d/c_s$ in the case of piles and groups of piles, where d denotes the pile diameter and c_s is the soil shear-wave velocity. The frequency-dependent stiffness dimensionless coefficients $S_{hh}(a_0)$, $S_{hr}(a_0)$ and $S_{rr}(a_0)$ are then decomposed into

a singular parts $S_{hh}^s(a_0)$, $S_{hr}^s(a_0)$ and $S_{rr}^s(a_0)$, and regular parts $S_{hh}^r(a_0)$, $S_{hr}^r(a_0)$ and $S_{rr}^r(a_0)$:

$$S_{hh}(a_0) = S_{hh}^s(a_0) + S_{hh}^r(a_0) \quad (4.13a)$$

$$S_{hr}(a_0) = S_{hr}^s(a_0) + S_{hr}^r(a_0) \quad (4.13b)$$

$$S_{rr}(a_0) = S_{rr}^s(a_0) + S_{rr}^r(a_0) \quad (4.13c)$$

being the singular parts decomposed, likewise, in:

$$S_{hh}^s(a_0) = \kappa_{hh}^\infty + ia_0\gamma_{hh}^\infty \quad (4.14a)$$

$$S_{hr}^s(a_0) = \kappa_{hr}^\infty + ia_0\gamma_{hr}^\infty \quad (4.14b)$$

$$S_{rr}^s(a_0) = \kappa_{rr}^\infty + ia_0\gamma_{rr}^\infty \quad (4.14c)$$

For simplicity, any indices indicating the impedance term are omitted in the following, e.g. $Z_{hh}(a_0)$, $Z_{hr}(a_0)$, $Z_{rr}(a_0) \sim Z(a_0)$. In Equation (4.14), κ^∞ and γ^∞ are two real constants which are selected so that $Z^0 S^s(a_0)$ provides the entire stiffness in the high-frequency limit $a_0 \rightarrow \infty$. The regular part $S^r(a_0)$ is the remaining part of the stiffness and is found as $S^r(a_0) = Z(a_0)/Z^0 - S^s(a_0)$.

Generally, a closed expression for $S^r(a_0)$ is unavailable. Hence, the regular part of a complex stiffness is usually obtained by fitting a rational filter to each impedance component. A rational approximation can be conveniently written as:

$$S^r(a_0) \approx \hat{S}^r(ia_0) = \frac{1 - \kappa^\infty + p_1(ia_0) + p_2(ia_0)^2 + \dots + p_{M-1}(ia_0)^{M-1}}{\prod_{n=1}^N (ia_0 - s_n)(ia_0 - s_n^*) \prod_{n=N+1}^{M-N} (ia_0 - s_n)}, \quad 2N \leq M \quad (4.15)$$

where an asterisk (*) denotes the complex conjugate [67, 68].

The curve-fitting of the rational filter to the regular part of the dynamic stiffness is made by a least-squares technique (see Equation (4.16)), where the roots s_n are identified as the optimization variables in addition to the coefficients of the numerator polynomial, $\mathbf{x} = [p_1, p_2, \dots, p_{M-1}, s_1, s_2, \dots, s_N, s_{N+1}, s_{N+2}, \dots, s_{M-N}]$.

$$\min_{\mathbf{x}} \|(\hat{S}^r(\mathbf{x}, ia_0) - S^r(a_0)) \Psi(a_0)\|_2^2 = \min_{\mathbf{x}} \sum_i ((\hat{S}^r(\mathbf{x}, ia_{0_i}) - S^r(a_{0_i})) \Psi(a_{0_i}))^2 \quad (4.16)$$

In order to obtain a stable solution in the time domain, the poles of $\hat{S}^r(ia_0)$ should all reside in the second and third quadrant of the complex plane [142], i.e. the real parts of the poles must all be constrained in the fitting procedure:

$$\text{Re}[s_n] < 0 \quad (4.17)$$

Due to the nature of a specific LPM, a bad fitting to the reference impedance functions in a particular frequency range can be obtained. So, in order to prioritize the fitting in a particular range, a frequency-dependent weight function $\Psi(a_0) | 0 \leq \Psi(a_0) \leq 1$ could be employed.

Experience shows that as many as possible of the roots should appear as complex conjugates [142]. In order to have all roots as complex conjugates, $N = M/2$ should be

used if M is even. This provides a good fit in most situations and may, at the same time, generate the LPM with fewest possible internal degrees of freedom. This leads to the following simplification in the rational approximation:

$$S^r(a_0) \approx \hat{S}^r(ia_0) = \frac{1 - \kappa^\infty + p_1(ia_0) + p_2(ia_0)^2 + \dots + p_{M-1}(ia_0)^{M-1}}{\prod_{n=1}^N (ia_0 - s_n)(ia_0 - s_n^*)}, \quad M = 2N \quad (4.18)$$

being the optimization variables in this case $\mathbf{x} = [p_1, p_2, \dots, p_{M-1}, s_1, s_2, \dots, s_N]$.

Once the poles and the coefficients in the numerator are calculated, they have little insight into the physics of the problem. In order to obtain physical meaningful coefficients, a recasting of Equation (4.18) into partial-fraction form should be carried out as

$$\hat{S}^r(ia_0) = \sum_{m=1}^M \frac{R_m}{(ia_0 - s_m)} \quad (4.19)$$

where s_m are the poles of $\hat{S}^r(ia_0)$, and R_m are the corresponding residues. If the two conjugate complex and the corresponding residues are added together, a second-order term with real coefficients appears, so the partial-fraction form can be rewritten as:

$$\hat{S}^r(ia_0) = \sum_{n=1}^N \frac{\beta_{0n} + \beta_{1n}ia_0}{\alpha_{0n} + \alpha_{1n}ia_0 + (ia_0)^2} \quad (4.20)$$

The real coefficients α_{0n} , α_{1n} , β_{0n} and β_{1n} are obtained through simple mathematical operations between poles and residues of the complex conjugate terms. This leads to:

$$\alpha_{0n} = \{\text{Re}(s_n)\}^2 + \{\text{Im}(s_n)\}^2 \quad (4.21a)$$

$$\alpha_{1n} = -2\{\text{Re}(s_n)\} \quad (4.21b)$$

$$\beta_{0n} = -2(\{\text{Re}(R_n)\}\{\text{Re}(s_n)\} + \{\text{Im}(R_n)\}\{\text{Im}(s_n)\}) \quad (4.21c)$$

$$\beta_{1n} = 2\{\text{Re}(R_n)\} \quad (4.21d)$$

$$(4.21e)$$

Regarding the second-order discrete-element scheme, among all different schemes existent in the literature (see e.g. [67, 142]), the one used herein is represented in Figure 4.13. This particular second-order model has one internal node with a concentrated mass, which is linked to the soil with a spring and a dashpot, and to the superstructure interface, i.e. the master node, with other spring and dashpot. Also, by using this second-order scheme, the master node is directly connected to the soil by another spring and dashpot. For harmonic loading, the equilibrium formulations between the master node (Node 0) and the hidden degree of freedom (Node n) is defined as follows:

$$\text{Node 0:} \quad \left(\frac{\gamma_n^2}{\varrho_n} - \kappa_{1n} - \gamma_n \frac{d}{c_s} (i\omega) \right) U_0 + \left(\kappa_{1n} + \gamma_n \frac{d}{c_s} (i\omega) \right) (U_0 - U_n) = F_0 \quad (4.22a)$$

$$\text{Node } n: \quad \left(\kappa_{2n} + \gamma_n \frac{d}{c_s} (i\omega) + \varrho_n \frac{d^2}{c_s^2} (i\omega)^2 \right) U_n + \left(\kappa_{1n} + \gamma_n \frac{d}{c_s} (i\omega) \right) (U_n - U_0) = 0 \quad (4.22b)$$

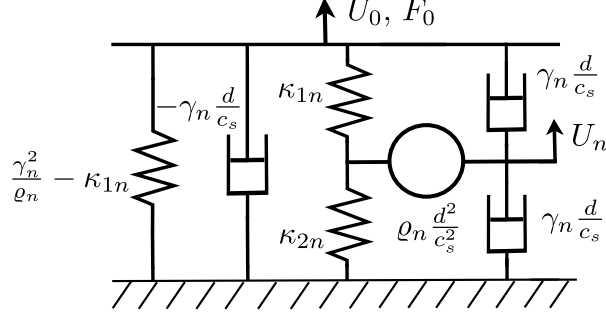


Figure 4.13: Adopted scheme for the second-order discrete-element model [99, 142, 143].

and recalling $\omega = a_0 c_s / d$, it leads to the equations in terms of a_0 instead of ω :

$$\text{Node 0:} \quad \left(\frac{\gamma_n^2}{\varrho_n} - \kappa_{1n} - \gamma_n(i a_0) \right) U_0 + (\kappa_{1n} + \gamma_n(i a_0)) (U_0 - U_n) = F_0 \quad (4.23a)$$

$$\text{Node n:} \quad (\kappa_{2n} + \gamma_n(i a_0) + \varrho_n(i a_0)^2) U_n + (\kappa_{1n} + \gamma_n(i a_0)) (U_n - U_0) = 0 \quad (4.23b)$$

After some rearrangement and elimination of the internal degree of freedom, the force-displacement relation of the second-order model is given by:

$$F_0 = \frac{\frac{\gamma_n^2}{\varrho_n}(\kappa_{1n} + \kappa_{2n}) - \frac{\kappa_{1n}^2}{\varrho_n} + 2 \left(\frac{\gamma_n^3}{\varrho_n^2} - \frac{\kappa_{1n}\gamma_n}{\varrho_n} \right) (i a_0)}{\frac{\kappa_{1n} + \kappa_{2n}}{\varrho_n} + \frac{2\gamma_n}{\varrho_n}(i a_0) + (i a_0)^2} U_0 \quad (4.24)$$

By equating the coefficients in Equation (4.24) to the terms of the second-order model in Equation (4.20), the four parameters κ_{1n} , κ_{2n} , γ_n and ϱ_n can be determined:

$$\alpha_{0n} = \frac{\kappa_{1n} + \kappa_{2n}}{\varrho_n} \quad (4.25a)$$

$$\alpha_{1n} = \frac{2\gamma_n}{\varrho_n} \quad (4.25b)$$

$$\beta_{0n} = \frac{\gamma_n^2}{\varrho_n^2}(\kappa_{1n} + \kappa_{2n}) - \frac{\kappa_{1n}^2}{\varrho_n} \quad (4.25c)$$

$$\beta_{1n} = 2 \left(\frac{\gamma_n^3}{\varrho_n^2} - \frac{\kappa_{1n}\gamma_n}{\varrho_n} \right) \quad (4.25d)$$

$$(4.25e)$$

The system of Equations (4.25) results in a quadratic equation for calculating ϱ_n :

$$(\alpha_{1n}^4 - 4\alpha_{0n}\alpha_{1n}^2)\varrho_n^2 + (16\beta_{0n} - 8\alpha_{1n}\beta_{1n})\varrho_n + \frac{16\beta_{1n}^2}{\alpha_{1n}} = 0 \quad (4.26)$$

and hence two possible solutions are obtained for ϱ_n . To ensure real values of ϱ_n , the following condition must be satisfied:

$$\left(2\frac{\beta_{0n}}{\beta_{1n}} - \alpha_{1n} \right)^2 - \alpha_{1n}^3 + 4\alpha_{0n}\alpha_{1n} \geq 0 \quad (4.27)$$

and in terms of the optimization variables:

$$\left(\frac{\{\text{Im}(R_n)\}}{\{\text{Re}(R_n)\}} \right)^2 - 2\{\text{Re}(s_n)\} \geq 0 \quad (4.28)$$

The real part of the poles of the rational filter have been constrained to positive values in the optimization process (see Equation (4.17)), so the expression shown in the left side of Equation (4.28) always leads to positive values, and hence Equation (4.26) always leads to real values of the ϱ_n parameter. Once the ϱ_n has been calculated, the remaining parameters of the second order scheme are obtained as follows:

$$\kappa_{1n} = \frac{\varrho_n \alpha_{1n}^2}{4} - \frac{\beta_{1n}}{\alpha_{1n}} \quad (4.29a)$$

$$\kappa_{2n} = \varrho_n \alpha_{0n} - \kappa_{1n} \quad (4.29b)$$

$$\gamma_n = \frac{\varrho_n \alpha_{1n}}{2} \quad (4.29c)$$

In some cases, deciding which one of the two values of ϱ_n to take is critical: a positive value is beneficial because the majority of the discrete springs and dampers will then be also positive as they depends on the mass value. The case with a higher amount of positive parameters values is better for ensuring stability in time domain executions. But, if ϱ_n results in a value various orders of magnitude higher, or smaller, than the other masses corresponding to the other second order schemes, contemplating the negative value could be beneficial.

As already stated, the approximation of an impedance function term consists of the sum of the singular part of the stiffness, and N second-order terms corresponding to the regular part of the stiffness. This leads to the final scheme shown in Figure 4.14.

Up to this point, the calculated values of the LPM (κ^∞ , γ^∞ , ϱ_n , κ_{1n} , κ_{2n} and γ_n) agree to the frequency-dependent stiffness dimensionless coefficient $S(a_0)$ but not to the frequency-dependent stiffness $Z(a_0)$. Then, the LPM values must be multiplied by the static stiffness Z^0 in order to obtain the final values related to $Z(a_0)$:

$$k^\infty = \kappa^\infty Z^0 \quad (4.30a)$$

$$c^\infty = \gamma^\infty Z^0 \quad (4.30b)$$

$$m_n = \varrho_n Z^0 \quad (4.30c)$$

$$k_{1n} = \left(\frac{\gamma_n^2}{\varrho_n} - \kappa_{1n} \right) Z^0 \quad (4.30d)$$

$$k_{2n} = \kappa_{1n} Z^0 \quad (4.30e)$$

$$k_{3n} = \kappa_{2n} Z^0 \quad (4.30f)$$

$$c_{1n} = -\gamma_n Z^0 \quad (4.30g)$$

$$c_{2n} = \gamma_n Z^0 \quad (4.30h)$$

$$c_{3n} = \gamma_n Z^0 \quad (4.30i)$$

If the impedance terms are preferred to be expressed in terms of ω , i.e. $Z(\omega)$ instead of $Z(a_0)$, the following values are used:

$$k^\infty = \kappa^\infty Z^0 \quad (4.31a)$$

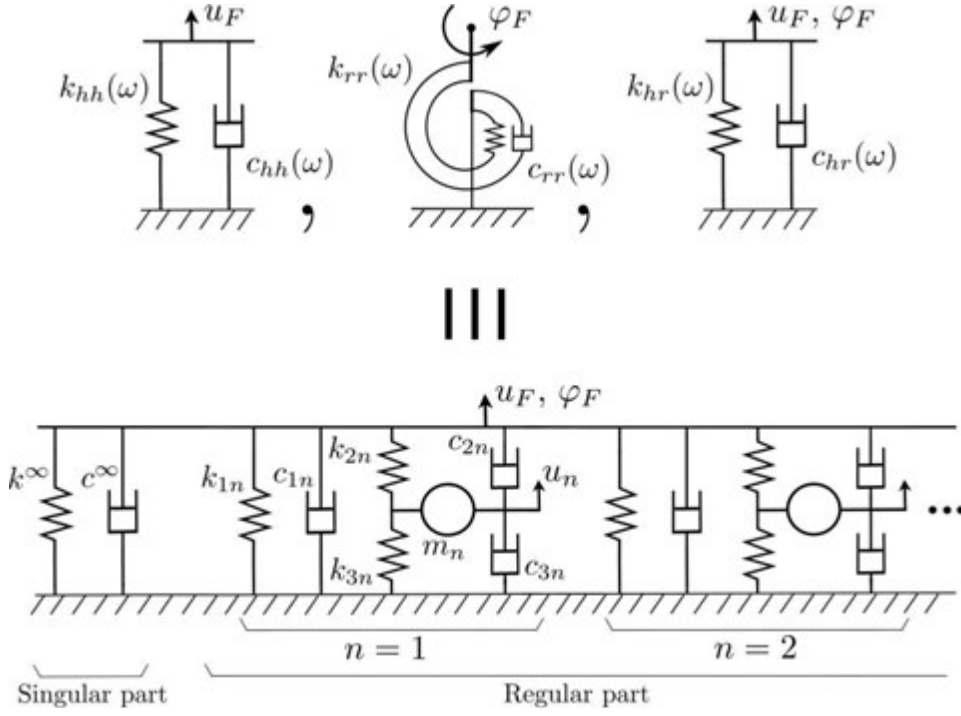


Figure 4.14: Proposed scheme for the consistent LPM.

$$c^\infty = \gamma^\infty Z^0 \frac{d}{c_s} \quad (4.31b)$$

$$m_n = \varrho_n Z^0 \frac{d^2}{c_s^2} \quad (4.31c)$$

$$k_{1n} = \left(\frac{\gamma_n^2}{\varrho_n} - \kappa_{1n} \right) Z^0 \quad (4.31d)$$

$$k_{2n} = \kappa_{1n} Z^0 \quad (4.31e)$$

$$k_{3n} = \kappa_{2n} Z^0 \quad (4.31f)$$

$$c_{1n} = -\gamma_n Z^0 \frac{d}{c_s} \quad (4.31g)$$

$$c_{2n} = \gamma_n Z^0 \frac{d}{c_s} \quad (4.31h)$$

$$c_{3n} = \gamma_n Z^0 \frac{d}{c_s} \quad (4.31i)$$

Finally, the arising system of equations considering hidden degrees of freedom is assembled according to Equation (4.7). The assemblage of the different LPM vectors and matrices that compounds the overall system of equations is as follows:

$$\mathbf{u}_l^T = [\mathbf{u}_{hh} \quad \mathbf{u}_{rh} \quad \mathbf{u}_{hr} \quad \mathbf{u}_{rr}] \quad (4.32a)$$

$$\bar{m}_{hh} = 0 \quad (4.32b)$$

$$\bar{m}_{hr} = 0 \quad (4.32c)$$

$$\bar{m}_{rr} = 0 \quad (4.32d)$$

$$\bar{\mathbf{M}}_{ll} = \begin{bmatrix} \mathbf{M}_{hh} & \mathbf{0} & \mathbf{0} & \mathbf{0} \\ \mathbf{0} & \mathbf{0} & \mathbf{M}_{hr} & \mathbf{0} \\ \mathbf{0} & \mathbf{M}_{hr} & \mathbf{0} & \mathbf{0} \\ \mathbf{0} & \mathbf{0} & \mathbf{0} & \mathbf{M}_{rr} \end{bmatrix} \quad (4.32e)$$

$$\bar{c}_{hh} = c_{hh}^{\infty} + \sum_{n=1}^N (c_{hh_{1n}} + c_{hh_{2n}}) \quad (4.32f)$$

$$\bar{c}_{hr} = c_{hr}^{\infty} + \sum_{n=1}^N (c_{hr_{1n}} + c_{hr_{2n}}) \quad (4.32g)$$

$$\bar{c}_{rr} = c_{rr}^{\infty} + \sum_{n=1}^N (c_{rr_{1n}} + c_{rr_{2n}}) \quad (4.32h)$$

$$\bar{\mathbf{c}}_{hl} = \begin{bmatrix} \mathbf{c}_{hh} & \mathbf{0} & \mathbf{c}_{hr} & \mathbf{0} \end{bmatrix} \quad (4.32i)$$

$$\bar{\mathbf{c}}_{rl} = \begin{bmatrix} \mathbf{0} & \mathbf{c}_{hr} & \mathbf{0} & \mathbf{c}_{rr} \end{bmatrix} \quad (4.32j)$$

$$\bar{\mathbf{C}}_{ll} = \begin{bmatrix} \mathbf{C}_{hh} & \mathbf{0} & \mathbf{0} & \mathbf{0} \\ \mathbf{0} & \mathbf{0} & \mathbf{C}_{hr} & \mathbf{0} \\ \mathbf{0} & \mathbf{C}_{hr} & \mathbf{0} & \mathbf{0} \\ \mathbf{0} & \mathbf{0} & \mathbf{0} & \mathbf{C}_{rr} \end{bmatrix} \quad (4.32k)$$

$$\bar{k}_{hh} = k_{hh}^{\infty} + \sum_{n=1}^N (k_{hh_{1n}} + k_{hh_{2n}}) \quad (4.32l)$$

$$\bar{k}_{hr} = k_{hr}^{\infty} + \sum_{n=1}^N (k_{hr_{1n}} + k_{hr_{2n}}) \quad (4.32m)$$

$$\bar{k}_{rr} = k_{rr}^{\infty} + \sum_{n=1}^N (k_{rr_{1n}} + k_{rr_{2n}}) \quad (4.32n)$$

$$\bar{\mathbf{k}}_{hl} = \begin{bmatrix} \mathbf{k}_{hh} & \mathbf{0} & \mathbf{k}_{hr} & \mathbf{0} \end{bmatrix} \quad (4.32o)$$

$$\bar{\mathbf{k}}_{rl} = \begin{bmatrix} \mathbf{0} & \mathbf{k}_{hr} & \mathbf{0} & \mathbf{k}_{rr} \end{bmatrix} \quad (4.32p)$$

$$\bar{\mathbf{K}}_{ll} = \begin{bmatrix} \mathbf{K}_{hh} & \mathbf{0} & \mathbf{0} & \mathbf{0} \\ \mathbf{0} & \mathbf{0} & \mathbf{K}_{hr} & \mathbf{0} \\ \mathbf{0} & \mathbf{K}_{hr} & \mathbf{0} & \mathbf{0} \\ \mathbf{0} & \mathbf{0} & \mathbf{0} & \mathbf{K}_{rr} \end{bmatrix} \quad (4.32q)$$

$$(4.32r)$$

where

$$\mathbf{u}_{hh} = \begin{bmatrix} u_{hh_1} & u_{hh_2} & \cdots & u_{hh_n} & \cdots & u_{hh_N} \end{bmatrix} \quad (4.33a)$$

$$\mathbf{u}_{rh} = \begin{bmatrix} \varphi_{rh_1} & \varphi_{rh_2} & \cdots & \varphi_{rh_n} & \cdots & \varphi_{rh_N} \end{bmatrix} \quad (4.33b)$$

$$\mathbf{u}_{hr} = \begin{bmatrix} u_{hr_1} & u_{hr_2} & \cdots & u_{hr_n} & \cdots & u_{hr_N} \end{bmatrix} \quad (4.33c)$$

$$\mathbf{u}_{rr} = \begin{bmatrix} \varphi_{rr_1} & \varphi_{rr_2} & \cdots & \varphi_{rr_n} & \cdots & \varphi_{rr_N} \end{bmatrix} \quad (4.33d)$$

$$\mathbf{M}_{hh} = \begin{bmatrix} m_{hh_1} & 0 & 0 & \cdots & \cdots & 0 \\ 0 & m_{hh_2} & 0 & \vdots & \vdots & \vdots \\ 0 & 0 & \ddots & 0 & \vdots & \vdots \\ \vdots & \cdots & 0 & m_{hh_n} & 0 & \vdots \\ \vdots & \cdots & \cdots & 0 & \ddots & 0 \\ 0 & \cdots & \cdots & \cdots & 0 & m_{hh_N} \end{bmatrix} \quad (4.33e)$$

$$\mathbf{M}_{hr} = \begin{bmatrix} m_{hr_1} & 0 & 0 & \cdots & \cdots & 0 \\ 0 & m_{hr_2} & 0 & \vdots & \vdots & \vdots \\ 0 & 0 & \ddots & 0 & \vdots & \vdots \\ \vdots & \cdots & 0 & m_{hr_n} & 0 & \vdots \\ \vdots & \cdots & \cdots & 0 & \ddots & 0 \\ 0 & \cdots & \cdots & \cdots & 0 & m_{hr_N} \end{bmatrix} \quad (4.33f)$$

$$\mathbf{M}_{rr} = \begin{bmatrix} m_{rr_1} & 0 & 0 & \cdots & \cdots & 0 \\ 0 & m_{rr_2} & 0 & \vdots & \vdots & \vdots \\ 0 & 0 & \ddots & 0 & \vdots & \vdots \\ \vdots & \cdots & 0 & m_{rr_n} & 0 & \vdots \\ \vdots & \cdots & \cdots & 0 & \ddots & 0 \\ 0 & \cdots & \cdots & \cdots & 0 & m_{rr_N} \end{bmatrix} \quad (4.33g)$$

$$\mathbf{c}_{hh} = \begin{bmatrix} -C_{hh_{21}} & -C_{hh_{22}} & \cdots & -C_{hh_{2n}} & \cdots & -C_{hh_{2N}} \end{bmatrix} \quad (4.33h)$$

$$\mathbf{c}_{hr} = \begin{bmatrix} -C_{hr_{21}} & -C_{hr_{22}} & \cdots & -C_{hr_{2n}} & \cdots & -C_{hr_{2N}} \end{bmatrix} \quad (4.33i)$$

$$\mathbf{c}_{rr} = \begin{bmatrix} -C_{rr_{21}} & -C_{rr_{22}} & \cdots & -C_{rr_{2n}} & \cdots & -C_{rr_{2N}} \end{bmatrix} \quad (4.33j)$$

$$\mathbf{C}_{hh} = \begin{bmatrix} C_{hh_{21}} + C_{hh_{31}} & 0 & 0 & \cdots & \cdots & 0 \\ 0 & C_{hh_{22}} + C_{hh_{32}} & 0 & \vdots & \vdots & \vdots \\ 0 & 0 & \ddots & 0 & \vdots & \vdots \\ \vdots & \cdots & 0 & C_{hh_{2n}} + C_{hh_{3n}} & 0 & \vdots \\ \vdots & \cdots & \cdots & 0 & \ddots & 0 \\ 0 & \cdots & \cdots & \cdots & 0 & C_{hh_{2N}} + C_{hh_{3N}} \end{bmatrix} \quad (4.33k)$$

$$\mathbf{C}_{hr} = \begin{bmatrix} C_{hr_{21}} + C_{hr_{31}} & 0 & 0 & \cdots & \cdots & 0 \\ 0 & C_{hr_{22}} + C_{hr_{32}} & 0 & \vdots & \vdots & \vdots \\ 0 & 0 & \ddots & 0 & \vdots & \vdots \\ \vdots & \cdots & 0 & C_{hr_{2n}} + C_{hr_{3n}} & 0 & \vdots \\ \vdots & \cdots & \cdots & 0 & \ddots & 0 \\ 0 & \cdots & \cdots & \cdots & 0 & C_{hr_{2N}} + C_{hr_{3N}} \end{bmatrix} \quad (4.33l)$$

$$\mathbf{C}_{rr} = \begin{bmatrix} c_{rr21} + c_{rr31} & 0 & 0 & \cdots & \cdots & 0 \\ 0 & c_{rr22} + c_{rr32} & 0 & \vdots & \vdots & \vdots \\ 0 & 0 & \ddots & 0 & \vdots & \vdots \\ \vdots & \cdots & 0 & c_{rr2n} + c_{rr3n} & 0 & \vdots \\ \vdots & \cdots & \cdots & 0 & \ddots & 0 \\ 0 & \cdots & \cdots & \cdots & 0 & c_{rr2N} + c_{rr3N} \end{bmatrix} \quad (4.33m)$$

$$\mathbf{k}_{hh} = \begin{bmatrix} -k_{hh21} & -k_{hh22} & \cdots & -k_{hh2n} & \cdots & -k_{hh2N} \end{bmatrix} \quad (4.33n)$$

$$\mathbf{k}_{hr} = \begin{bmatrix} -k_{hr21} & -k_{hr22} & \cdots & -k_{hr2n} & \cdots & -k_{hr2N} \end{bmatrix} \quad (4.33o)$$

$$\mathbf{k}_{rr} = \begin{bmatrix} -k_{rr21} & -k_{rr22} & \cdots & -k_{rr2n} & \cdots & -k_{rr2N} \end{bmatrix} \quad (4.33p)$$

$$\mathbf{K}_{hh} = \begin{bmatrix} k_{hh21} + k_{hh31} & 0 & 0 & \cdots & \cdots & 0 \\ 0 & k_{hh22} + k_{hh32} & 0 & \vdots & \vdots & \vdots \\ 0 & 0 & \ddots & 0 & \vdots & \vdots \\ \vdots & \cdots & 0 & k_{hh2n} + k_{hh3n} & 0 & \vdots \\ \vdots & \cdots & \cdots & 0 & \ddots & 0 \\ 0 & \cdots & \cdots & \cdots & 0 & k_{hh2N} + k_{hh3N} \end{bmatrix} \quad (4.33q)$$

$$\mathbf{K}_{hr} = \begin{bmatrix} k_{hr21} + k_{hr31} & 0 & 0 & \cdots & \cdots & 0 \\ 0 & k_{hr22} + k_{hr32} & 0 & \vdots & \vdots & \vdots \\ 0 & 0 & \ddots & 0 & \vdots & \vdots \\ \vdots & \cdots & 0 & k_{hr2n} + k_{hr3n} & 0 & \vdots \\ \vdots & \cdots & \cdots & 0 & \ddots & 0 \\ 0 & \cdots & \cdots & \cdots & 0 & k_{hr2N} + k_{hr3N} \end{bmatrix} \quad (4.33r)$$

$$\mathbf{K}_{rr} = \begin{bmatrix} k_{rr21} + k_{rr31} & 0 & 0 & \cdots & \cdots & 0 \\ 0 & k_{rr22} + k_{rr32} & 0 & \vdots & \vdots & \vdots \\ 0 & 0 & \ddots & 0 & \vdots & \vdots \\ \vdots & \cdots & 0 & k_{rr2n} + k_{rr3n} & 0 & \vdots \\ \vdots & \cdots & \cdots & 0 & \ddots & 0 \\ 0 & \cdots & \cdots & \cdots & 0 & k_{rr2N} + k_{rr3N} \end{bmatrix} \quad (4.33s)$$

$$(4.33t)$$

4.9.2 Simplified LPM

As shown in Figure 4.15, this scheme is constituted by a two degree-of-freedom LPM characterized by a translational mass m_h and a mass moment of inertia I_r at the foundation-structure interface, connected to the soil through translational and rotational pairs of constant springs and dashpots k_h , c_h , k_r and c_r . Furthermore, masses are connected to an additional eccentric translational mass m_t , spring k_t and dashpot c_t through rigid massless links of lengths h_3 , and h_2 , respectively. The dynamic impedances arising from this model can be expressed as:

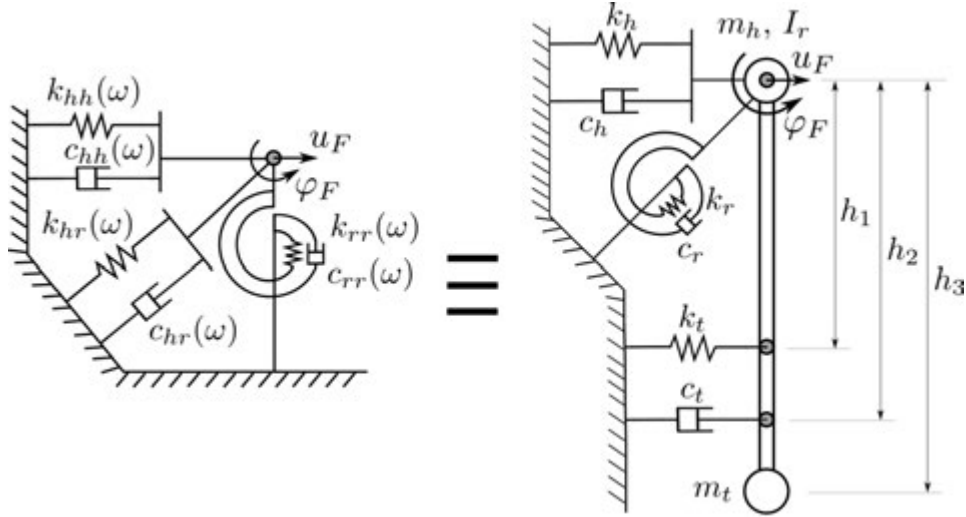


Figure 4.15: Scheme of the simplified LPM [133].

$$k_{hh}(\omega) \approx k_h + k_t - \omega^2(m_h + m_t) \quad (4.34a)$$

$$c_{hh}(\omega) \approx c_h + c_t \quad (4.34b)$$

$$k_{rr}(\omega) \approx k_r + k_t h_1^2 - \omega^2(I_r + m_t h_3^2) \quad (4.34c)$$

$$c_{rr}(\omega) \approx c_r + c_t h_2^2 \quad (4.34d)$$

$$k_{hr}(\omega) \approx k_t h_1 - \omega^2 m_t h_3 \quad (4.34e)$$

$$c_{hr}(\omega) \approx c_t h_2 \quad (4.34f)$$

where all real and imaginary terms are parabolic and linear functions of ω , respectively.

The presence of the additional mass m_t at a certain depth makes the model able to capture the coupled roto-translational dynamic response of the foundation, and contrary to the approach adopted for the consistent LPM, the fitting process of the translational, rotational and coupled impedance functions are made simultaneously. Also, thanks to the rigid link, the dynamic stiffness matrix of the LPM can be condensed on the degrees of freedom of the master node on the foundation-structure interface (i.e. there are no hidden nodes). Another advantage of this configuration is the possibility of an easy implementation in many commercial software. However, conventional software usually do not allow the introduction of negative values of masses, dampers and springs, so, in order to maintain this advantage in the simplified model, all real constants of the scheme are forced to be positive, with the only exception of the different lengths of the rigid link (h_1 , h_2 and h_3). The resulting parabolic horizontal and rocking stiffness functions are concave due to the positive values of the masses, with a positive static value. On the contrary, the crossed stiffness can be convex and the static value can be positive or not, depending on the sign of h_1 and h_3 . Furthermore, since the hidden variable condensation produces non-diagonal terms in the mass matrix of the system, it may be convenient to introduce the rigid link and the eccentric mass when simulating with structural analysis software since non-diagonal mass matrices are often not available.

All the parameter values $\mathbf{x} = [k_h, k_r, k_t, c_h, c_r, c_t, m_h, I_r, m_t, h_1, h_2, h_3]$ that define the model are found directly through a nonlinear least square fitting procedure of the re-

sponse of the LPM in terms of impedance functions to the reference impedance functions (see Equation (4.34)):

$$\begin{aligned} & \min_{\mathbf{x}} \|((\hat{Z}_{hh}(\mathbf{x}, \omega) - Z_{hh}(\omega)) + (\hat{Z}_{hr}(\mathbf{x}, \omega) - Z_{hr}(\omega)) + (\hat{Z}_{rr}(\mathbf{x}, \omega) - Z_{rr}(\omega))) \Psi(\omega)\|_2^2 = \\ & = \min_{\mathbf{x}} \sum_i (((\hat{Z}_{hh}(\mathbf{x}, \omega_i) - Z_{hh}(\omega_i)) + (\hat{Z}_{hr}(\mathbf{x}, \omega_i) - Z_{hr}(\omega_i)) + (\hat{Z}_{rr}(\mathbf{x}, \omega_i) - Z_{rr}(\omega_i))) \Psi(\omega_i))^2 \end{aligned} \quad (4.35)$$

where the weight function $\Psi(\omega) | 0 \leq \Psi(\omega) \leq 1$ could be employed, similarly to the consistent LPM, to prioritize the fitting in a range.

In the case of this simplified approach, the LPM parameters are assembled in the system of equations (Equation (4.7)) as follows:

$$\mathbf{u}_l = \emptyset \quad (4.36a)$$

$$\bar{m}_{hh} = m_h + m_t \quad (4.36b)$$

$$\bar{m}_{hr} = m_t h_3 \quad (4.36c)$$

$$\bar{m}_{rr} = I_r + m_t h_3^2 \quad (4.36d)$$

$$\bar{\mathbf{M}}_{ll} = \emptyset \quad (4.36e)$$

$$\bar{c}_{hh} = c_h + c_t \quad (4.36f)$$

$$\bar{c}_{hr} = c_t h_2 \quad (4.36g)$$

$$\bar{c}_{rr} = c_r + c_t h_2^2 \quad (4.36h)$$

$$\bar{\mathbf{c}}_{hl} = \emptyset \quad (4.36i)$$

$$\bar{\mathbf{c}}_{rl} = \emptyset \quad (4.36j)$$

$$\bar{\mathbf{C}}_{ll} = \emptyset \quad (4.36k)$$

$$\bar{k}_{hh} = k_h + k_t \quad (4.36l)$$

$$\bar{k}_{hr} = k_t h_1 \quad (4.36m)$$

$$\bar{k}_{rr} = k_r + k_t h_1^2 \quad (4.36n)$$

$$\bar{\mathbf{k}}_{hl} = \emptyset \quad (4.36o)$$

$$\bar{\mathbf{k}}_{rl} = \emptyset \quad (4.36p)$$

$$\bar{\mathbf{K}}_{ll} = \emptyset \quad (4.36q)$$

Chapter 5

Influence of the soil damping model and the lumped parameter representations of the foundation

5.1 Introduction

In this chapter, the influence on the computed seismic response of bridge piers on pile groups of two closely related aspects is quantified: i) the adoption of the classical non-causal hysteretic damping model for the soil, or the causal Biot's damping model; and ii) the implementation of a relatively complex consistent LPM based on a rational approximation, or a more simplified LPM, to represent the behaviour of the foundation. As will be shown later, both aspects are studied simultaneously because the choice of soil damping can significantly influence the ability of the LPMs to capture the impedances of the pile group foundations. To achieve this goal, a wide parametric study involving different soil profiles and superstructures is carried out in order to be able to draw general conclusions. The analysis is carried out into a linear-elastic framework so that the conclusions of the study provide an informed starting point for the study of the more involved nonlinear case addressed in Chapter 6. The dynamic problem is both solved in the frequency domain and in the time domain (see Section 4.5), by adopting the two different LPMs described in Section 4.9 to approximate the soil-foundation system behaviour.

5.2 Configurations under study

Four realistic superstructures, characterised by fundamental periods $T_n = 0.2$ s, $T_n = 0.5$ s, $T_n = 1.0$ s and $T_n = 1.5$ s, are considered in this study (see Table 5.1). Mass and geometric properties comply with steel-concrete composite continuous bridge decks with span length of 25 m. A force-based approach is adopted to design the FB piers on both soil deposits, obtaining longitudinal reinforcement ratios ranging between 1.3–3.0%. Piers are founded on six different pile foundations, constituted by 2×2 and 3×3 vertical piles groups with diameter $d = 1.0$ m, pile length $L = 20.0$ m, and three different pile-to-pile spacings s (3, 5 and 7 m). Foundations are selected to balance the need of parametrically addressing the effects of the foundation deformability on the superstructure response with that of considering realistic scenarios. Overall, they comply

Superstructure	1	2	3	4
T_n [s]	0.2	0.5	1.0	1.5
f_n [Hz]	5.0	2.0	1.0	0.6
m_d [t]	305.8	305.8	305.8	305.8
I_d [t m ²]	2466.6	2466.6	2466.6	2466.6
h_d [m]	0.59	0.59	0.59	0.59
m_c [t]	88.3	88.3	88.3	88.3
I_c [t m ²]	426.6	426.6	426.6	426.6
h_c [m]	1.80	1.80	1.80	1.80
m_p [t]	57.6	121.1	196.0	253.6
h_p [m]	5.0	10.5	17.0	22.0
K_ϕ [MN/rad]	23067.6	10984.6	6784.6	5242.6
Real period [s]	0.2001	0.5082	1.0076	1.4841

Table 5.1: Superstructures parameters.

	2×2 ($\theta = 0^\circ, 5^\circ$ and 10°)			3×3		
	$s = 3$ [m]	$s = 5$ [m]	$s = 7$ [m]	$s = 3$ [m]	$s = 5$ [m]	$s = 7$ [m]
h_f [m]	1.5	2.0	2.5	2.0	2.5	3.0
m_f [t]	93.75	245.00	506.25	320.00	900.00	1920.00
I_f [t m ²]	212.89	1082.08	3680.86	1813.33	11268.75	42400.00

Table 5.2: Pile cap properties depending on foundation layout for CB model.

with stress resultants at the pier bases in the 80% of cases, being the 2×2 layout with spacing 3 m and 3×3 layout with spacing 7 m border line configurations. The pile cap mass and inertial properties, which depend on the foundation layouts, are summarized in Table 5.2. Finally, pile inclination can exert an important influence on the response of the superstructure [94, 95]. For this reason, inclined piles are also considered in the analyses of the 2×2 foundations, with rake angles θ of 5° and 10° .

Piles Young's modulus and density are $E_p = 30.0$ GPa and $\rho_p = 2.5$ t/m³, respectively. The pier elastic flexural spring (K_ϕ) is calibrated to reproduce the fundamental period of the system, while the damping coefficient (C_ϕ) is calibrated to obtain a 5% viscous damping ratio at the fundamental period of the pier. FB models will be also considered (Figure 4.12), whose results will be used to address and discuss the significance of the SSI effects.

5.3 Soil properties and seismic actions

Foundations are assumed to be embedded in two different soil deposits, representative of a soil type D (loose-to-medium cohesionless soil or predominantly soft-to-firm cohesive soil) and of a soil type C (dense or medium-dense sand, gravel or stiff clay), according to Eurocode 8 [109]. With reference to the softer soil deposit, a soil density $\rho_s = 1.56$ t/m³, shear wave velocity $c_s = 117.1$ m/s, soil Poisson's ratio $\nu_s = 0.4$ and soil damping coefficient $\xi_s = 5\%$ are assumed, while for the stiffer deposit, representative of a ground type C, a soil density $\rho_s = 1.67$ t/m³, shear wave velocity $c_s = 253.5$ m/s, Poisson's ratio $\nu_s = 0.4$ and soil damping coefficient $\xi_s = 5\%$ are considered.

<i>Database</i>	<i>Earthquake WC-EC</i>	<i>Station ID</i>	<i>Date</i> [dd/mm/yy]	Δ [km]	<i>Magnitude</i> [M_w]	<i>PGA</i> [m/s^2]
ITACA	Val Nerina 138-036	BVG	19/09/1979	38.0	5.8	0.222 y-dir
ITACA	Umbria-Marche 1 st shock 363-099	BVG	26/09/1997	24.9	5.7	0.372 x-dir
ITACA	Umbria-Marche 2 nd shock 394-100	RTI	26/09/1997	65.0	6.0	0.184 y-dir
ITACA	App. Umbro-Marchigiano 429-111	BVG	06/10/1997	21.9	5.4	0.349 x-dir
ITACA	Umbria-Marche 3 rd shock 482-118	BVG	14/10/1997	23.8	5.6	0.359 y-dir
ESD	Izmit (aftershock) 6947-2154	3270	31/08/1999	39	5.1	0.358 y-dir
ESD	Izmit (aftershock) 6967-0473	767	13/09/1999	120	5.8	0.391 x-dir

Table 5.3: Selected records for ground type D (WC: Waveform Code and EC: Earthquake Code) [119, 123].

The seismic action is constituted by a set of 7 real accelerograms for each soil deposit, selected from the European and Italian strong motion databases [119, 123]. The selection criterion is based on both the Magnitude ($M_w > 5$) and the site classification (records registered on soil type C and D); the limited number of eligible records for selection required the inclusion of mainshock and aftershocks of the same event. The selected records are reported in Tables 5.3 and 5.4 for deposits D and C, respectively; also their acceleration time histories are shown in Figures 5.1 and 5.2 for deposits D and C, respectively. For each superstructure, accelerograms are scaled in order to obtain the matching of the pseudo spectral acceleration of each accelerogram with the response spectrum proposed in the standard [109] at the fundamental periods of the FB systems, as shown in Figure 5.3 in which the mean response spectrum of the scaled set of accelerograms are reported for each superstructure on both soil deposits.

5.4 Error measurement

The large number of cases involved in the study requires a way to synthesize the results so that the influence of the different parameters can be evaluated. Firstly, the effectiveness of the different LPMs when used to obtain the system response in time domain is measured using Equation (5.1), where x stands for the degree of freedom under consideration (φ_S , u_F or φ_F), “sdm” stands for the soil damping model considered (hysteretic or Biot’s), and “lpm” stands for the LPM used (simplified or consistent). This measure of the differences takes into account the entire earthquake duration of the seismic signal, being P the total amount of time steps in the time history. Results obtained through the frequency domain method of response are chosen as reference.

$$\varepsilon_{x_{lpm}}^{sdm} = \sqrt{\frac{\sum_{i=0}^P (x_{lpm,i}^{sdm} - x_{freq. domain,i}^{sdm})^2}{\sum_{i=0}^P (x_{freq. domain,i}^{sdm})^2}} \quad (5.1)$$

On the other hand, the influence of the soil damping model is quantified using Equa-

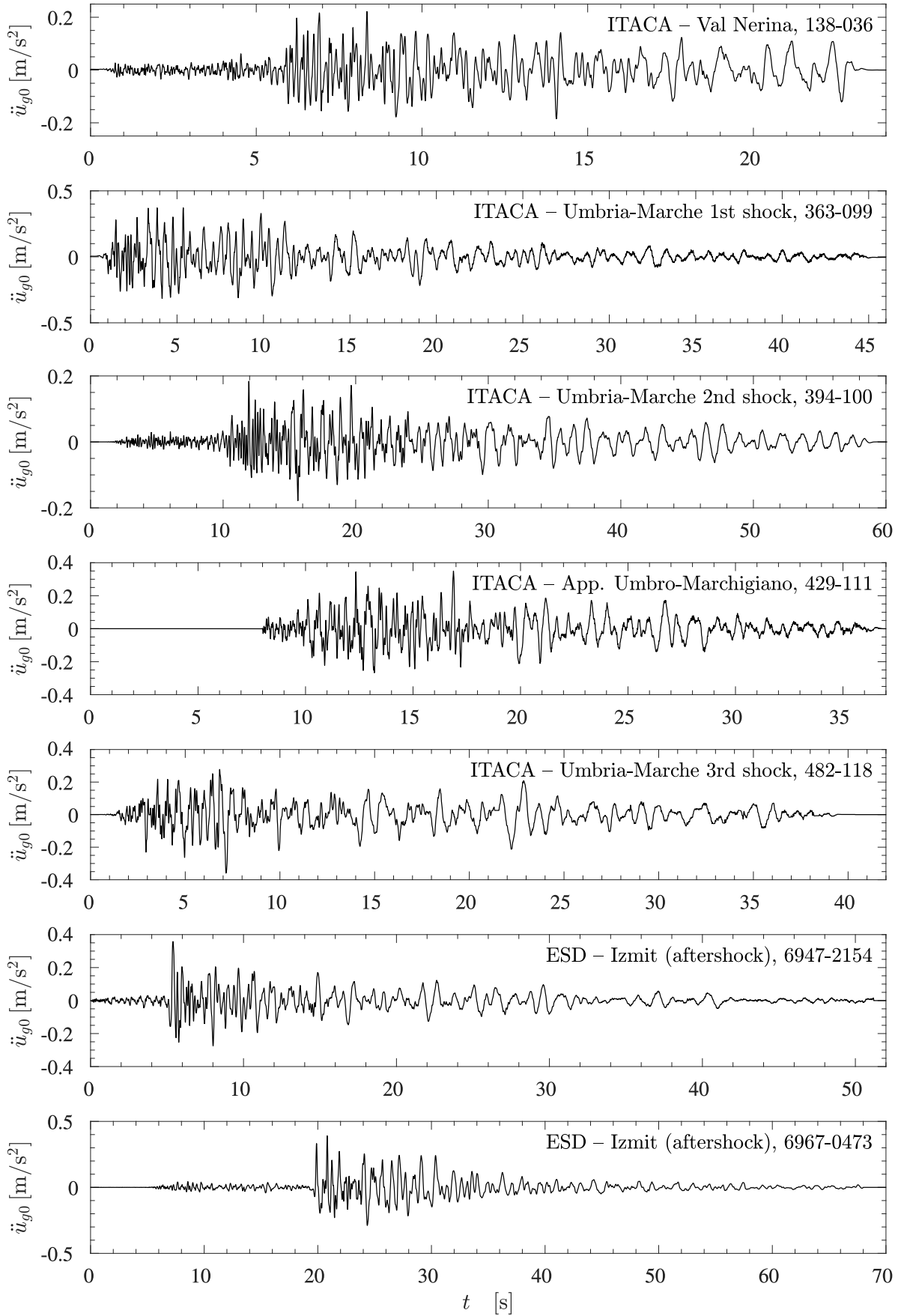


Figure 5.1: Time histories of the selected records for ground type D (see Table 5.3).

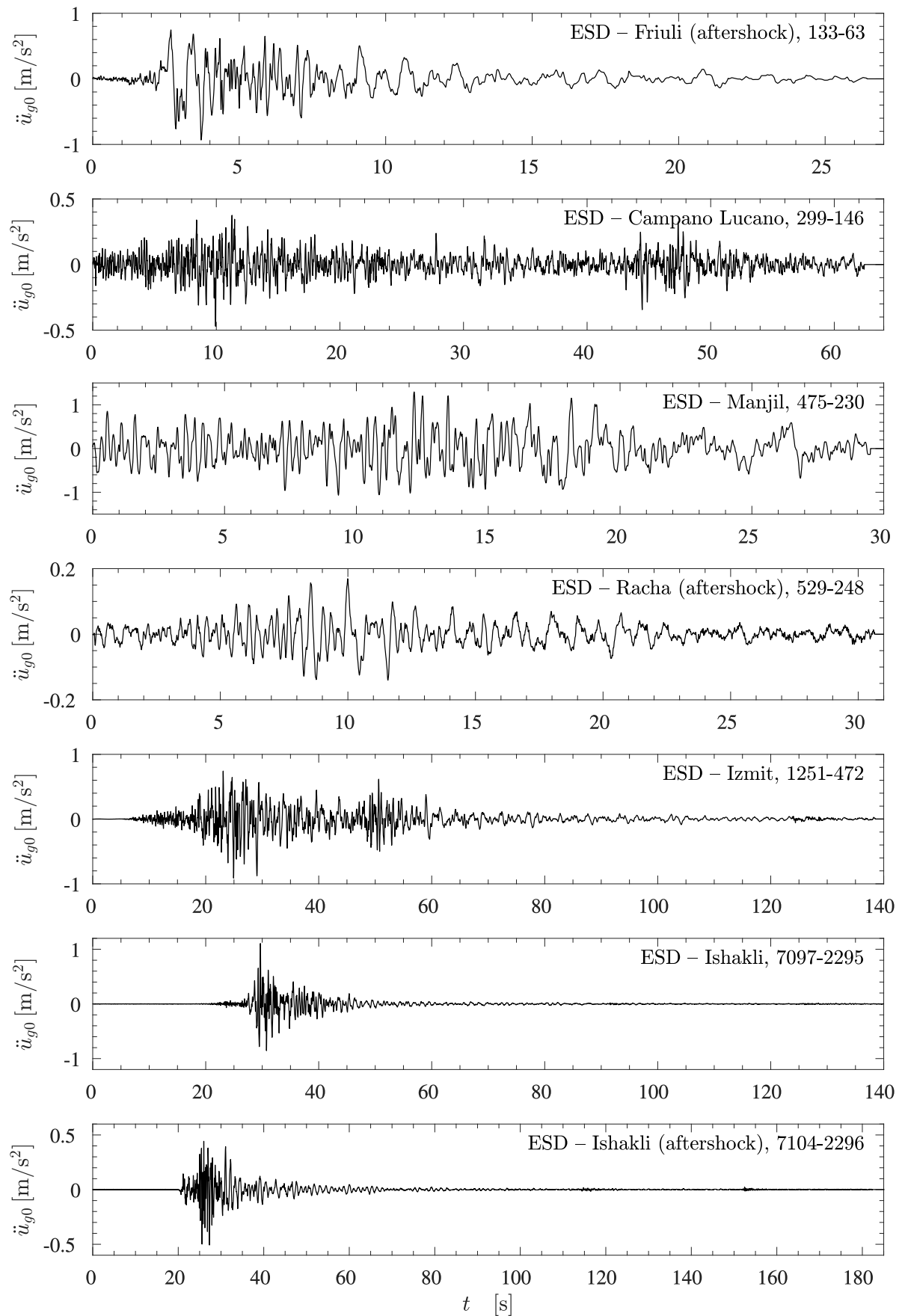


Figure 5.2: Time histories of the selected records for ground type C (see Table 5.4).

<i>Database</i>	<i>Earthquake WC-EC</i>	<i>Station ID</i>	<i>Date</i> [dd/mm/yy]	Δ [km]	<i>Magnitude</i> [M _w]	<i>PGA</i> [m/s ²]
ESD	Friuli (aftershock) 133-63	33	15/09/1976	9	6.0	0.932 <i>y-dir</i>
ESD	Campano Lucano 299-146	105	23/11/1980	52	6.9	0.471 <i>x-dir</i>
ESD	Manjil 475-230	184	20/06/1990	91	7.4	1.295 <i>x-dir</i>
ESD	Racha (aftershock) 529-248	199	15/06/1991	72	6.0	0.169 <i>x-dir</i>
ESD	Izmit 1251-472	773	17/08/1999	92	7.6	0.911 <i>x-dir</i>
ESD	Ishakli 7097-2295	856	03/02/2002	66	6.5	1.106 <i>x-dir</i>
ESD	Ishakli (aftershock) 7104-2296	856	03/02/2002	35	5.8	0.507 <i>y-dir</i>

Table 5.4: Selected records for ground type C (WC: Waveform Code and EC: Earthquake Code) [119].

tion (5.2). Again, this measure of the differences takes into account the entire earthquake duration of the seismic signal. In this case, all responses are computed through the frequency domain method of response analysis. Results corresponding to the hysteretic soil damping model are chosen as reference.

$$\chi_x = \sqrt{\frac{\sum_{i=0}^P (x_{\text{Biot},i} - x_{\text{hysteretic},i})^2}{\sum_{i=0}^P x_{\text{hysteretic},i}^2}} \quad (5.2)$$

5.5 Influence of soil damping model on impedance and kinematic interaction functions

As a first step, impedance and kinematic interaction (KI) functions in the frequency domain must be computed in order to build the different substructuring models used in the analyses. When doing so, soil damping is considered using either Biot's or hysteretic damping, so that its influence on the overall response can later be analysed. In order to illustrate the effects on impedance functions of assuming one damping model or the other, horizontal, rocking and crossed-coupled impedance functions ($Z_{ij}(\omega) = k_{ij}(\omega) + i\omega c_{ij}(\omega)$) are presented in Figure 5.4 in terms of stiffness ($k_{ij}(\omega)$) and damping ($c_{ij}(\omega)$) functions, for both hysteretic and Biot's models (see solid and dashed black lines, respectively), for the specific case of a 2×2 vertical pile group, embedded in a type D ground and with a pile-to-pile spacing $s = 7$ m. The impedance functions related to all the soil-foundations systems used in this Chapter 5 are presented in Appendix A.

The main difference between both models lies in the damping coefficient at very low frequencies. As anticipated, the hysteretic model produces a damping function such that the imaginary part of the impedance function is non-zero at $\omega = 0$, while Biot's model leads to a finite damping function at zero, which implies an imaginary part of the impedance function that vanishes for a static situation. On the contrary, the damping functions obtained with both models are almost coincident for frequencies

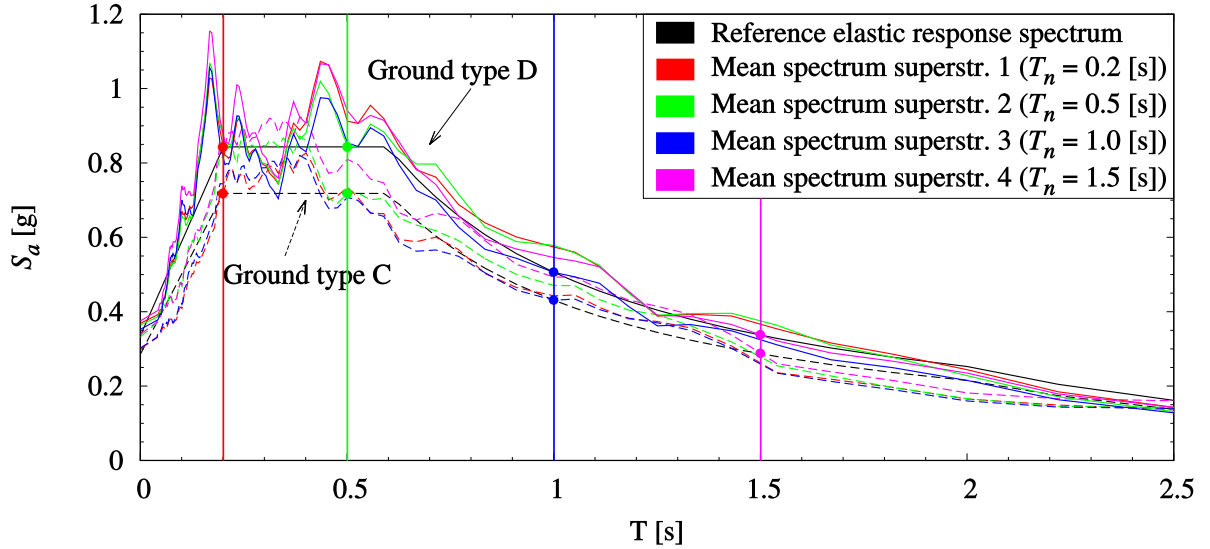


Figure 5.3: Mean response spectrum of the resulting sets of accelerograms scaled for each superstructure and ground type (Ground type D in continuous line and Ground type C in dashed line).

above 5 Hz. Stiffness functions, on the other hand, coincide at low frequencies, but differ at frequencies above 10 Hz, with Biot's model leading to larger stiffness values. In this work, a value of $\epsilon_b = 0.15c_s/(2\pi d)$ Hz is chosen for the Biot's model (see Section 4.7), which derives in two cases depending on the soil type, $\epsilon_b = 2.80$ Hz for D case and $\epsilon_b = 6.05$ Hz for C.

Kinematic interaction factors are also affected by the soil damping model chosen for the analysis. In order to illustrate the magnitude of this effect, Figure 5.5 presents modulus and phase of the translational and rotational kinematic interaction factors obtained for the same configuration presented above (see curves for the vertical case), together with the normalized mean Fourier amplitude spectrum of the ground motion, scaled for superstructure 3 ($T_n = 1.0$ s). The classical hysteretic soil damping model predicts a slightly larger filtering effect for the translational kinematic interaction factors, with a larger induced rotation of the foundation for frequencies below 11 Hz. On the contrary, Biot's soil damping model predicts larger rotations for frequencies above 11 Hz. On the other hand, the phase of the rotational kinematic interaction function illustrates very clearly the incoherences arising from the use of the standard hysteretic damping model, with a non-zero phase delay for the static situation. Apart from this, the phase of the translational motion is larger when the hysteretic model is assumed. The kinematic interaction factors related to all the soil-foundations systems used in this Chapter 5 are presented in Appendix A.

In any case, the relevance of the differences between impedance or kinematic interaction functions obtained from one damping model or the other will depend on other aspects such as the magnitude of the SSI effects, or the natural frequencies of the superstructure. Depending on the properties of the superstructure, foundation and/or seismic input, certain differences in one function or frequency range can be important or totally anecdotal. Therefore, the influence of the damping model must also be assessed analysing the magnitude of the differences arising in the superstructural response due to this aspect. For this reason, subsequent sections will focus not on impedance or kine-

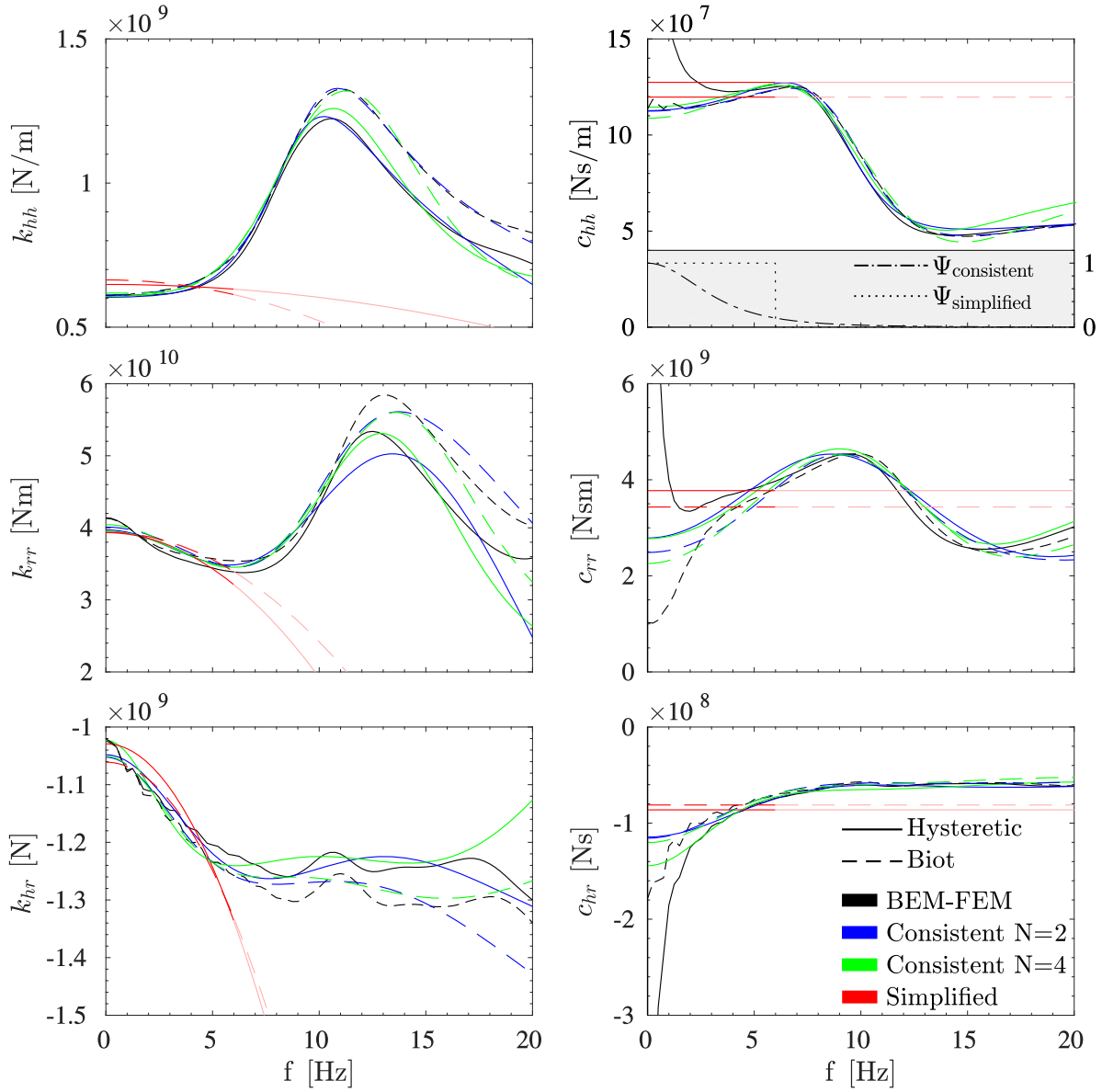


Figure 5.4: Illustration of the computed and fitted impedance functions for one of the configurations analyzed (vertical 2×2 , $s = 7$ m foundation layout in ground type D). Continuous and dashed black lines represent impedance functions assuming hysteretic and Biot's damping models, respectively; blue and green lines represent fitted functions using consistent LPM with orders $N = 2$ and $N = 4$, respectively; red lines represent fitted functions using simplified LPM; and Ψ represents the weight functions used by the LPM approaches (defined in Equations (5.3a) and (5.3b)).

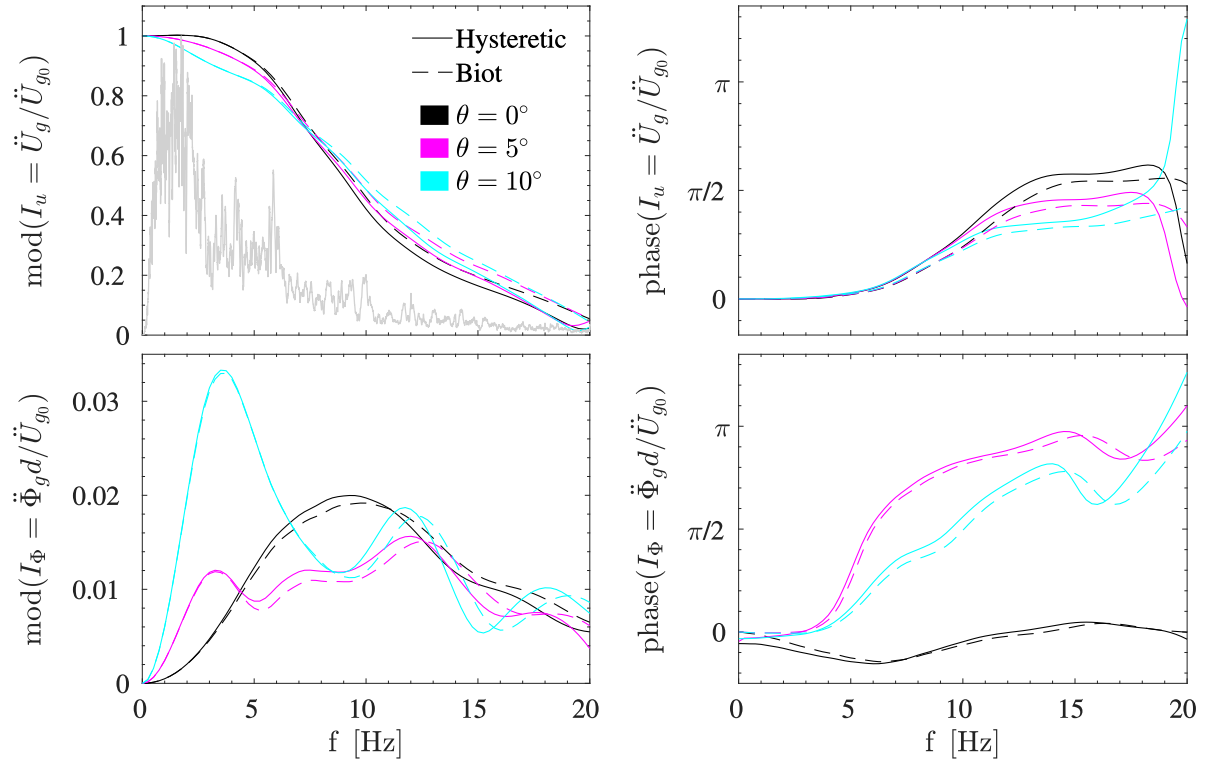


Figure 5.5: Illustration of the computed kinematic interaction factors for 2×2 , $s = 7$ m foundation layout in ground type D with vertical and inclined piles. Continuous and dashed black lines represent kinematic interaction factors assuming hysteretic and Biot’s damping models, respectively; the gray line represents normalized mean Fourier amplitude spectrum of the ground motion, scaled for superstructure 3 ($T_n = 1.0$ s).

matic interaction functions, but on differences on the response at the superstructure. As an illustration example in this case, the effect of the differences highlighted above between impedances and kinematic interaction functions for the particular case of the 2×2 pile group, will be examined below.

Firstly, the small differences appreciated in the kinematic interaction factors between damping models translate to even smaller differences when observing the translational kinematic input motion \ddot{u}_g shown in Figure 5.6 together with the free field ground motion \ddot{u}_{g0} and the rotational kinematic input motion $\ddot{\varphi}_g$ for the same specific case subjected to 429–111 earthquake (see Table 5.3) and scaled for superstructure 3 ($T_n = 1.0$ s). For instance, the magnitude of the differences arising at one of the most significant peaks of the signal (at $t = 9.915$ s) can be quantified in 1.6% and 8.3% for the translational and the rotational kinematic interaction functions, respectively. It is worth noting that, as illustrated in Figure 5.5, the predominant frequencies of the ground motion are located in the range where the filtering produced by the foundation is still not significant.

Regarding the LPM fitting necessary for time domain analyses, the initial fitting frequency range is 0–20 Hz. However, due to its nature, a bad fitting of damping coefficients in the lower frequency range is obtained, even if a high LPM order is used, when trying to fit functions obtained with the hysteretic soil damping model. In this case, the reference damping functions tend to infinity when approaching a zero frequency; a behaviour that cannot be reproduced by the LPM models (see Paronesso and Wolf [144]). Consis-

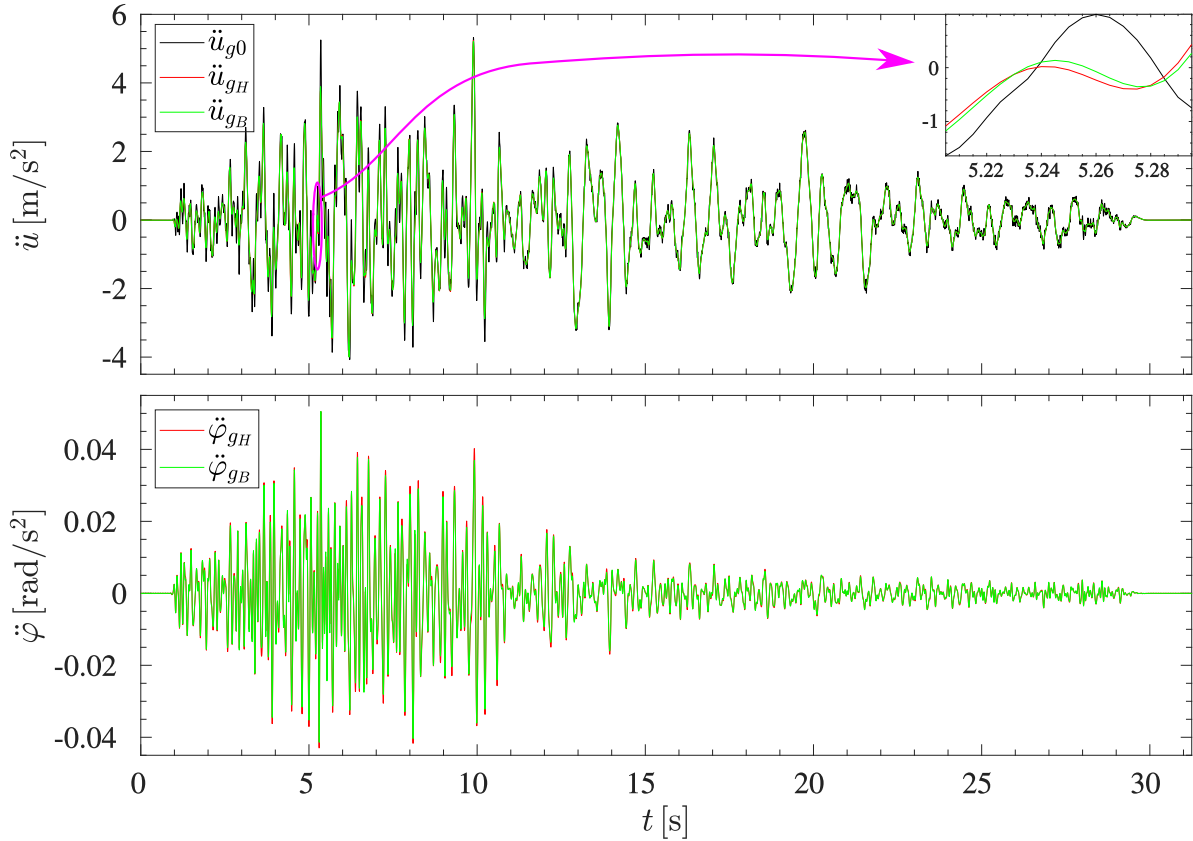


Figure 5.6: Time history of 429–111 earthquake acceleration (Table 5.3), scaled for superstructure 3 ($T_n = 1.0$ s); and FIM derived from soil-foundation kinematic interaction analysis. Vertical 2×2 , $s = 7$ m foundation layout in ground type D.

tent LPM functions are symmetric with respect to frequency, which implies a null slope at the static frequency, fact that strongly influences the result of the fitting procedure. Simplified LPM functions, on the other hand, can not catch fluctuations of the reference impedance functions, so that the models' ability to reproduce the soil-foundation impedances in a selected frequency range strongly depends on their variability with frequency. For the present study, the variability associated to pile-to-pile resonant peaks tends to appear at frequencies above the superstructure fundamental frequencies considered herein. It is also worth mentioning that the influence of the static stiffness in the problem at hand makes it mandatory to give somehow more importance to the lower frequency range. For this reasons, in order to balance the bad fitting at lower frequency range, the following frequency-dependent weight functions depending on the LPM model are employed:

$$\Psi_{\text{consistent}}(\omega) = \left(1 + \left(c_1 \frac{c_s}{d} \omega\right)^{c_2}\right)^{-c_3} \quad (5.3a)$$

$$\Psi_{\text{simplified}}(\omega) = H(f_c) \quad (5.3b)$$

with $c_1 = 4.0$, $c_2 = 2.0$ and $c_3 = 2.0$ in the first function [142,143], f_c a cut-off frequency set at 6 Hz, and $H()$ being the unit step function. With these expressions, represented in Figure 5.4 for reference, substantially more importance is given to the frequency range where the superstructure fundamental frequencies reside, and significantly more accurate

	χ	ε (hysteretic)			ε (Biot)		
		Cons. $N = 2$	Cons. $N = 4$	Simpl.	Cons. $N = 2$	Cons. $N = 4$	Simpl.
φ_S	0.136	0.079	0.087	0.018	0.056	0.040	0.095
u_F	0.168	0.099	0.102	0.055	0.063	0.049	0.156
φ_F	0.169	0.102	0.112	0.037	0.071	0.050	0.111

Table 5.5: Differences between damping models and errors committed by using the different LPM approaches in the results shown in Figure 5.7.

structural responses are obtained. The resulting fittings of the impedance functions, either through the simplified LPM or the consistent LPM with $N = 2$, related to all the soil-foundations systems used in this Chapter 5 are presented in Appendix A.

On the other hand, Figure 5.7 presents results corresponding to the response of the particular case of the $T_n = 1.0$ s superstructure, founded on the vertical 2×2 pile group on soil deposit D, whose impedance and kinematic interaction functions were presented above, and subject to earthquake 429–111 (see Table 5.3), so that the corresponding FIM is the one shown in Figure 5.6. The response of the system in terms of the three degrees of freedom defined above (translation u_F and rotation φ_F of the foundation, and relative rotation of the pier with respect to the foundation φ_S) is computed by solving Equation (4.5) directly in the frequency domain and considering both hysteretic and Biot’s models (see black lines). FB response is also presented for reference. The difference between FB and CB responses illustrates the relevance of the SSI effects. Differences between the two soil damping models (differences between continuous and dashed black lines) are much less important than those due to SSI effects (differences between continuous or dashed black lines and the dotted black line), being the influence of the soil damping model on the response of the superstructure smaller than that on the response at the foundation level, i.e. the differences between the continuous and dashed black lines are higher in u_F and φ_F than in φ_S . The quantification, in this particular case, of the differences between results obtained from both damping models (χ) is presented in Table 5.5 for illustration purposes together with the error committed when using the LPM approaches (ε).

5.6 Parametric analysis

The combination of the superstructures, foundation layouts, soil deposits, soil damping models and seismic actions described above defines the set of configurations whose seismic response is analysed in the present study. In short, four different bridge superstructures characterized by different fundamental periods ($T_n = 0.2$ s, $T_n = 0.5$ s, $T_n = 1.0$ s and $T_n = 1.5$ s) can be founded on twelve groups of piles layouts on the foundation (2×2 and 3×3 vertical pile groups, and 2×2 inclined pile groups with $\theta = 5^\circ$ and $\theta = 10^\circ$, with spacings of 3, 5 and 7 m) embedded on two different deposits (D and C), subjected to seven different seismic signals for each ground type. At the same time, two different soil damping models are considered (hysteretic and Biot’s), and the problems are solved by means of three different methodologies; the frequency-domain method of response, and two time-stepping approaches computed through the Newmark’s linear acceleration method [131], in which the foundation behaviour is modelled through the different LPMs described above (simplified and consistent). Overall, also including FB cases, a total of

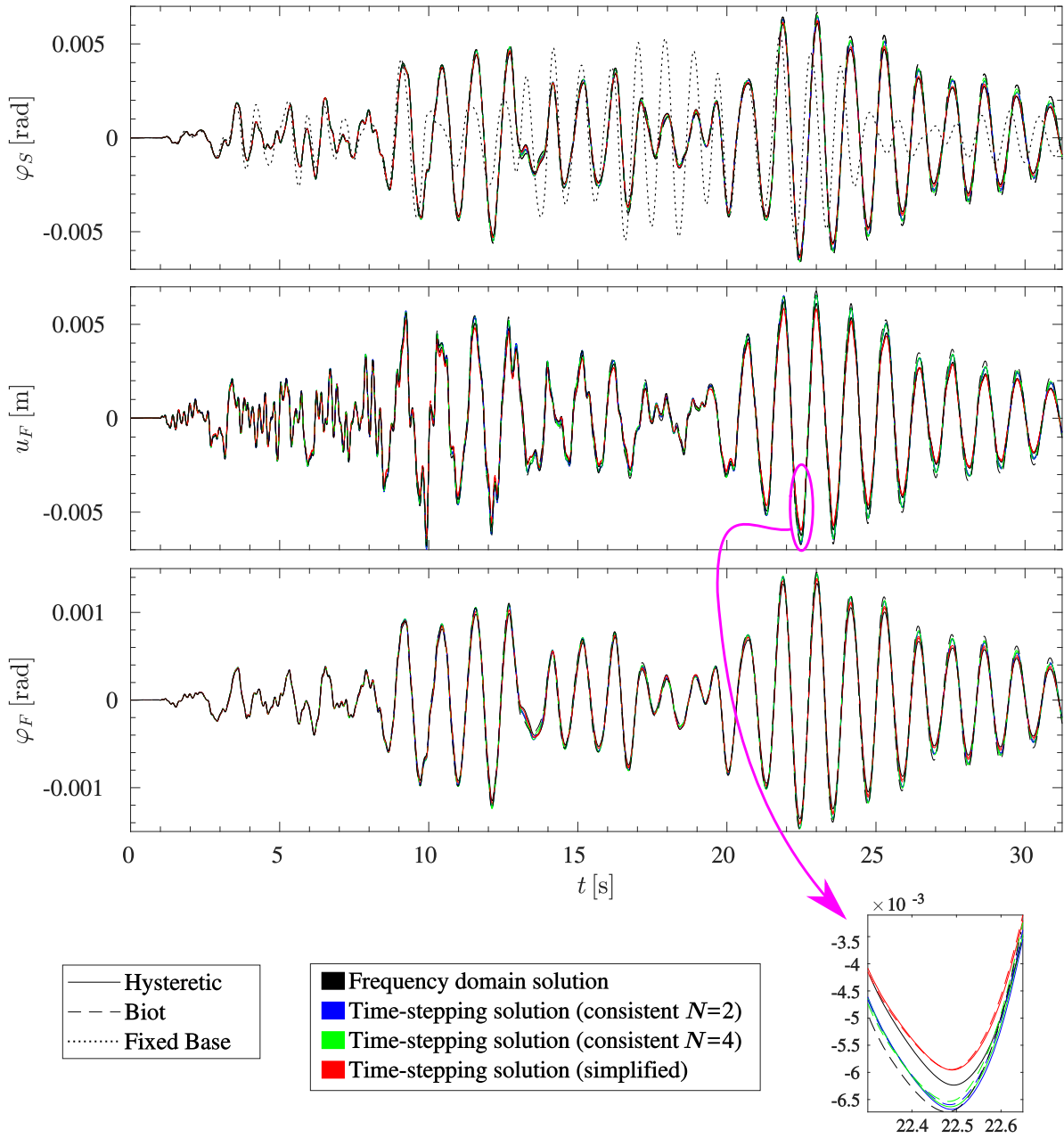


Figure 5.7: Time history of superstructure and pile cap degrees of freedom. Particular case of vertical 2×2 , $s = 7$ m foundation layout in ground type D (impedance functions and kinematic interaction factors shown in Figures 5.4 and 5.5 respectively) using superstructure 3 ($T_n = 1.0$ s) and earthquake 429–111 (Table 5.3).

	Histeretic	Biot
k_{hh}^{∞} [kN/m]	$6.0376 \cdot 10^5$	$6.4897 \cdot 10^5$
c_{hh}^{∞} [kNs/m]	$2.5885 \cdot 10^4$	$1.1521 \cdot 10^4$
k_{hh11} [kN/m]	$-1.3088 \cdot 10^7$	$-1.5287 \cdot 10^5$
c_{hh11} [kNs/m]	$-3.5064 \cdot 10^4$	$-6.6897 \cdot 10^3$
k_{hh21} [kN/m]	$3.5913 \cdot 10^7$	$1.3731 \cdot 10^6$
k_{hh31} [kN/m]	$2.1167 \cdot 10^7$	$3.8616 \cdot 10^5$
m_{hh1} [t]	$5.3864 \cdot 10^1$	$3.6674 \cdot 10^1$
c_{hh21} [kNs/m]	$3.5064 \cdot 10^4$	$6.6897 \cdot 10^3$
c_{hh31} [kNs/m]	$3.5064 \cdot 10^4$	$6.6897 \cdot 10^3$
k_{hh12} [kN/m]	$4.4108 \cdot 10^5$	$5.7124 \cdot 10^5$
c_{hh12} [kNs/m]	$-2.9833 \cdot 10^3$	$-4.3366 \cdot 10^3$
k_{hh22} [kN/m]	$-3.7489 \cdot 10^5$	$-4.6775 \cdot 10^5$
k_{hh32} [kN/m]	$8.5036 \cdot 10^5$	$1.2250 \cdot 10^6$
m_{hh2} [t]	$1.3445 \cdot 10^2$	$1.8173 \cdot 10^2$
c_{hh22} [kNs/m]	$2.9833 \cdot 10^3$	$4.3366 \cdot 10^3$
c_{hh32} [kNs/m]	$2.9833 \cdot 10^3$	$4.3366 \cdot 10^3$

Table 5.6: Resulting parameter values from the fitting with the consistent LPM with $N = 2$. Horizontal impedance component. Particular case of vertical 2×2 , $s = 7$ m foundation layout in ground type D (impedance functions shown in Figure 5.4).

4088 different cases have been analysed. The results of this large set are synthesized below.

This section presents the results of the parametric analyses studying the influence of the soil damping model and of the LPM, on the seismic response of the system. Given the large number of cases under analysis, the results are synthesized and presented in different ways in order to highlight different effects. For a better understanding of such statistical analysis and of the methodology used to produce the base results, the response of the specific configuration tackled in the previous section is first presented in detail in terms of its time response.

After having computed impedance and kinematic interaction functions, the second step in every analysis is to obtain the LPM that represents the compliance of the foundation under consideration. For the specific 2×2 vertical pile group discussed above, embedded in the soil deposit D and with a pile spacing of $s = 7$ m, Figure 5.4 presents three different sets of fitted impedance functions together with the original stiffness and damping functions, already discussed above, computed with the BEM-FEM approach for both soil damping models. One of the fitted sets is obtained through the simplified LPM proposal, while the two other sets are obtained through the consistent LPM approach with two and four internal degrees of freedom ($N = 2$ and $N = 4$), respectively. The resulting parameter values from the fitting with the LPMs are shown in Tables 5.6 to 5.12 for this particular case.

The LPMs obtained through the consistent approach are able to fit the stiffness functions very accurately along the whole frequency range, with errors increasing with frequency, as can be expected taking into account the weighting function that has been used. The fitting of the damping functions is also quite remarkable except for the very low frequencies when fitting the hysteretic impedances. In this case, the damping functions

		Histeretic	Biot
k_{rr}^∞	[kNm]	$1.4687 \cdot 10^6$	$1.6007 \cdot 10^7$
c_{rr}^∞	[kNsm]	$8.4595 \cdot 10^5$	$6.1664 \cdot 10^5$
k_{rr11}	[kNm]	$-3.9741 \cdot 10^7$	$-3.4534 \cdot 10^6$
c_{rr11}	[kNsm]	$4.3145 \cdot 10^4$	$7.9177 \cdot 10^2$
k_{rr21}	[kNm]	$3.3130 \cdot 10^7$	$3.2977 \cdot 10^6$
k_{rr31}	[kNm]	$-3.9741 \cdot 10^7$	$-3.4534 \cdot 10^6$
m_{rr1}	[tm ²]	$-2.8159 \cdot 10^2$	$-4.0258 \cdot 10^0$
c_{rr21}	[kNsm]	$-4.3145 \cdot 10^4$	$-7.9177 \cdot 10^2$
c_{rr31}	[kNsm]	$-4.3145 \cdot 10^4$	$-7.9177 \cdot 10^2$
k_{rr12}	[kNm]	$2.2829 \cdot 10^7$	$-1.0129 \cdot 10^7$
c_{rr12}	[kNsm]	$-2.7550 \cdot 10^4$	$1.4873 \cdot 10^6$
k_{rr22}	[kNm]	$-2.1071 \cdot 10^7$	$-4.5973 \cdot 10^7$
k_{rr32}	[kNm]	$2.4682 \cdot 10^7$	$-1.5552 \cdot 10^8$
m_{rr2}	[tm ²]	$4.3167 \cdot 10^2$	$-3.9427 \cdot 10^4$
c_{rr22}	[kNsm]	$2.7550 \cdot 10^4$	$-1.4873 \cdot 10^6$
c_{rr32}	[kNsm]	$2.7550 \cdot 10^4$	$-1.4873 \cdot 10^6$

Table 5.7: Resulting parameter values from the fitting with the consistent LPM with $N = 2$. Rocking impedance component. Particular case of vertical 2×2 , $s = 7$ m foundation layout in ground type D (impedance functions shown in Figure 5.4).

		Histeretic	Biot
k_{hr}^∞	[kN]	$-1.0003 \cdot 10^6$	$-9.7033 \cdot 10^5$
c_{hr}^∞	[kNs]	$-9.1292 \cdot 10^3$	$-7.3646 \cdot 10^3$
k_{hr11}	[kN]	$5.0570 \cdot 10^6$	$-4.3993 \cdot 10^5$
c_{hr11}	[kNs]	$5.5595 \cdot 10^4$	$5.3784 \cdot 10^2$
k_{hr21}	[kN]	$-1.1232 \cdot 10^7$	$3.4987 \cdot 10^5$
k_{hr31}	[kN]	$4.0406 \cdot 10^6$	$-4.6733 \cdot 10^5$
m_{hr1}	[tm]	$-5.0054 \cdot 10^2$	$-3.2120 \cdot 10^0$
c_{hr21}	[kNs]	$-5.5595 \cdot 10^4$	$-5.3784 \cdot 10^2$
c_{hr31}	[kNs]	$-5.5595 \cdot 10^4$	$-5.3784 \cdot 10^2$
k_{hr12}	[kN]	$-7.8921 \cdot 10^6$	$-9.8656 \cdot 10^5$
c_{hr12}	[kNs]	$1.7903 \cdot 10^5$	$1.8462 \cdot 10^4$
k_{hr22}	[kN]	$-6.3652 \cdot 10^6$	$-5.0011 \cdot 10^4$
k_{hr32}	[kN]	$-7.8927 \cdot 10^6$	$-9.8656 \cdot 10^5$
m_{hr2}	[tm]	$-2.2482 \cdot 10^3$	$-3.2882 \cdot 10^2$
c_{hr22}	[kNs]	$-1.7903 \cdot 10^5$	$-1.8462 \cdot 10^4$
c_{hr32}	[kNs]	$-1.7903 \cdot 10^5$	$-1.8462 \cdot 10^4$

Table 5.8: Resulting parameter values from the fitting with the consistent LPM with $N = 2$. Cross-coupled horizontal-rocking impedance component. Particular case of vertical 2×2 , $s = 7$ m foundation layout in ground type D (impedance functions shown in Figure 5.4).

		Histeretic	Biot
k_{hh}^∞	[kN/m]	$6.3282 \cdot 10^5$	$2.0564 \cdot 10^6$
c_{hh}^∞	[kNs/m]	$1.1757 \cdot 10^4$	$9.4935 \cdot 10^3$
k_{hh11}	[kN/m]	$5.0907 \cdot 10^6$	$-9.2414 \cdot 10^5$
c_{hh11}	[kNs/m]	$-1.8984 \cdot 10^4$	$-1.9428 \cdot 10^3$
k_{hh21}	[kN/m]	$-5.0678 \cdot 10^6$	$1.2836 \cdot 10^6$
k_{hh31}	[kN/m]	$9.2743 \cdot 10^8$	$1.7265 \cdot 10^5$
m_{hh1}	[t]	$1.5776 \cdot 10^4$	$1.0050 \cdot 10^1$
c_{hh21}	[kNs/m]	$1.8984 \cdot 10^4$	$1.9428 \cdot 10^3$
c_{hh31}	[kNs/m]	$1.8984 \cdot 10^4$	$1.9428 \cdot 10^3$
k_{hh12}	[kN/m]	$1.8358 \cdot 10^5$	$-1.3106 \cdot 10^6$
c_{hh12}	[kNs/m]	$-2.4158 \cdot 10^2$	$-1.5163 \cdot 10^5$
k_{hh22}	[kN/m]	$-1.5322 \cdot 10^5$	$1.0179 \cdot 10^7$
k_{hh32}	[kN/m]	$1.8358 \cdot 10^5$	$1.2070 \cdot 10^7$
m_{hh2}	[t]	$1.9226 \cdot 10^0$	$2.5926 \cdot 10^3$
c_{hh22}	[kNs/m]	$2.4158 \cdot 10^2$	$1.5163 \cdot 10^5$
c_{hh32}	[kNs/m]	$2.4158 \cdot 10^2$	$1.5163 \cdot 10^5$
k_{hh13}	[kN/m]	$-4.4100 \cdot 10^5$	$-1.0784 \cdot 10^6$
c_{hh13}	[kNs/m]	$-5.9645 \cdot 10^4$	$-1.7783 \cdot 10^3$
k_{hh23}	[kN/m]	$4.4530 \cdot 10^6$	$1.1693 \cdot 10^6$
k_{hh33}	[kN/m]	$2.1860 \cdot 10^6$	$-9.6508 \cdot 10^5$
m_{hh3}	[t]	$8.8673 \cdot 10^2$	$3.0477 \cdot 10^1$
c_{hh23}	[kNs/m]	$5.9645 \cdot 10^4$	$1.7783 \cdot 10^3$
c_{hh33}	[kNs/m]	$5.9645 \cdot 10^4$	$1.7783 \cdot 10^3$
k_{hh14}	[kN/m]	$9.7057 \cdot 10^5$	$1.2716 \cdot 10^6$
c_{hh14}	[kNs/m]	$-7.2473 \cdot 10^3$	$-2.7744 \cdot 10^4$
k_{hh24}	[kN/m]	$-7.4169 \cdot 10^5$	$7.0808 \cdot 10^5$
k_{hh34}	[kN/m]	$1.7759 \cdot 10^6$	$1.2718 \cdot 10^6$
m_{hh4}	[t]	$2.2947 \cdot 10^2$	$3.8881 \cdot 10^2$
c_{hh24}	[kNs/m]	$7.2473 \cdot 10^3$	$2.7744 \cdot 10^4$
c_{hh34}	[kNs/m]	$7.2473 \cdot 10^3$	$2.7744 \cdot 10^4$

Table 5.9: Resulting parameter values from the fitting with the consistent LPM with $N = 4$. Horizontal impedance component. Particular case of vertical 2×2 , $s = 7$ m foundation layout in ground type D (impedance functions shown in Figure 5.4).

tend to infinity as frequency approaches zero, a behaviour that the LPMs are unable to reproduce because consistent LPM functions are symmetric, and therefore their slope at frequency zero must be horizontal. It is also worth to highlight that the use of more than two internal degrees of freedom does not always improve this fitting and, in general, does not improve the overall result, reason why configurations with $N = 2$ will be used in the following.

The fitted functions obtained using the simplified LPM approach are quite different and, a priori, do not fit the original functions very well, although it will be shown later that, in general, they are able to produce very good results. Simplified LPM stiffness functions are parabolic, so can not accommodate complex phenomena as the group effect present in this illustrated configuration. However, the fitting at the low frequency range,

		Histeretic	Biot
k_{rr}^∞	[kNm]	$3.9498 \cdot 10^7$	$4.0207 \cdot 10^7$
c_{rr}^∞	[kNsm]	$6.8390 \cdot 10^5$	$5.6024 \cdot 10^5$
k_{rr11}	[kNm]	$-2.6908 \cdot 10^9$	$1.1490 \cdot 10^7$
c_{rr11}	[kNsm]	$-5.5213 \cdot 10^6$	$6.5419 \cdot 10^5$
k_{rr21}	[kNm]	$2.7519 \cdot 10^9$	$-6.6612 \cdot 10^7$
k_{rr31}	[kNm]	$2.6388 \cdot 10^{11}$	$-2.8429 \cdot 10^8$
m_{rr1}	[tm ²]	$4.9888 \cdot 10^5$	$-7.7640 \cdot 10^3$
c_{rr21}	[kNsm]	$5.5213 \cdot 10^6$	$-6.5419 \cdot 10^5$
c_{rr31}	[kNsm]	$5.5213 \cdot 10^6$	$-6.5419 \cdot 10^5$
k_{rr12}	[kNm]	$2.7526 \cdot 10^6$	$2.1769 \cdot 10^7$
c_{rr12}	[kNsm]	$-8.1327 \cdot 10^6$	$7.6624 \cdot 10^3$
k_{rr22}	[kNm]	$1.2740 \cdot 10^9$	$-2.3097 \cdot 10^7$
k_{rr32}	[kNm]	$1.8424 \cdot 10^8$	$2.1769 \cdot 10^7$
m_{rr2}	[tm ²]	$5.1804 \cdot 10^4$	$-4.4194 \cdot 10^1$
c_{rr22}	[kNsm]	$8.1327 \cdot 10^6$	$-7.6624 \cdot 10^3$
c_{rr32}	[kNsm]	$8.1327 \cdot 10^6$	$-7.6624 \cdot 10^3$
k_{rr13}	[kNm]	$-1.3506 \cdot 10^8$	$5.6676 \cdot 10^6$
c_{rr13}	[kNsm]	$-9.5502 \cdot 10^5$	$-1.1572 \cdot 10^6$
k_{rr23}	[kNm]	$2.2145 \cdot 10^8$	$4.2724 \cdot 10^7$
k_{rr33}	[kNm]	$-5.7865 \cdot 10^7$	$2.6769 \cdot 10^8$
m_{rr3}	[tm ²]	$1.0556 \cdot 10^4$	$2.7672 \cdot 10^4$
c_{rr23}	[kNsm]	$9.5502 \cdot 10^5$	$1.1572 \cdot 10^6$
c_{rr33}	[kNsm]	$9.5502 \cdot 10^5$	$1.1572 \cdot 10^6$
k_{rr14}	[kNm]	$8.7862 \cdot 10^7$	$-1.1337 \cdot 10^8$
c_{rr14}	[kNsm]	$-8.2939 \cdot 10^5$	$-3.4416 \cdot 10^5$
k_{rr24}	[kNm]	$-5.2937 \cdot 10^7$	$1.4113 \cdot 10^8$
k_{rr34}	[kNm]	$2.0935 \cdot 10^8$	$-9.4571 \cdot 10^7$
m_{rr4}	[tm ²]	$1.9696 \cdot 10^4$	$4.2671 \cdot 10^3$
c_{rr24}	[kNsm]	$8.2939 \cdot 10^5$	$3.4416 \cdot 10^5$
c_{rr34}	[kNsm]	$8.2939 \cdot 10^5$	$3.4416 \cdot 10^5$

Table 5.10: Resulting parameter values from the fitting with the consistent LPM with $N = 4$. Rocking impedance component. Particular case of vertical 2×2 , $s = 7$ m foundation layout in ground type D (impedance functions shown in Figure 5.4).

prevalent when computing the response of the system, can be considered adequate, especially for the rocking component. The resulting damping function is frequency-independent, and represents the average damping in the frequency range of interest.

The fitted LPM functions for each configuration are used to compute the response of the system using a time-domain step-by-step scheme. Figure 5.7 presents a comparison between the time-history response of the system computed directly in the frequency domain or in time domain with both LPM approaches, for the case discussed above and for both soil damping models. From an engineering point of view, both LPMs are indeed able to simulate well the soil-foundation compliance since quite small differences arise between any one of them and the reference frequency domain results. In fact, the errors induced by approximating the impedance functions through the LPM approaches are

	Histeretic	Biot
k_{hr}^{∞} [kN]	$-1.0230 \cdot 10^6$	$-1.6705 \cdot 10^6$
c_{hr}^{∞} [kNs]	$-1.2237 \cdot 10^4$	$-8.4932 \cdot 10^3$
k_{hr11} [kN]	$-2.7528 \cdot 10^6$	$-7.5732 \cdot 10^4$
c_{hr11} [kNs]	$2.5442 \cdot 10^4$	$1.0839 \cdot 10^3$
k_{hr21} [kN]	$1.2823 \cdot 10^6$	$1.6004 \cdot 10^4$
k_{hr31} [kN]	$-5.2529 \cdot 10^7$	$-1.0086 \cdot 10^6$
m_{hr1} [tm]	$-4.4016 \cdot 10^2$	$-1.9670 \cdot 10^0$
c_{hr21} [kNs]	$-2.5442 \cdot 10^4$	$-1.0839 \cdot 10^3$
c_{hr31} [kNs]	$-2.5442 \cdot 10^4$	$-1.0839 \cdot 10^3$
k_{hr12} [kN]	$-9.4689 \cdot 10^6$	$-5.3106 \cdot 10^5$
c_{hr12} [kNs]	$1.3730 \cdot 10^5$	$3.6800 \cdot 10^4$
k_{hr22} [kN]	$-9.2571 \cdot 10^6$	$-4.1843 \cdot 10^6$
k_{hr32} [kN]	$-1.8569 \cdot 10^7$	$-3.5199 \cdot 10^6$
m_{hr2} [tm]	$-1.0067 \cdot 10^3$	$-2.8720 \cdot 10^2$
c_{hr22} [kNs]	$-1.3730 \cdot 10^5$	$-3.6800 \cdot 10^4$
c_{hr32} [kNs]	$-1.3730 \cdot 10^5$	$-3.6800 \cdot 10^4$
k_{hr13} [kN]	$1.3040 \cdot 10^7$	$4.9831 \cdot 10^7$
c_{hr13} [kNs]	$-1.3045 \cdot 10^5$	$3.0126 \cdot 10^6$
k_{hr23} [kN]	$5.4237 \cdot 10^6$	$-2.7849 \cdot 10^8$
k_{hr33} [kN]	$1.3070 \cdot 10^7$	$4.9590 \cdot 10^7$
m_{hr3} [tm]	$9.2165 \cdot 10^2$	$-3.9691 \cdot 10^4$
c_{hr23} [kNs]	$1.3045 \cdot 10^5$	$-3.0126 \cdot 10^6$
c_{hr33} [kNs]	$1.3045 \cdot 10^5$	$-3.0126 \cdot 10^6$
k_{hr14} [kN]	$-9.8858 \cdot 10^4$	$-5.2719 \cdot 10^7$
c_{hr14} [kNs]	$6.2903 \cdot 10^2$	$6.7139 \cdot 10^6$
k_{hr24} [kN]	$7.4956 \cdot 10^4$	$-4.0509 \cdot 10^8$
k_{hr34} [kN]	$-9.8859 \cdot 10^4$	$-6.2738 \cdot 10^7$
m_{hr4} [tm]	$-1.6554 \cdot 10^1$	$-9.8462 \cdot 10^4$
c_{hr24} [kNs]	$-6.2903 \cdot 10^2$	$-6.7139 \cdot 10^6$
c_{hr34} [kNs]	$-6.2903 \cdot 10^2$	$-6.7139 \cdot 10^6$

Table 5.11: Resulting parameter values from the fitting with the consistent LPM with $N = 4$. Cross-coupled horizontal-rocking impedance component. Particular case of vertical 2×2 , $s = 7$ m foundation layout in ground type D (impedance functions shown in Figure 5.4).

smaller than the differences found between the responses of the system assuming one damping model or the other ($\varepsilon < \chi$, shown in Table 5.5).

However, for this particular case, a significant aspect is worth of notice: when a hysteretic damping model is assumed for the soil, the overall error obtained by using the simplified LPM is smaller than the one resulting from the use of the consistent LPM ($\varepsilon_{\text{simplified}}^H < \varepsilon_{\text{consistent}}^H$) for all the degrees of freedom of the superstructure. Taking into account that the structural response is mainly dominated by the fundamental frequency of the CB system, this result should be related to a lower accuracy of the consistent LPM, with respect to the simplified one, in reproducing the soil–foundation impedances around that fundamental frequency. Taking a look at the hysteretic rocking damping function at

	Histeretic	Biot
k_h [N/m]	$1.2312 \cdot 10^8$	$1.6737 \cdot 10^8$
c_h [Ns/m]	$9.1413 \cdot 10^5$	$5.7727 \cdot 10^5$
m_h [kg]	$2.1381 \cdot 10^3$	$2.6333 \cdot 10^4$
k_r [Nm]	$3.7314 \cdot 10^{10}$	$3.7114 \cdot 10^{10}$
c_r [Nsm]	$5.9098 \cdot 10^8$	$5.3738 \cdot 10^8$
I_r [kgm ²]	$8.4807 \cdot 10^2$	$6.4363 \cdot 10^4$
k_t [N/m]	$5.2498 \cdot 10^8$	$4.9652 \cdot 10^8$
h_1 [m]	$-1.9603 \cdot 10^0$	$-2.1368 \cdot 10^0$
c_t [Ns/m]	$1.9365 \cdot 10^7$	$1.8479 \cdot 10^7$
h_2 [m]	$-7.0859 \cdot 10^{-1}$	$-6.9881 \cdot 10^{-1}$
m_t [kg]	$9.2165 \cdot 10^3$	$9.5746 \cdot 10^3$
h_3 [m]	$2.3496 \cdot 10^1$	$1.9879 \cdot 10^1$

Table 5.12: Resulting parameter values from the fitting with the simplified LPM. Particular case of vertical 2×2 , $s = 7$ m foundation layout in ground type D (impedance functions shown in Figure 5.4).

the CB fundamental frequency of this system (0.89 Hz for the $f_n = 1$ Hz superstructure) on Figure 5.4, the values obtained with the simplified approach around this point are closer to the reference function (that tends to infinity at low frequencies) than the ones obtained from the consistent approach. The opposite occurs assuming Biot’s damping model, $\varepsilon_{\text{simplified}}^{\text{B}} > \varepsilon_{\text{consistent}}^{\text{B}}$. In this case, for which the reference function is perfectly bounded, the fitting obtained using the consistent approach is much more satisfactory. It is worth noting that, as observed before, the use of a higher number of internal degrees of freedom in the consistent LPM does not always lead to better results. For instance, for a hysteretic soil damping model, the error is larger for $N = 4$ than for $N = 2$ (see Table 5.5).

The way in which all these observations are affected by the properties of the system under study will be discussed in the following. First of all, the magnitude of the SSI effects will be evaluated (through Figures 5.8 and 5.9), given that all the aspects discussed here are relevant only when this phenomenon is important (stiff soil–foundation systems will be less affected by errors in the fitted functions because of the small relevance of considering a CB system). Then, results will be synthesized to study the influence of ground type, superstructure fundamental frequency, pile foundation configuration, and pile inclination.

Thus, Figure 5.8 presents the contribution of the different degrees of freedom to the horizontal displacement of the bridge deck for the 2016 vertical-pile cases considered in this study. For each possible configuration, the mean maximum bridge deck displacement over the seven earthquakes is presented in one vertical bar. Each of these bars is divided in three sections, each one representing the contribution of a different degree of freedom (foundation rotation, foundation displacement and superstructure rotation). To represent the contribution of both rotations, φ_S and φ_F , to the lateral displacement of the bridge deck, they are respectively multiplied by the length from the S node (base of the pier) to the bridge deck centroid D ($h_S = h_p + h_c + h_d$), and the length from the F node (ground level) to the bridge deck centroid D ($h_F = h_f + h_p + h_c + h_d$), Figures 4.2 and 4.12. At the same time, these bars are grouped in sets of threes, each one in the

set representing the results obtained following the frequency–domain method of response analysis, or a time–stepping procedure in which the soil–foundation system is obtained using a consistent ($N = 2$) or a simplified LPM approach. Finally, a different set of bars is presented for each one of the configurations considered for a different superstructure, foundation and soil damping model. FB response is also included for reference. Note that the vertical scales used for different superstructures (plots in different rows within the figure) change, with increasing ranges for increasing fundamental periods.

From the comparison between FB and CB models, it becomes clear that SSI phenomena is relevant in most configurations. It is also worth noting that deck displacements are always smaller if a hysteretic damping model is considered due to its higher foundation damping at low frequencies.

Bridge deck maximum motions arising in the stiffest (and shortest) configurations are much smaller than those arising in the softer (and taller) cases, but the relative contribution of pile cap degrees of freedom is much more important in the first situation. On the other hand, for any specific superstructure, deck displacements increase by reducing the pile spacing or the number of piles constituting the group, as the stiffness of the soil–foundation system decreases and, as a consequence, the contribution of the foundation displacement and rocking increases. As expected, the contribution of the foundation rocking is very significant for the soft soil D and tight foundations. In fact, for the stiffest superstructures ($T_n = 0.2$ s and $T_n = 0.5$ s) on 2×2 pile groups, it represents more than 50% of the total motion. This can be observed more clearly in Figure 5.9, where the mean maximum magnitudes of foundation rotation and superstructure relative rotations computed in frequency domain are compared in a format similar to that of Figure 5.8. The relative importance of the foundation rotation over the superstructure relative rotation depends not only on the soil–foundation system compliance, but also on the stiffness (and height) of the superstructure. The relative rotation of the superstructure is prevalent for the three softest structures ($T_n = 0.5$ s, $T_n = 1.0$ s and 1.5 s) with the only exception of the $T_n = 0.5$ s superstructure on the softest foundation. On the other hand, foundation rotation is prevalent in the case of the stiffest superstructure on a soft foundation. In this regard, it is interesting to note that, for a given foundation and ground type, the magnitude of the foundation rotations tends not to change significantly for different superstructures (while, as expected, the contribution of the superstructure relative rotation increases significantly with softer superstructures). It is also worth noting that Biot’s soil damping model (which predicts a slightly softer foundation rocking response) tends to anticipate larger foundation rotations and, therefore, larger superstructure deformations.

Figure 5.10 presents the contribution of the different degrees of freedom to the horizontal displacement of the bridge deck for the 2016 inclined-pile cases considered in this study (2×2 configurations with rake angles of 5° and 10°), together with the vertical-pile results for reference. As expected, inclined-pile configurations present significantly smaller deck motions. This effect is more important for stiff structures in soft soils. The reduction of displacements may be attributed to the contribution of the rocking component of the FIM that is responsible for inertia forces in the superstructure that are opposite in sign with respect to those produced by the horizontal component [94,95] (see Figure 5.5). This observation is enforced by the fact that the fundamental frequencies of the CB systems do not change significantly with the pile rake angles. More precisely, when piles are inclined from $\theta = 0^\circ$ to $\theta = 10^\circ$, the increase of the fundamental frequency of the system is always below 10%, depending on the soil-structure relative stiffness, as

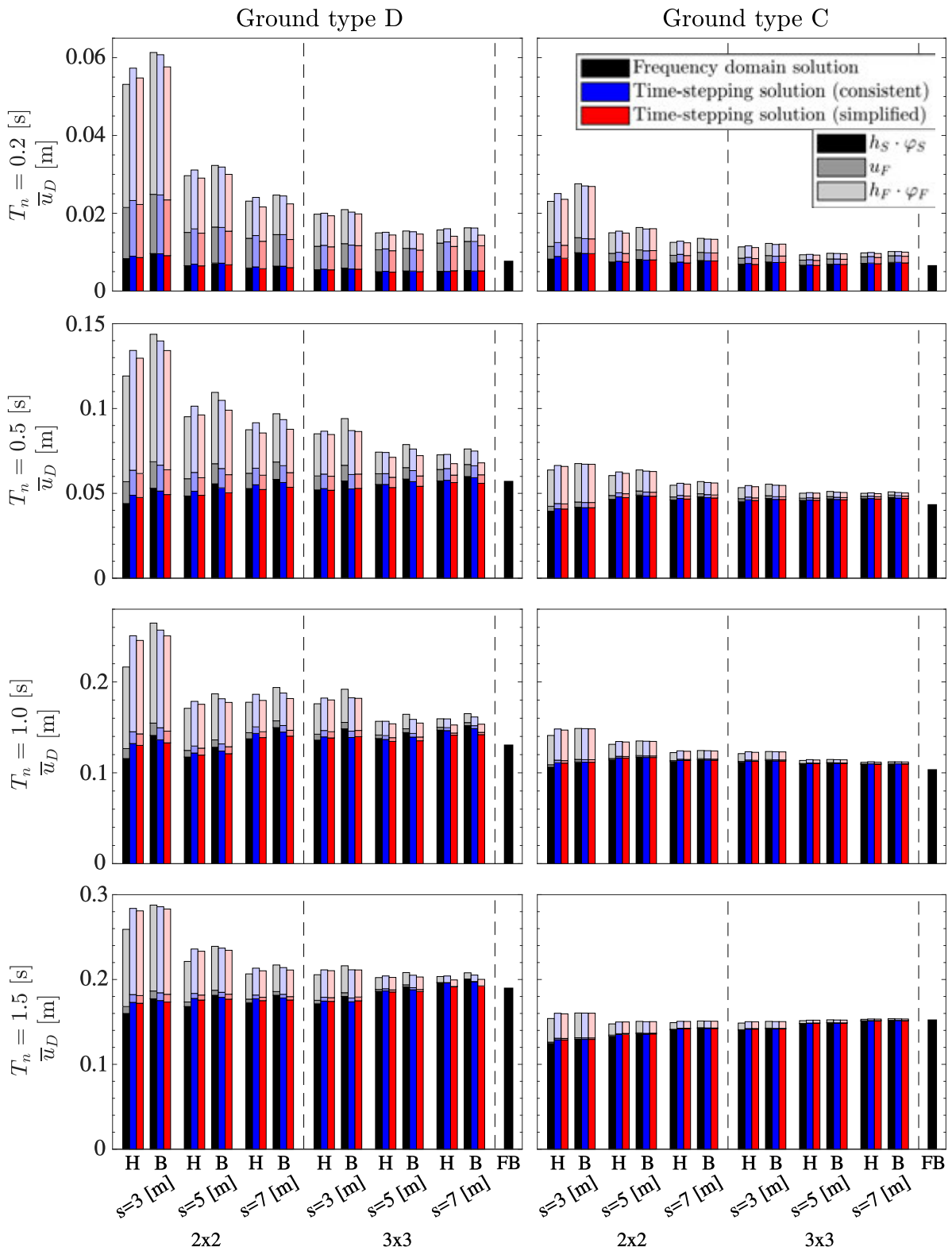


Figure 5.8: Contribution of the different degrees of freedom to the mean maximum lateral displacement of the bridge deck u_D (H: hysteretic damping model and B: Biot's damping model).

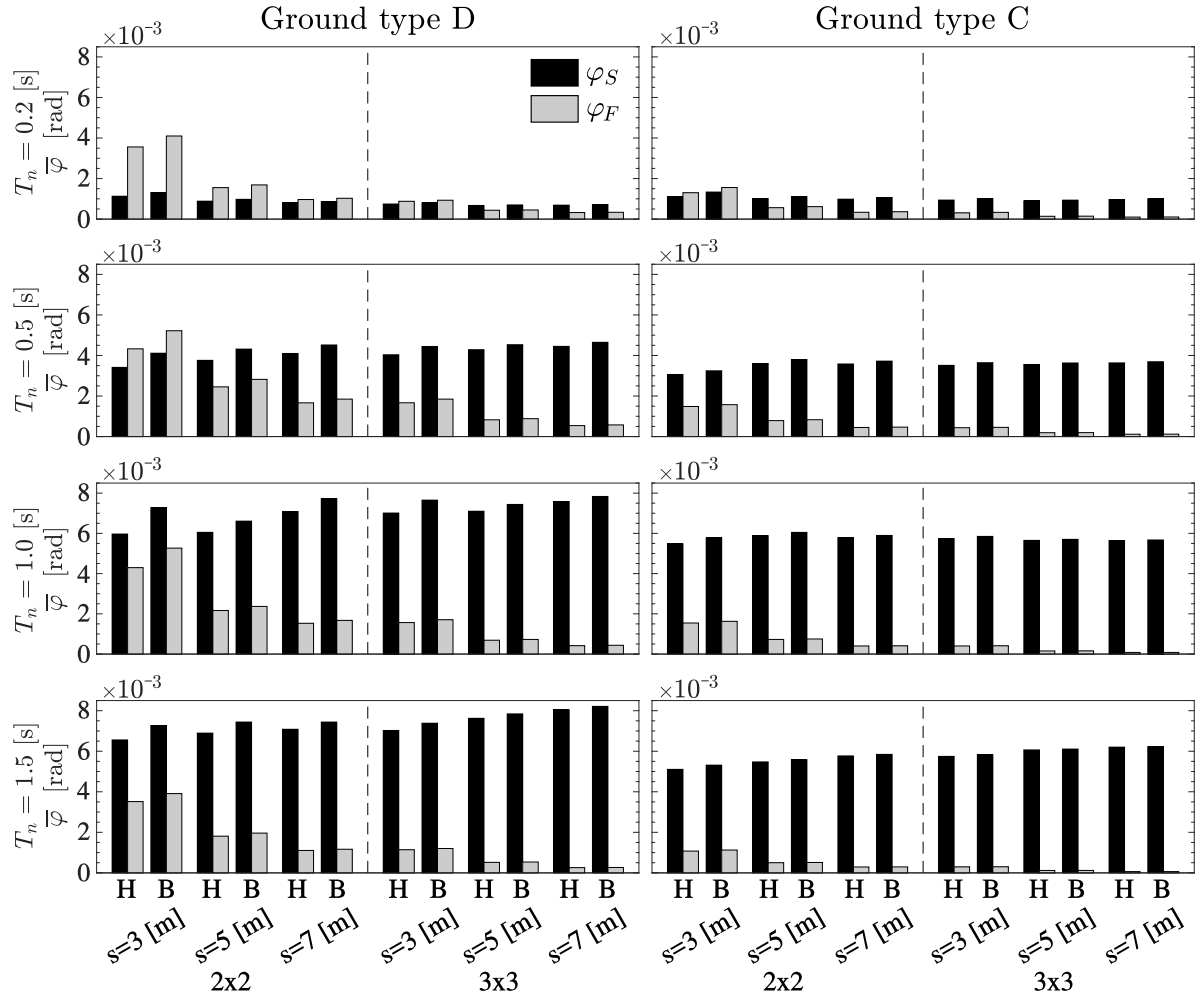


Figure 5.9: Comparison between the mean maximum magnitudes of foundation rotation and superstructure relative rotation using frequency domain approach (H: hysteretic damping model and B: Biot's damping model).

reported by Medina et al [145].

Figures 5.8 and 5.10 show how the three solution approaches adopted (frequency-domain solution with the original impedance functions, and the two time-stepping approaches using two different LPM approaches to model the foundation response) provide slightly different solutions. If hysteretic damping is assumed, the time-stepping approaches tend to predict bridge maximum motions that are slightly larger than those obtained from the frequency-domain solution, being this the situation in 77.5% of the cases analysed. On the contrary, when Biot's damping is assumed, the bridge deck maximum lateral displacements predicted by the time-stepping approaches are smaller than those of the frequency-domain solution in almost all cases (93.2% of the cases). This is so because the responses computed directly in the frequency-domain are much more sensitive to changing from Hysteretic to Biot's damping than time-domain approaches (see Figure 5.8), as part of the information is lost during the fitting process of the LPM. However, in order to evaluate which of the four considered approaches could be considered as more conservative in terms of structural integrity, the variable of interest should be the peak superstructure relative rotation φ_S . When the result obtained for this magnitude

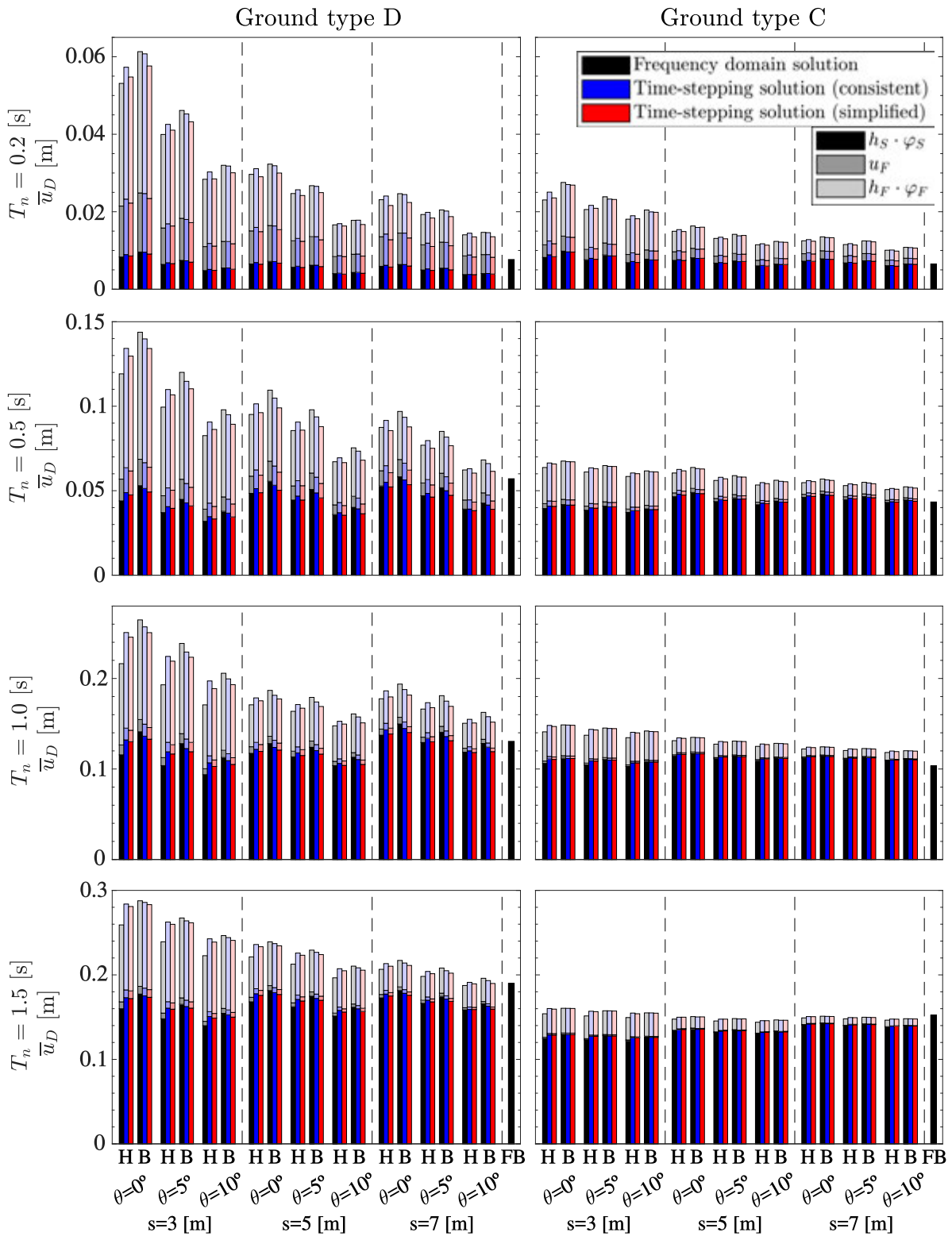


Figure 5.10: Contribution of the different degrees of freedom to the mean maximum lateral displacement of the bridge deck u_D considering inclined piles of 2×2 cases (H: hysteretic damping model and B: Biot's damping model).

is compared among the four possible approaches, the assumption of Biot's damping together with the adoption of the consistent LPM provides the highest relative rotations in 72.9% of the cases which indicates that such approach could be adopted as the most conservative option.

In order to assess the reliability of the two LPM approaches when used in this kind of problems, it is mandatory though to quantify these differences, and to study how they are affected by different aspects of the problem. For this reason, the next sections will quantify the errors committed, with respect to the reference frequency-domain approach, as a function of ground type, superstructure configuration, foundation layout and pile inclination. Errors between each time-stepping procedure and the reference frequency-domain solution (ε) and differences between soil damping models (χ) will be presented in standard box-and-whisker diagrams (Figures 5.11 to 5.17), with results grouped in the relevant way for each aspect. In all cases, differences between damping models are presented in grey tones on the left side of the plots, while errors committed when using one of the lumped parameter equivalent models is presented in blue (consistent, $N = 2$) and red (simplified) colors. Results obtained from hysteretic and Biot's damping assumptions are presented separately in two adjacent subplots. All cases are plotted as a set of three box-and-whisker representation, each of them representing the error or difference measured on one of the three degrees-of-freedom of the system, in different levels of darkness (as shown in the legends).

5.6.1 Influence of ground type on the accuracy of the responses computed using LPMs

Figure 5.11 presents errors and differences for all vertical piles configurations grouped according to the ground type D (left) or C (right), respectively. Errors arising in systems founded on type C grounds (medium stiffness soils) tend to be significantly smaller than those observed on type D grounds (soft soils). This is due to two main causes: a) as expected, the magnitude of the SSI effects is much larger for the latter, i.e., the contribution of the foundation response, where the approximations related to the LPMs lie, is more relevant; and b) changing from type C to D grounds, resonances peaks that characterise the impedances trends moves towards lower frequencies and impedances present more regular trends that can be better approximated by LPMs. From an engineering point of view, errors committed are very low, specially in type C grounds, and are largely compensated by practical advantages deriving from the use of the LPM approaches (i.e. possibility of using time-domain solution approaches, and of using dedicated computer software for structural analysis that usually perform time domain analysis).

Regarding the influence of soil damping model, the overall errors obtained by considering the consistent and simplified LPMs are very similar when the hysteretic model is assumed, though for medium stiffness soil the error deriving from the use of the simplified LPM is slightly lower than that of the consistent LPM. For Biot's damping model, on the other hand, the overall error obtained with the consistent LPM is always lower than that resulting from the simplified option. From an engineering point of view, the median errors resulting from the LPM approach are limited (always below $\varepsilon = 0.1$, except for the simplified option in the case of Biot's damping model in soft soils). However, errors are significantly scattered around the median values, except for the case of systems on type C grounds considering Biot's damping model.

It is worth noting that differences in the seismic response of the system deriving from

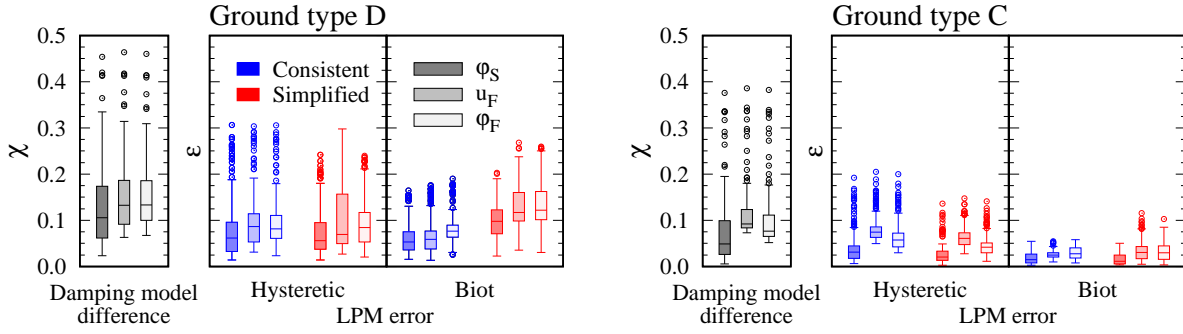


Figure 5.11: Differences due to the use of hysteretic or Biot's soil damping model, and errors due to the use of LPM approaches. Influence of ground type.

the use of one damping model or the other are of the same order of magnitude (though always slightly higher) than the errors produced by the approximation of the impedance functions, which suggests that the errors committed when using any of these LPMs to represent the foundation are less relevant than the effect of the simplifying assumptions of the original model.

5.6.2 Influence of superstructure fundamental periods on the accuracy of the responses computed using LPMs

Figures 5.12 and 5.13 synthesizes errors and differences for all vertical piles configurations grouped according to the superstructure involved in each case, with the first figure referring to structures on soft soils, and the second to medium soils. In general, overall errors obtained by considering the consistent and simplified LPMs are very similar to each other if soil hysteretic damping is assumed, although maximum errors committed with the first option tend to be largest in stiff structures on medium soils, while those committed with the second option are the ones that tend to be larger for stiff structures on soft soils. With the exception of these specific cases, no advantage is clearly evident from the use of one LPM or the other. On the other hand, when assuming Biot's damping model, the overall errors committed due to the use of the consistent LPM tend to be lower than that resulting from the simplified model.

The magnitude of the errors is almost independent of the fundamental period of the superstructure (the median value is always around $0.08 < \varepsilon < 0.12$). This observation can be explained by the fact that soil-foundation impedances are well reproduced by both LPMs in the frequency range covering the fundamental superstructure frequencies. The soil-foundation impedances do not present articulated trends with frequency, namely no resonance peaks occur in the frequency range where fundamental frequencies lie (except for the 3×3 , $s = 7$ m specific case) that cannot be captured by the simplified LPM. When soil hysteretic damping is assumed, the LPM errors observed for superstructures with the smallest fundamental period ($T_n = 0.2$ s) are much smaller than those obtained for the rest of superstructures because their fundamental frequencies go beyond the frequency range for which damping coefficients are unbounded.

Regarding soil type C, as already observed, errors are much lower than those arising for soil type D. Furthermore, errors are also less scattered around the median value. This is reasonably due to the even simpler trends of the soil-foundation impedances in the frequency range in which the superstructure fundamental frequencies fall, and the lower

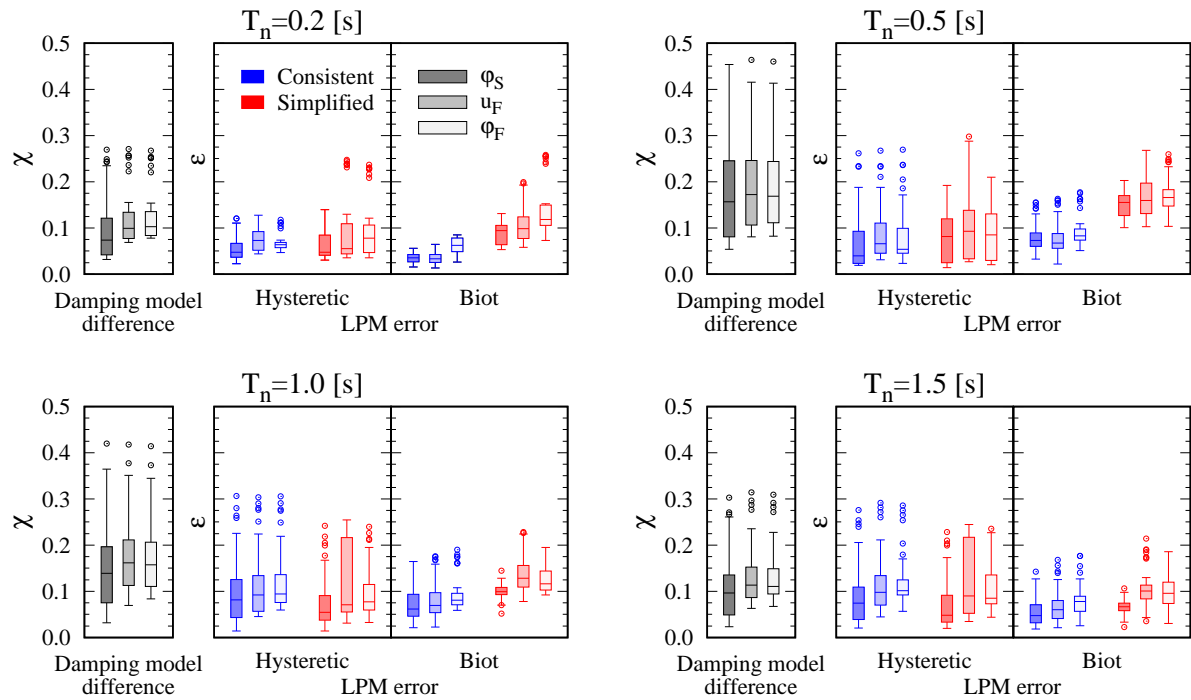


Figure 5.12: Differences due to the use of hysteretic or Biot's soil damping model, and errors due to the use of LPM approaches. Influence of superstructure fundamental periods (ground type D).

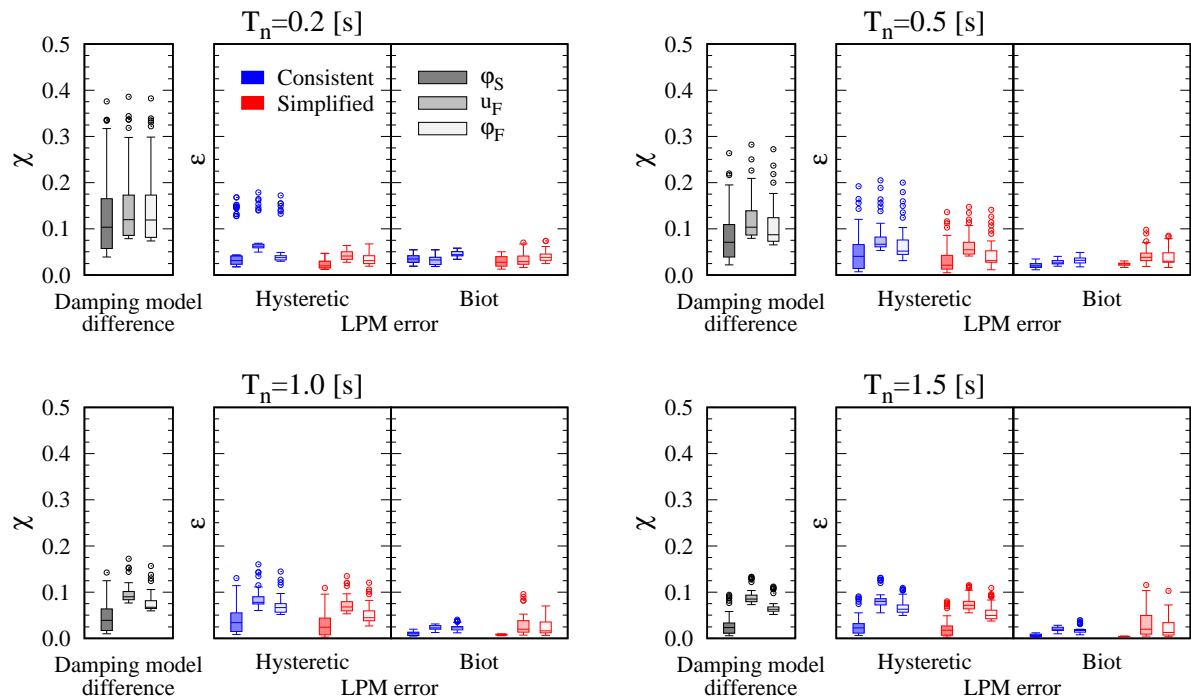


Figure 5.13: Differences due to the use of hysteretic or Biot's soil damping model, and errors due to the use of LPM approaches. Influence of superstructure fundamental periods (ground type C).

magnitude of SSI.

5.6.3 Influence of pile foundation layouts on the accuracy of the responses computed using LPMs

Figure 5.14 presents LPM errors for all vertical piles configurations in type D grounds, grouped by foundation layout. As well known, by increasing the pile spacing, peaks of the soil–foundation impedances due to group effects move towards lower frequencies. Thus, for increasing pile spacing, the simplified LPM is no longer able to capture the actual frequency behaviour of the soil–foundation impedances in the selected frequency range. This observation is consistent with the significant increase of the overall errors observed for the 3×3 cases when increasing the pile spacing (of around 100% from $s = 3$ m to $s = 7$ m), independently from the adopted soil damping model. It is also consistent with the fact that, for $s = 7$ m, the errors committed when using the simplified LPM are significantly larger than those committed when using the consistent approach, for both 2×2 and 3×3 configurations. For the 2×2 pile foundations, an increase of errors with pile spacing is not observed because pile group resonances do not arise in impedance functions in the frequency range 0–6 Hz.

The largest errors arise for the softest soil–foundation configuration (2×2 and $s = 3$ m) when a hysteretic soil damping model is assumed, with errors much larger than those for Biot’s option or for other configurations. This is caused by the CB fundamental frequency falling below 0.9 Hz, i.e. in a range where none of the LPM approaches is able to capture the unbounded tendency of the damping function, and where, for the analysed cases, the SSI effects are more relevant. Therefore, differences between reference and approximated impedance functions have more influence on the final results.

Regarding the influence of soil damping model on the accuracies, when the hysteretic damping model is assumed, the results obtained when using the simplified LPM tends to be better than those obtained from the consistent option (except for $s = 7$ m). On the contrary, when Biot’s soil damping model is assumed, the results obtained when using the consistent LPM tends to be better (except for the 3×3 and $s = 3$ m configuration).

On the other hand, Figure 5.15 presents LPM errors for all vertical piles configurations in type C grounds, grouped by foundation layout. As stated in Section 5.6.1, lower error values are obtained if compared with soil type D results (Figure 5.14 vs. Figure 5.15). Previous observations concerning the increase of errors as the pile spacing increases do not hold, since impedance functions of pile foundations systems embedded in soil type C lack of resonant peaks due to pile-to-pile interaction in the frequency range of interest.

5.6.4 Influence of pile inclination on the accuracy of the responses computed using LPMs

Figures 5.16 and 5.17 synthesize LPM errors for all configurations with inclined piles in type D and C grounds, respectively. From the comparison between Figures 5.14 vs. 5.16 and Figures 5.15 vs. 5.17, it can be inferred that the influence of pile inclination on the errors committed is negligible. The general shape of impedance functions does not change significantly with pile inclination (see for instance [136]) as resonant peaks reside on the same frequency ranges, so that the ability of both lumped parameter methods to approximate impedance functions is not altered. Only a subtle reduction in the overall

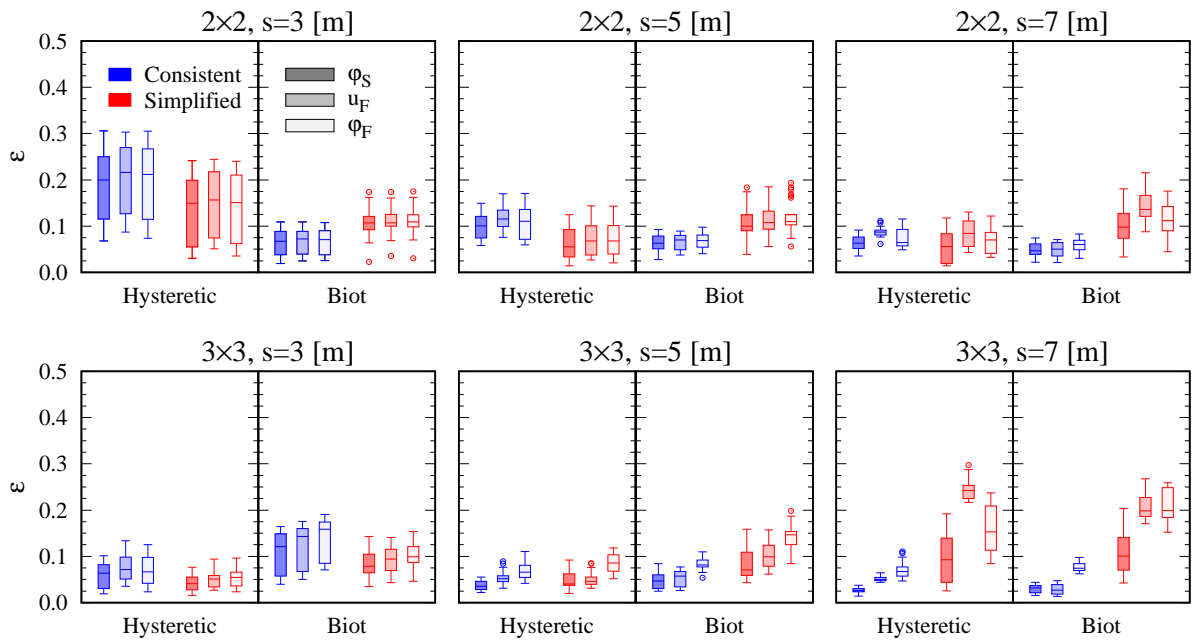


Figure 5.14: Differences due to the use of hysteretic or Biot's soil damping model, and errors due to the use of LPM approaches. Influence of foundation layouts (ground type D).

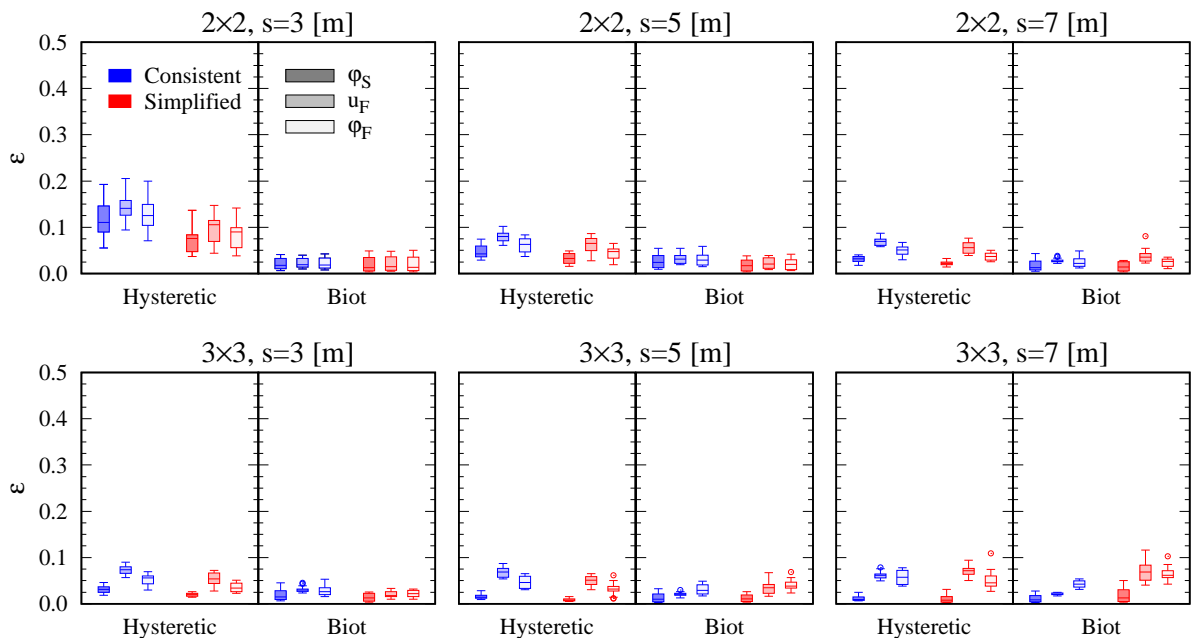


Figure 5.15: Differences due to the use of hysteretic or Biot's soil damping model, and errors due to the use of LPM approaches. Influence of foundation layouts (ground type C).

errors is observed with pile inclination, mainly due to slight decrease in the magnitude of the SSI phenomena (see Figure 5.10).

5.7 Conclusions

A wide parametric analysis has been performed in order to elucidate the influence of soil damping model and type of LPM on the computed seismic response of bridge piers on pile groups in cases where SSI phenomena are relevant. The study involved 4 different bridge pier superstructures, 12 pile foundation configurations (with vertical or inclined piles), 2 soil deposits and 2 soil damping models (classical hysteretic and Biot's damping model), with the system subjected to 7 real earthquake signals scaled for each soil type. The response of the system was computed using a substructuring approach in the frequency domain and also in the time domain by approximating the response of the foundation using two alternative LPMs of different complexity. Including also FB cases for reference, 4088 different cases in total were studied.

The impedance and kinematic interaction functions (previously computed using a harmonic 3D BEM-FEM code) are dependent on the chosen soil damping model. The most relevant differences appear in the low-frequency part of the damping functions, as the damping coefficient provided by the classical hysteretic model is unbounded at zero frequency, which leads to numerical difficulties for its fitting with LPMs. At higher frequencies, on the contrary, differences grow in the stiffness and the kinematic interaction functions.

Both the consistent and the simplified LPMs lead to approximated impedance functions that are continuous and symmetric with respect to frequency, which make them unable to fit the nonphysical unbounded tendency of the damping coefficient of the classical hysteretic damping model at zero frequency. The consequence is the impossibility of a good matching at very low frequencies when such hysteretic damping model is assumed for the soil, which is of special relevance in bridge piers, characterized by low fundamental frequencies. In any case, from an engineering point of view, both LPMs used in the study provide, in general, sufficiently low errors.

The magnitude of the influence of the soil damping model adopted for the study is, as could not be otherwise, not as large as that of the SSI effects, being the influence at the foundation level more relevant than that at the superstructure. It is also worth noting that larger displacements at the deck are predicted when Biot's model is adopted for the soil instead of the classical hysteretic model (due to the higher damping at low frequencies provided by the latter one). At the same time, the errors induced by approximating the impedance functions through the consistent or the simplified LPM are generally slightly lower than the differences arising from assuming the classical hysteretic or the causal Biot's models, i.e., the use of the simplified or the more accurate consistent LPM has, in general, less influence on the computed responses than the different assumptions that are made in the process of building the structural model. In terms of structural integrity, the assumption of Biot's damping together with the adoption of the consistent LPM could be adopted as the most conservative option, although the limited magnitude of the differences among approaches can justify the use of the simplest approach in most situations. However, it is worth noting that, in the present document, superstructures are modelled as one degree-of-freedom systems in their FB configuration, and are characterized by their fundamental frequency. This is one of the reasons why even the simplified LPM, for which fitting errors can be significant after a

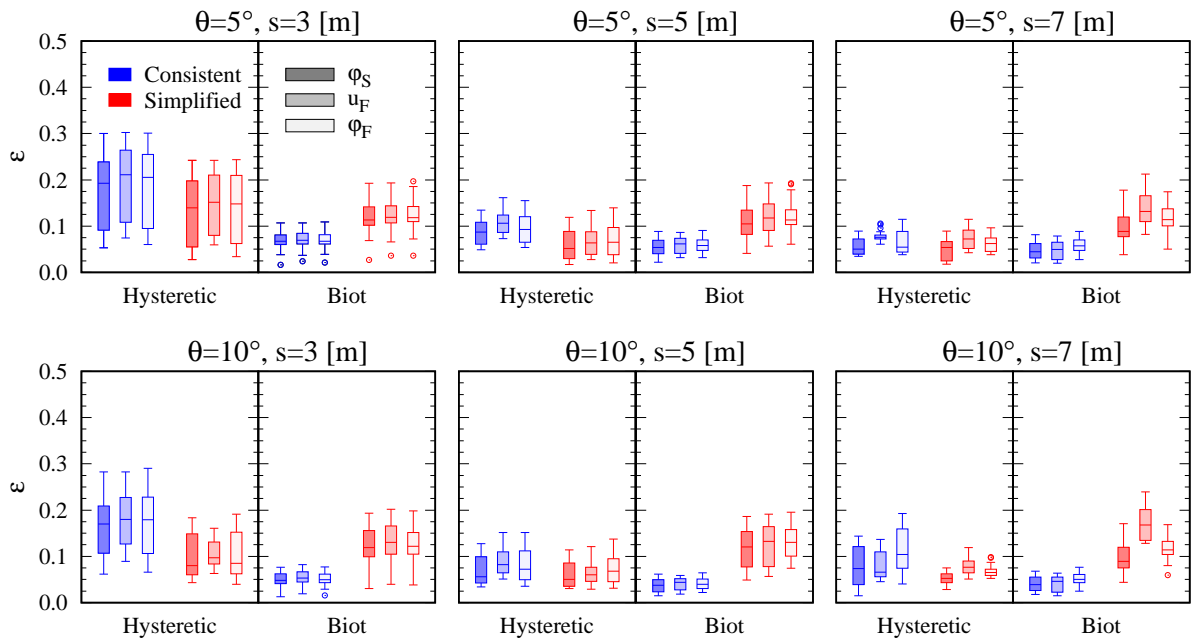


Figure 5.16: Differences due to the use of hysteretic or Biot's soil damping model, and errors due to the use of LPM approaches. Influence of pile inclination in 2×2 pile groups (ground type D).

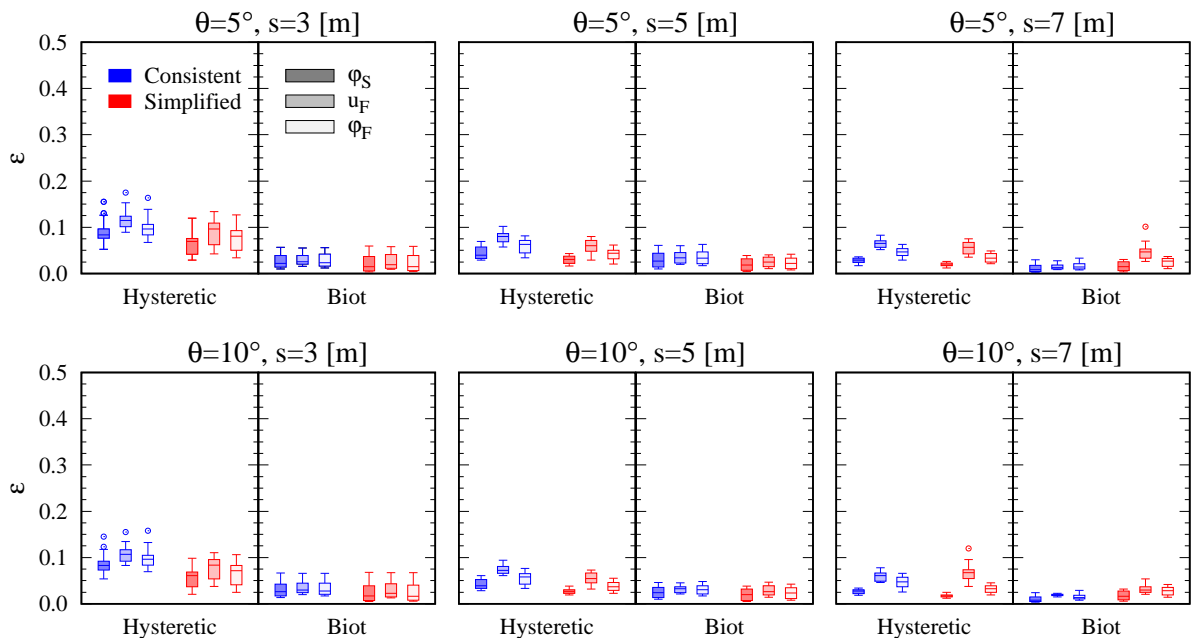


Figure 5.17: Differences due to the use of hysteretic or Biot's soil damping model, and errors due to the use of LPM approaches. Influence of pile inclination in 2×2 pile groups (ground type C).

given frequency, provides good results in most of the cases studied herein. Therefore, for other types of superstructures, better characterized as multi degree-of-freedom systems, more elaborate LPMs able to represent impedance functions accurately in a wider range of frequencies (such as the consistent approach) would possibly be needed in order to represent correctly the contribution of all vibration modes, so the simplest approaches would probably not be suitable. The non-physical behaviour provided by the classical hysteretic damping model for the soil at zero frequency makes the overall error committed by using the simplified LPM to model the foundation response smaller than the one obtained when using the more elaborate consistent approach for medium stiffness soil deposits. On the contrary, when assuming the causal Biot's damping model for the soil, the consistent LPM leads to consistently more accurate results. These conclusions hold for foundation configurations with both vertical and inclined piles, though this latter configuration leads to smaller deck displacements.

The study has been performed assuming a linear elastic behaviour for both the soil-foundation system and the superstructure. Concerning the soil-foundation system, the assumption of linearity is generally adopted dealing with SSI problems, justified by the capacity design of foundations and the complexity of handling the complex frequency-dependent nonlinear nature of soil. As for the superstructures, the assumption of linearity is realistic for low and moderate intensity earthquakes while for high intensity events plastic hinges at the piers base are expected to develop. Nevertheless, in the latter cases, linear approaches may provide an estimate of the displacement demand of nonlinear piers, according to the well-known equal energy and equal displacement rules [74]. It is also important to highlight the fact that some of the conclusions can also change when layered grounds are studied, as the appearance of cut-off frequencies will affect the ability of both LPMs, but especially the simplified approach, to catch more intricate impedance functions, and will also affect the influence of the adoption of one soil damping model or the other. These aspects are tackled in next sections.

Chapter 6

Benefits of inclined pile foundations in earthquake resistant design of bridges

6.1 Introduction

The beneficial effects of the use of inclined pile foundations on linear systems have been already addressed and discussed in [94,95], and briefly shown in Chapter 5 of this dissertation. But, on the other hand, the effects of pile inclination on the ductility demand of bridge piers have not been studied yet. This chapter focuses on its potential benefits for the piers foundations of multi-span bridges in earthquake-prone areas. To this end, a set of bridges characterized by different pier heights and span lengths are defined together with their corresponding pile foundations. The structures are designed following a displacement-based approach [111], and both linear and nonlinear behaviours are taken into account assuming different target ductility demands. For each foundation, four different pile rake angles are considered (including the vertical case), and the response of all resulting configurations, each subject to a set of seven scaled real accelerograms, is computed and analysed making use of a substructuring approach [58] and nonlinear time-domain analysis. The nonlinear behaviour of the bridge piers is modelled using both Takeda's [112] and a bilinear model. On the other hand, the frequency-dependent behaviour of the pile foundations is incorporated in the analysis by Lumped Parameter Models (LPM) calibrated to reproduce impedance functions previously computed for each specific case.

Results are presented in terms of ductility demand and energy dissipated by damping or by yielding. The results suggest that inclined piles are clearly beneficial to the seismic response of bridges, contributing to significantly reduce the ductility demand of piers due to the particular kinematic seismic response of this type of foundations and the associated reductions in the input seismic energy to the system.

Bridges characterised by different span lengths L (25, 50 and 75 m) and piers heights H (10, 15 and 30 m) are assumed, covering a sufficiently wide scenario of aspect ratio L/H , and the design is performed taking advantage of the above assumptions on the deck restraints. In addition, bridges with both a ductile and non-ductile behaviour are designed imposing the displacement ductility demand of piers through a displacement-based design approach [111]. Finally, pile foundations are designed following standard guidelines, taking into account design action effects at the base of each pier, evaluated

	<i>Depth</i>		c_s [ms ⁻¹]	ρ_s [tm ⁻³]
	<i>from</i> [m]	<i>to</i> [m]		
Lithotype 1:	0.0	15.0	120.0	1.8
normally consolidated clay	15.0	30.0	180.0	1.8
Lithotype 2:	30.0	40.0	600.0	2.0
over consolidated clay	40.0	∞	800.0	2.0

Table 6.1: Soil profile and lithotypes.

according to hierarchy principles [113], and the site class.

6.2 Soil properties and seismic actions

A layered type D soil, representative of loose-to-medium cohesionless soil or predominantly soft-to-firm cohesive soil, according to EC8-1 [109], profile is considered in this study. The soil is assumed to be constituted by two fundamental lithotypes, normally and over consolidated (geological bedrock) clays characterized by the properties reported in Table 6.1, with an ascending soil shear wave's velocity c_s from 120.0 m/s to 800.0 m/s. A constant Poisson's ratio $\nu_s = 0.4$ is assumed for both lithotypes.

The seismic action is constituted by a set of seven scaled real accelerograms, chosen from the Selected Input Motions for displacement-Based Assessment and Design database, SIMBAD [122]. The records selection is based on the earthquake Magnitude ($5.0 < M_w < 7.3$), the epicentral distance ($0.0 < \Delta < 35.0$ km) and the mean pseudo-acceleration and displacement response spectra compatibility with the design ones, defined according to the EC8-1 [109], for which a peak ground acceleration of 0.3375g is expected on soil D at the life safety limit state. Compatibility of the mean pseudo-acceleration and displacement response spectra with the code ones is assured within the superstructures minimum and maximum fundamental periods, considering both the elastic and the expected inelastic (i.e. effective) periods, resulting from the displacement-based design procedure, as it will be briefly shown in the sequel. In detail, the mean spectral ordinates result no lower than the 90% of the relevant ones of the code in the range $0.71 < T < 5.00$ s, corresponding to the minimum elastic and maximum effective periods of the analysed bridges. Finally, in order to limit bias in the structural response caused by the ground motion selection [126–128], earthquakes requiring small scale factors (1.00–1.35) are employed. The selected records are detailed in Table 6.2, whose acceleration time histories are shown in Figure 6.1. The elastic response spectrum (in terms of pseudo-acceleration and displacement) of each scaled record is compared with the design spectra in Figure 6.2. In addition, the mean spectra of the selection are shown with a continuous black line, while mean spectra plus and minus the standard deviation are reported with dashed lines to provide a pictorial view of the scattering of spectral ordinates.

<i>Earthquake label</i>	<i>Name WC-EC</i>	<i>Station ID</i>	<i>Date</i> [dd/mm/yy]	Δ [km]	<i>Magnitude</i> [M _w]	<i>PGA</i> [ms ⁻²]	<i>Scale factor</i>
E1	Gazli 440-86	KAR	17/05/1976	12.8	6.7	7.04 <i>x-dir</i>	1.25
E2	Gazli 440-86	KAR	17/05/1976	12.8	6.7	5.97 <i>y-dir</i>	1.05
E3	Imperial Valley 446-89	EC05	15/10/1979	27.7	6.5	5.09 <i>y-dir</i>	1.25
E4	Imperial Valley 447-89	EC06	15/10/1979	27.4	6.5	4.03 <i>y-dir</i>	1.00
E5	Loma Prieta 456-94	ST_58065	18/10/1989	27.6	6.9	3.18 <i>x-dir</i>	1.35
E6	Northridge 461-99	ST_24279	17/01/1994	20.3	6.7	5.78 <i>y-dir</i>	1.00
E7	Erzincan 465-78	ERZ	13/03/1992	8.97	6.6	4.86 <i>x-dir</i>	1.18

Table 6.2: Selected records for input motion (WC: Waveform Code, EC: Earthquake Code, Δ : epicentral distance and PGA: Peak Ground Acceleration.) [122].

6.3 Decks design

Bridges with span lengths L of 25.0, 50.0 and 75.0 m are considered and twin girders steel-concrete composite decks with a slab width of 12.0 m and thickness ranging between 25.0 and 35.0 cm (Figure 6.3a) are designed. Since, as already stated, decks are not strongly involved in the seismic response of the bridges, a design for vertical loads is performed considering two types of cross-sections, representative of hogging and sagging deck regions (Figure 6.3b).

The steel beams height l_2 is evaluated by assuming $L/l_2 = 26.0$, while thicknesses of webs as well as widths and thicknesses of bottom and top flanges are determined through an elastic analysis of the most stressed cross-sections of the hogging and sagging regions, assuming steel grade S355 for girders and concrete grade C25/30 for the slab. As for the slab, typical longitudinal and transversal reinforcement ratios, corresponding to 1% and 2% for the sagging and hogging cross-sections, respectively, are assumed (Figure 6.3a). For the sake of completeness, Table 6.3 shows bending moments obtained from the deck analyses subjected to vertical loads (self-weight, moving and permanent loads), and the girders plates dimensions of the hogging and sagging cross-sections relevant to the span lengths of 25, 50 and 75 m.

All permanent loads of each deck case are defined in Table 6.4, which not only include girders carpentry weights but also the concrete slab and non-structural members self weights; effective mass of the pier (half of the total mass) and that of the pier bent are also taken into account.

6.4 Piers design

Piers of investigated bridges are designed to withstand the seismic action with both a ductile and non-ductile behaviour, in order to evaluate effects of SSI on both linear and nonlinear systems. Piers have been designed, in sufficient level of detail for the present analysis, following the displacement-based seismic design method [111] depicted in Section 4.2. Plastic hinges will appear at the pier base when an earthquake occurs,

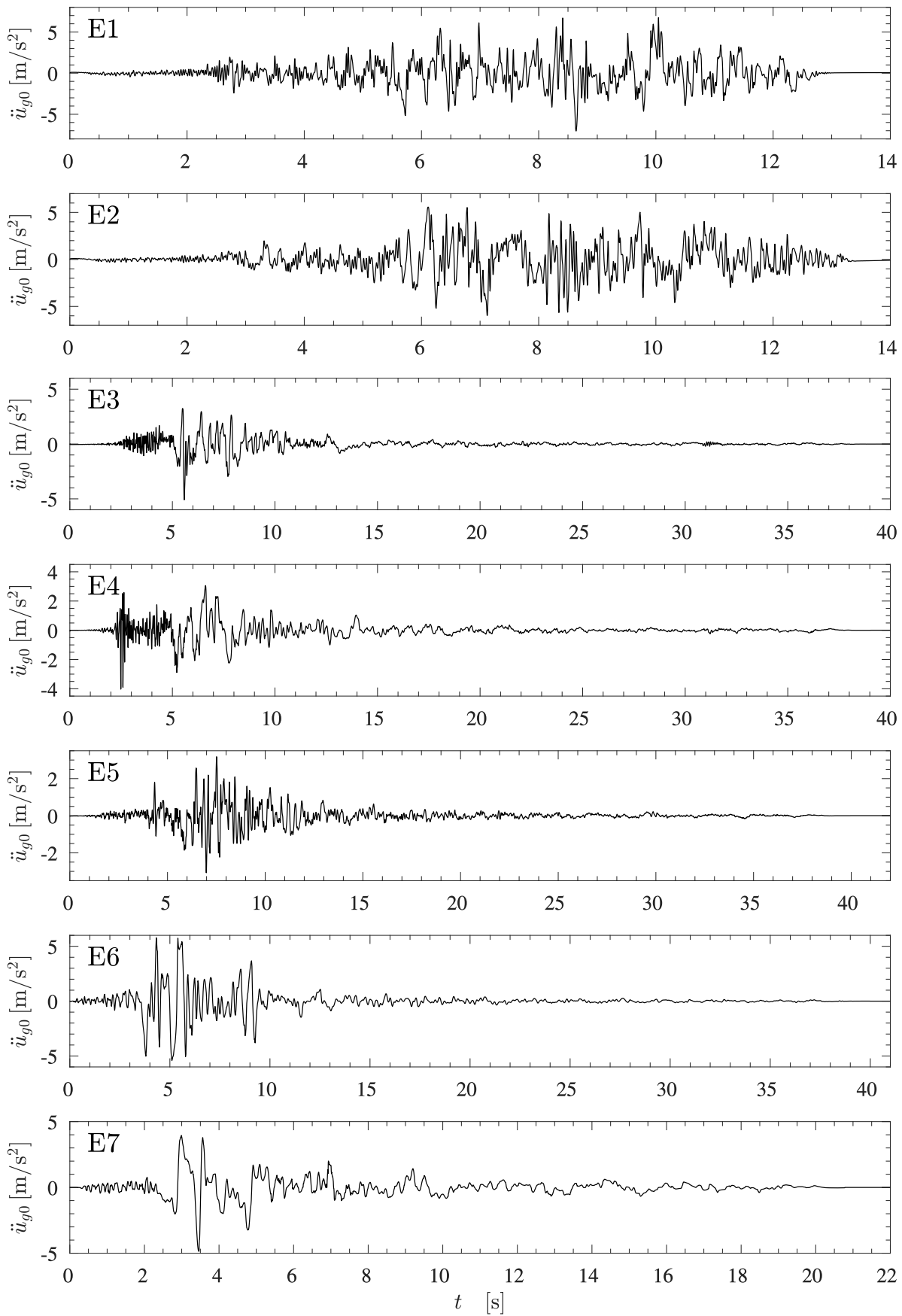


Figure 6.1: Time histories of the selected records (see Table 6.2).

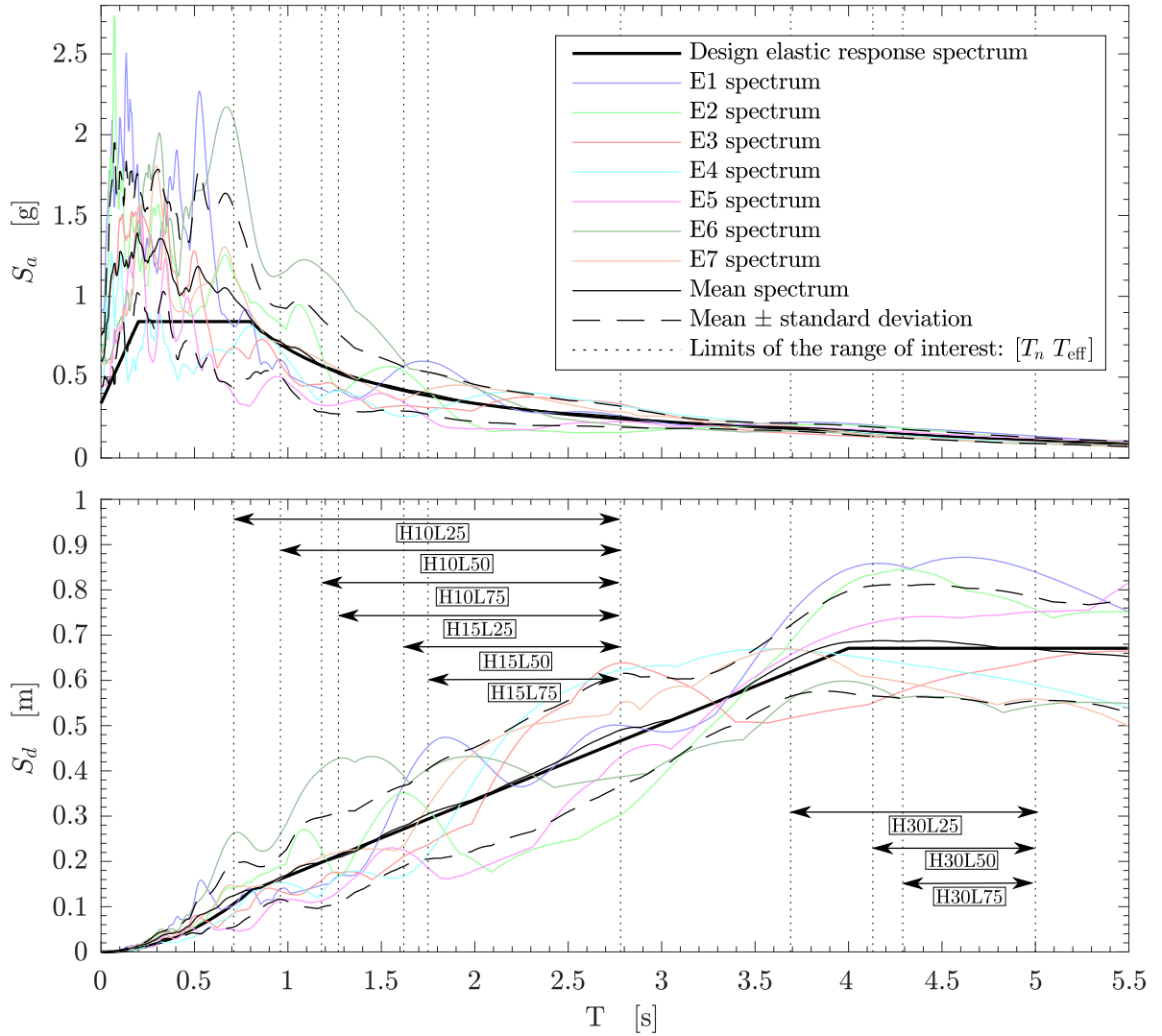
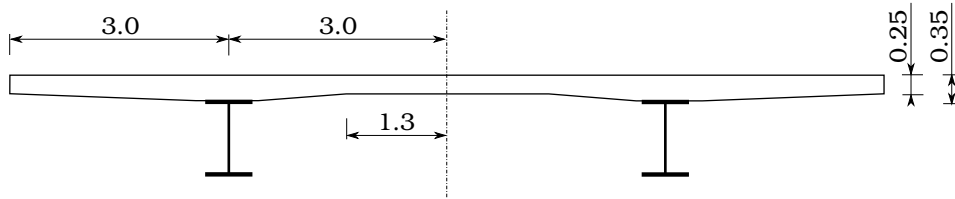


Figure 6.2: Elastic response spectrum of the selected earthquakes (see Table 6.2), in terms of accelerations (top) and displacements (bottom).

so the pier nonlinear behaviour and a target ductility demand must be defined.

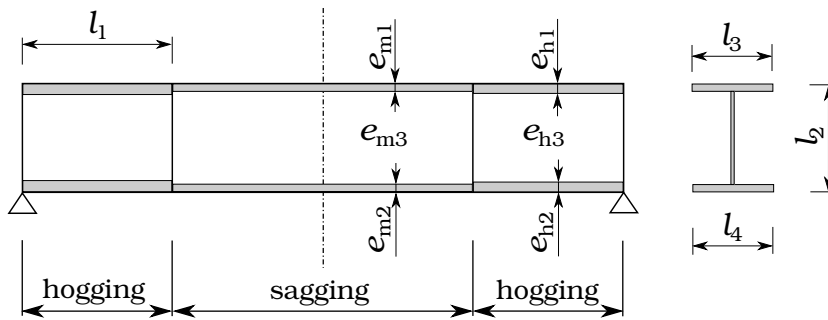
In details, piers with elastic behaviour ($\mu = 0.98$) as well as piers with a displacement expected ductility demand equal to 2.02 and 4.05 are designed, corresponding to piers heights of 10, 15 and 30 m, respectively. The latter are all combined with the three span lengths, generating the nine analysis cases reported in Table 6.5. Each of the different nine configurations will be identified through this section using the label defined in the first row of Table 6.5. The design procedure is repeated to design all piers of the analysed bridges, considering r.c. piers with circular cross-section of diameter $D = 2.4$ m and assuming a concrete grade C35/45. Furthermore, reinforcements of steel grade B450C and diameter of 40 and 22 mm are used for the longitudinal and transverse reinforcements, respectively. Table 6.5 reports details of the design procedure in addition to already defined quantities, being N_{Sd} the design axial force, and M_{Sd} and M_{Rd} the design bending moment and the bending moment resistance, respectively.

It is worth noting that the standard [113] requires a minimum longitudinal reinforcement ratio of 1% and dictates increasing the design bending moment if the stability index



reinforcement ratio of hogging section = 2.0%
 reinforcement ratio of sagging section = 1.0%

(a)



(b)

Figure 6.3: (a) Decks cross-section (values in meters), (b) girders plates thicknesses and dimensions (values in Table 6.3).

L [m]	$M_{hogging}$ [MNm]	$M_{sagging}$ [MNm]	l_1 [m]	l_2 [m]	l_3 [m]	l_4 [m]	e_{h1} [mm]	e_{h2} [mm]	e_{h3} [mm]	e_{m1} [mm]	e_{m2} [mm]	e_{m3} [mm]
25.0	-10.7	7.2	6.25	1.0	0.6	0.6	50.0	50.0	15.0	20.0	30.0	10.0
50.0	-43.0	29.0	12.5	1.9	0.8	1.0	65.0	65.0	22.0	25.0	40.0	12.0
75.0	-98.4	66.1	18.75	2.9	1.0	1.2	85.0	85.0	30.0	35.0	55.0	15.0

Table 6.3: Bending moments due to self weights, and girders plates thicknesses and dimensions (scheme in Figure 6.3b).

L [m]	<i>Metal</i> <i>carpentry</i> [KN/m]	<i>Concrete</i> <i>slab</i> [KN/m]	<i>Non-structural</i> <i>members</i> [KN/m]	<i>Total</i> [KN/m]
25.0	13.0	88.8	33.0	134.8
50.0	18.0	88.8	33.0	139.8
75.0	25.0	88.8	33.0	146.8

Table 6.4: Analysis of deck permanent loads due to self weights.

<i>Case label</i>		H10L25	H10L50	H10L75	H15L25	H15L50	H15L75	H30L25	H30L50	H30L75
H	[m]	10.0	10.0	10.0	15.0	15.0	15.0	30.0	30.0	30.0
L	[m]	25.0	50.0	75.0	25.0	50.0	75.0	25.0	50.0	75.0
D	[m]	2.4	2.4	2.4	2.4	2.4	2.4	2.4	2.4	2.4
N_{Sd}	[MN]	-5.16	-8.78	-12.80	-5.73	-9.35	-13.37	-7.43	-11.05	-15.06
Δ_y	[m]	0.080	0.080	0.080	0.176	0.176	0.176	0.682	0.682	0.682
Δ_d	[m]	0.325	0.325	0.325	0.355	0.355	0.355	0.670	0.670	0.670
μ		4.05	4.05	4.05	2.02	2.02	2.02	0.98	0.98	0.98
Stability index		0.064	0.098	0.127*	0.076	0.103*	0.100	0.177*	0.178*	0.167*
ξ_{eq}	[%]	15.6	15.6	15.6	12.1	12.1	12.1	5.0	5.0	5.0
T_{eff}	[s]	2.78	2.78	2.78	2.78	2.78	2.78	5.00	5.00	5.00
M_{Sd}	[MNm]	9.21	17.81	32.86	15.79	31.75	44.44	27.17	41.24	60.08
No. of long. rebars		36	36	37	36	41	65	36	56	90
Long. reforc. ratio	[%]	1.00**	1.00**	1.03	1.00**	1.14	1.81	1.00**	1.56	2.50
M_{Rd}	[MNm]	26.25	29.26	32.88	26.74	32.33	47.56	28.19	41.56	60.46
Stirrups spacing	[cm]	17.0	14.0	9.0	18.0	13.0	9.0	16.0	11.0	9.0

* M_{Sd} has been overestimated according to stability index higher than 0.1 [113].

** Minimum amount of reinforcement required by the standard [113].

Table 6.5: Definition of cases of studies, case labels and pier properties.

exceeds 0.1 in order to account for second order effects. It is worth mentioning that for some investigated bridges, piers have been oversized to comply with code requirements, with consequences on the relevant seismic behaviour with respect to the expected one.

6.5 Pile foundations design

Pile foundations are designed according to hierarchy principles, following indications available in [113], relevant to structures designed through nonlinear analyses. A 2×2 square piles layout is considered for $H = 10$ m bridges, while a 3×2 layout (with the line of 3 piles oriented in the bridge transverse direction) is assumed for $H = 15$ and $H = 30$ m bridges. Piles diameter \varnothing_p , length and spacing s are calculated for each bridge with standard methodologies for cohesive soils. For soft normally consolidated clay deposits, the undrained strength C_u is assumed to increase linearly with the vertical lithostatic stress, while for the geological bedrock (constituted by over consolidated clay) $C_u = 600$ kPa is considered. The actions at the base of piers result from the above design methodology. Foundation parameters are summarized in Table 6.6. Piles Young's modulus $E_p = 30.0$ GPa and density $\rho_p = 2.5$ t/m³ are considered, and different pile rake angles θ are hypotheses to address the relevant contribution to the superstructure response. In details, $\theta = 0^\circ$ (vertical piles), 5° , 10° and 15° are considered, according to the layouts of Figure 4.2.

<i>Case label</i>	N_{Sd} [MN]	M_{Rd} [MNm]	V_{Rd} [MN]	<i>Layout</i>	\varnothing_p [m]	s/\varnothing_p	<i>Piles length</i> [m]
H10L25	-5.16	26.25	2.63	2 × 2	1.2	3.0	31.0
H10L50	-8.78	29.26	2.93	2 × 2	1.2	3.0	35.0
H10L75	-12.80	32.88	3.29	2 × 2	1.2	3.0	45.0
H15L25	-5.73	26.74	1.78	3 × 2	1.2	3.0	31.0
H15L50	-9.35	32.33	2.16	3 × 2	1.2	3.0	35.0
H15L75	-13.37	47.56	3.17	3 × 2	1.2	3.0	40.0
H30L25	-7.43	28.19	0.94	3 × 2	1.5	3.0	32.0
H30L50	-11.05	41.56	1.39	3 × 2	1.5	3.0	32.0
H30L75	-15.06	60.46	2.02	3 × 2	1.5	3.0	40.0

Table 6.6: Design action effects at the foundation level and pile foundations dimensions.

	H10L25	H10L50	H10L75	H15L25	H15L50	H15L75	H30L25	H30L50	H30L75
m_d [t]	343.5	712.5	1122.3	343.5	712.5	1122.3	343.5	712.5	1122.3
I_d [t m ²]	2906.4	6585.3	11933.3	2906.4	6585.3	11933.3	2906.4	6585.3	11933.3
h_d [m]	0.97	1.53	2.08	0.97	1.53	2.08	0.97	1.53	2.08
m_c [t]	88.3	88.3	88.3	88.3	88.3	88.3	88.3	88.3	88.3
I_c [t m ²]	426.6	426.6	426.6	426.6	426.6	426.6	426.6	426.6	426.6
h_c [m]	1.80	1.80	1.80	1.80	1.80	1.80	1.80	1.80	1.80
m_p [t]	94.5	94.5	94.5	152.18	152.18	152.18	325.1	325.1	325.1
h_p [m]	8.20	8.20	8.20	13.20	13.20	13.20	28.20	28.20	28.20
m_f [t]	78.4	78.4	78.4	257.6	257.6	257.6	503.1	503.1	503.1
I_f [t m ²]	211.4	211.4	211.4	1902.8	1902.8	1902.8	5806.9	5806.9	5806.9
h_f [m]	1.00	1.00	1.00	2.00	2.00	2.00	2.50	2.50	2.50
T_n [s]	0.71	0.96	1.18	1.27	1.62	1.75	3.69	4.13	4.29
T_n^* [s]	1.08	1.20	1.28	1.62	1.73	1.83	4.28	4.56	4.74
T_{eff} [s]	2.78	2.78	2.78	2.78	2.78	2.78	5.00	5.00	5.00

Table 6.7: Set of parameters defining the different FB and CB systems (see Figure 4.12) used to model the superstructure considered for each case of analysis.

6.6 Results

Parameters of the structural models depicted in Figure 4.12 representative of all the superstructures considered in this study are reported on Table 6.7. This table also presents the natural T_n and effective T_{eff} periods of each superstructure, together with the natural period T_n^* resulting from relaxing the requirement over minimum reinforcement content and stability index established by [113].

6.6.1 Piers plastic hinge parameters

Final results of the moment-curvature relationship obtained with the CUMBIA software [114] for all nine bridge piers, and using constitutive models of concrete and steel reinforcement defined in Section 4.3, are shown in Figure 6.4 together with its relevant elasto-plastic approximation. Equal scaling is applied in all sub-graphs, it is important to notice how the reinforcement content increases the yield strength of the pier section

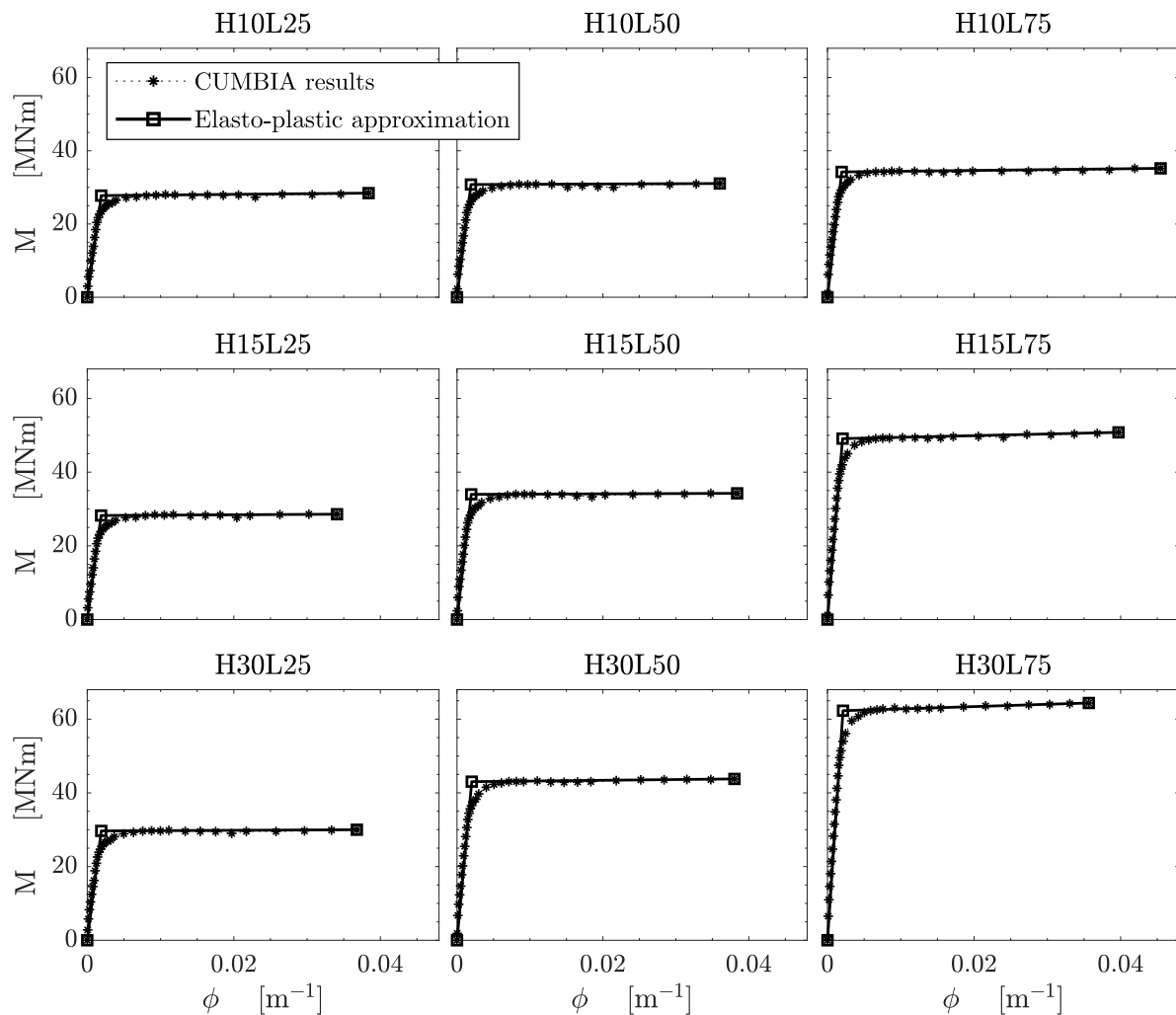


Figure 6.4: Moment-curvature relationships of piers cross sections [114].

maintaining an almost identical yield curvature, though all piers have equal diameter $D = 2.4$ m (Table 6.5).

Table 6.8 summarises parameters of the constitutive bilinear moment-chord rotation laws of the lumped plastic hinges for the backbone construction, identified through the yielding M_y and ultimate M_u bending moments and the relevant yielding φ_{Sy} and ultimate φ_{Su} rotations. Data within parenthesis refers to analyses disregarding code provisions concerning reinforcement detailing and stability issues. The hysteretic cyclic behaviour of the plastic hinges is defined adopting different models, considering and disregarding the stiffness degradation of reinforced concrete members due to cyclic loading. The stiffness degradation effect is taken into account through the Takeda's hysteresis model [112], while by using the bilinear hysteresis model no degradation effect is taken into account (Figure 6.5).

6.6.2 Impedance functions and kinematic interaction factors

Impedance functions and kinematic interaction factors of the pile foundations were computed, for reference and for comparison, using two different frequency-domain models: a) the Winkler-type model developed by Dezi et al. [9], and b) the BEM-FEM developed

<i>Case label</i>	M_y [MNm]	M_u [MNm]	φ_{Sy} [rad]	φ_{Su} [rad]
H10L25	27.77 (9.67)	28.44 (10.15)	0.0063 (0.0051)	0.0454 (0.0628)
H10L50	30.78 (17.98)	31.06 (18.19)	0.0064 (0.0058)	0.0429 (0.0565)
H10L75	34.23 (28.43)	35.20 (29.07)	0.0065 (0.0063)	0.0531 (0.0572)
H15L25	28.24 (16.61)	28.58 (16.84)	0.0095 (0.0091)	0.0549 (0.0745)
H15L50	33.98 (28.97)	34.25 (29.52)	0.0098 (0.0095)	0.0612 (0.0654)
H15L75	49.10 (44.05)	50.79 (45.15)	0.0103 (0.0101)	0.0635 (0.0654)
H30L25	29.67 (21.02)	29.99 (21.29)	0.0191 (0.0182)	0.1038 (0.1181)
H30L50	43.04 (34.04)	43.78 (34.61)	0.0202 (0.0195)	0.1077 (0.1166)
H30L75	62.30 (49.80)	64.39 (51.01)	0.0212 (0.0207)	0.1027 (0.1083)

Table 6.8: Parameters for the plastic hinge modelling. Data within parenthesis refers to analyses disregarding code provisions concerning reinforcement detailing and stability issues.

Takeda's hysteresis model

Bilinear hysteresis model

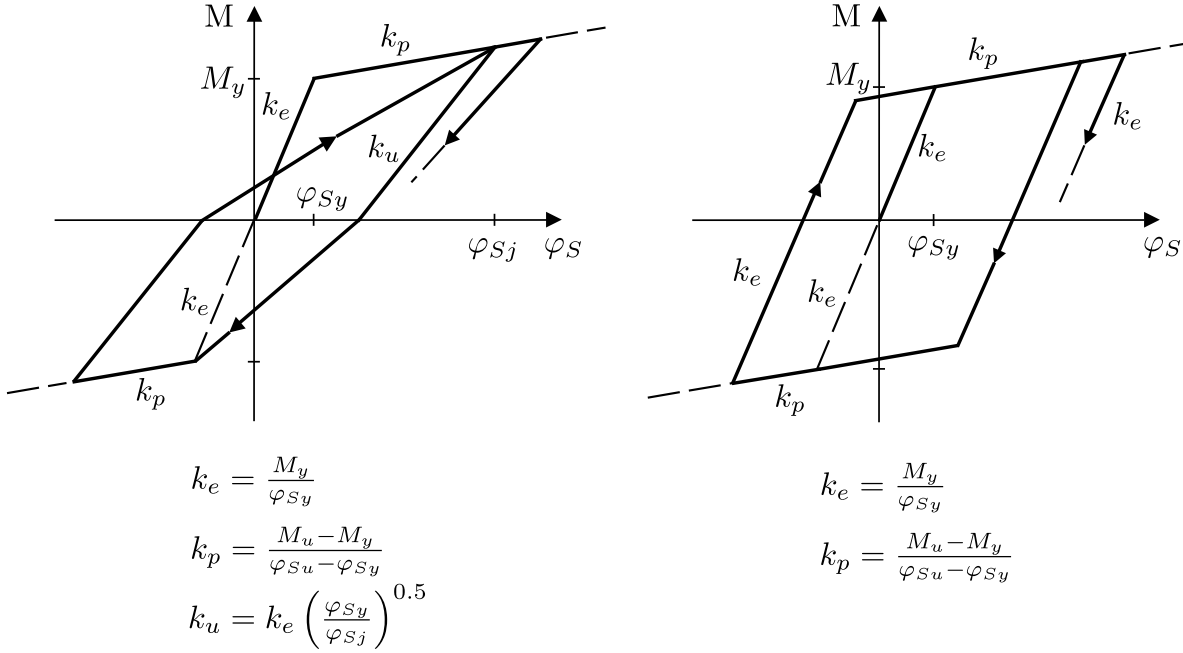


Figure 6.5: Hysteretic cyclic rules adopted to model the nonlinear response of the plastic hinge.

by Padrón et al. [23] (see Section 4.6). Although some differences between models appear in the mentioned functions, the differences observed later in terms of ductility demand are remarkably negligible (see Section 6.6.3). The embedment of the pile cap has been included in the BEM-FEM analyses for completeness, although its influence is expected to be negligible. Figure 6.6 shows the discretization used for the soil.

Impedance functions obtained through the two models are shown in Figure 6.7. Through the BEM-FEM, continuous lines, the stratified nature of the investigated soil profile is clearly evident in the impedance functions through the cut-off frequencies that can be observed in the damping functions, and the multiple resonance frequencies appear-

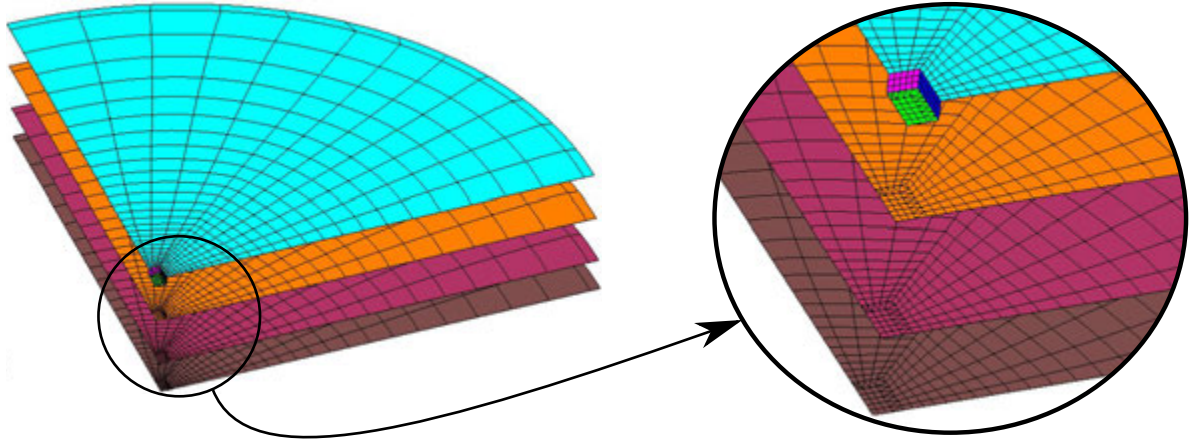


Figure 6.6: Example of BEM discretization for the computation of impedance functions and kinematic interaction factors (only a quarter of the geometry is shown).

ing in the stiffness functions in the frequency range 0 – 2 Hz. The last can't be observed in the Winkler-type model results, dashed lines, because it not considers the soil continuity. A significant increase in stiffness and damping capacity with number of piles and pile diameter can also be observed. Although strong differences in the impedance functions arise in the resonant peaks related with pile interaction for some terms, those peaks appear beyond 10 Hz, quite far from the maximum fundamental frequency over the studied systems, 1.41 Hz (for the H10L25 case in the elastic range). This is one of the main reasons why soil-foundation-superstructure systems responses are not altered in terms of ductility demand depending on the model used for computing impedance functions.

Kinematic interaction factors obtained through the two models are shown in Figure 6.8. Strong differences in the comparison between the BEM-FEM and Winkler-type model appear beyond 8 Hz, continuous vs. dashed lines. It is important to notice that the amount of energy of the ground motions is mainly concentrated in the frequency range of 0 – 7 Hz as shows the grey line in Figure 6.8. This line represents the normalized mean Fourier amplitude spectrum of the selected ground motions. Being the differences on the kinematic interaction factors between the two models almost negligible in the 0 – 7 Hz frequency range, soil-foundation-superstructure systems responses in terms of ductility demand are not altered depending on the model used for computing kinematic interaction factors.

Impedance functions corresponding to all pile layouts are presented in Figures 6.9 and 6.10 (solid lines) obtained through the BEM-FEM or the Winkler model, respectively. Also the kinematic interaction factors corresponding to all pile layouts are presented in Figures 6.11 and 6.12. In both representations, the functions corresponding to the different pile inclinations are presented in different columns. As expected, the horizontal stiffness is shown to increase with rake angle while rocking stiffnesses decrease only slightly with pile inclination. Regarding the kinematic interaction factors (see, e.g., Figure 6.11), translational factors tend to decrease with the rake angle, while rotation factors experiment a significant increase. This induced rotation is responsible for structural anti-phase displacements and accelerations, with respect to those induced by translation, and its effects on linear systems have been already addressed and discussed in [94,95], and in Chapter 5 of this dissertation. In order to help interpreting the relevance of the trends

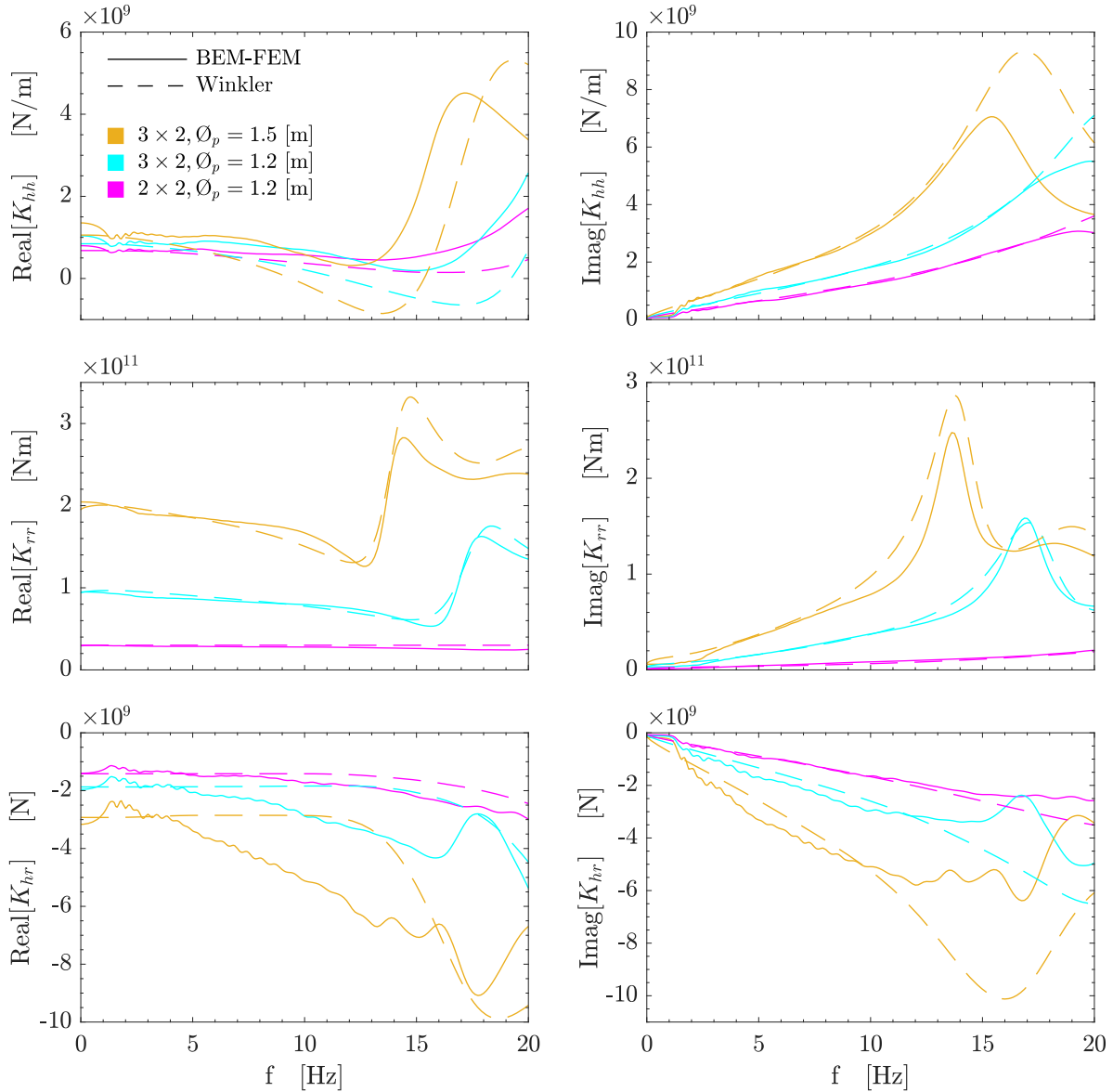


Figure 6.7: Computed impedance functions for vertical foundation layouts comparing BEM-FEM and Winkler-type models.

shown in Figures 6.11 and 6.12, the normalized mean Fourier amplitude spectrum of the selected ground motions (Table 6.2) is also included as a grey line in the first plot. As stated before, it shows that the energy content of ground motions is mainly concentrated between 0 and 7 Hz, range within which the variations in the kinematic interaction factors (and most importantly, the rotational factor) are not negligible.

For the study of the benefits of inclined pile foundations in earthquake resistant design of bridges, the adopted LPM scheme is the one described in Section 4.9.2. LPM impedances resulting from the fitting procedure are shown in dashed line in Figures 6.9 and 6.10 superposed to the BEM-FEM and Winkler impedances, respectively, for a qualitative comparison. The fitting frequency range has been assumed to be 0–5 Hz. The latter is assumed to be sufficiently wide, given that the maximum fundamental frequency of the investigated bridges (in the elastic range) is 1.41 Hz (for the H10L25 case) and that results achieved in [97], and presented in the previous chapter, demonstrate that

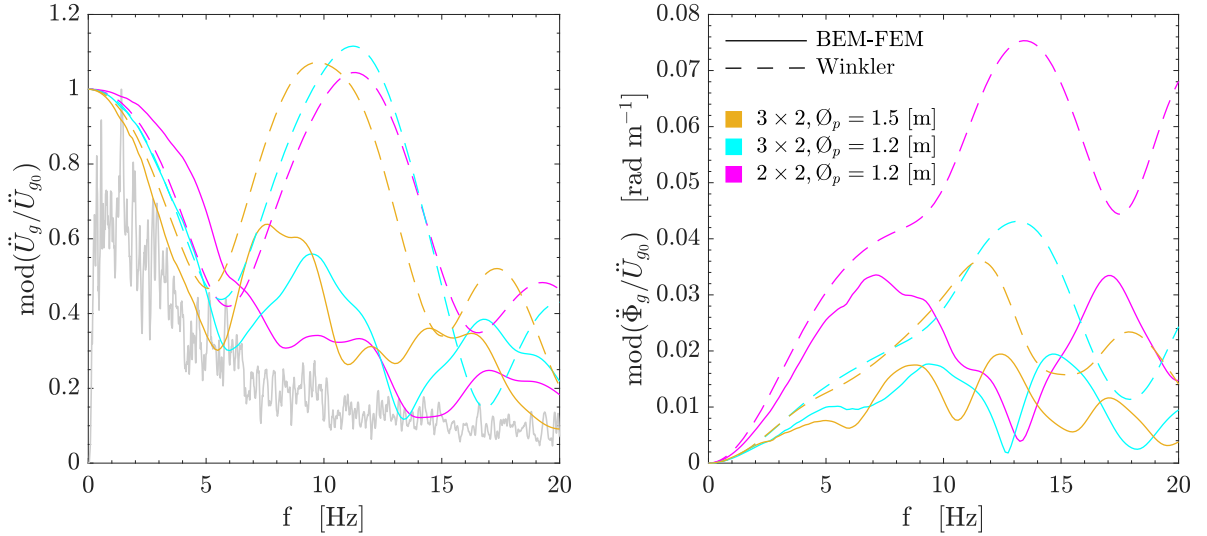


Figure 6.8: Computed kinematic interaction factors for vertical foundation layouts comparing BEM-FEM and Winkler-type models (the gray line represents normalized mean Fourier amplitude spectrum of the selected ground motions).

an optimization of impedance functions nearby the fundamental structural frequency is sufficient to achieve accurate results for this type of structures. As shown in Figures 6.9 and 6.10, the derived LPMs are not able to reproduce exactly all the trends captured by the original impedance functions. However, these differences will be shown to have no impact whatsoever on the results of interest in this study (see Section 6.6.3).

6.6.3 Inelastic responses

In order to provide an idea of the structural responses computed through the presented methodology, Figure 6.13 shows the time history of the pier bending moment (right) and bending moment-chord rotation for the analysis case H15L50 (bridge with spans length of 50 m and piers height of 15 m) subjected to input motion E7 (Table 6.2), considering vertical (upper plots) or $\theta = 15^\circ$ inclined (lower plots) piles. Results computed using both Takeda's and bilinear approaches for modelling the nonlinear response of the pier hinge are shown together with the response obtained by assuming a linear model. The lengthening of the system period with pier degradation using Takeda's law becomes evident from the comparison of the responses by the three models.

The target ductility used in the design is also represented in Figure 6.13, for reference, with a circle. The ductility demand computed considering vertical piles and the Takeda's hysteretic rule coincides with the target ductility. On the contrary, in the configuration employing inclined piles, the magnitude of the response is significantly smaller, with a resulting ductility demand ($\mu = 1.35$) much smaller than the target ductility ($\mu = 2.02$).

In order to elucidate the differences in terms of the pier ductility demand depending on the model used for representing the soil-foundation compliant behaviour, i.e. the BEM-FEM or the Winkler-type model, ductilities have been computed through the equal displacement rule [74] both in the frequency-domain for all superstructures and input motions. The equal displacement rule assumes that the maximum displacement of the elastoplastic system is equal to the maximum displacement of the corresponding

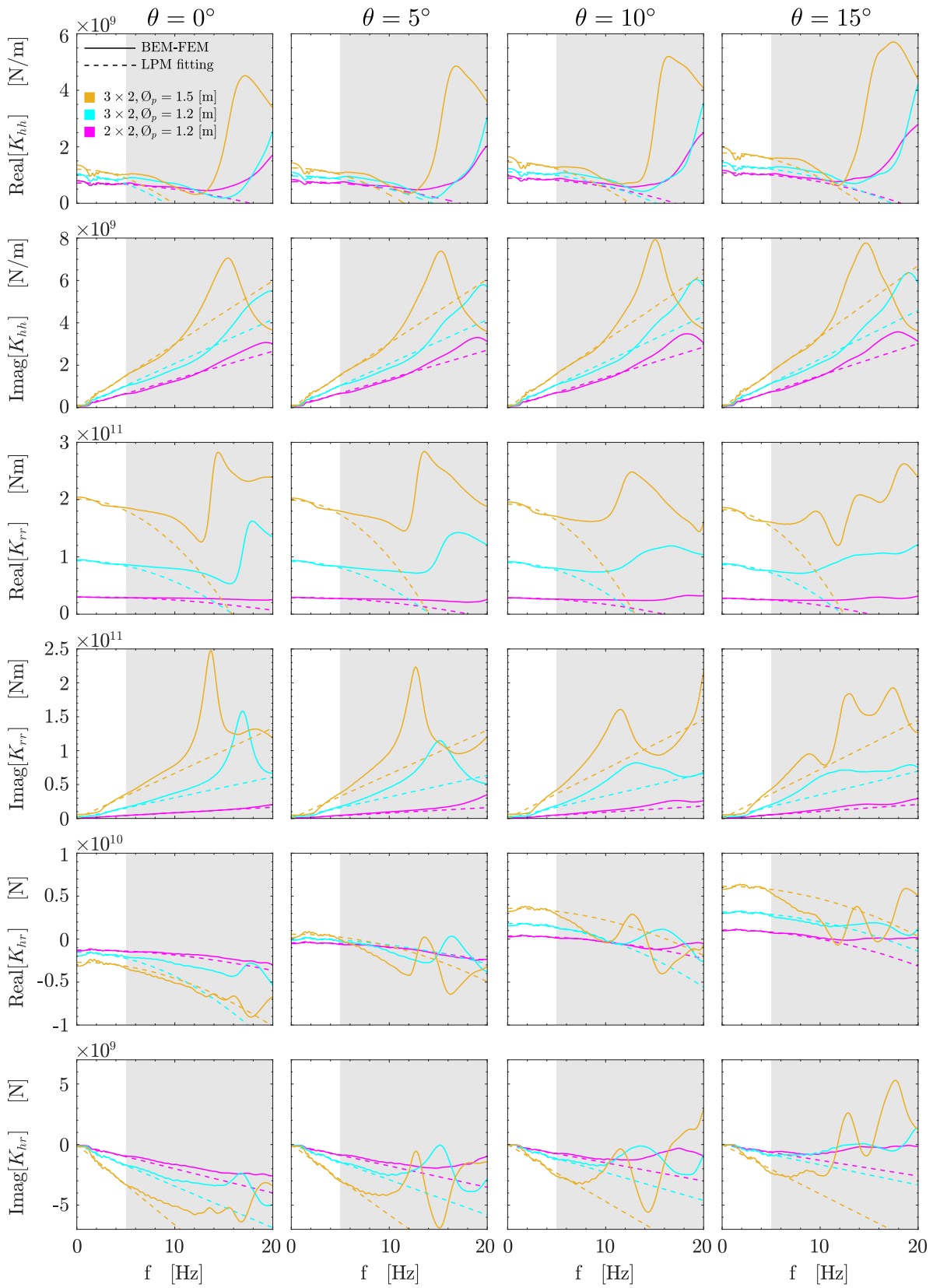


Figure 6.9: Computed and fitted impedance functions for all foundations layouts. Impedance functions computed through the BEM-FEM.

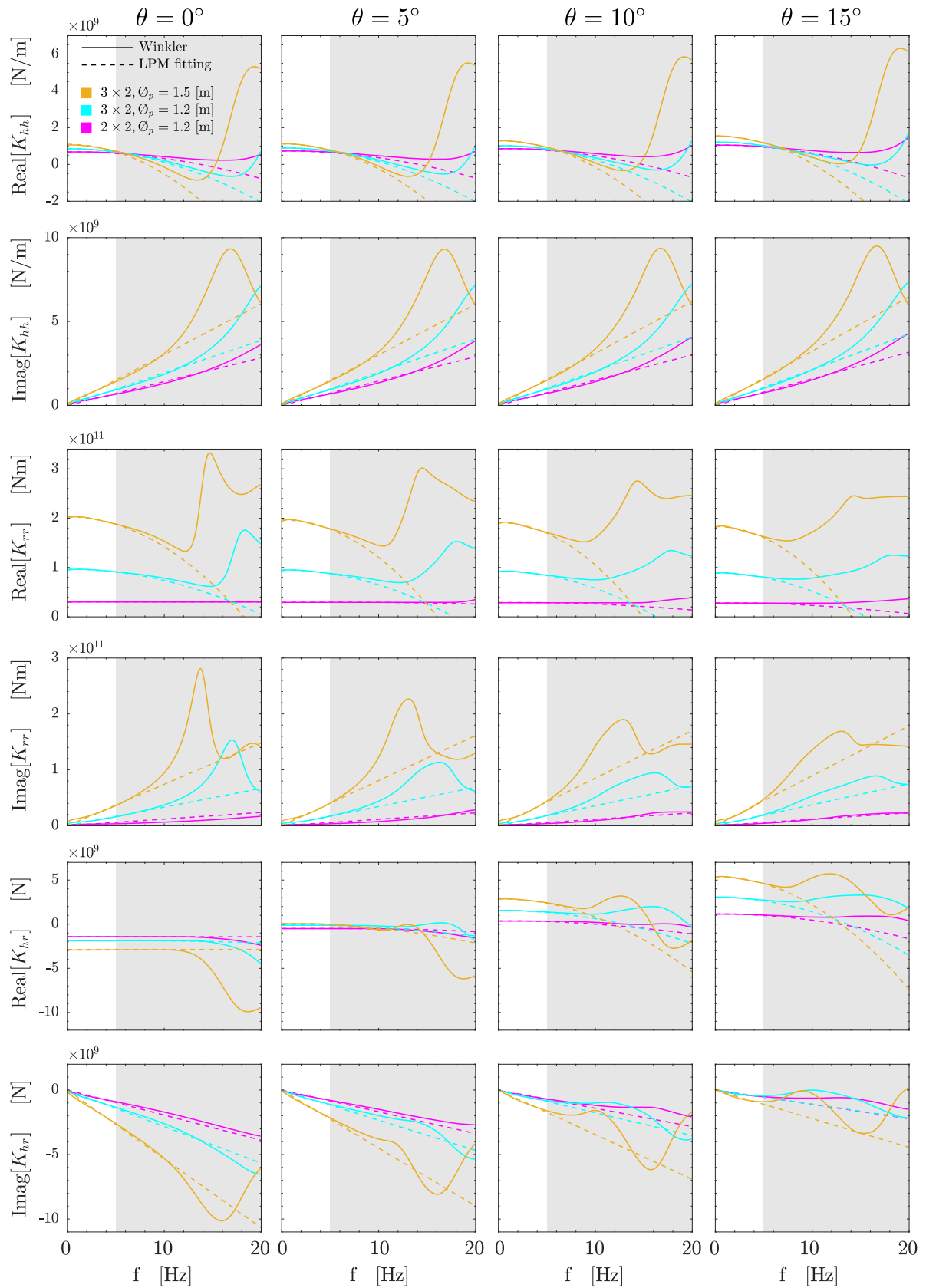


Figure 6.10: Computed and fitted impedance functions for all foundations layouts. Impedance functions computed through the Winkler model.

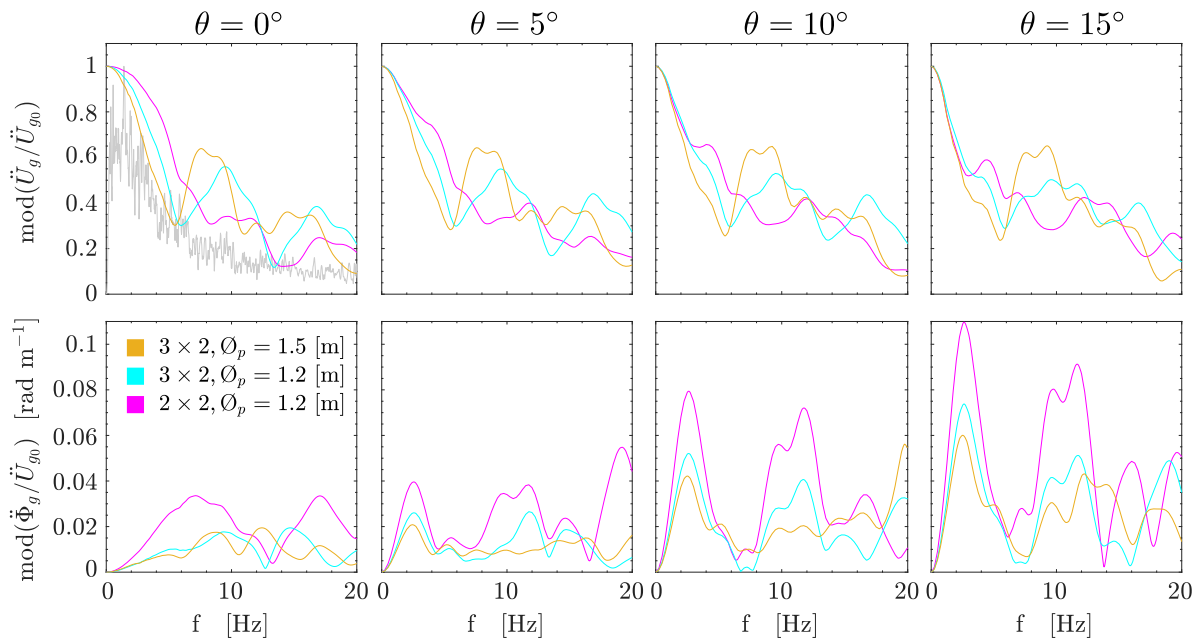


Figure 6.11: Computed kinematic interaction factors of pile foundations (the gray line represents normalized mean Fourier amplitude spectrum of the selected ground motions). Kinematic interaction factors computed through the BEM-FEM.

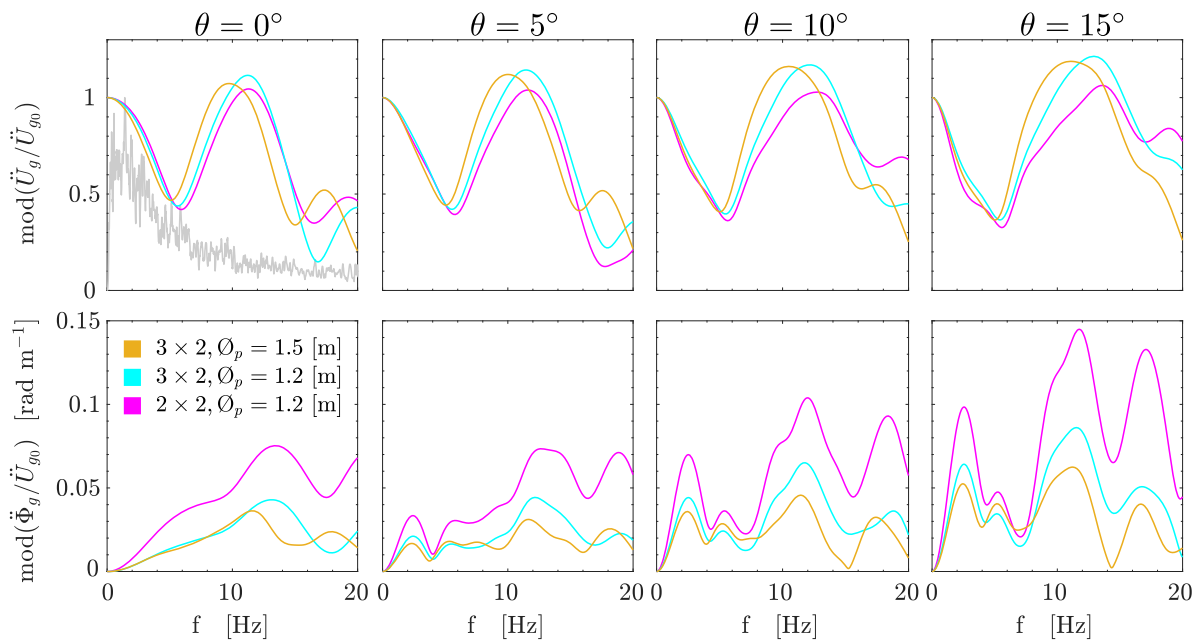


Figure 6.12: Computed kinematic interaction factors of pile foundations (the gray line represents normalized mean Fourier amplitude spectrum of the selected ground motions). Kinematic interaction factors computed through the Winkler model.

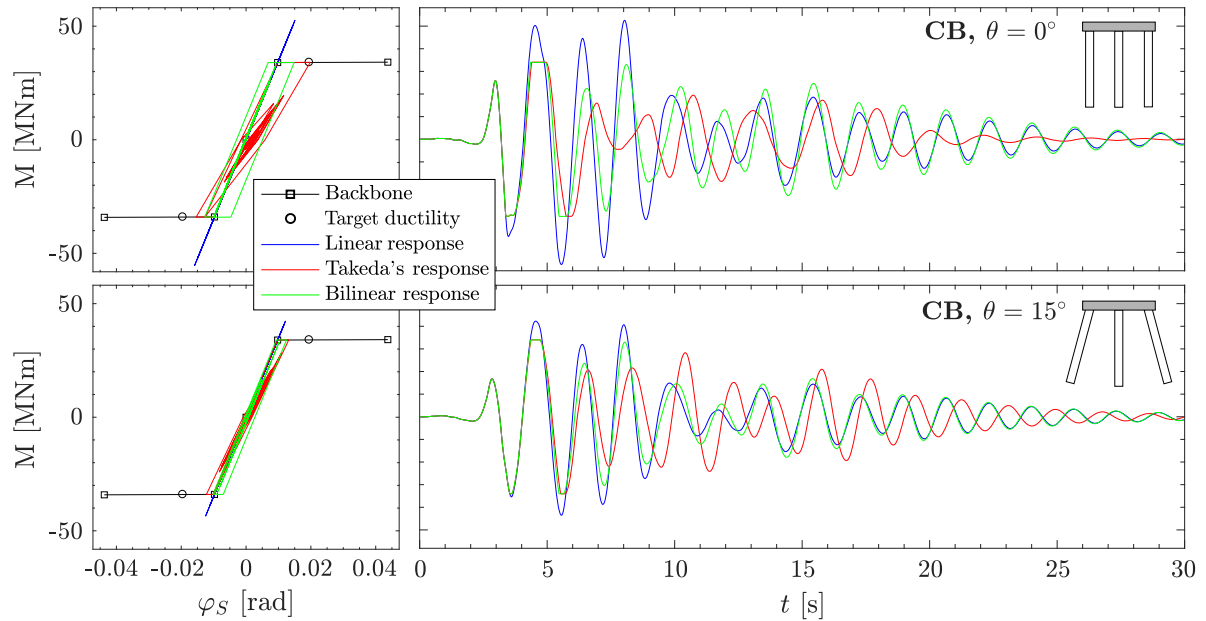


Figure 6.13: Hysteresis cycles and pier bending moment time histories for the H15L50 case (Table 6.5) with input motion E7 (Table 6.2).

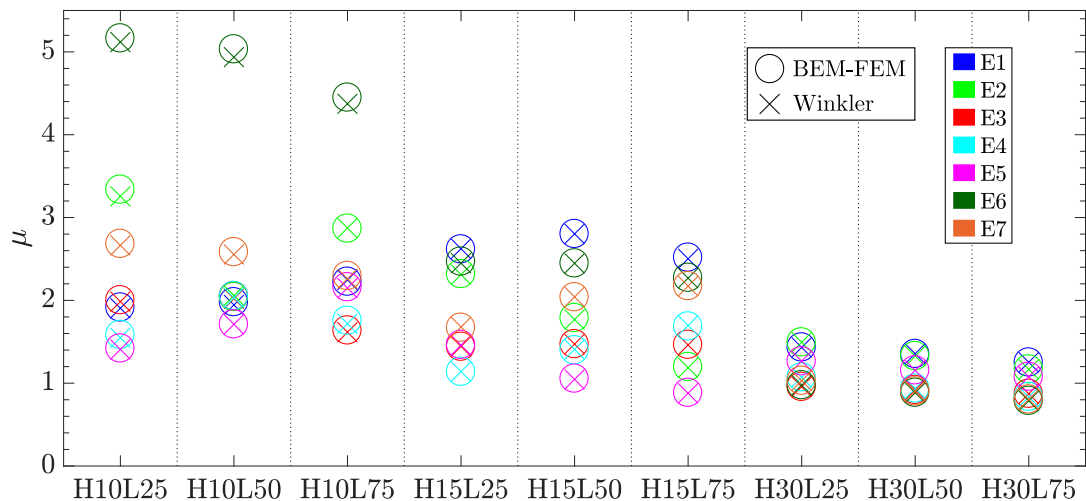


Figure 6.14: Comparison between the ductility demands, computed through the equal displacement rule in the frequency domain, and using the BEM-FEM or the Winkler-type model for obtaining impedances and kinematic interaction factors. Vertical piles cases.

linear system. Figure 6.14 presents the results for the vertical pile foundations; each column corresponds to a different configuration and different colours are used for each earthquake. As for the results scattering between the different seismic inputs, this is due to the different spectral ordinates of signals, in conjunction with the natural period of each superstructure (see Figure 6.2). It can be observed that ductility demands computed from the impedances and kinematic interaction factors obtained from the two models, i.e. BEM-FEM and Winkler-type, coincide for each signal.

At this point, it is important to remember that the nonlinear response of the sys-

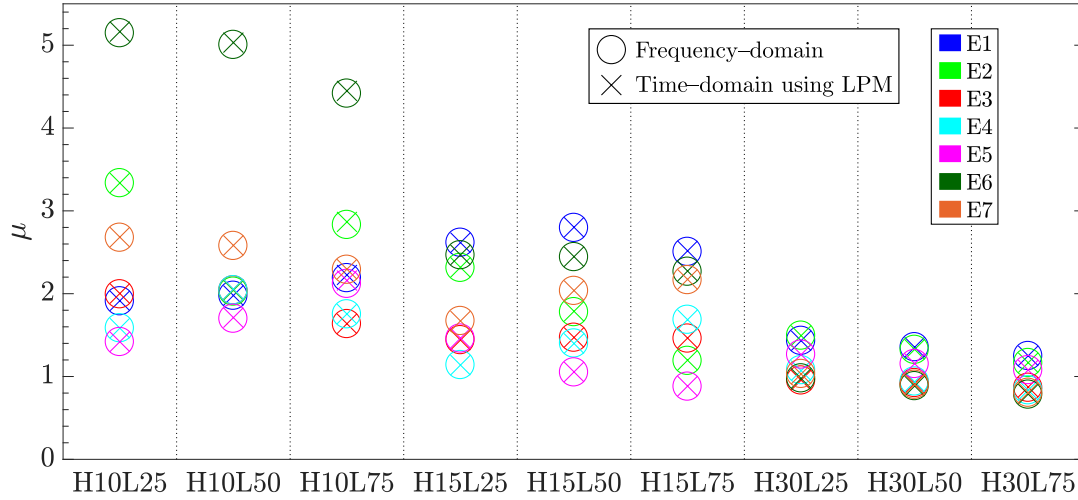


Figure 6.15: Comparison between the ductility demands, computed through the equal displacement rule, obtained in the frequency domain using the original impedance functions, and in the time domain using the LPM approximations. Vertical piles cases.

tem is evaluated through a substructuring approach in which the frequency-dependent impedances of the foundations are incorporated using a simplified LPM. As discussed in Section 4.9, such simplified LPMs are not able to capture all the intricacies of both stiffness and damping functions (see, e.g., Figure 6.9). For instance, resonance peaks due to the soil profile and to pile group effects are not correctly represented by the simplified model, and even static stiffnesses are not always perfectly estimated. In the case of the damping, the evolution of the function below the cut-off frequency is neither correctly captured. These variations could imply the variable of interest in this study (ductility demand) to be incorrectly computed, reason why validation of the proposed approach is needed. To this end, ductility demands for all superstructures and input motions have been computed through the equal displacement rule [74] both in the frequency-domain, using the original impedance functions, and in the time-domain, using the derived LPM, finding that the differences between the two approaches are negligible. Here, simulations in time domain have been carried out through the central difference method in terms of absolute values of displacements, velocities and accelerations instead of incremental values more typical on Newmark’s integration schemes. To simulate in terms of absolute values allows an easier control of the nonlinear behaviour. Figure 6.15 presents the results for the vertical pile foundations; each column corresponds to a different configuration, and different colours are used for each earthquake. It can be observed that ductility demands computed from the two approaches coincide for each signal. The loss in accuracy in terms of the variable of interest, i.e. the ductility demand, is almost negligible in all cases when computing in the time domain by using the adopted LPM.

6.6.4 Ductility demand

The ductility demands computed for all cases included in the study are shown in Figure 6.16. For each particular pier length-deck length configuration, results are presented for both FB and CB assumptions and, in the latter case, for the different piles rake angles, ($\theta = 0^\circ, 5^\circ, 10^\circ$ and 15°). Ductility demands obtained for each single input accelerogram

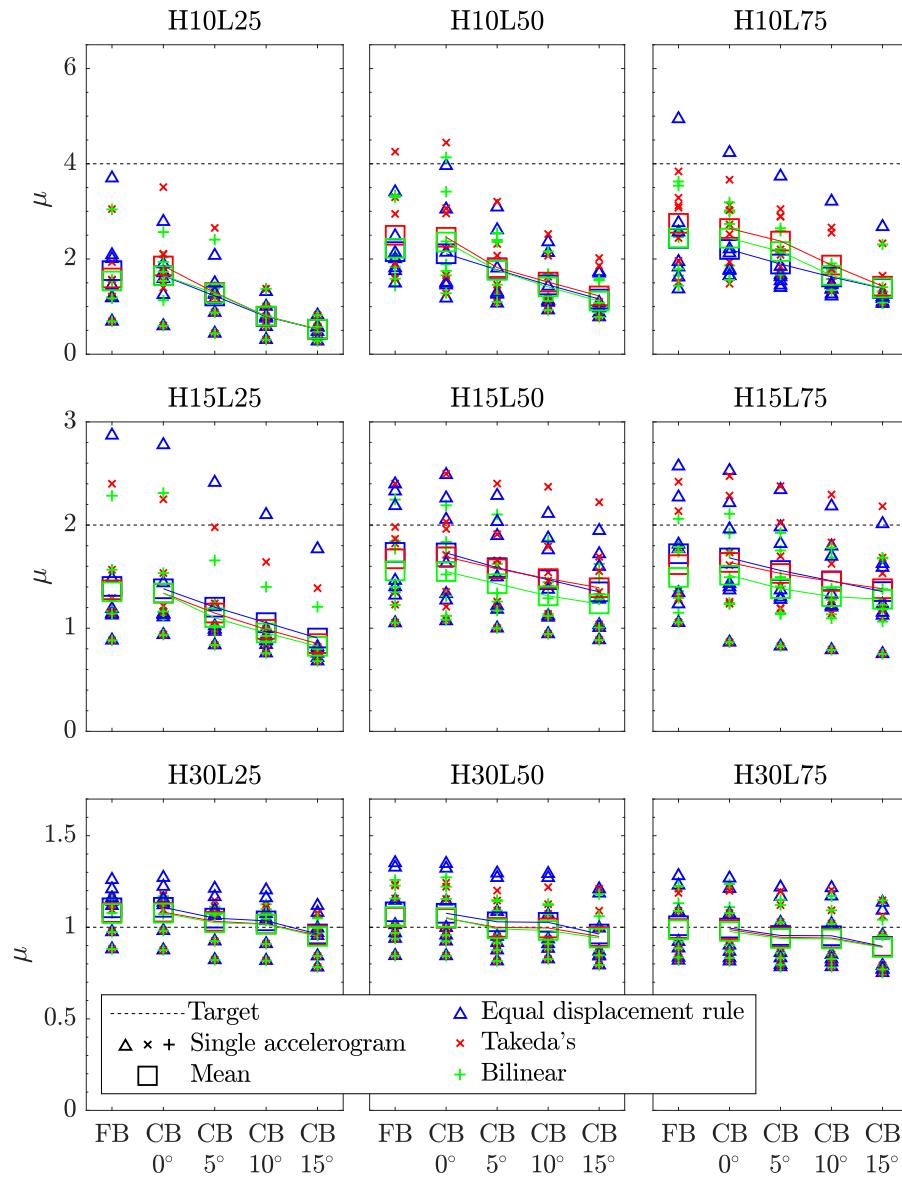


Figure 6.16: Ductility demand of all simulated cases. (a) Piers designed according to [111, 113].

are obtained using the equal displacement rule [74] (blue triangle), Takeda's (red x) or bilinear (green +) hysteretic rules; while the mean value over the seven accelerograms is represented by a square. The scattering obtained between cases is due to the differences between elastic response spectra in the period range between the superstructure fundamental period T_n and the effective period T_{eff} (see Figure 6.2).

It is important to highlight that the ductility demands computed for many of the configurations are significantly smaller than the target ductility (even in FB cases and in configurations with vertical piles) because in most cases the reinforcement content has been overestimated due to standard requirements [113], either because of high stability indexes or because of the required minimum reinforcement ratio, corresponding to 1.0%, as stated in Section 6.4. From an overall point of view, the increase in the number of rebars leads to higher yield strength and hence to a lower ductility demand. If standard requirements are not taken into consideration, and the guidelines of the displacement-

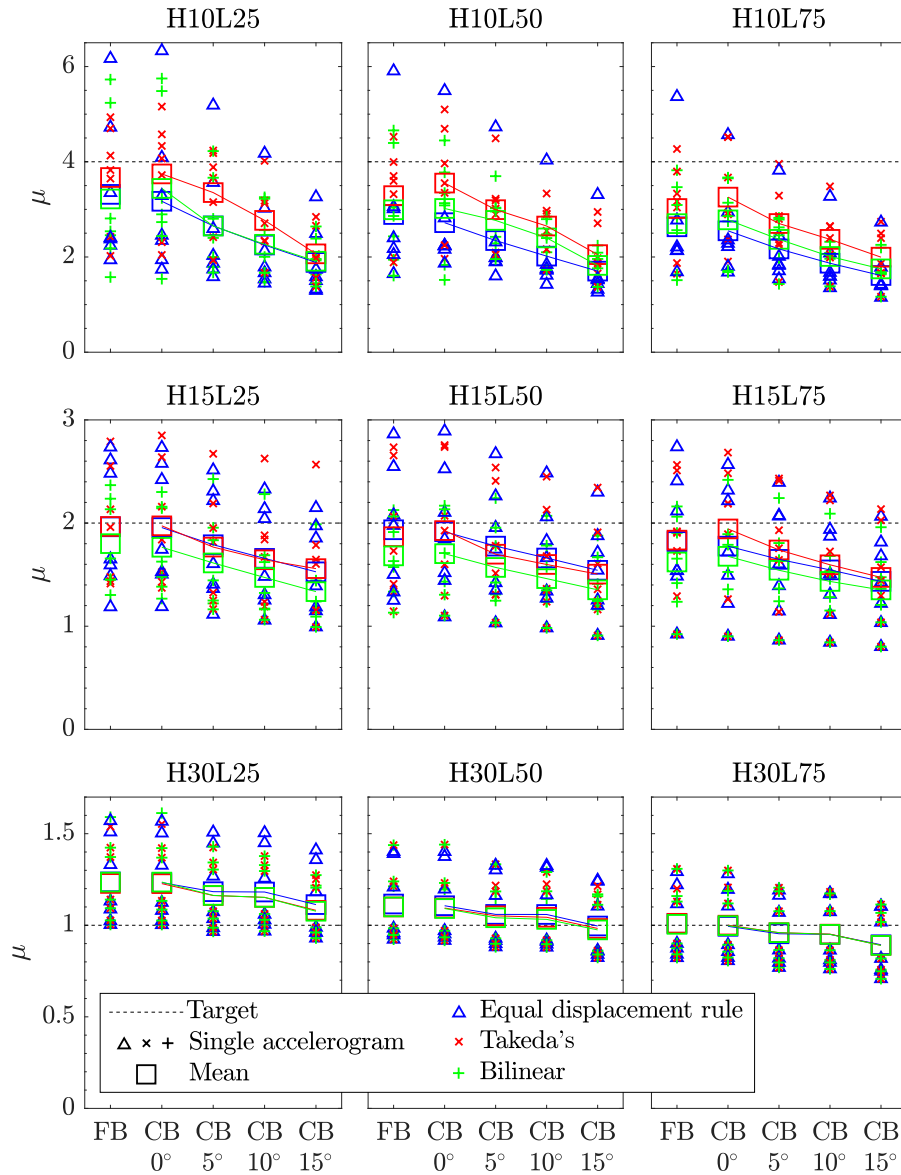


Figure 6.17: Ductility demand of all simulated cases. Piers designed according to [111] relaxing the restraints over minimum content of reinforcement and stability index [113].

based seismic design method are followed, results in terms of mean ductility demand match better with the target ductility (see Figure 6.17).

As expected, the use of Takeda's hysteretic rule leads, in general, to a better agreement with the target ductility demand when compared to the bilinear law assumption. In this sense, it is important to mention that the equivalent damping ratio ξ_{eq} adopted for the piers design within the displacement-based procedure was calibrated for Takeda's type hysteretic model (see Section 4.2). The general tendency in the underestimation of the ductility demand seen in Figures 6.16 and 6.17 when computed with a bilinear law is due to a higher amount of energy absorbed by the hysteresis cycle. Also, it is important to highlight the good estimations obtained following the equal displacement rule through linear analyses.

The higher the rake angle, the smaller is the ductility demand. A drastic reduction is observed for cases with the highest target ductility demand for rake angles of $\theta = 15^\circ$:

for instance, the mean ductility demand decreases from $\mu = 3.8$ to $\mu = 2.0$ (-47%) for the H10L25 case when piers are designed according to displacement-based procedure relaxing the standard restraints (Figure 6.17), and from $\mu = 1.9$ to $\mu = 0.5$ (-74%) when the standard restraints are considered (Figure 6.16). On the other hand, in higher piers with lower ductility demand, the reduction is much smaller, changing from a mean value of $\mu = 1.1$ to a mean value of $\mu = 1.0$ (-9%) in the H30L50 case, for example, when piers are designed according to displacement-based procedure relaxing the standard constraints (Figure 6.17), and from $\mu = 1.0$ to $\mu = 0.9$ (-10%) when the restraints are considered (Figure 6.16). The main cause of the reduction in the ductility demand is the conjunction of lower translational FIM and larger anti-phase induced translations due to rotations (see Figures 6.11 and 6.12) arising from the filtering action of the inclined pile foundations.

These results show that SSI effects can have a very significant influence on the piers ductility demand. However, standards usually recommend to include SSI effects in the analyses only when the soil-foundation flexibility contributes significantly to the total displacement at the top of the pier. For example, Eurocode 8–Part 2 [113] recommends in Section 4.1.4.(2) to include SSI if its contribution in terms of displacement obtained under the action of a unit horizontal load at the deck level is higher than 20%. Table 6.9 presents the percentage contribution due to the pier deflection $((h_d + h_c + h_p)\varphi_S)$, the foundation translation (u_F) and the foundation rotation $((h_d + h_c + h_p + h_f)\varphi_F)$ to the total displacement of the deck under a static force applied at the deck level. It is shown that the contribution of the soil-foundation flexibility is larger than 20% only in the H10L75 case, although the effect of SSI is quite significant in many of the rest of configurations. Furthermore, inclined piles reduce the contribution of the soil-foundation flexibility to the overall deck displacement, with respect to vertical piles, and their use tend to reduce significantly the ductility demand.

6.6.5 Energy

Figure 6.18 shows a typical result obtained from the analyses in terms of the energy time history for the H15L50 case with input motion E7, considering both vertical piles (upper plots) and inclined piles with $\theta = 15^\circ$ (lower plots). The first column presents the energy terms computed assuming a linear-elastic system. The second and third columns, on the other hand, present the energy terms corresponding to the nonlinear models in which the response of the pier plastic hinge is modelled adopting either Takeda's or the bilinear hysteretic rules, respectively. The input energy to the system (E_{in}) is represented by a black continuous line. As stated in Section 4.8.2, at each time step the input energy is balanced by the sum of the recoverable kinetic energy (E_I , blue continuous line), the dissipated energy by damping (E_D , orange continuous line), the recoverable strain energy and, in the nonlinear cases, the dissipated energy by pier yielding (E_K , magenta continuous line). The dissipated energy by damping and the recoverable strain energy are, at the same time, divided into the contributions of the superstructure or the soil-foundation system (dotted and dashed lines respectively). As time goes to infinity, the kinetic and the strain recoverable energies vanish, and all the input energy to the system has been dissipated by viscous damping in the superstructure and soil-foundation systems, and by yielding in the pier plastic hinge.

Important differences in the input energy, depending on whether inclined or vertical pile foundations are considered, can be observed. Furthermore, slight differences in

θ	H10L25				H10L50				H10L75			
	0°	5°	10°	15°	0°	5°	10°	15°	0°	5°	10°	15°
$h_S\varphi_S$	88.9	90.6	91.7	92.2	83.3	85.8	87.3	88.0	77.8	80.8	82.7	83.5
u_F	2.93	2.05	1.32	0.74	4.17	2.92	1.86	1.02	5.28	3.70	2.34	1.25
$h_F\varphi_F$	8.22	7.33	6.98	7.04	12.5	11.3	10.9	11.0	16.9	15.5	15.0	15.2

θ	H15L25				H15L50				H15L75			
	0°	5°	10°	15°	0°	5°	10°	15°	0°	5°	10°	15°
$h_S\varphi_S$	96.3	96.9	97.2	97.4	94.2	95.1	95.6	95.7	92.1	93.2	93.9	94.1
u_F	0.95	0.66	0.41	0.20	1.46	1.01	0.61	0.29	1.92	1.32	0.79	0.36
$h_F\varphi_F$	2.71	2.42	2.35	2.44	4.38	3.94	3.83	3.99	6.03	5.46	5.33	5.57

θ	H30L25				H30L50				H30L75			
	0°	5°	10°	15°	0°	5°	10°	15°	0°	5°	10°	15°
$h_S\varphi_S$	99.1	99.3	99.3	99.3	98.7	98.9	99.0	98.9	98.2	98.5	98.6	98.5
u_F	0.14	0.08	0.03	0.00	0.20	0.12	0.05	-0.01	0.27	0.16	0.06	-0.01
$h_F\varphi_F$	0.73	0.66	0.67	0.72	1.09	0.99	1.00	1.09	1.49	1.35	1.37	1.49

Table 6.9: Degrees of freedom contribution (in percentage) to the total displacement at the deck ($h_S = h_d + h_c + h_p$, $h_F = h_d + h_c + h_p + h_f$), according to Eurocode 8–Part 2 [113].

the input energy can be observed depending on the model adopted (linear, Takeda’s or bilinear). This is due to the fact that the input energy (Equation (4.10)) not only depends on the input accelerations, \ddot{u}_g and $\ddot{\varphi}_g$, and the mass of the system, but also on the velocities time histories, $\dot{\varphi}_S$, \dot{u}_F and $\dot{\varphi}_F$. When yielding occurs, part of the input energy is now dissipated by yielding instead of by viscous damping. At the same time, the higher effective periods imply smaller velocities in the system which, in turn, lead to smaller values of the energy components associated to viscous damping.

Figure 6.19 shows the mean over the seven accelerograms of the different energy terms at the end of the time history analyses in all structural cases relaxing the restraints over minimum content of reinforcement and stability index in the piers [113]. The different terms ($E_{D_{\text{super}}}$ (black), $E_{D_{\text{found}}}$ (dark grey) and $E_{K_{\text{super}}}$ (light grey)) are represented with stacked bar graphs that are grouped for FB or CB models, the latter presented separately for the vertical or inclined piles. Within each group, results are also separated for the Linear (L) models and for the nonlinear models assuming Takeda’s (T) or Bilinear (B) behaviours. The sum of the quantities in each vertical bar equals the mean input energy to the system (E_{in}) at the end of the time history analysis.

Generally, the energy dissipation through the foundation is relatively low (4.6% of the input energy considering all CB systems). The input energy tends to increase with higher span lengths because of the associated higher masses. For increasing pier heights, the input energy is generally lower because of the lower velocities obtained in the system response. When the system behaves nonlinearly, the input energy to the system decreases, in almost all configurations, with respect to the linear-elastic case and, the higher the target ductility demand (short pier cases), the smaller is the energy dissipated by viscous damping in the superstructure, effect that is counteracted by the energy dissipation by pier yielding.

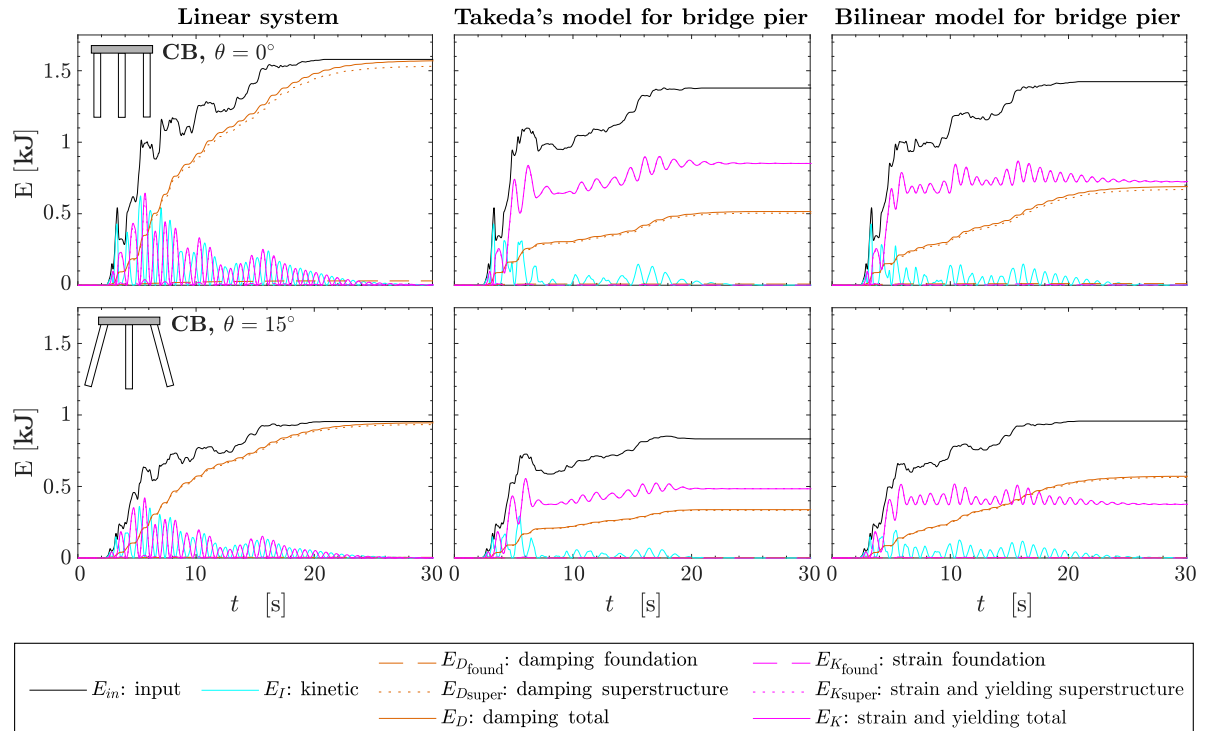


Figure 6.18: Time history of the energy terms for the H15L50 case with input motion E7.

As pile rake angle increases, the system receives less seismic energy. Again, this effect is more noticeable in the systems with highest ductility demand. The decrease in the input energy redounds more to the decrease of the dissipation energy by pier yielding than by viscous damping. The energy dissipated by pier yielding reduces drastically in some cases, as can be observed, for example, in H10L75 case. In this configuration, and considering for instance the model that assumes Takeda's hysteretic rule, the input energy to the system reduces by a significant 47% when inclined piles with $\theta = 15^\circ$ are assumed instead of vertical piles, with reductions of the energies dissipated by yielding or by viscous damping of 53% and 31%, respectively.

6.7 Conclusions

SSI effects on the seismic design and response of bridges founded on piles in soft soils have been investigated focusing on the role of pile inclination. Bridges with expected linear and nonlinear behaviours have been designed according to a displacement-based approach, making use of bridge-deck-pier subsystems representative of the whole structural behaviour and assuming a FB hypothesis. Bridges with different piers heights and span lengths are included in the investigation. The SSI contribution to the seismic structural response has been studied in the spirit of the substructure approach through nonlinear dynamic time history analyses considering a set of suitably selected real accelerograms.

Even in cases of complex soil profiles as the one considered in this study, the adopted low-order LPM is able to represent the frequency-dependent impedance functions of the different soil-foundation systems with enough accuracy when used to compute ductility

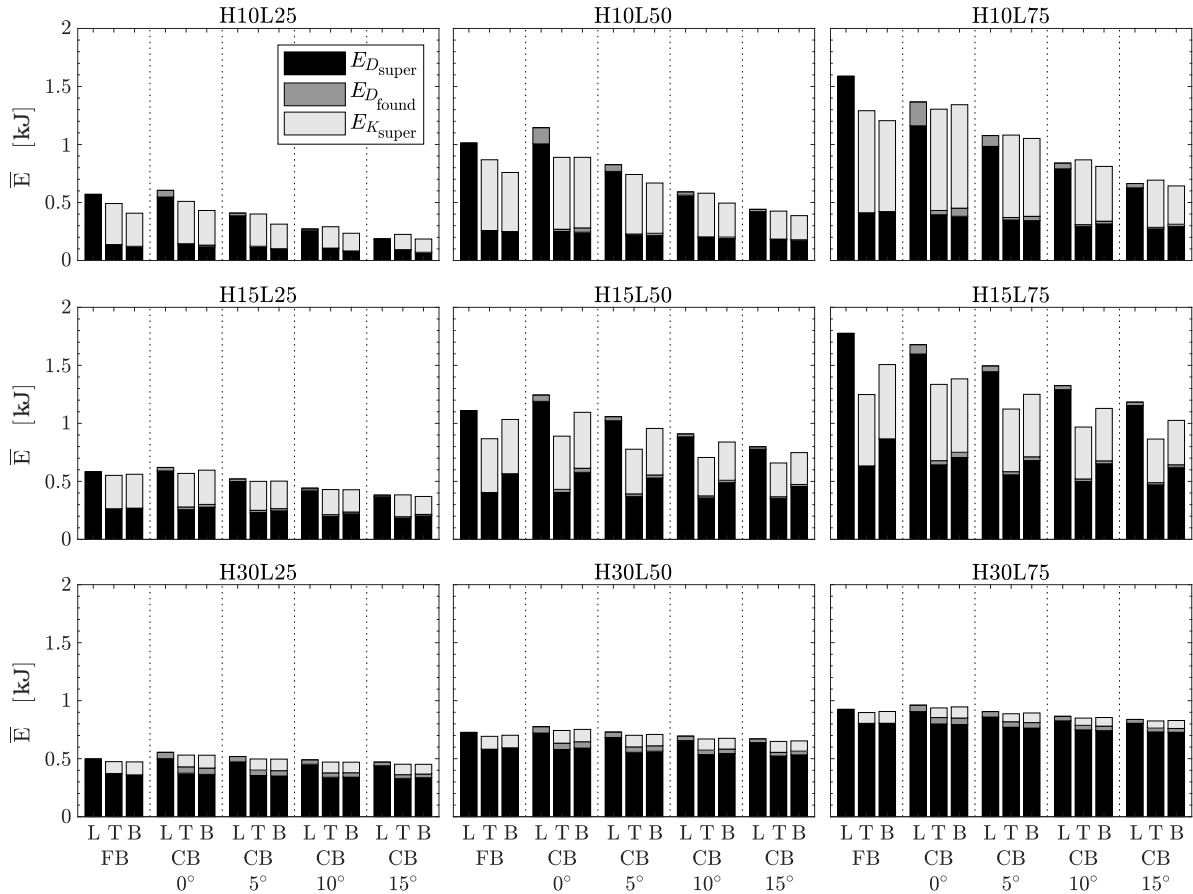


Figure 6.19: Mean over the 7 accelerograms of the energy balances at the end of the time history analyses for all structural cases. L: linear, T: Takeda’s constitutive law, B: bilinear constitutive law.

demands and energy balances, even though such LPM is not able to reproduce all the intricacies of the impedance functions of the configurations considered in the analysis. In this regards, it has also being found that impedance functions and kinematic interaction factors computed through either a Winkler-type model or a coupled BEM-FEM model leads to virtually identical results.

Takeda’s model is used to represent the nonlinear response of the hinge developed at the pier’s base. However, for the cases studied herein, it is shown that a good estimation of the ductility demand can also be obtained through a linear equivalent simulation adopting the equal displacement rule while a good estimation of ductility demand and energy dissipation by yielding can be obtained adopting a simple bilinear hysteresis law.

Strong variations in the inelastic response are obtained depending on the records used in the simulations, as previously observed, for instance, by Elnashai and McClure [88]. This leads to a strong scattering in the results in some cases. In this regard, a set of properly scaled records was proposed.

Disregarding SSI and referring to FB systems, if the seismic detailing prescribed by modern codes (e.g. Eurocode 8 [72,109,113]) is guaranteed, the actual structural response may differ sensibly from the expected one, driven by the design methodology, for all cases in which greater amounts of reinforcements are needed to comply with standards.

Concerning SSI effects, the following main conclusions can be drawn:

- Despite only one particular case fall within conditions defined by Eurocode 8 for which SSI analyses are mandatory, the compliance of soil-foundation systems with inclined piles affect sensibly the bridge response in all cases.
- Foundations with inclined piles promote a less pronounced nonlinear behaviour of the superstructure and the ductility demand of piers reduces by increasing the pile inclination.
- The last can be explained by the peculiarities of the FIM of inclined pile foundations, characterised by rotations inducing anti-phase displacements in the superstructure with respect to the translational component of the motion, which are responsible for reductions in the seismic energy that enters the system and must be dissipated through viscous damping or yielding.
- The application of displacement-based design methodologies to bridges founded on inclined piles in soft soils requires the definition of a suitable strategy to account for the soil-foundation compliance in the design methodology.

Provided that a proper design is performed, accounting for the peculiar resisting mechanisms of inclined pile foundations, the latter appear beneficial for the bridge seismic response since, from an overall point of view, they are responsible for a reduction of the plastic rotation demand of piers hinges.

Chapter 7

General conclusions and future research directions

7.1 Summary and conclusions

This dissertation proposes new ideas for the nonlinear modelling of structures where SSI plays a significant role. The document, being divided into two parts, is a faithful reflection of how the research process has been carried out along these last years.

In the Part I of the document, an equivalent linear model for estimating the dynamic horizontal response of piles considering soil degradation along the soil-pile interface has been presented, implemented and calibrated. The formulation proposed herein incorporates the possibility of modelling an imperfect or damaged soil-pile interface along which bonded contact conditions no longer apply. The proposal has been based on a coupled BEM-FEM approach, uniting the advantages of both methods: the piles are modelled as beam with finite elements; the degraded or imperfect pile-soil interface is represented by distributed springs and dashpots whose properties vary with depth; and the soil beyond the degraded interface is modelled by boundary elements.

The proposed coupled BEM-FEM formulation is not only computationally more efficient, but it is also more versatile, and requires much less work in mesh generation if compared with other models available in the literature. This will now allow to study more complex problems. The efficiency of the model will also allow to perform parametric analyses or be incorporated in processes that require a large number of evaluations, such as in many optimization techniques.

Part II studies the seismic response of bridge piers founded on pile groups. For the nonlinear modelling of the piers, it is necessary to simulate the response of the system in the time domain. The soil-foundation system usually has a strong frequency-dependent character, changing its behaviour depending on the oscillation frequency of the bridge. This hinders the dynamic analysis in the time domain. Among the different alternatives existent in the literature for the dynamic analysis in time domain with frequency-dependent reaction forces, two possible methodologies are commonly used, the convolution integration of the frequency-dependent reaction forces, or the use of equivalent discrete physical models, also known as LPM [130]. There also exist hybrid time domain – frequency domain methodologies. Here, two LPM alternatives have been studied and implemented. By adopting a substructuring scheme, the soil-foundation system is substituted by a frequency-independent combination of masses, springs and dashpots that reproduce its complex behaviour. This way, when an earthquake occurs,

the degradation on the bridge piers can be evaluated depending on the foundation design.

Both implemented LPMs have shown to have its own advantages and disadvantages. The implementation of the one labelled as “*consistent*” is more complicated than the other labelled as “*simplified*”, but the consistent is able to fit more intricate patterns of the impedance functions of the foundation. On the other hand, if only the fitting of a short frequency range is needed, as in the study case tackled here, this simplified LPM is a sufficiently accurate option. Furthermore, through the parametric analyses carried out, it has been shown that there are other modelling assumptions that have a higher influence in the system response. For example, the traditionally assumed non-causal, and hence non-realistic, hysteretic damping model for the material damping of the soil media leads to an overestimation of the foundation resistant forces if compared with the causal Biot’s damping model. Differences in the response due to assumed damping models have been shown to be higher than differences due to the LPM used. However, it is worth noting that, in the present dissertation, superstructures are modelled as one degree-of-freedom systems, and are characterized by their fundamental frequency. For other types of superstructures, better characterized as multi degree-of-freedom systems, the more elaborate consistent LPM would possibly be needed in order to represent correctly the contribution of all vibration modes, so the simplest approaches would probably not be suitable.

On the other hand, and also in the Part II of the dissertation, the SSI effects on the seismic design, response and damage of bridges founded on piles in soft soils have been investigated focusing on the role of pile inclination. The nonlinear Takeda’s and bilinear models have been used to represent the hinge developed at the pier’s base. Through the substructuring scheme, the adopted low-order simplified LPM is shown to be able to represent the frequency-dependent impedance functions of the different soil-foundation systems with enough accuracy when used to compute ductility demands and energy balances, even though such LPM is not able to reproduce all the intricacies of the impedance functions of the configurations considered in the analysis. In this regards, it has also been found that impedance functions and kinematic interaction factors computed through either a Winkler-type model or a coupled BEM-FEM model leads to virtually identical results. Also, for the cases studied herein, it is shown that a good estimation of piers ductility demands can be obtained through a linear equivalent simulation adopting the equal displacement rule while a good estimation of ductility demand and energy dissipation by yielding can be obtained adopting a simple bilinear hysteresis law.

Finally, regarding the influence of pile inclination on the seismic response of the bridges, the compliance of soil-foundation systems with inclined piles reveals to affect sensibly the bridge response in all cases. This is so even when only one of the studied cases falls within conditions defined by Eurocode 8 for which SSI analyses are mandatory. Therefore, the application of displacement-based design methodologies to bridges founded on inclined piles in soft soils requires the definition of a suitable strategy to account for the soil-foundation compliance in the design methodology.

7.2 Future research directions

Regarding the equivalent linear model presented in Part I for estimating the dynamic horizontal response of piles considering soil degradation along the soil-pile interface, some issues have to be developed yet. Once the formulation has been verified for the

lateral analysis of a single pile case, it can now be extended to model pile groups, as the boundary element approach used to model the soil allows to take rigorously into account pile-soil-pile interaction effects. It can also be calibrated for the longitudinal analyses and generalized to raked piles. The model can be used to obtain results for substructuring analyses, or can incorporate the superstructure or other elements for direct analyses of complete soil-foundation-superstructure systems. At the same time, the definition of the properties of distributed stiffness and damping along the interface could also incorporate more complex models of soil degradation depending for instance on shear strain levels, such as those cited in the literature review (Section 1.3.1).

Thanks to the soil degradation curves (see for instance Figure 2.1), a soil shear modulus in the degraded domain can be stated depending on the induced soil shear strain levels. In this sense, it would be necessary to adopt an iterative procedure introducing on each iteration the shear moduli that agrees with the strain levels at each depth obtained in the previous iteration. When no variation is obtained in the soil shear modulus, the iterative procedure concludes. At the end, the resistant forces of the foundation are obtained consistently with the induced load levels. It would be needed to analyse the proper methodological tools for this particular case.

The model has been verified by comparison against numerical results obtained from a more rigorous model, but due to time constraints, it has not been yet validated against empirical results for specific cases of interest. For the same reason, the comparison of results obtained with the model against other nonlinear models for the computation of soil-pile foundations systems accounting for soil and interface nonlinearities has not been yet carried out. There exist relevant experimental results that could be of interest, including full scale and centrifuge experiments. In the following, as a proposal for the future research directions, an overview of some of those experimental test results is presented.

Experimental tests presented by Goit and Saitoh [14,34], and by Goit et al. [32,33,35], are a priori, the more tempting ones because they show the results in terms of impedance functions and kinematic interaction factors of piles and group of piles. Through the experimental analyses presented in [14], a nonlinear behaviour is shown in the impedance functions of inclined single piles. Different values of the resistant forces are obtained when loading or unloading due to the different path evolution of contact gaps when the piles are inclined. In [33], the effects of soil nonlinearity on the active lengths of piles is studied. They analyse the displacement field of the soil surrounding the piles for different load levels, and how the active length of piles varies. Similarly to [14] for the single pile experiments, in [34] the analysis of nonlinearities in fixed-head inclined pile groups is shown. The resonant peaks of the impedance functions increase as the excitation load amplitude increases, denoting a strong nonlinear behaviour. In [35], the experimental tests show that not only a degraded soil domain surrounding each pile exist, but also a wider degraded soil domain enclosing all the pile groups would appear when the piles are so close between them, or the excitation load is so high.

Centrifuge tests, on the other hand, are extremely valuable in geotechnics due to the possibility of obtaining in the scaled model states of stress equivalent to those developed in the full-scale case. This aspect is very important when nonlinearities in the problem might be relevant, as it is the case of pile foundations subjected to large seismic excitations that could generate nonlinear responses of the soil or along the pile-soil interface. For this reason, comparison against centrifuge results of the seismic response of pile foundations would be of great interest in order to understand the validity of the

proposed assumptions, calibrate the model, set ranges of applicability or propose modifications to the model. Some papers of interest in this regard are those of Li et al. [37] and Hussien et al. [38]. Li et al. [37] use a shaking table inside a centrifuge machine for the analysis of vertical and batter pile foundations under earthquake excitations. On the other hand, Hussien et al. [38] perform kinematic and inertial interaction analysis of soil-pile-structure systems by using a strong container, i.e. with rigid lateral boundaries. The reproduction of those cases using the model proposed herein is expected to be very useful for further development and calibration of the model, even though the task is not straightforward due to the complexity of the set-ups and the input signals employed by the authors.

There also exist the alternative of reproducing full-scale experiment results. For example, El-Marsafawi et al. [146] obtained, through field experiments, the vertical harmonic response of two pile groups varying the excitation amplitude. Then, those results were compared against the linear ones published by Kaynia and Kausel [147], and also to the simulated with the DINA3 computer program of Novak et al. [148] which includes the cylindrical annular degraded zone formulation firstly proposed by Novak and Sheta [53]. Future research would compare again the experimental results but with the new tool presented herein. Some concerns arise about the experimental tests because, in many cases, the experimental results for the lower level of excitation magnitude don't agree with the widely adopted linear model of Kaynia and Kausel. More recently, Banna and Bayda analysed the vertical vibration response of single piles [29, 149], and later, Biswas et al. [31] their horizontal-rocking coupled response. The obtained experimental results for the different excitations levels are presented observing a clear nonlinear behaviour. A comparison against FEM analyses is carried out in their study where some discrepancies can be seen in some cases. Also, the equivalent linear annular degraded zone model of Novak and Sheta [53] is used in some of these studies [29, 31]. It includes a cylindrical soil boundary zone around the pile with lesser soil shear modulus and higher soil damping in comparison with the outer soil zone.

Finally, the study of the bending moments and shear strain variations along the piles as the soil degrades is another field to be explored with the model proposed herein. Also variations in the seismic envelopes due to the soil interface degradation would be analysed with the proposed model.

For the analysis of the seismic response of bridge piers tackled in Part II, the two typologies of LPM implemented have allowed the analyses of piers damage incorporating the effects of SSI. Those implemented LPM can be used to study the dynamic response, in time domain, of other types of structures. They are intended to be incorporated in dedicated software widely extended in the technical and scientific community.

On the other hand, some simplifying hypotheses have been assumed for the linear and nonlinear analyses of viaducts. First, an intermediate single pier has been assumed to be representative of the dynamic behaviour of an entire viaduct. This consideration is only valid for some situations where all piers have the same height. Second, the consideration of only a transversal seismic excitation might be a strong limitation. And third, three degrees of freedom have been assumed to be enough for the superstructure modelling. Complete models of all the viaduct will show contribution of higher modes than the fundamental one. Other pier typologies can be introduced to the model, where the plastic hinges not necessarily evolve at the pier base, and the assumption of a lumped spring and damper at the pier base would not be valid. If this is the case, more complex models would be necessary for taking into account the behaviour of the pier.

Now, all the knowledge collected thanks to the analysed case can be used for the study of complete bridge structures. Different damage mechanisms would appear when considering other bridge typologies and also considering all the system in the simulations, and the conclusions derived from this research would not be valid in that cases.

The study of the CB system of the bridge piers has focused on the superstructure response and on the damage produced on bridge piers depending on the design considerations in the soil-foundation, as for example the different pile group layouts considered and the piles inclination. Some of the design considerations that have shown to be beneficial for the superstructure, could be detrimental for the soil-pile system. The stress supported by the piles, for example in terms of bending moments and shear forces, and the loads transmitted to the soil domain, should be explored in the future in order to understand the possible consequences that the use of inclined piles might have on the foundation system.

In Part I of this research, a model that considers soil degradation in the interface between piles and soil has been developed; and in Part II, the pier damage evaluation of viaducts taking into account SSI has been carried out. Finally, the effects of soil degradation on the nonlinear response of bridge piers can be evaluated using the model developed in Part I and the substructuring scheme proposed in Part II. For sure many issues will appear, so novel strategies will be needed to overcome the different limitations. For instance, as the impedance functions of the pile foundation systems depend on the induced load levels, further developments on the LPMs are needed for including the load level as a parameter.

Appendix A

Kinematic interaction factors, and computed and fitted impedance functions of the soil-foundations systems used in Chapter 5

In this appendix, the kinematic interaction factors, the impedance functions and the resulting fittings of the impedance functions, either through the simplified LPM or the consistent LPM with $N = 2$, related to all the soil-foundations systems used in Chapter 5 are presented. Such soil-foundation system configurations resulted from the combination of two different ground types, D and C, with $c_s = 117.1$ m/s and $c_s = 253.5$ m/s, respectively, and six different layouts of piles that constitute the foundation: 2×2 and 3×3 vertical piles groups with diameter $d = 1.0$ m, pile length $L = 20.0$ m, and three different pile-to-pile spacings s (3, 5 and 7 m). Inclined piles were also considered in the analyses of the 2×2 foundations, with rake angles θ of 5° and 10° . The rest of parameters needed for the computation of the soil-pile foundation impedances and kinematic interaction factors are shown in Chapter 5.

In the fitting procedure of the impedance functions, the weight functions shown in Equations (5.3a) and (5.3b) have been used for the consistent and simplified LPM cases, respectively.

A.1 Kinematic interaction factors

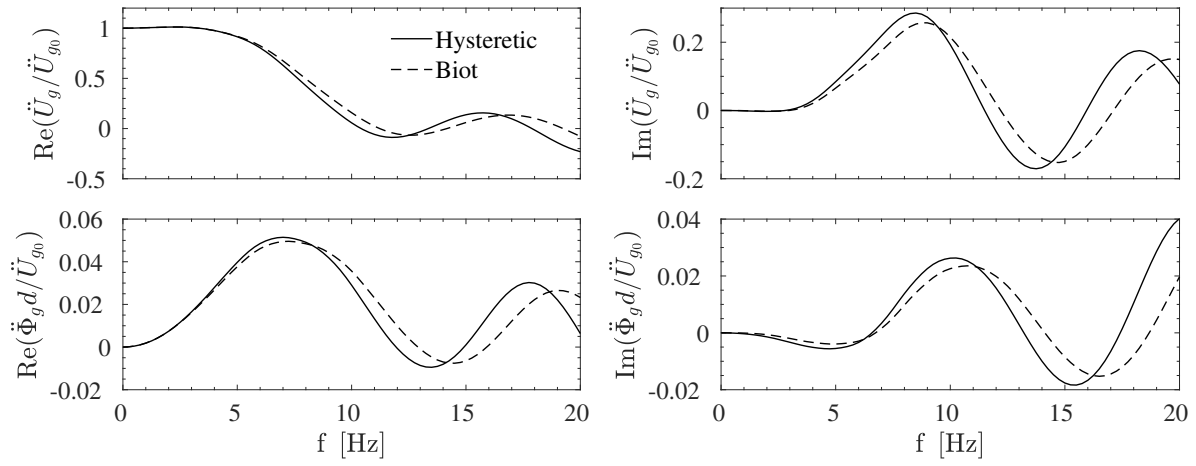


Figure A.1: Kinematic interaction factors of the vertical 2×2 , $s = 3$ m foundation layout in ground type D.

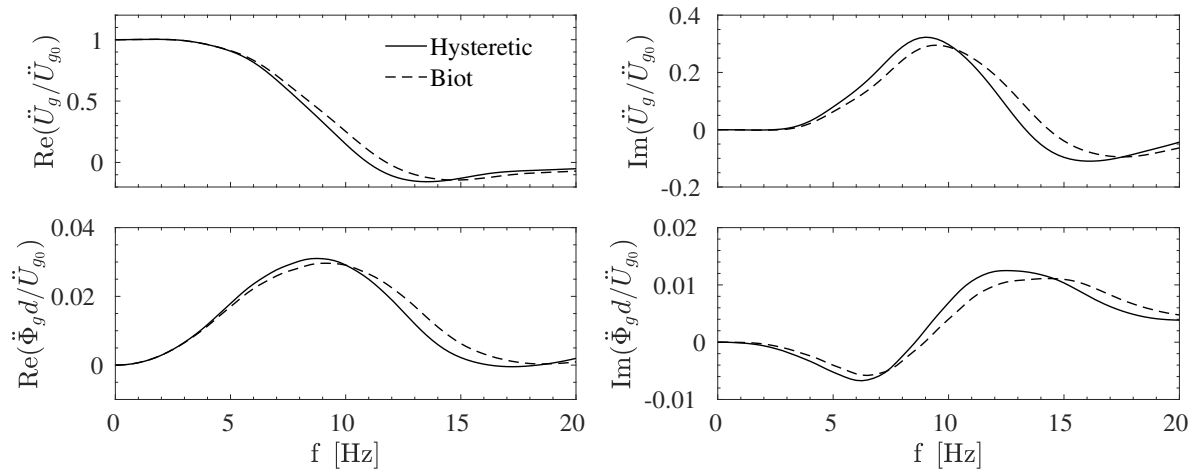


Figure A.2: Kinematic interaction factors of the vertical 2×2 , $s = 5$ m foundation layout in ground type D.

Appendix A. Kinematic interaction factors, and computed and fitted impedance functions of the soil-foundation systems used in Chapter 5

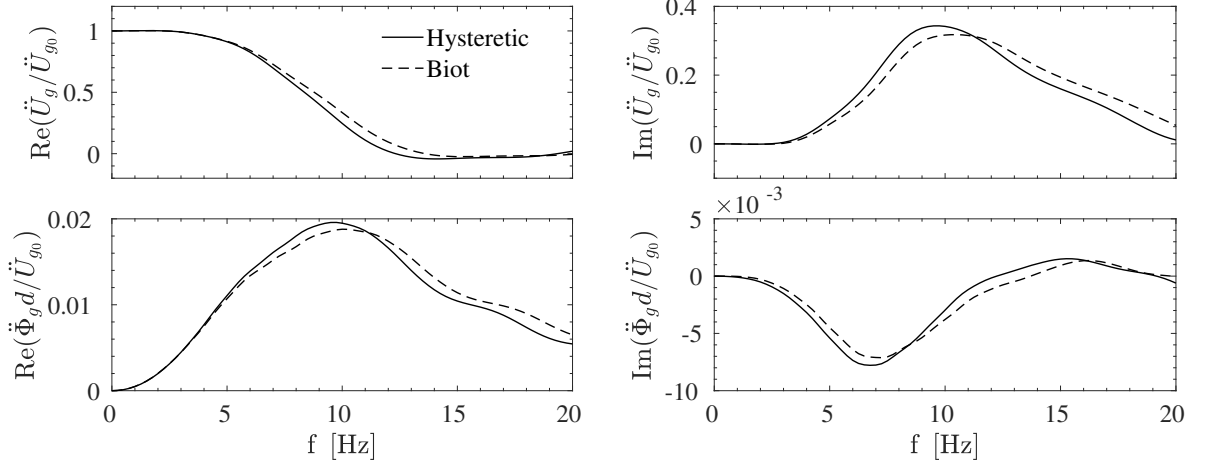


Figure A.3: Kinematic interaction factors of the vertical 2×2 , $s = 7$ m foundation layout in ground type D.

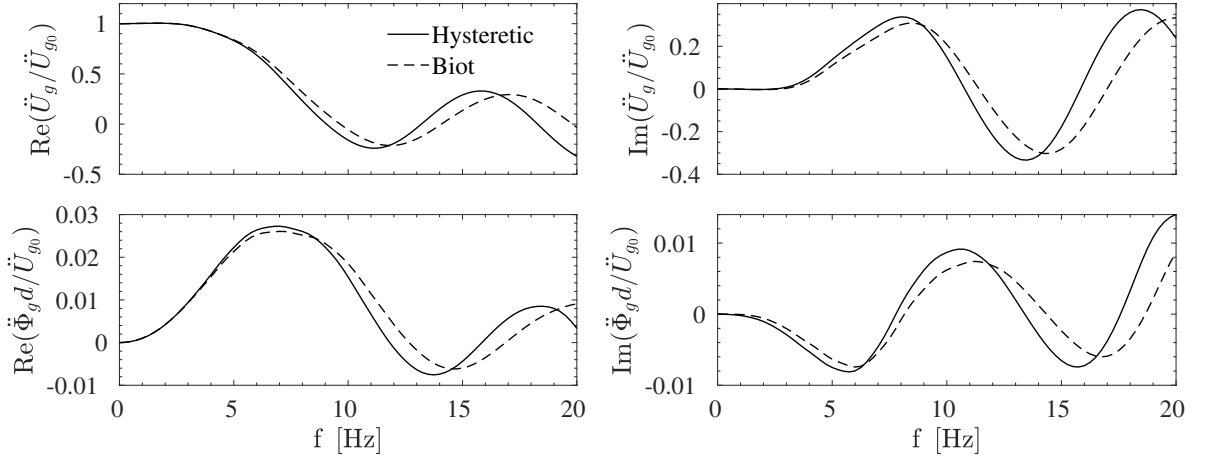


Figure A.4: Kinematic interaction factors of the vertical 3×3 , $s = 3$ m foundation layout in ground type D.

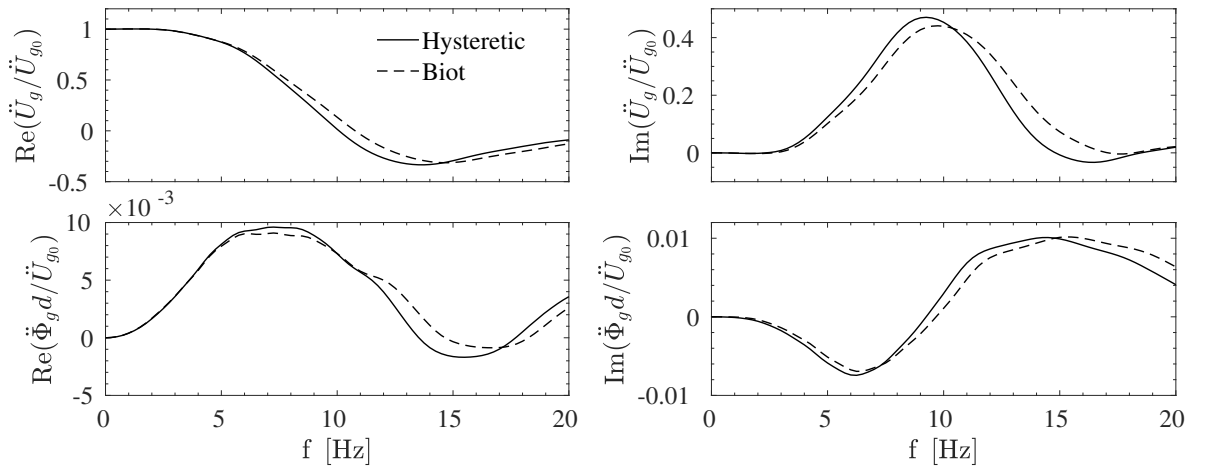


Figure A.5: Kinematic interaction factors of the vertical 3×3 , $s = 5$ m foundation layout in ground type D.

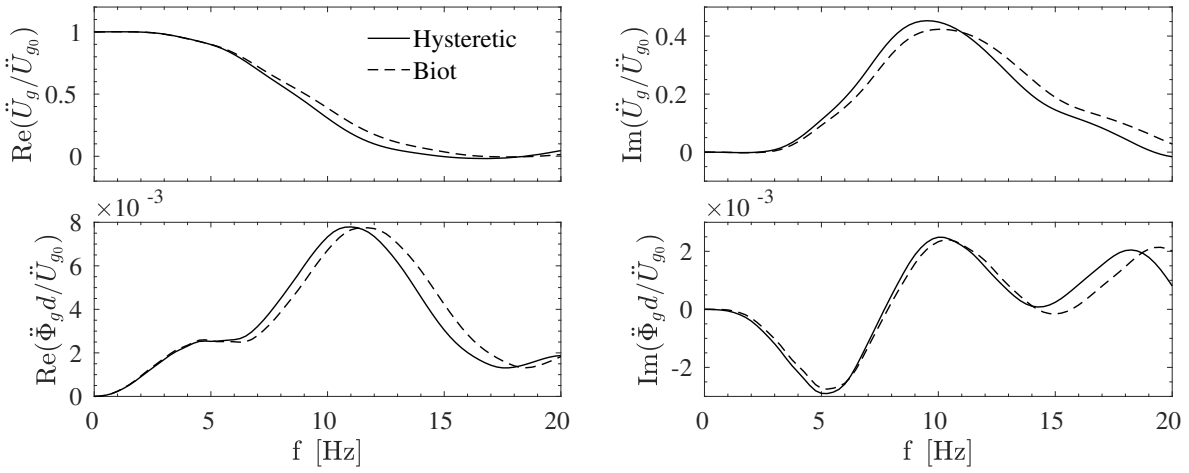


Figure A.6: Kinematic interaction factors of the vertical 3×3 , $s = 7$ m foundation layout in ground type D.

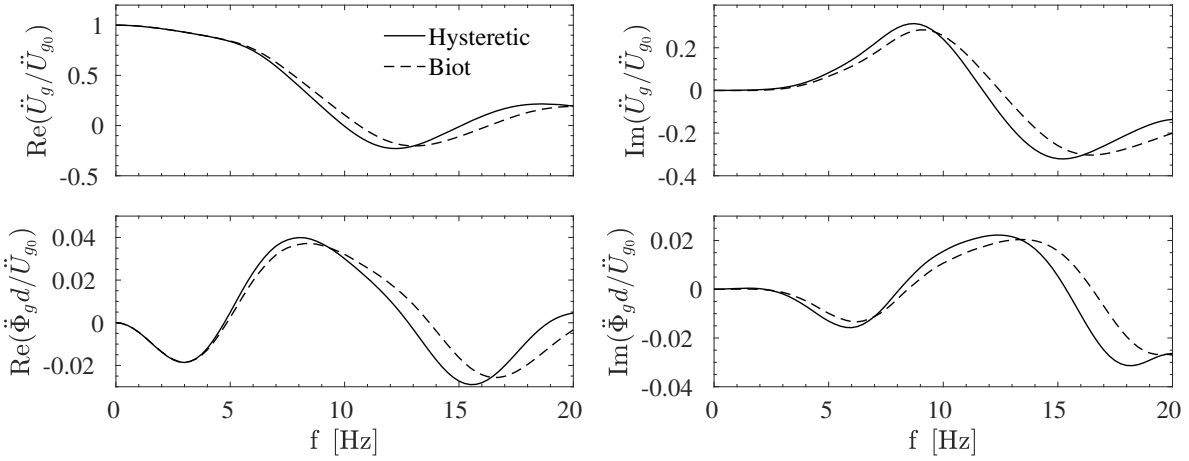


Figure A.7: Kinematic interaction factors of the $\theta = 5^\circ$ inclined 2×2 , $s = 3$ m foundation layout in ground type D.

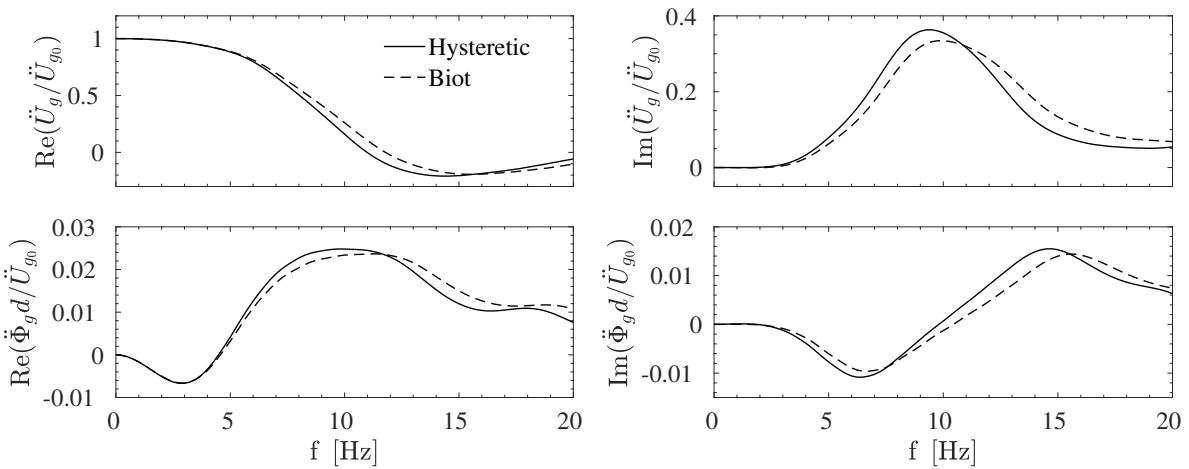


Figure A.8: Kinematic interaction factors of the $\theta = 5^\circ$ inclined 2×2 , $s = 5$ m foundation layout in ground type D.

Appendix A. Kinematic interaction factors, and computed and fitted impedance functions of the soil-foundation systems used in Chapter 5

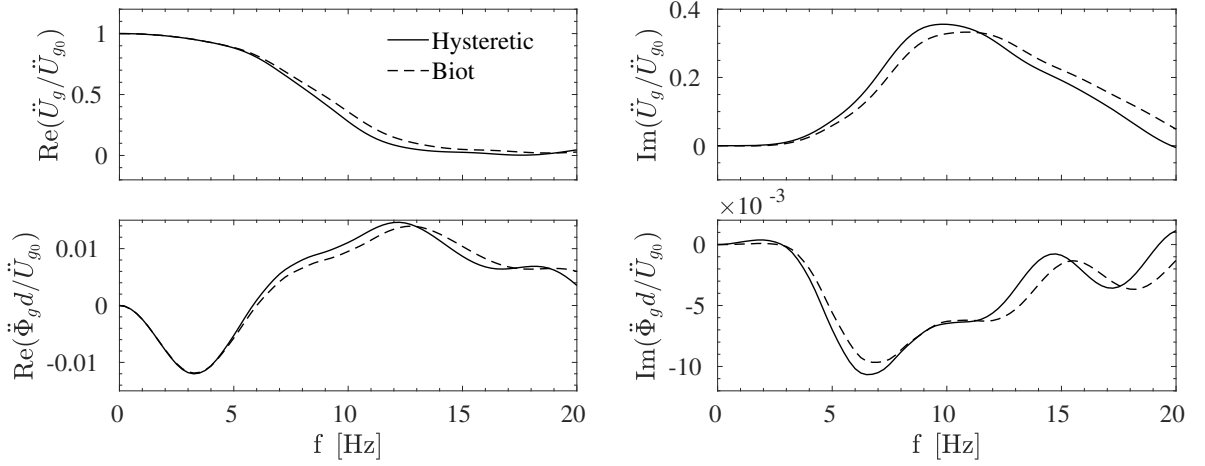


Figure A.9: Kinematic interaction factors of the $\theta = 5^\circ$ inclined 2×2 , $s = 7$ m foundation layout in ground type D.

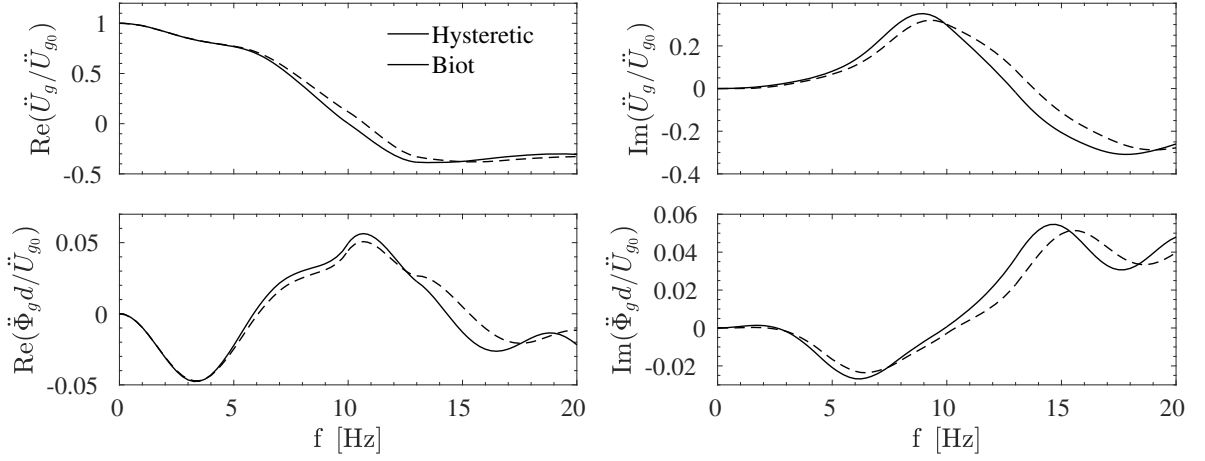


Figure A.10: Kinematic interaction factors of the $\theta = 10^\circ$ inclined 2×2 , $s = 3$ m foundation layout in ground type D.

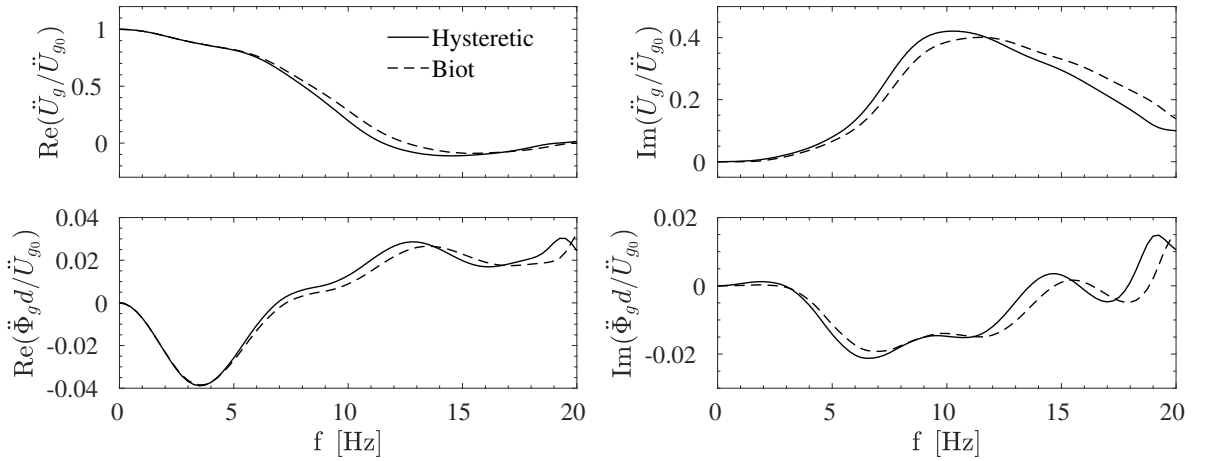


Figure A.11: Kinematic interaction factors of the $\theta = 10^\circ$ inclined 2×2 , $s = 5$ m foundation layout in ground type D.

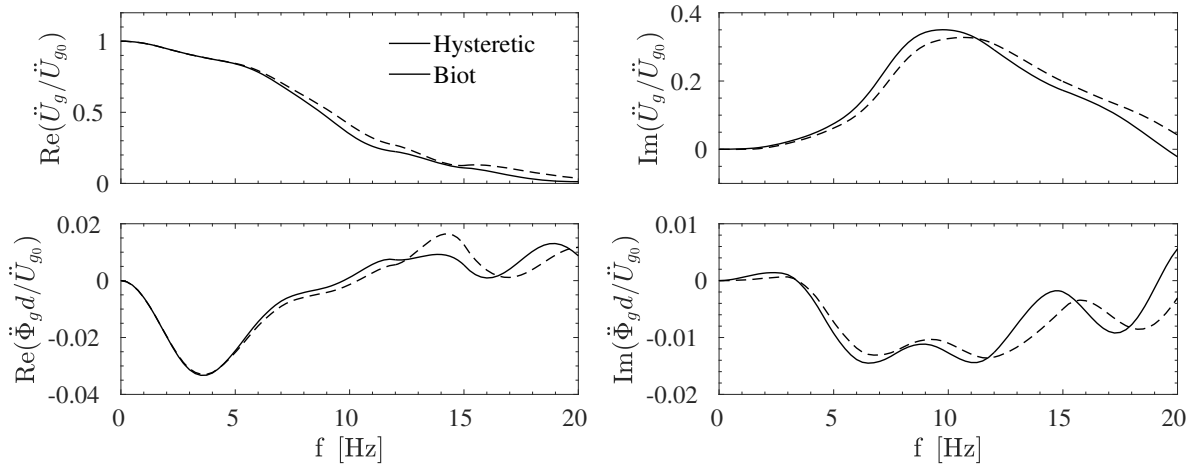


Figure A.12: Kinematic interaction factors of the $\theta = 10^\circ$ inclined 2×2 , $s = 7$ m foundation layout in ground type D.

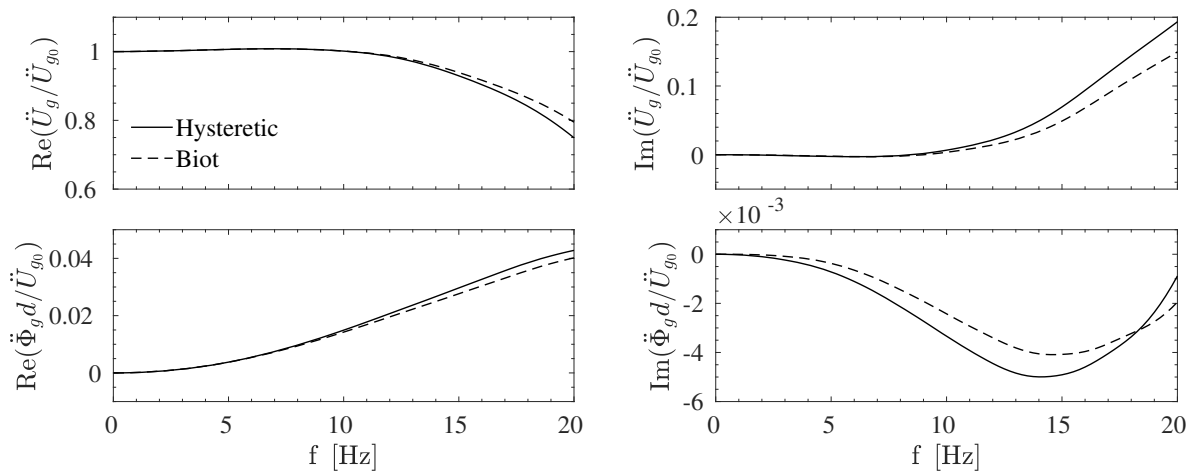


Figure A.13: Kinematic interaction factors of the vertical 2×2 , $s = 3$ m foundation layout in ground type C.

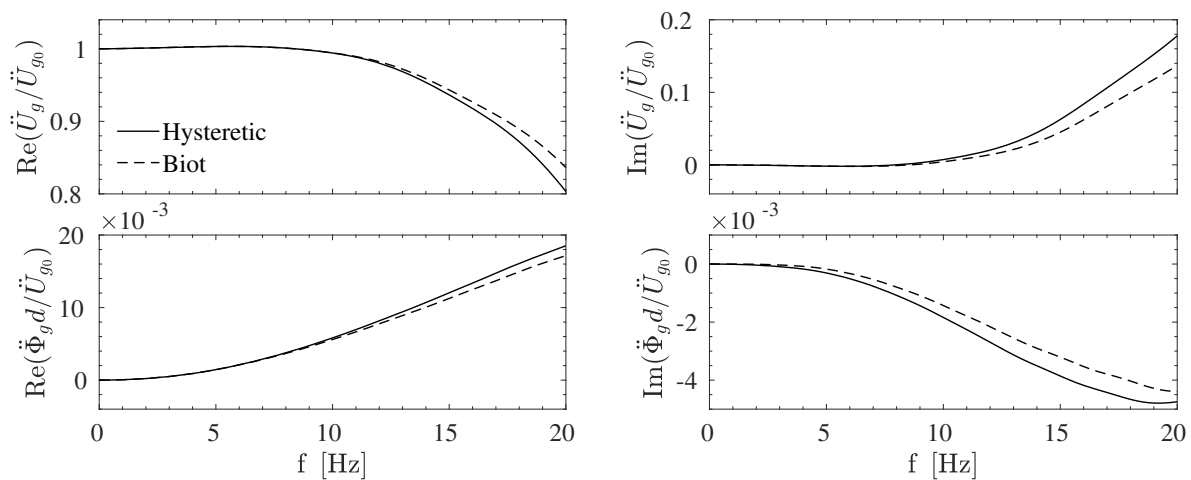


Figure A.14: Kinematic interaction factors of the vertical 2×2 , $s = 5$ m foundation layout in ground type C.

Appendix A. Kinematic interaction factors, and computed and fitted impedance functions of the soil-foundation systems used in Chapter 5

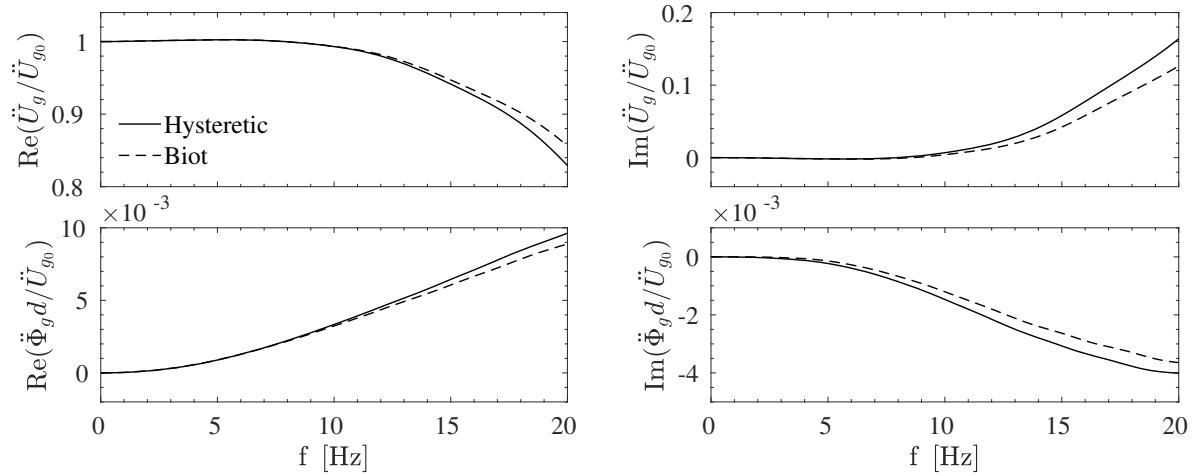


Figure A.15: Kinematic interaction factors of the vertical 2×2 , $s = 7$ m foundation layout in ground type C.

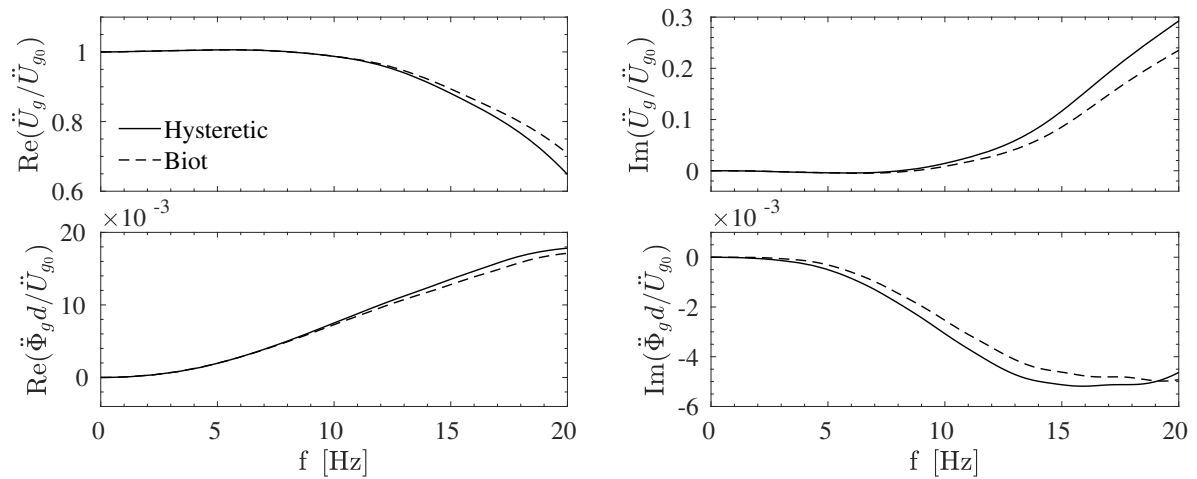


Figure A.16: Kinematic interaction factors of the vertical 3×3 , $s = 3$ m foundation layout in ground type C.

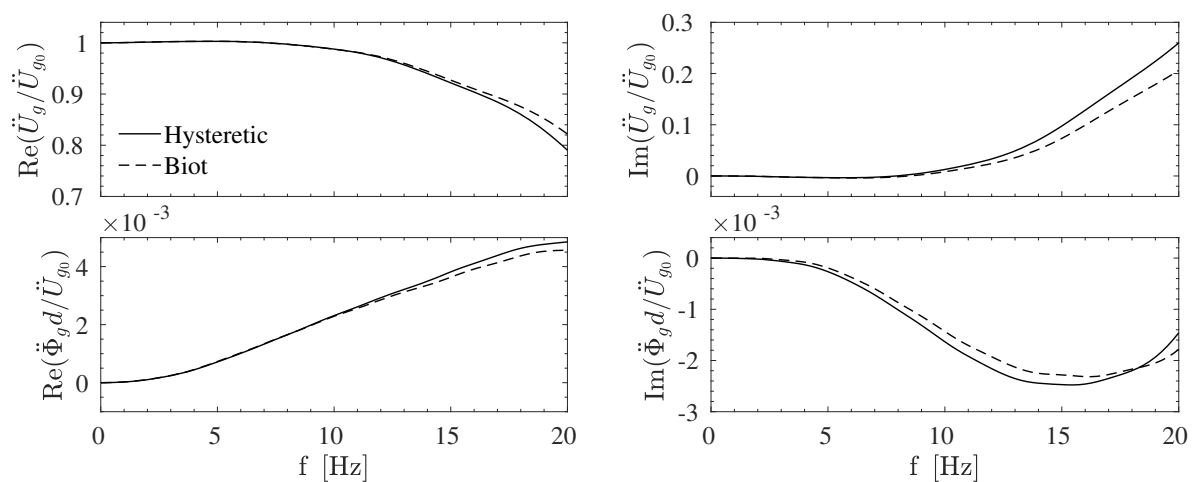


Figure A.17: Kinematic interaction factors of the vertical 3×3 , $s = 5$ m foundation layout in ground type C.

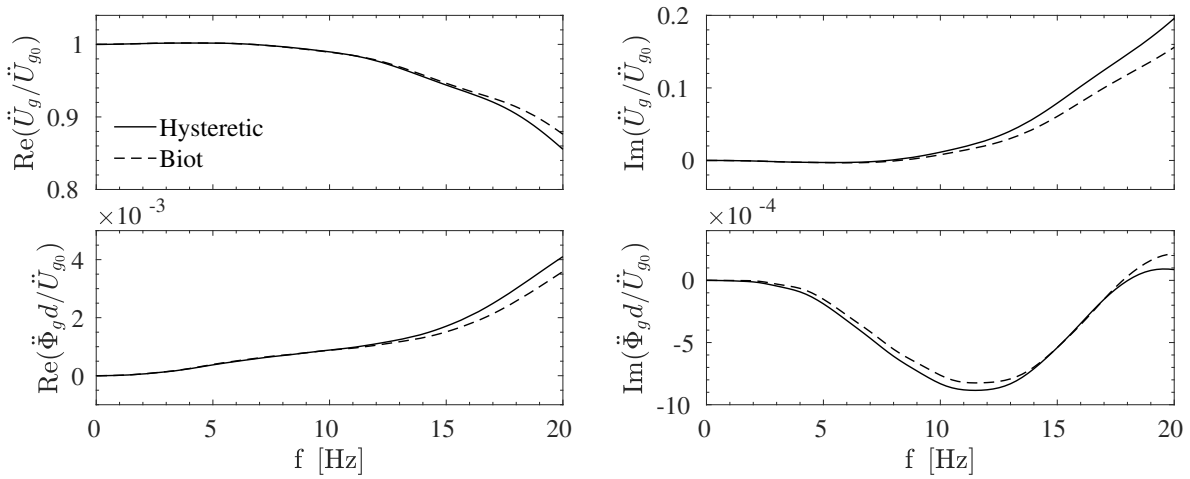


Figure A.18: Kinematic interaction factors of the vertical 3×3 , $s = 7$ m foundation layout in ground type C.

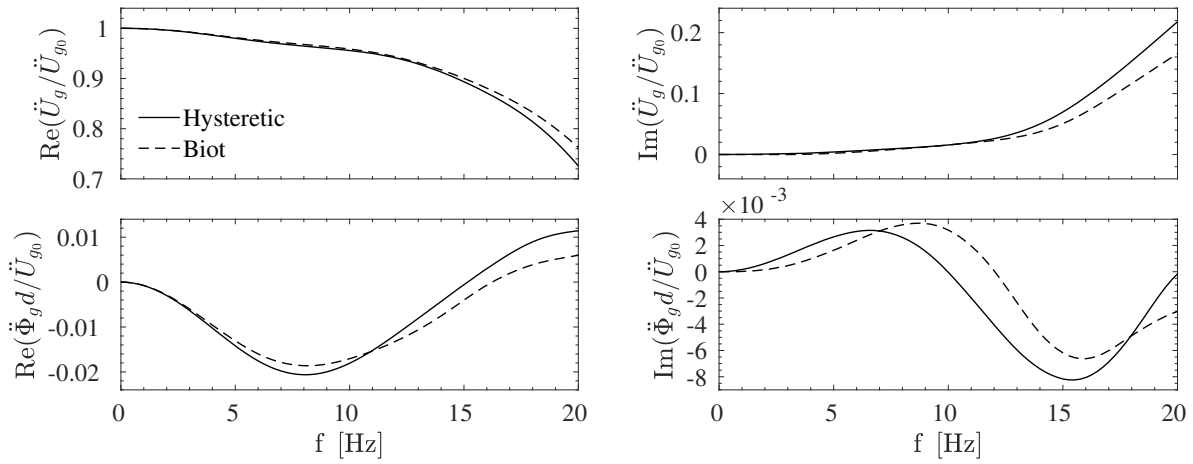


Figure A.19: Kinematic interaction factors of the $\theta = 5^\circ$ inclined 2×2 , $s = 3$ m foundation layout in ground type C.

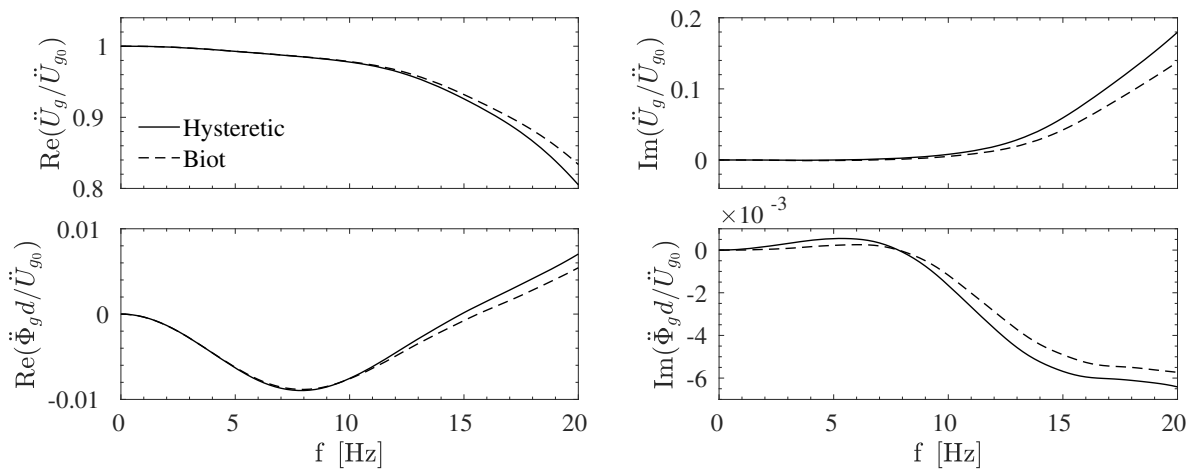


Figure A.20: Kinematic interaction factors of the $\theta = 5^\circ$ inclined 2×2 , $s = 5$ m foundation layout in ground type C.

Appendix A. Kinematic interaction factors, and computed and fitted impedance functions of the soil-foundation systems used in Chapter 5

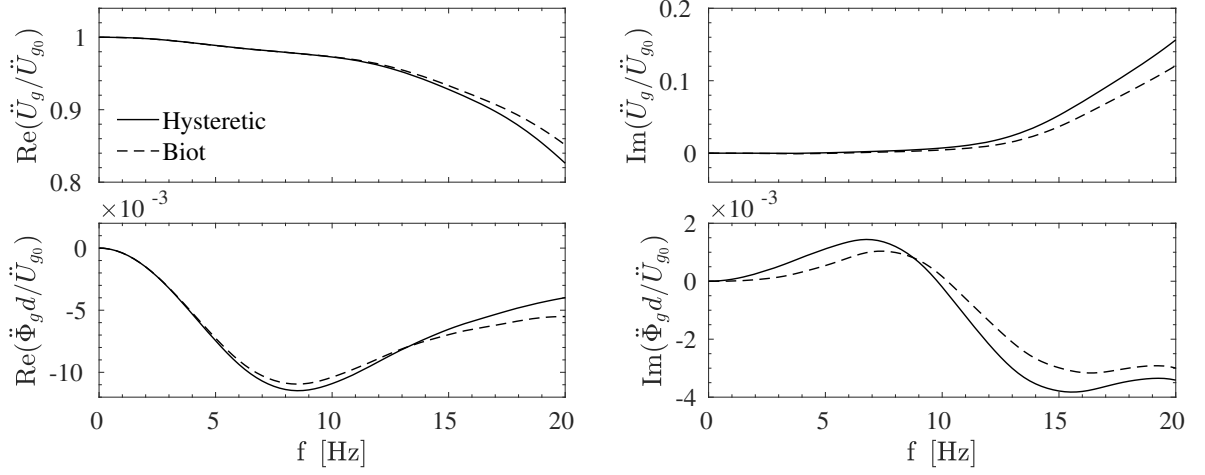


Figure A.21: Kinematic interaction factors of the $\theta = 5^\circ$ inclined 2×2 , $s = 7$ m foundation layout in ground type C.

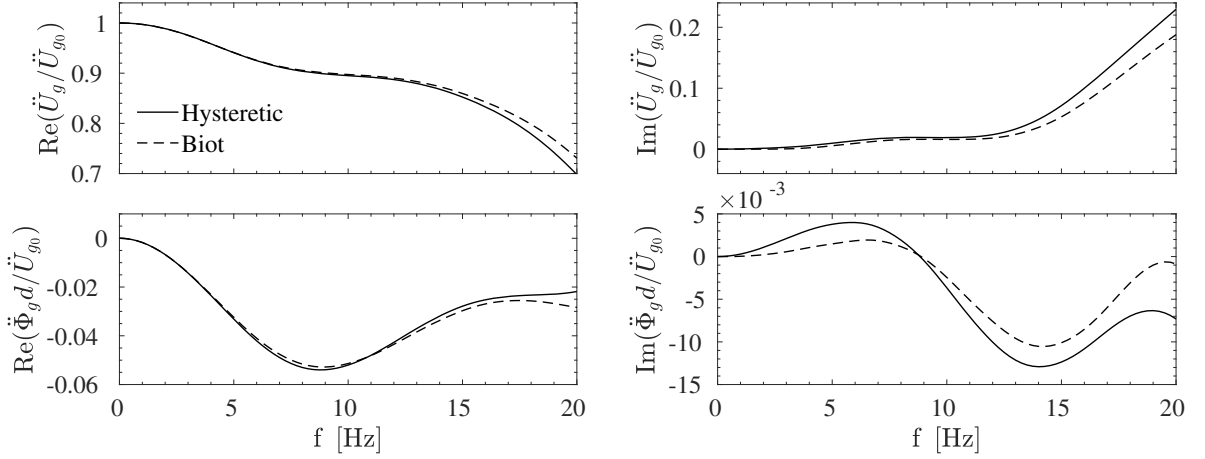


Figure A.22: Kinematic interaction factors of the $\theta = 10^\circ$ inclined 2×2 , $s = 3$ m foundation layout in ground type C.

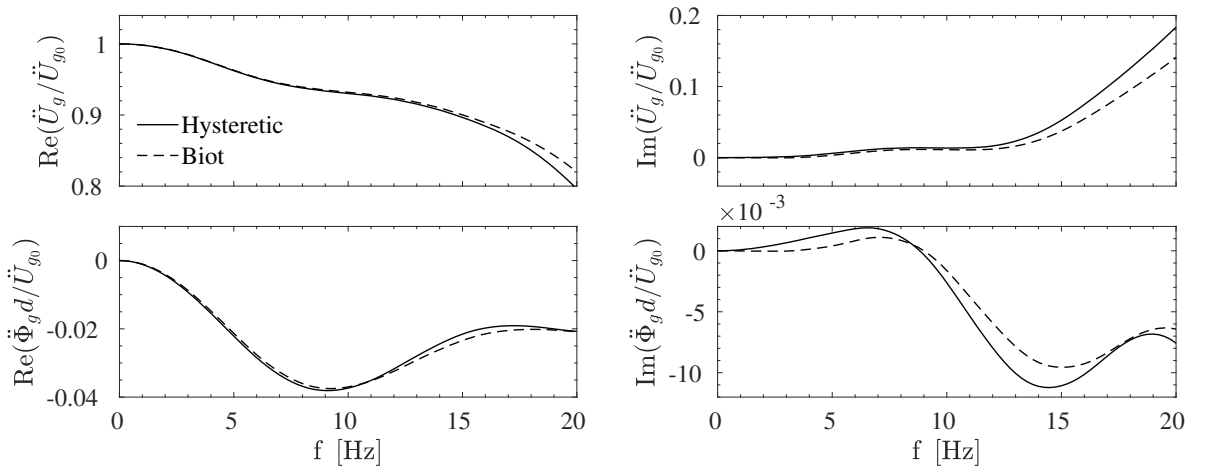


Figure A.23: Kinematic interaction factors of the $\theta = 10^\circ$ inclined 2×2 , $s = 5$ m foundation layout in ground type C.

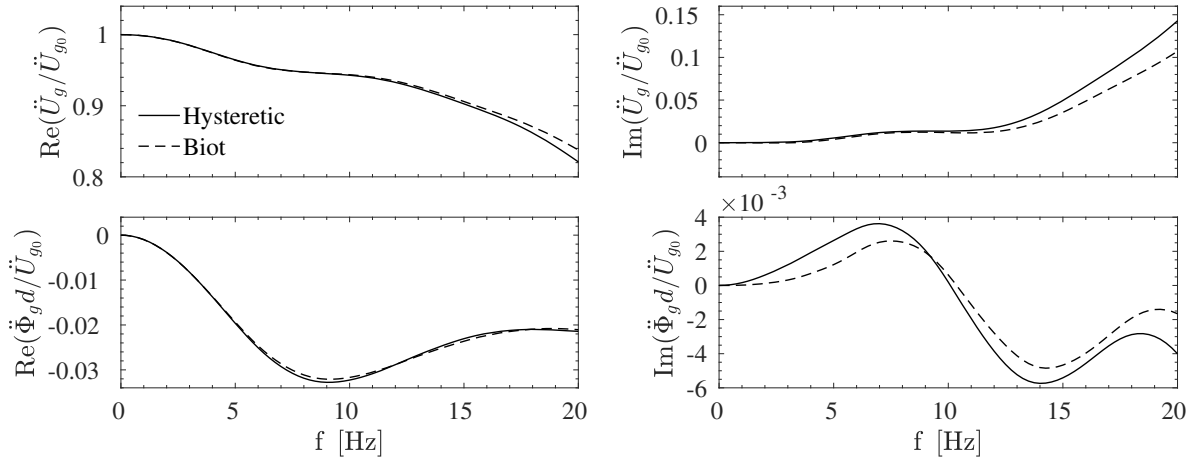


Figure A.24: Kinematic interaction factors of the $\theta = 10^\circ$ inclined 2×2 , $s = 7$ m foundation layout in ground type C.

A.2 Impedance functions and LPM fitting results

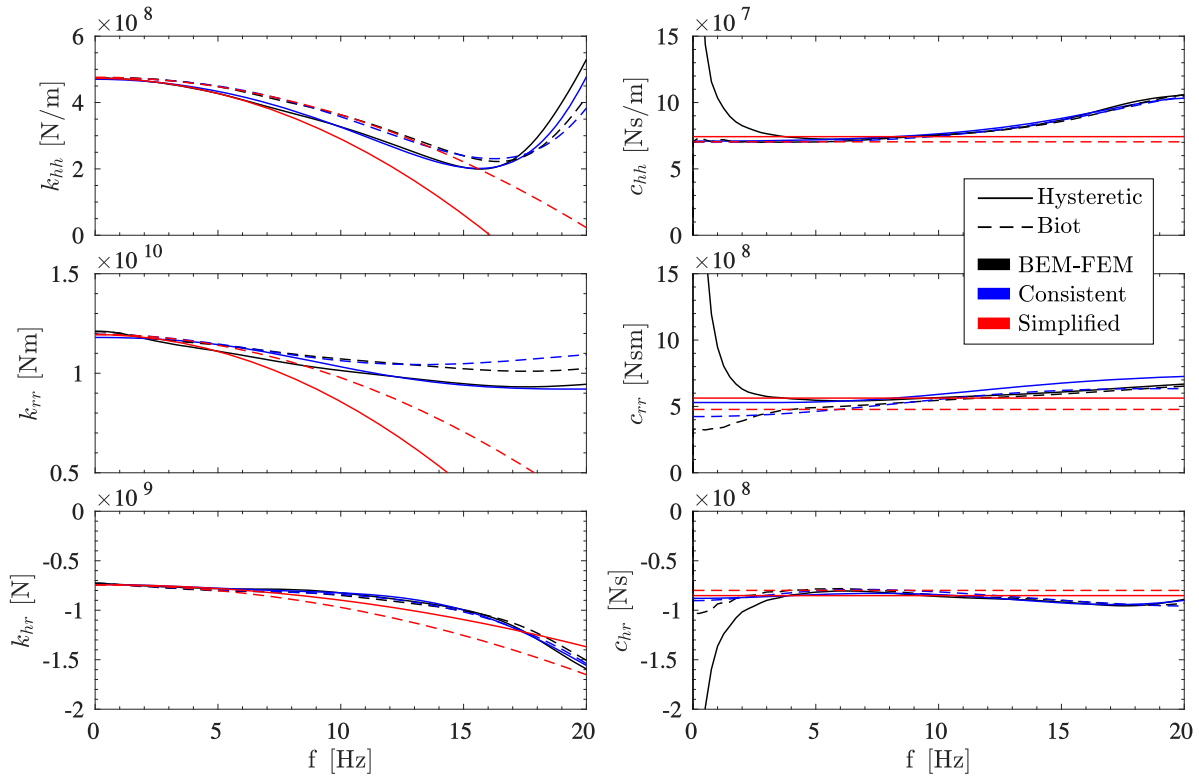


Figure A.25: Computed and fitted impedance functions of the vertical 2×2 , $s = 3$ m foundation layout in ground type D.

Appendix A. Kinematic interaction factors, and computed and fitted impedance functions of the soil-foundation systems used in Chapter 5

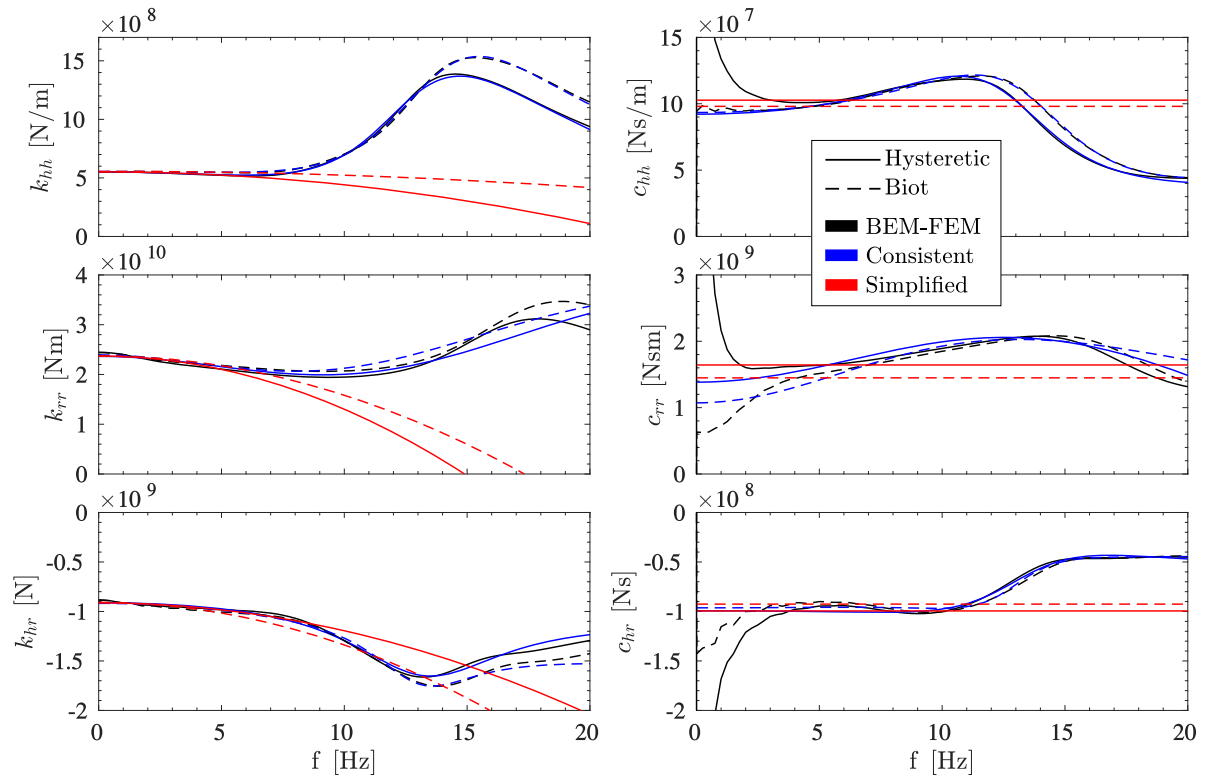


Figure A.26: Computed and fitted impedance functions of the vertical 2×2 , $s = 5$ m foundation layout in ground type D.

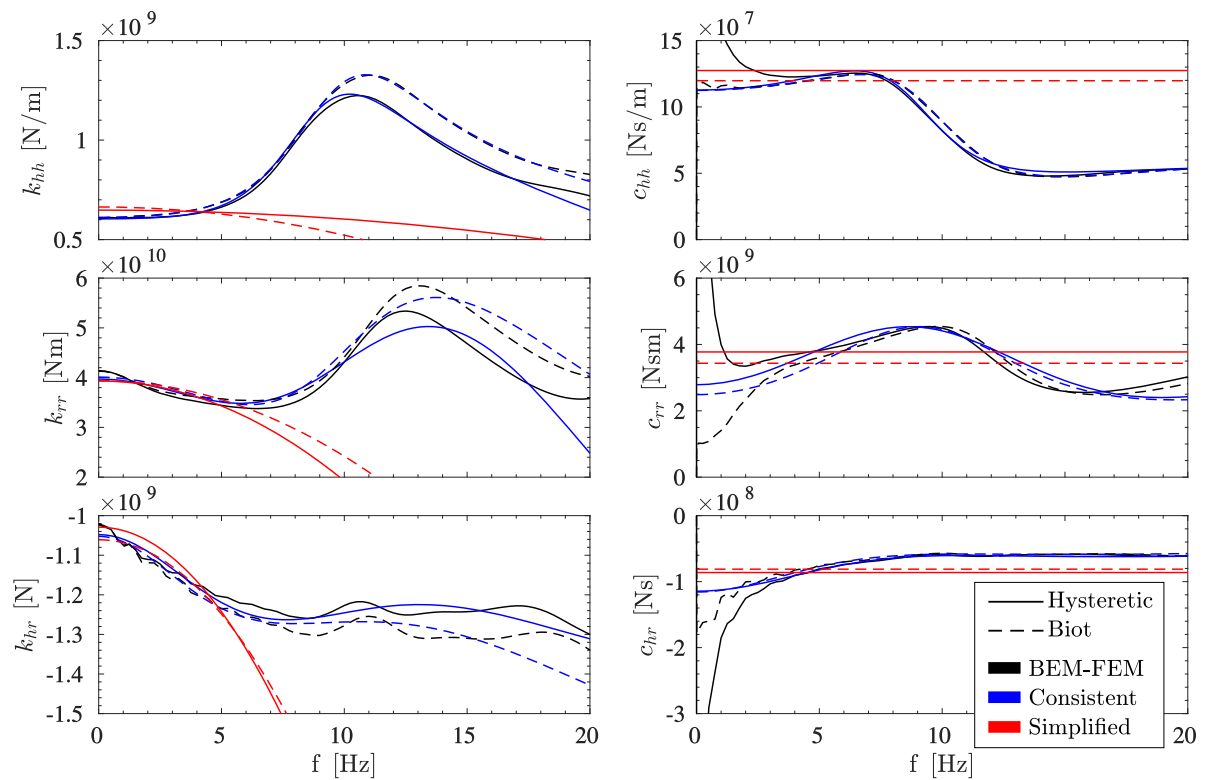


Figure A.27: Computed and fitted impedance functions of the vertical 2×2 , $s = 7$ m foundation layout in ground type D.

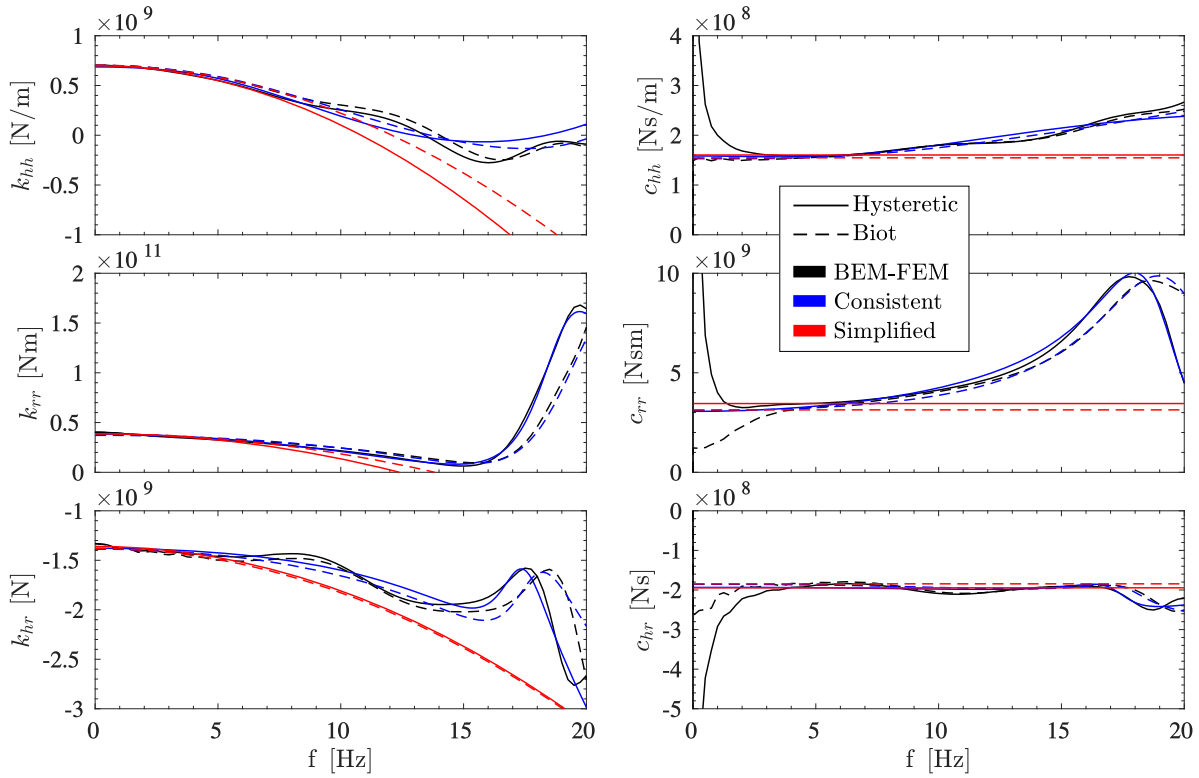


Figure A.28: Computed and fitted impedance functions of the vertical 3×3 , $s = 3$ m foundation layout in ground type D.

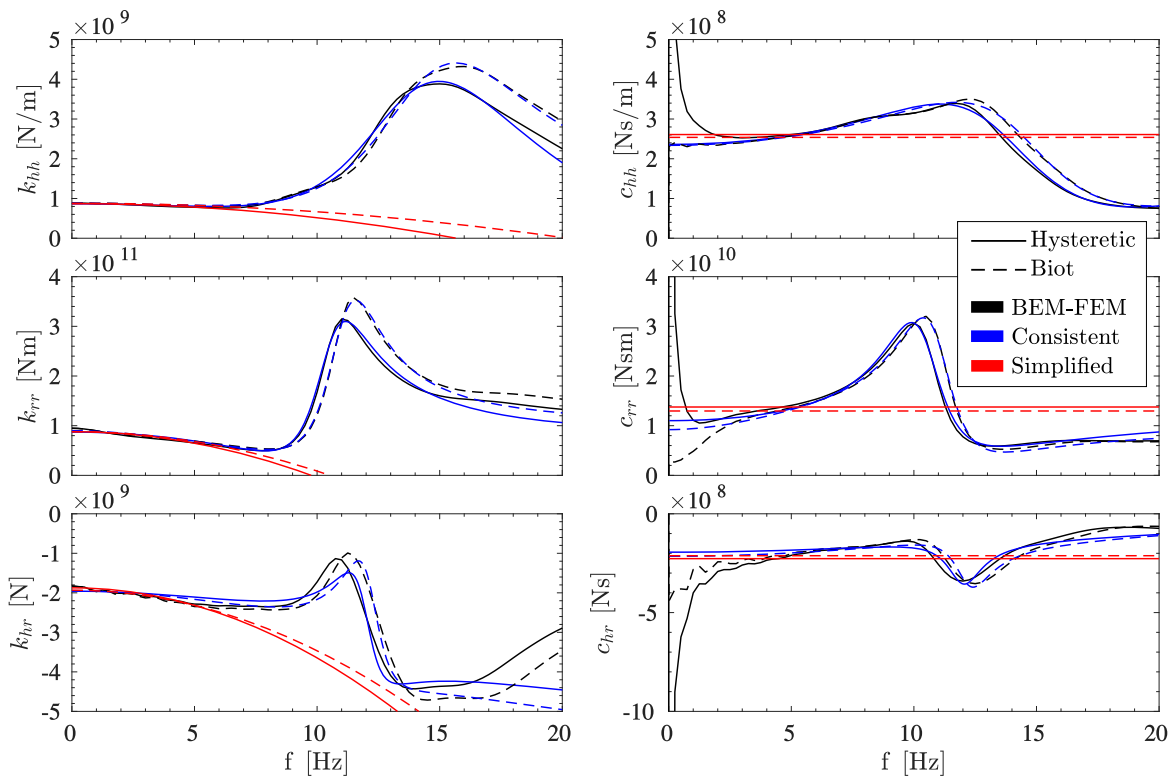


Figure A.29: Computed and fitted impedance functions of the vertical 3×3 , $s = 5$ m foundation layout in ground type D.

Appendix A. Kinematic interaction factors, and computed and fitted impedance functions of the soil-foundation systems used in Chapter 5

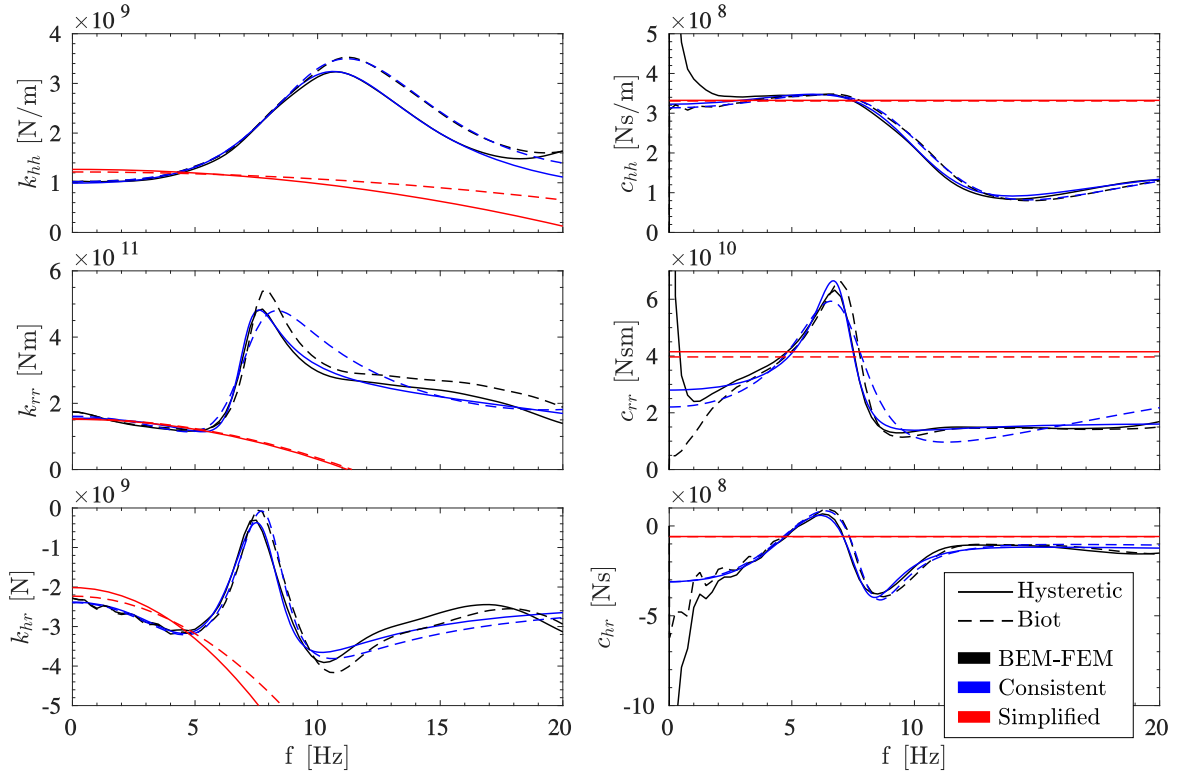


Figure A.30: Computed and fitted impedance functions of the vertical 3×3 , $s = 7$ m foundation layout in ground type D.

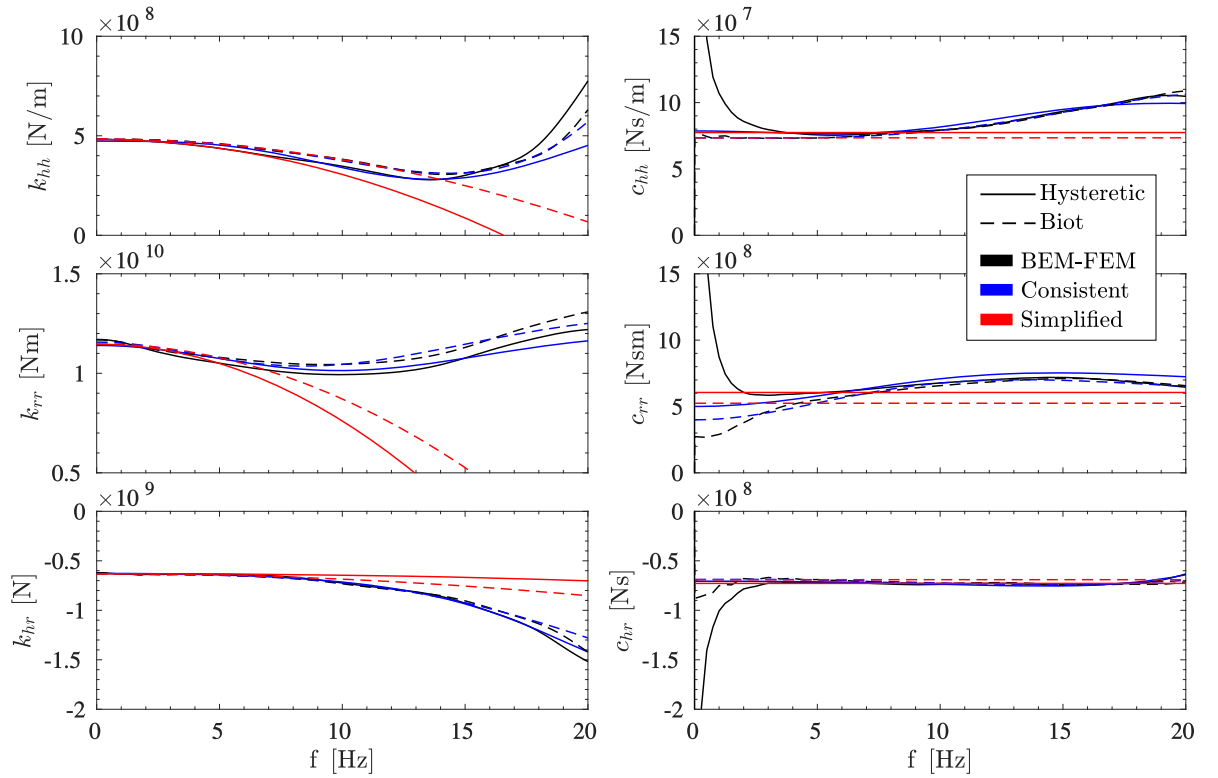


Figure A.31: Computed and fitted impedance functions of the $\theta = 5^\circ$ inclined 2×2 , $s = 3$ m foundation layout in ground type D.

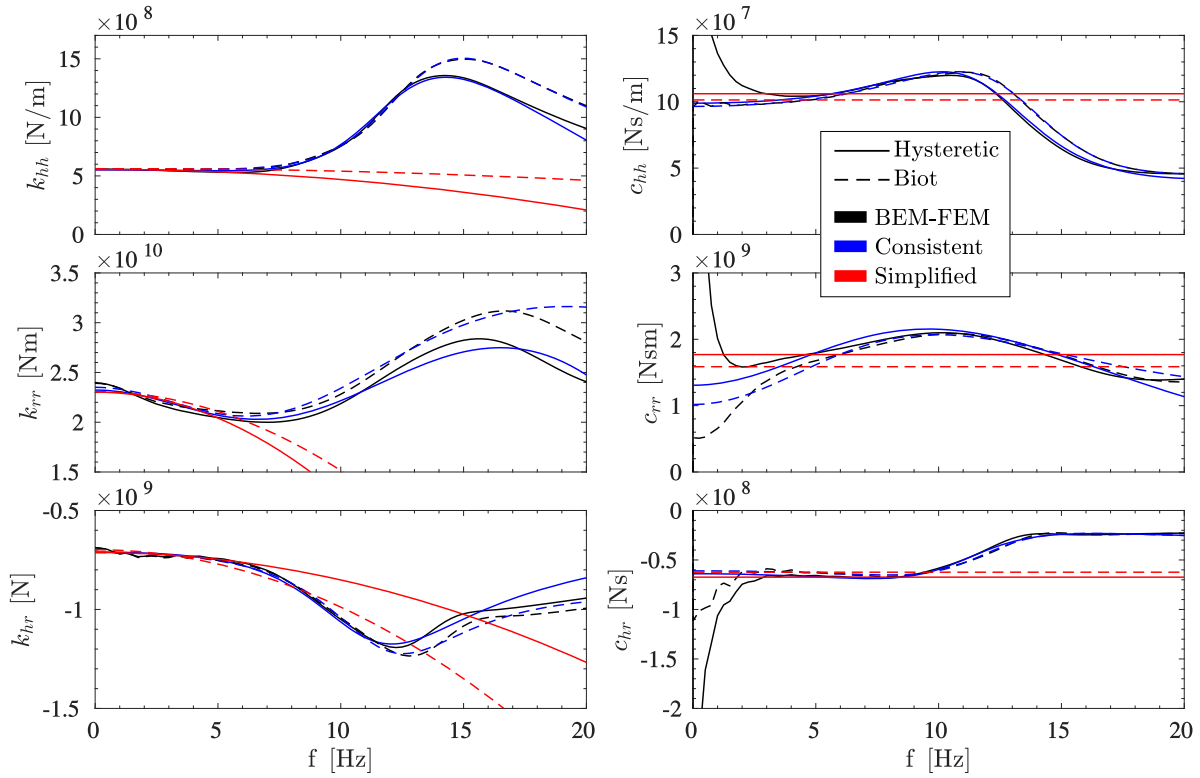


Figure A.32: Computed and fitted impedance functions of the $\theta = 5^\circ$ inclined 2×2 , $s = 5$ m foundation layout in ground type D.

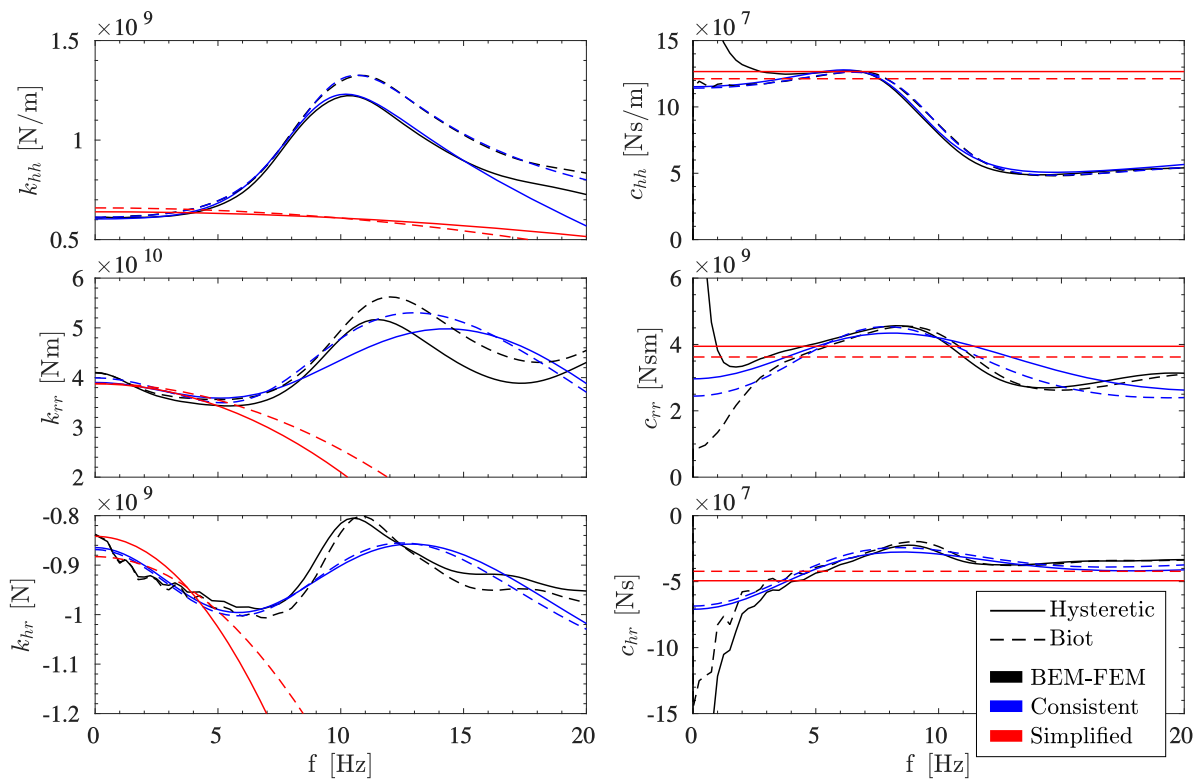


Figure A.33: Computed and fitted impedance functions of the $\theta = 5^\circ$ inclined 2×2 , $s = 7$ m foundation layout in ground type D.

Appendix A. Kinematic interaction factors, and computed and fitted impedance functions of the soil-foundation systems used in Chapter 5

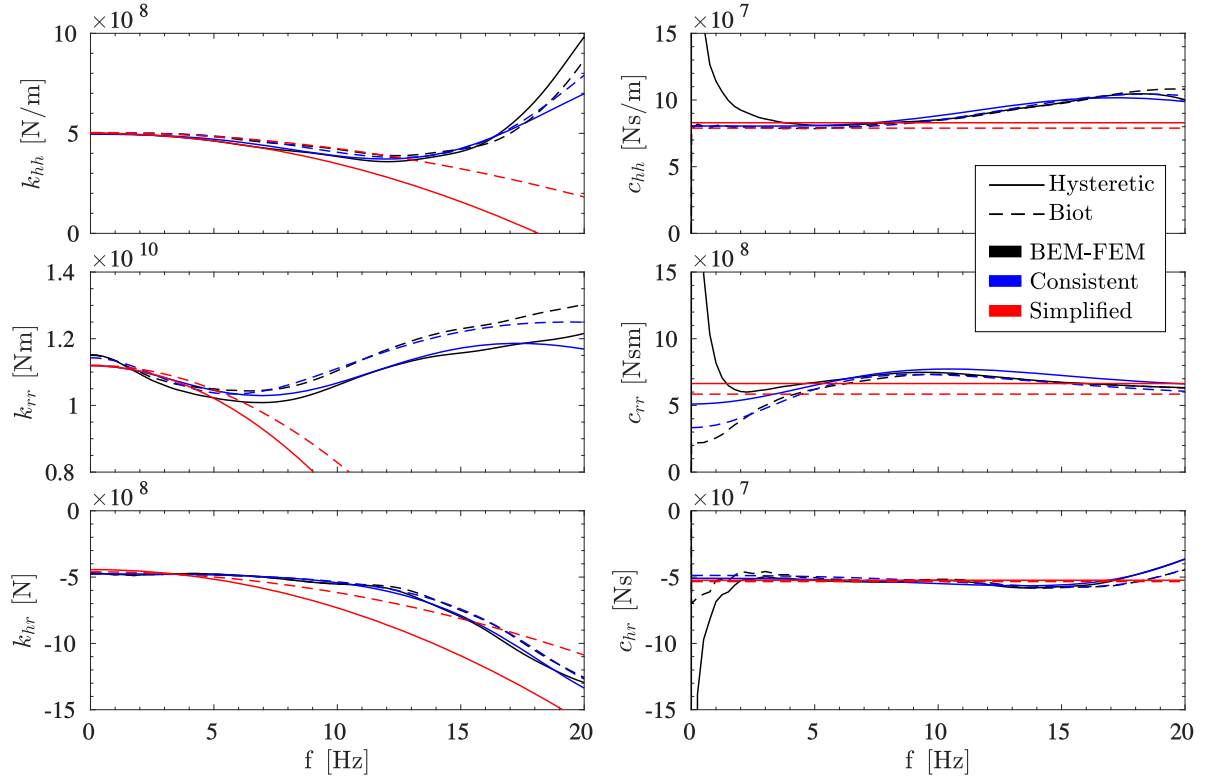


Figure A.34: Computed and fitted impedance functions of the $\theta = 10^\circ$ inclined 2×2 , $s = 3$ m foundation layout in ground type D.

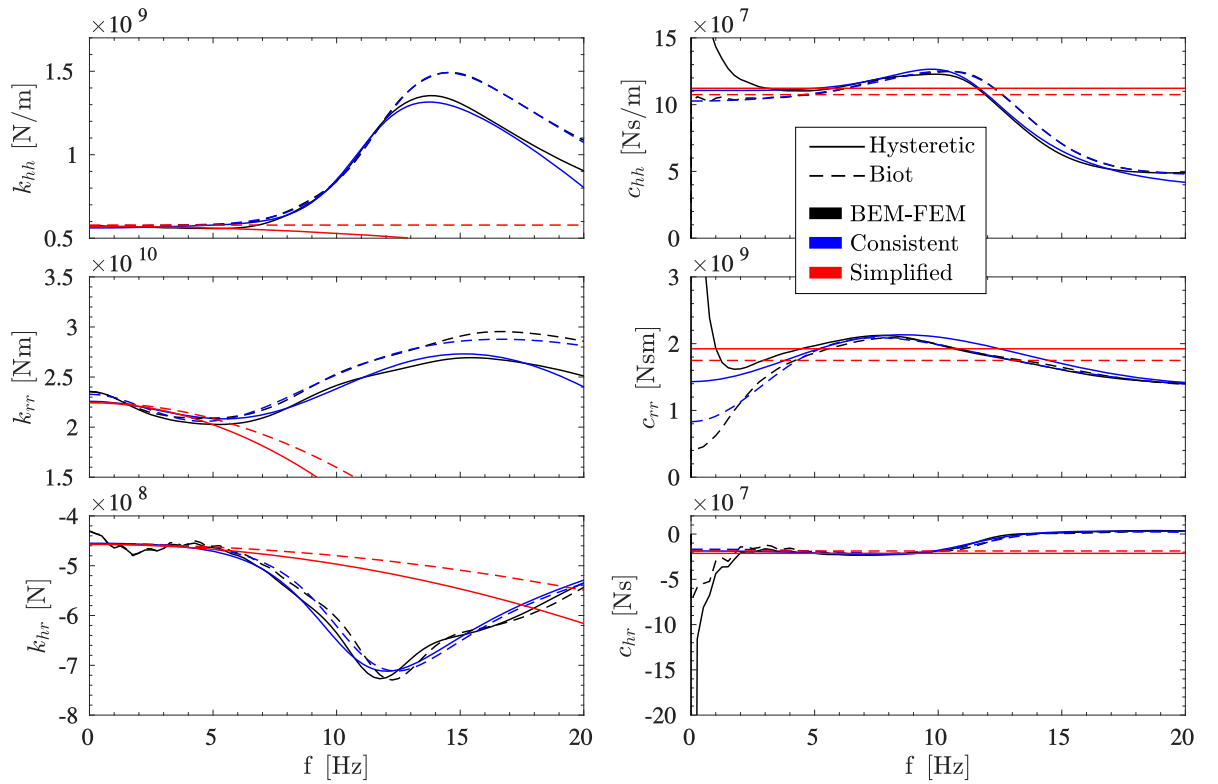


Figure A.35: Computed and fitted impedance functions of the $\theta = 10^\circ$ inclined 2×2 , $s = 5$ m foundation layout in ground type D.

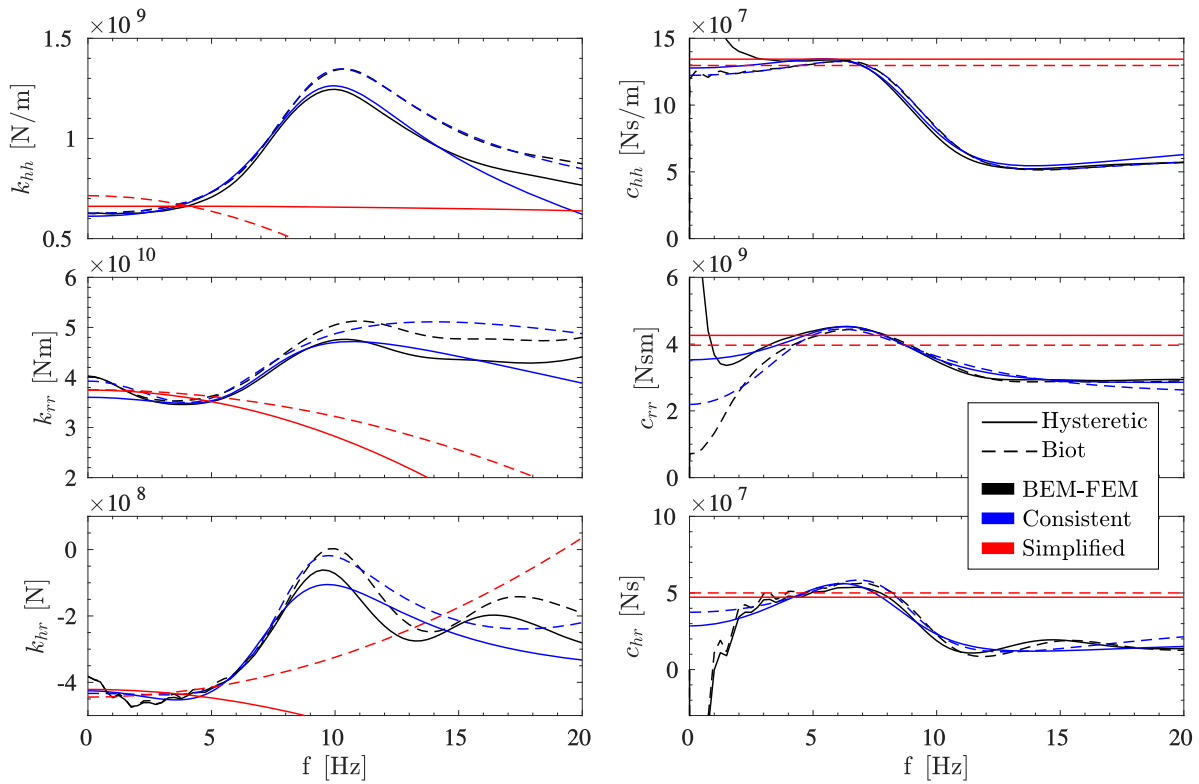


Figure A.36: Computed and fitted impedance functions of the $\theta = 10^\circ$ inclined 2×2 , $s = 7$ m foundation layout in ground type D.

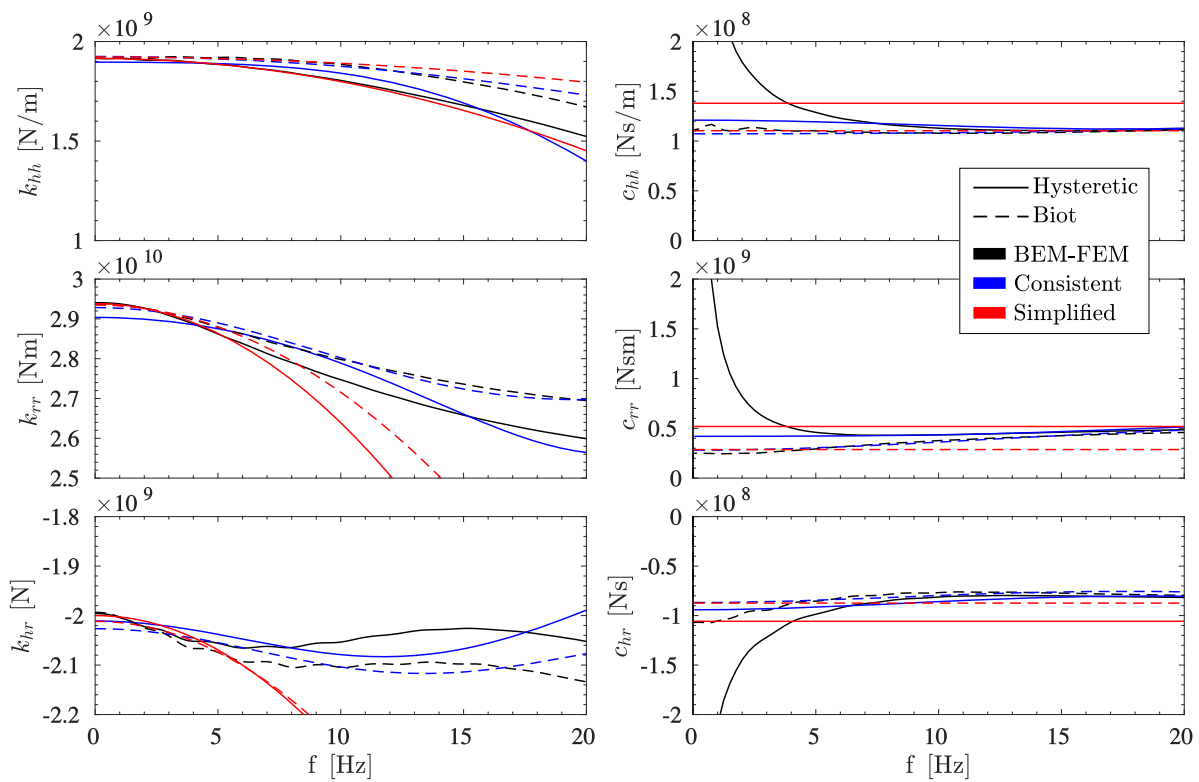


Figure A.37: Computed and fitted impedance functions of the vertical 2×2 , $s = 3$ m foundation layout in ground type C.

Appendix A. Kinematic interaction factors, and computed and fitted impedance functions of the soil-foundation systems used in Chapter 5

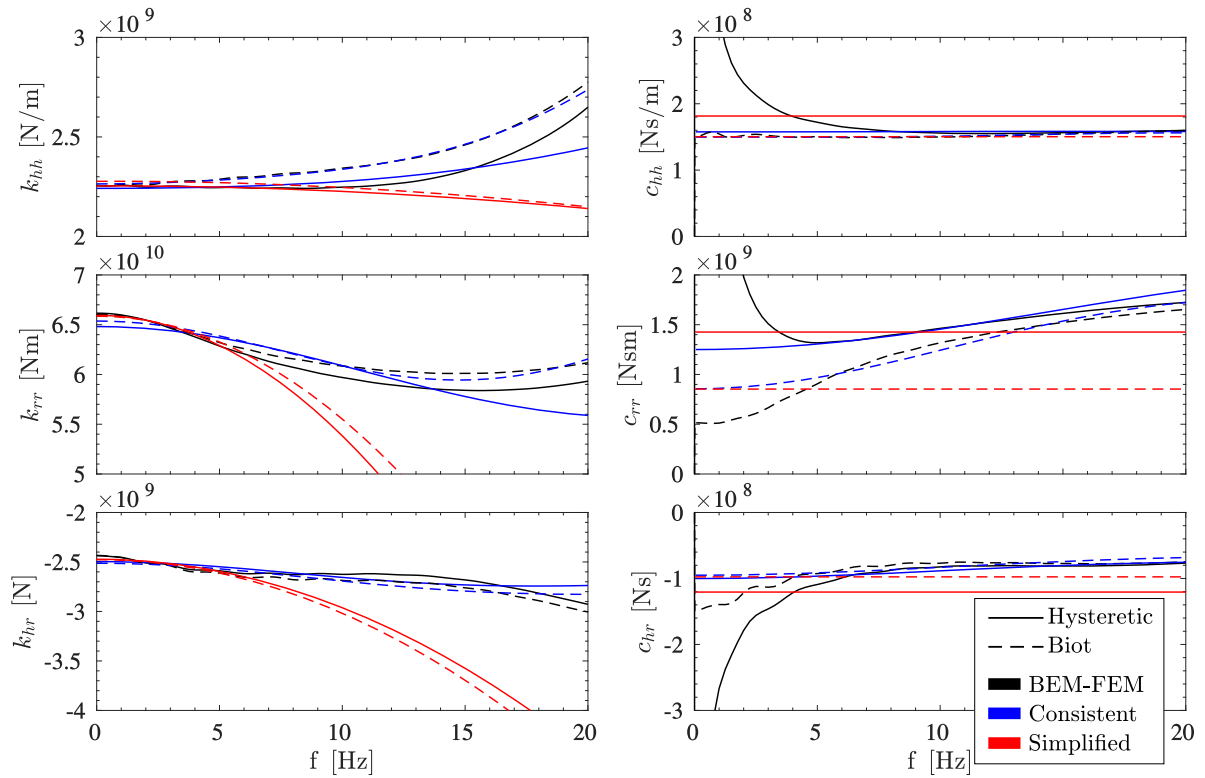


Figure A.38: Computed and fitted impedance functions of the vertical 2×2 , $s = 5$ m foundation layout in ground type C.

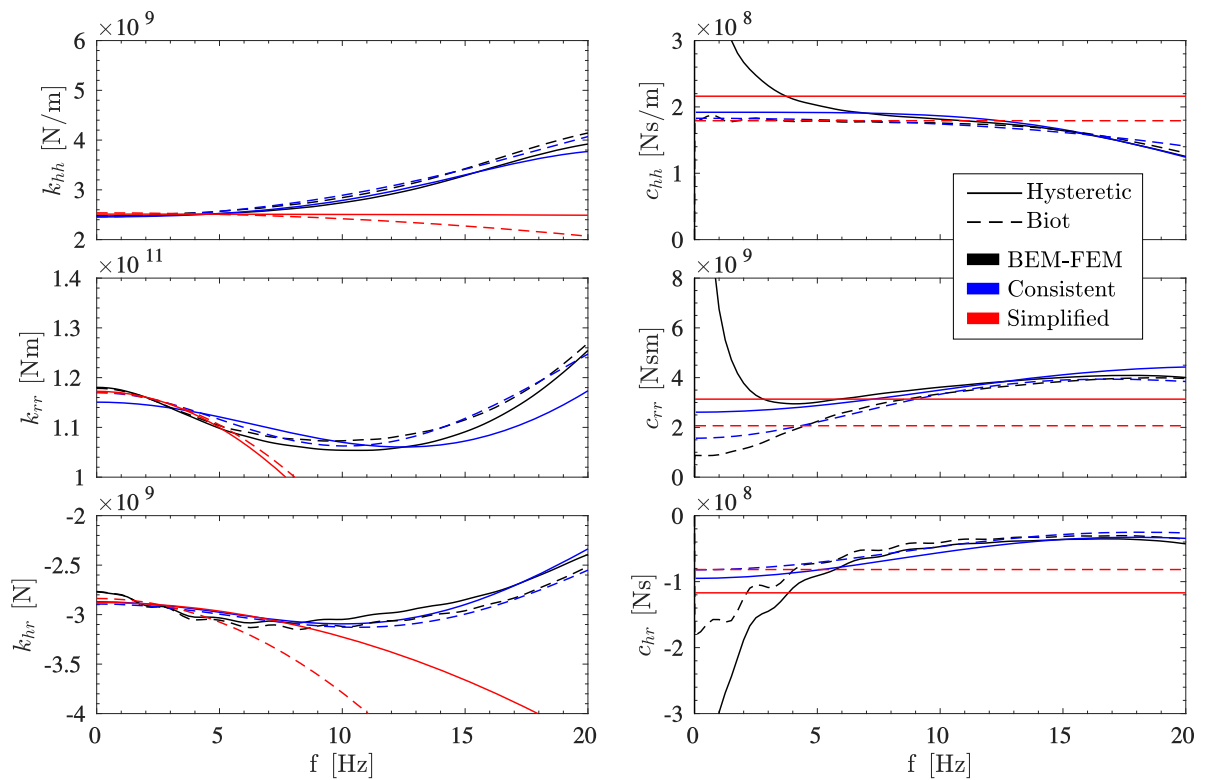


Figure A.39: Computed and fitted impedance functions of the vertical 2×2 , $s = 7$ m foundation layout in ground type C.

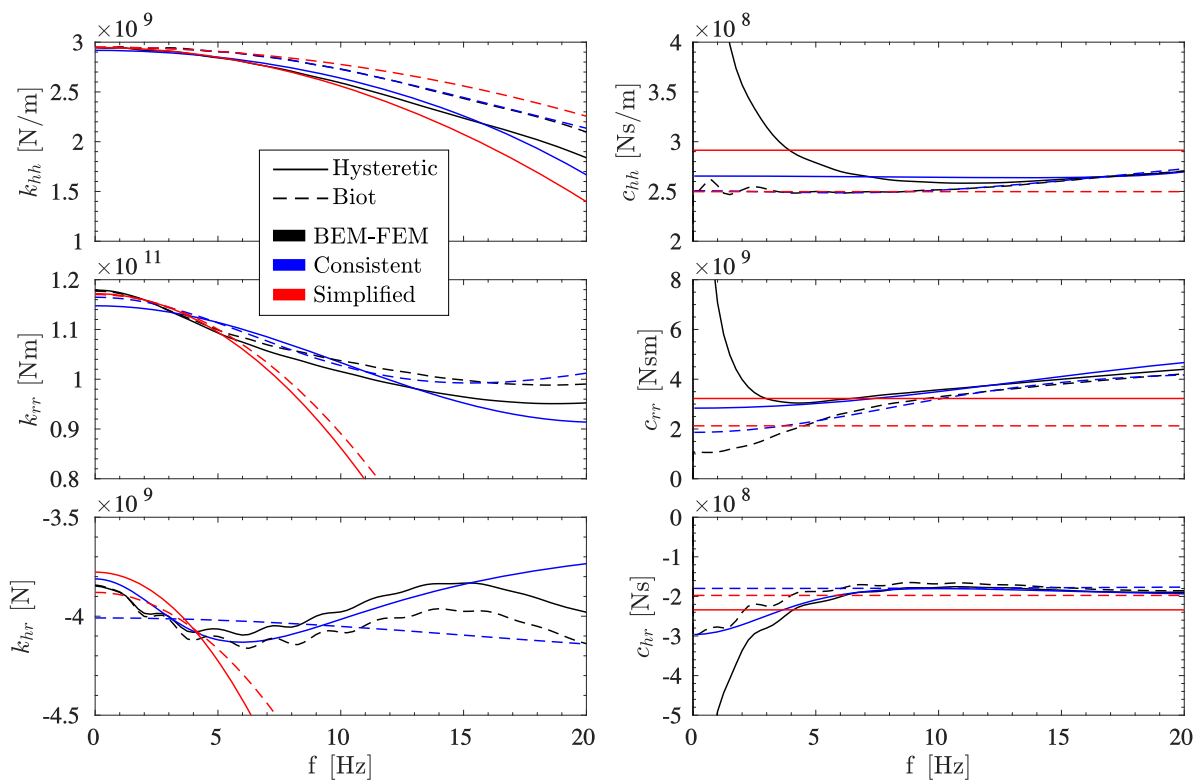


Figure A.40: Computed and fitted impedance functions of the vertical 3×3 , $s = 3$ m foundation layout in ground type C.

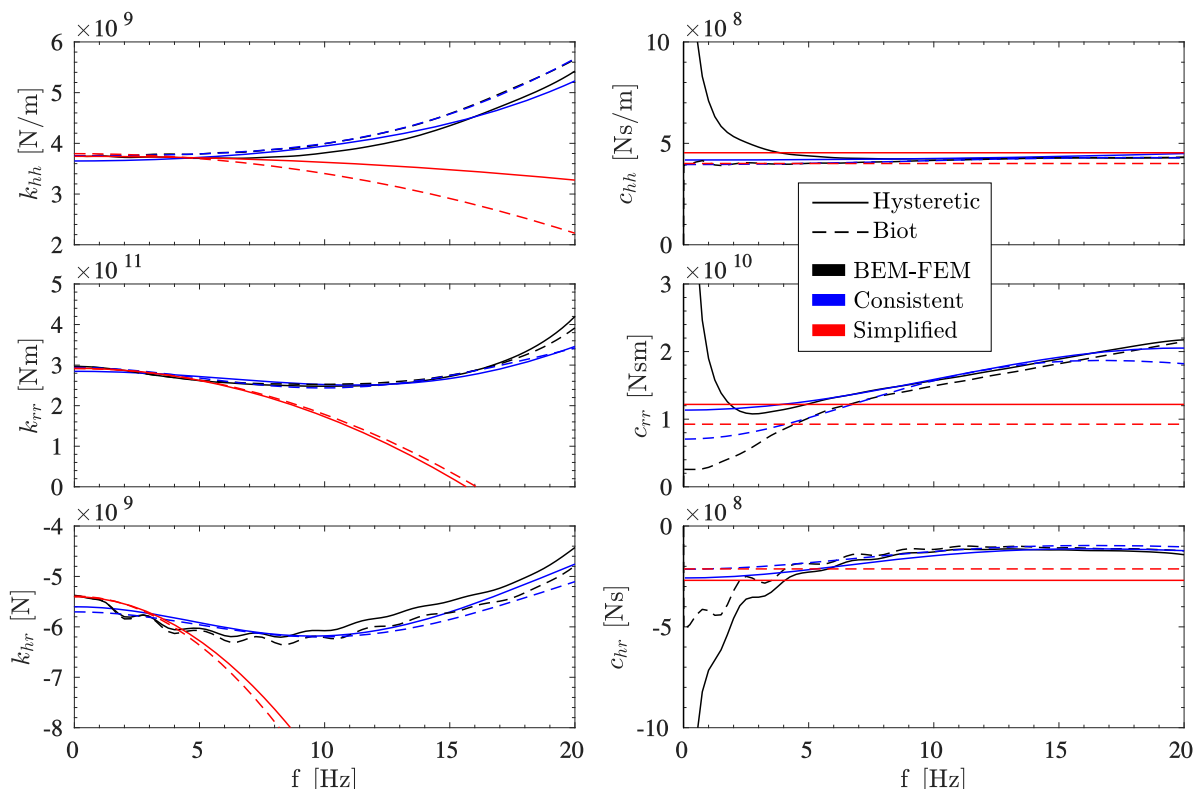


Figure A.41: Computed and fitted impedance functions of the vertical 3×3 , $s = 5$ m foundation layout in ground type C.

Appendix A. Kinematic interaction factors, and computed and fitted impedance functions of the soil-foundation systems used in Chapter 5

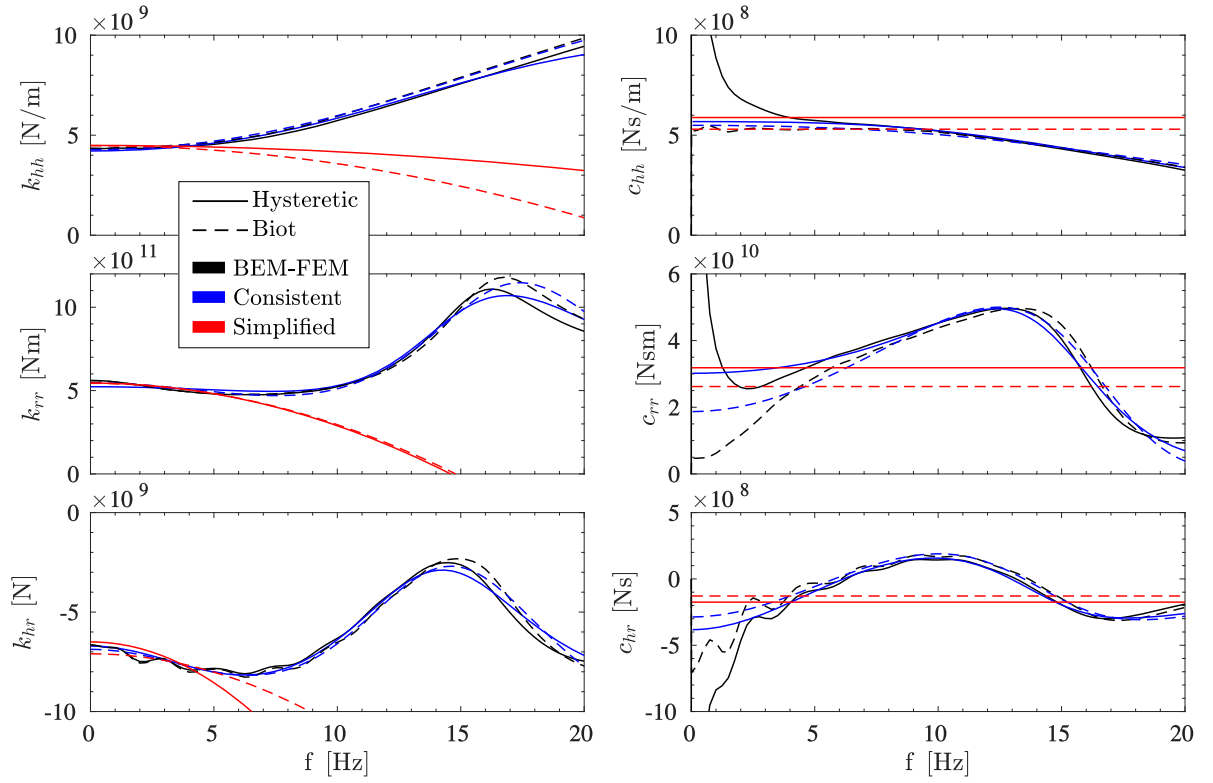


Figure A.42: Computed and fitted impedance functions of the vertical 3×3 , $s = 7$ m foundation layout in ground type C.

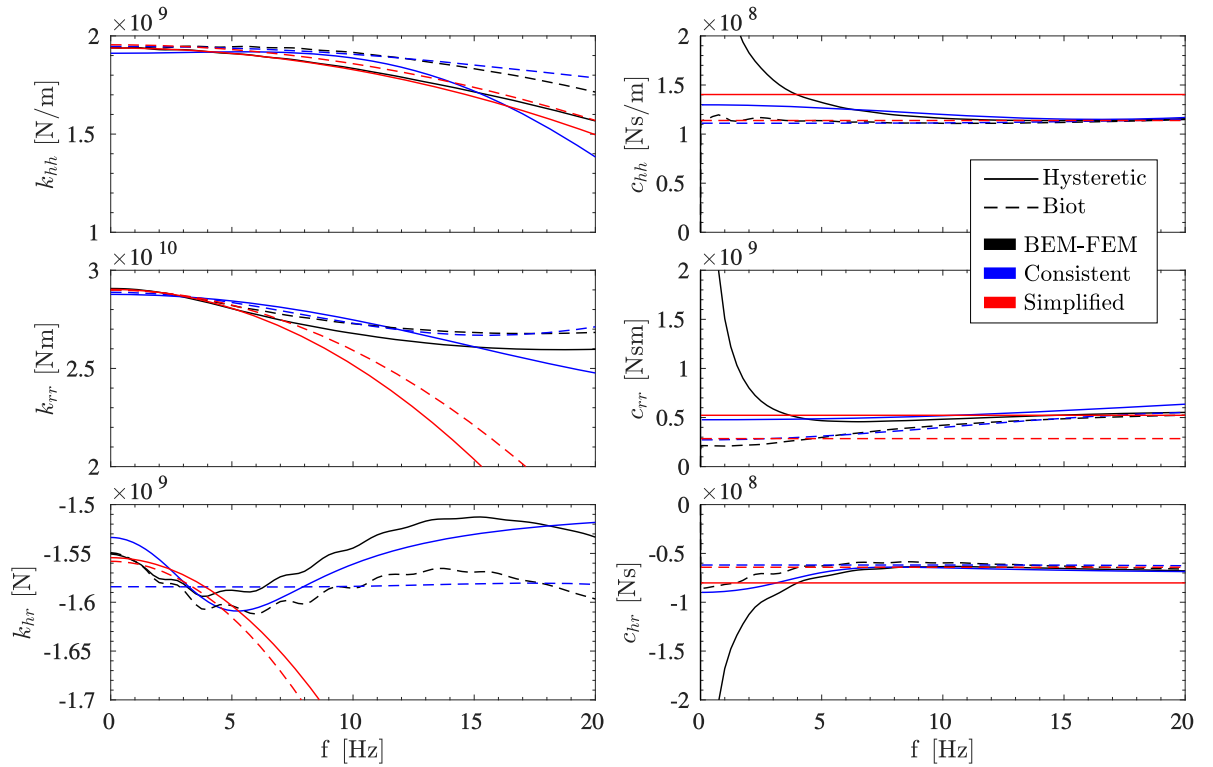


Figure A.43: Computed and fitted impedance functions of the $\theta = 5^\circ$ inclined 2×2 , $s = 3$ m foundation layout in ground type C.

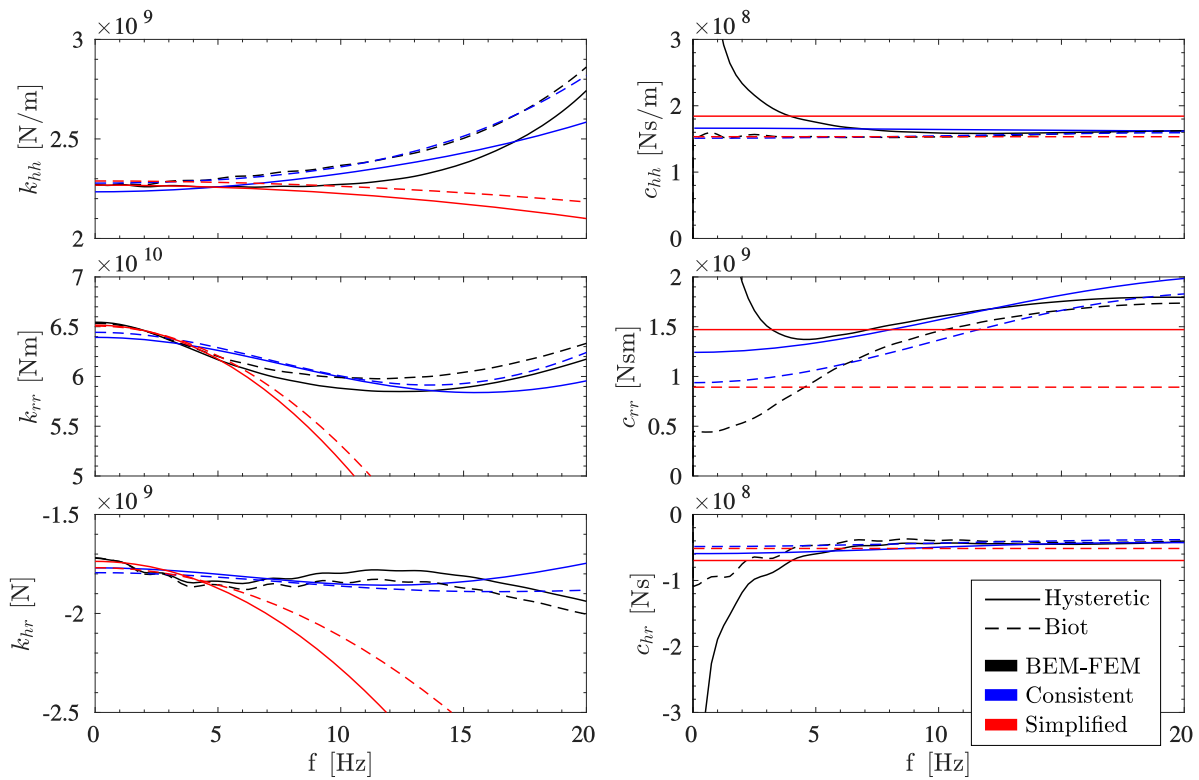


Figure A.44: Computed and fitted impedance functions of the $\theta = 5^\circ$ inclined 2×2 , $s = 5$ m foundation layout in ground type C.

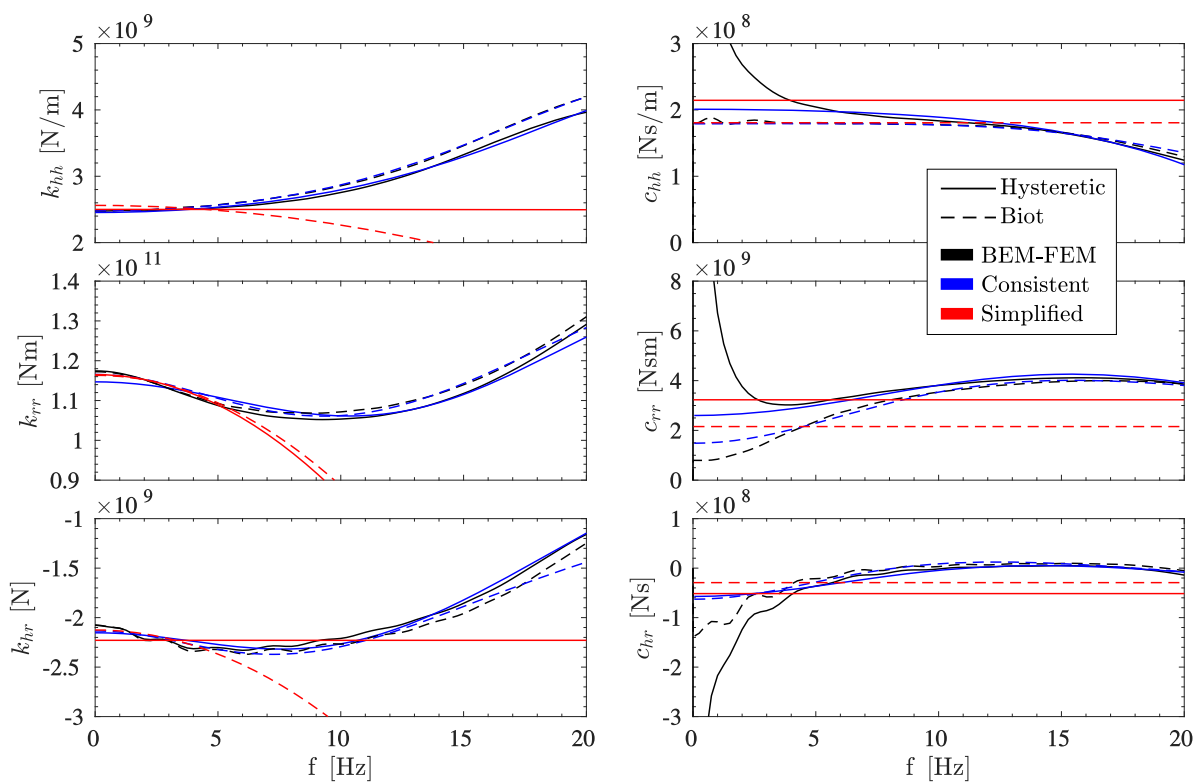


Figure A.45: Computed and fitted impedance functions of the $\theta = 5^\circ$ inclined 2×2 , $s = 7$ m foundation layout in ground type C.

Appendix A. Kinematic interaction factors, and computed and fitted impedance functions of the soil-foundation systems used in Chapter 5

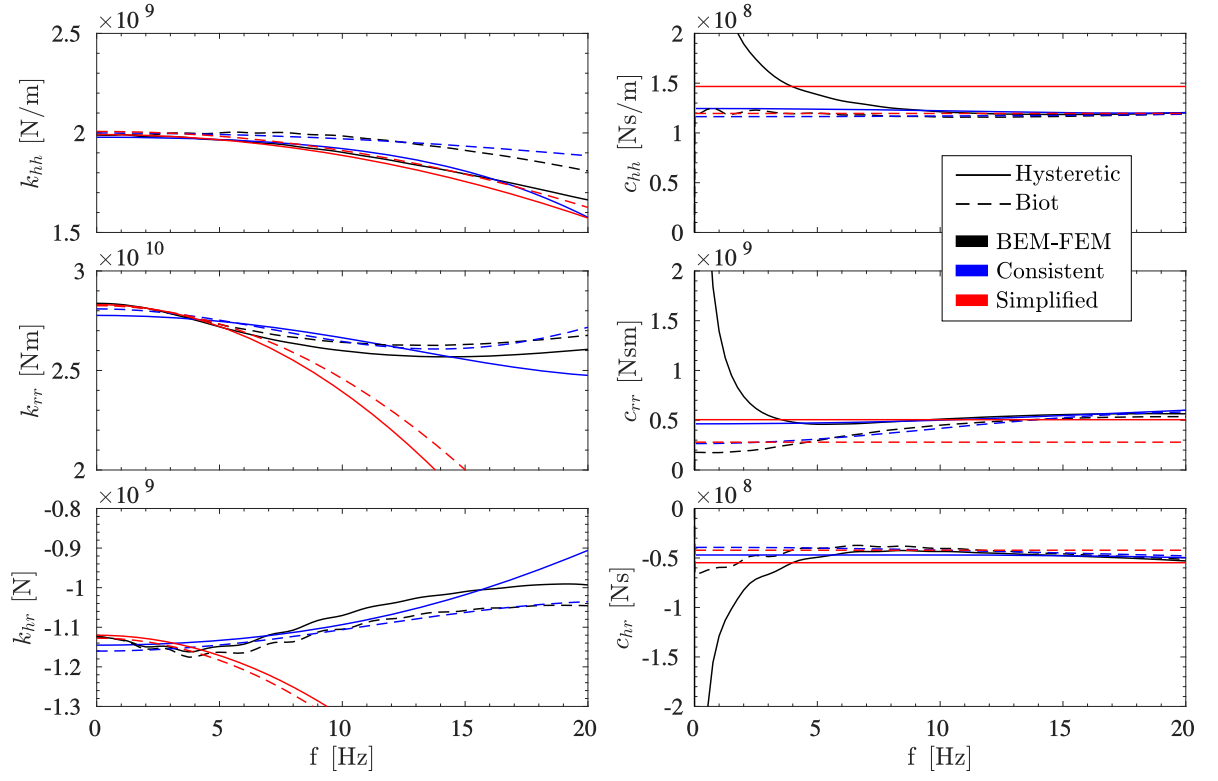


Figure A.46: Computed and fitted impedance functions of the $\theta = 10^\circ$ inclined 2×2 , $s = 3$ m foundation layout in ground type C.

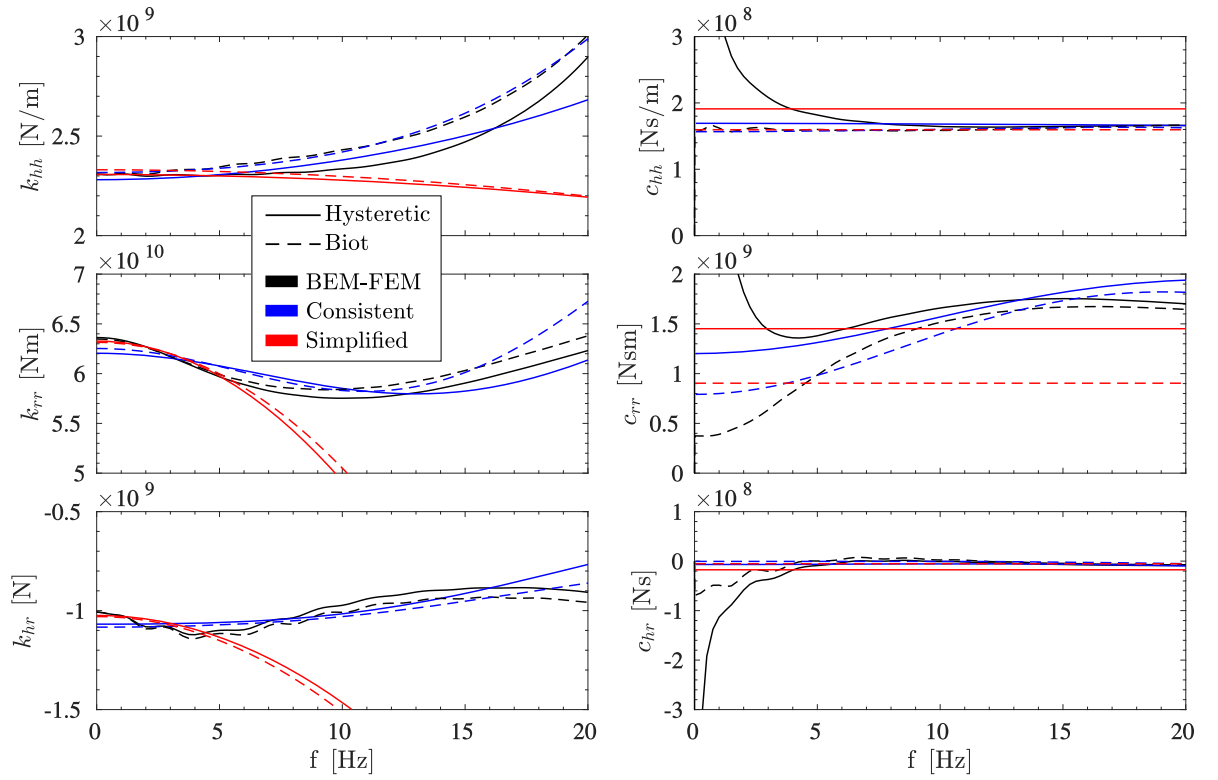


Figure A.47: Computed and fitted impedance functions of the $\theta = 10^\circ$ inclined 2×2 , $s = 5$ m foundation layout in ground type C.

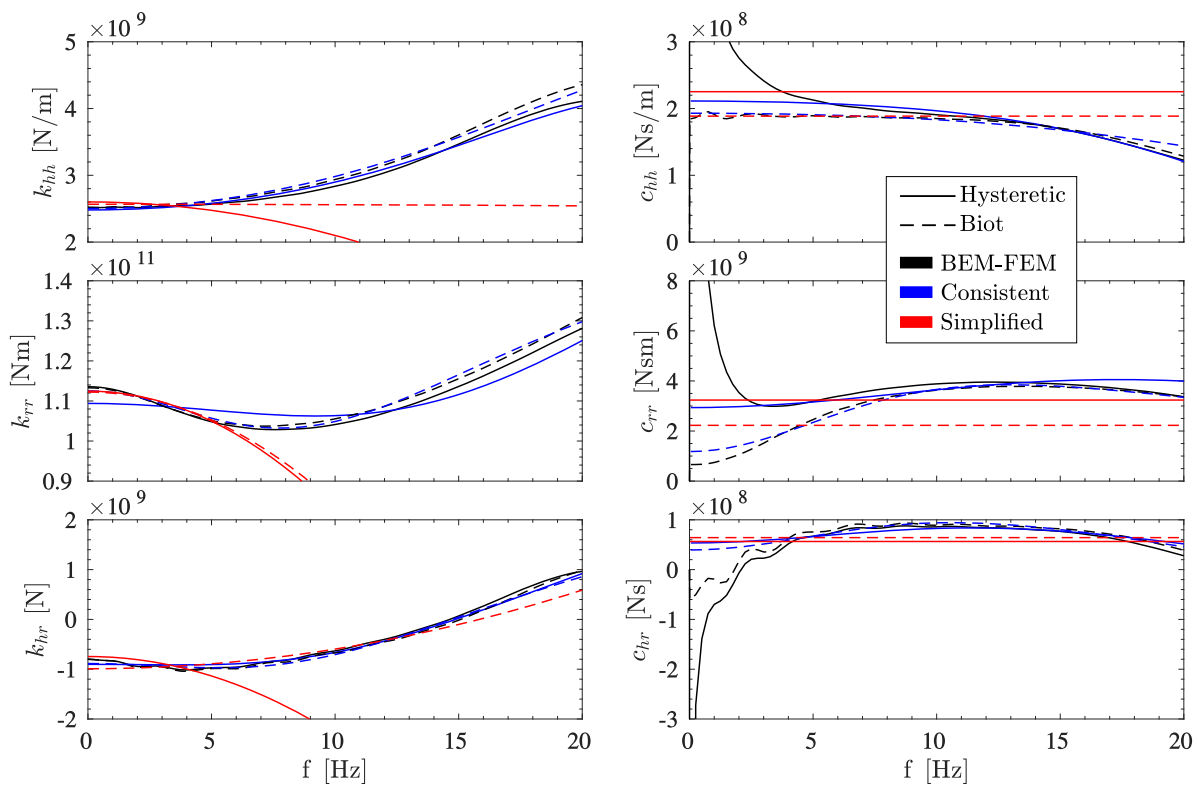


Figure A.48: Computed and fitted impedance functions of the $\theta = 10^\circ$ inclined 2×2 , $s = 7$ m foundation layout in ground type C.

Appendix B

Summary in Spanish / Resumen en castellano

Título de la Tesis Doctoral: Desarrollo de modelos numéricos para el análisis de comportamientos no lineales en problemas dinámicos de interacción suelo-estructura¹

B.1 Motivación y antecedentes

Si bien es verdad que hoy en día existe un conocimiento considerable en el ámbito de la ingeniería sísmica, el hecho es que los terremotos siguen causando la muerte a al menos cientos de personas cada año, incluso decenas de miles en años concretos [1]. Por si fuera poco, el daño causado en áreas urbanas, ciudades e infraestructuras civiles suele ser devastador. Como en cualquier situación catastrófica, no todas las regiones del planeta tienen la misma capacidad de reponerse. Es por ello que es completamente necesario y esencial el desarrollo de nuevas técnicas más baratas para el diseño y cálculo de estructuras resistentes a terremotos.

Para hacer esto, es muy común en ingeniería la resolución de problemas dinámicos que involucren la propagación de ondas mecánicas a través de un medio continuo. El análisis de la respuesta de estructuras o componentes mecánicos a cargas variables en el tiempo, como es un terremoto, requiere altos niveles de precisión en la búsqueda de diseños más seguros y optimizados. Esto se ha convertido en un problema bastante común, no siendo abordado únicamente por grandes estudios y empresas de ingeniería.

La forma en la que las propiedades y el movimiento del suelo influyen la respuesta de una estructura y, a su vez, la forma en la que el movimiento de la estructura influye la respuesta del suelo, comúnmente se denomina interacción suelo-estructura (SSI de sus siglas en inglés *Soil-Structure Interaction*). Este concepto se refiere a fenómenos tanto estáticos como dinámicos mediados por un suelo flexible y una estructura más rígida

¹En este apéndice se presenta un breve resumen en castellano de la Tesis Doctoral de entre 5 y 20 páginas, en el que se incluyen los objetivos y las conclusiones, de acuerdo con el Artículo 10 del Reglamento de Estudios de Doctorado de la Universidad de Las Palmas de Gran Canaria (BOULPGC de 4 de marzo de 2019).

que el suelo. Frecuentemente, los cálculos estructurales omiten la SSI dando lugar a diseños demasiado conservadores. Sin embargo, como se ha mostrado en el desarrollo de este documento, SSI puede mostrar efectos perjudiciales en la respuesta del sistema en algunos casos en concreto. La literatura muestra una multitud de evidencias sobre la existencia de escenarios donde la SSI debe ser tomada en cuenta. Cuando una estructura se encuentra parcialmente incrustada en el suelo, y cuando la categoría del suelo es blanda, SSI se convierte en un fenómeno decisivo. En estos casos, el diseño adecuado de la cimentación juega un papel clave, pudiendo mitigar los efectos perjudiciales a la estructura.

Esta tesis se centra en el caso particular de cimentaciones pilotadas, y aborda diferentes problemas que tienen en cuenta la respuesta dinámica y sísmica de pilotes y estructuras pilotadas. Por tanto, estos problemas incluyen el análisis de la SSI dinámica, y además, fenómenos no lineales que se desarrollan tanto en sistemas pilote-suelo como en las superestructuras. Más concretamente, en una parte del documento se propone un modelo lineal equivalente de elementos finitos y elementos de contorno acoplado (BEM-FEM) para el análisis de la respuesta dinámica de cimentaciones pilotadas que considera degradación del suelo en la interfase entre pilote y suelo. La otra parte del documento estudia diferentes formas de construir un modelo numérico para el análisis de la respuesta sísmica de viaductos pilotados. Haciendo uso de este modelo se estudia la influencia de varios aspectos, como puede ser, por ejemplo, la reducción en el daño a los pilares cuando se utilizan pilotes inclinados en la cimentación.

Los códigos desarrollados para el análisis del sistema suelo-cimentación son verificados a través de dar resultado a problemas ya conocidos, y también a otros casos cuya solución es desconocida donde se compara con el resultado proporcionado por otros códigos disponibles en el grupo de investigación. Una calibración cuidadosa de los parámetros del modelo es necesaria para garantizar la estabilidad y la precisión en los resultados. Los correspondientes estudios paramétricos son llevados a cabo dependiendo de las características de la estructura, el tipo de carga y la naturaleza no lineal del problema.

El doctorando ha estado adscrito al Instituto Universitario de Sistemas inteligentes y Aplicaciones Numéricas en Ingeniería (SIANI), más concretamente en la División de Mecánica de los Medios Continuos y Estructuras. El instituto SIANI ha estado activo desde hace ya dos décadas, proporcionando toda la infraestructura necesaria, incluyendo un centro de procesamiento de datos de alto rendimiento que alberga un *cluster* de propósito general. El instituto se encuentra situado en el edificio central del Parque Científico y Tecnológico de la Universidad de Las Palmas de Gran Canaria.

El grupo de investigación en el que se integra el doctorando ha trabajado desde hace más de tres décadas en el desarrollo de modelos de elementos finitos y elementos de contorno para el análisis dinámico de problemas de mecánica estructural. En los problemas abordados por el grupo, los fenómenos de SSI han sido clave, pero siempre se han realizado los análisis en el régimen lineal de su comportamiento. Es por ello, que en los años recientes, la contribución realizada en forma de modelos y códigos de ordenador en esta materia es considerable, así como también el análisis en profundidad de problemas de interés, como pueden ser el análisis de la respuesta sísmica de presas, estructuras enterradas y estructuras de construcción cimentadas sobre pilotes.

B.2 Objetivos

Los análisis lineales pueden ser los adecuados en muchos casos, en cambio, en muchos otros, es necesario usar modelos capaces de incorporar ciertos fenómenos no lineales. El objetivo de esta Tesis es avanzar en el modelado numérico de no linealidades en problemas dinámicos de SSI, y también ha tenido el propósito de avanzar el desarrollo de los códigos existentes en el seno del Grupo de Investigación incluyendo estas formulaciones que permiten abordar problemas con comportamiento no lineal en el ámbito de la SSI dinámica. Los modelos resultantes permiten un análisis más realista de problemas prácticos.

Esta tesis tiene, como primer objetivo, la formulación e implementación de un modelo de elementos finitos y elementos de contorno acoplado para el análisis dinámico de cimentaciones pilotadas que exhiban un comportamiento no lineal en el contacto entre pilote y suelo. Se tiene en cuenta, a través de un modelo lineal equivalente, la degradación del suelo alrededor de los pilotes.

El segundo objetivo es el desarrollo de una herramienta para el análisis del comportamiento no lineal de estructuras teniendo en cuenta la SSI dinámica y la dependencia en frecuencia de las fuerzas de reacción del sistema suelo-cimentación.

Para alcanzar estos objetivos generales, una secuencia de objetivos parciales han tenido que ser completados:

- Desarrollo de un modelo BEM-FEM lineal equivalente para el análisis aproximado de la respuesta armónica lateral de pilotes considerando degradación del suelo a lo largo de la interfase entre pilote y suelo.
- Estudio de las bases teóricas de los modelos de parámetros agrupados (LPMs de sus siglas en inglés, *Lumped Parameter Models*), e implementación de un esquema paso-a-paso lineal para el estudio de estructuras cimentadas sobre pilotes.
- Estudio de los criterios de selección y tratamiento de señales sísmicas.
- Análisis de la influencia del tipo de modelo de amortiguamiento para el medio material del suelo en la respuesta de la superestructura.
- Análisis de la influencia del tipo de LPM en la respuesta de la superestructura.
- Implementación de la regla de comportamiento no lineal asociada a la superestructura objeto de estudio, i.e. pilares de puente. Desarrollo de los esquemas de subestructuración para el análisis de su respuesta.
- Análisis de la influencia de los efectos de la SSI en la respuesta dinámica no lineal de puentes pilotados y viaductos.
- Evaluación de la reducción del daño sísmico en viaductos cuando se utilizan pilotes inclinados en la cimentación.

B.3 Estructura del documento

El fenómeno de SSI puede ser tenido en cuenta adoptando un esquema de subestructuración. De esta forma se puede estudiar el sistema suelo-cimentación y la superestructura separadamente. Tradicionalmente, los efectos no lineales que se pueden apreciar

en la respuesta del sistema han sido clasificados en tres categorías, comportamientos no lineales del material, no linealidades geométricas principalmente debidas a grandes deformaciones, y condiciones de contorno no lineales. Un comportamiento no lineal puede aparecer tanto en el sistema suelo-cimentación y/o en la superestructura. El documento de tesis ha sido estructurado en dos partes, una centrada en el desarrollo de un modelo lineal equivalente del sistema suelo-cimentación, y el otro centrado en la respuesta no lineal de superestructuras teniendo en cuenta efectos de SSI.

En cuanto al sistema suelo-cimentación, en la Parte I del documento un modelo numérico es desarrollado con el objetivo de reproducir el comportamiento dinámico de la cimentación pilotada. El modelo incluye la posibilidad de reproducir efectos no lineales debido a fallos de contacto y plastificación del suelo en la interfase entre pilote y suelo a través de consideraciones lineales equivalentes. En primer lugar, en el Capítulo 2, el problema que se aborda es definido, para luego describir el modelo BEM-FEM acoplado. Las ecuaciones BEM que gobiernan el dominio constituido por el suelo son resumidas al principio, justo después de haber descrito la discretización adoptada para los contornos del suelo e interfases del mismo, y para los pilotes. Las ecuaciones FEM que gobiernan el comportamiento dinámico de los pilotes son entonces descritas en detalle. Finalmente, la sección donde se describe el modelado concluye con la implementación de las ecuaciones lineales equivalentes de acoplamiento que unen los pilotes con el suelo.

En el segundo capítulo de la Parte I, i.e. Capítulo 3, el modelo es calibrado para diferentes niveles de degradación del suelo en su comportamiento lateral. Para hacer esto, se ha usado un BEM multidominio de forma que el dominio degradado se encuentra explícitamente incluido en las simulaciones. Las bases del BEM multidominio son brevemente presentadas al principio de la sección. Después de que la calibración del BEM-FEM haya sido realizada a través de funciones de impedancia horizontal del sistema suelo-cimentación, se muestra la verificación del amortiguamiento del dominio degradado y también del uso de distintas formas de dominio degradado. Una porción significativa del contenido de la Parte I está incluida en un artículo científico ya enviado para su publicación [96].

La Parte II del documento se centra en la respuesta sísmica de pilares de puentes cimentados sobre grupos de pilotes. Esta parte comienza, en el Capítulo 4, con la definición del problema, la descripción de las bases del procedimiento de diseño adoptado, y la descripción de la metodología empleada para el computo de la respuesta del sistema. Luego, el capítulo continúa con la descripción del esquema de subestructuración adoptado y los modelos utilizados para caracterizar el comportamiento del sistema suelo-cimentación. Más adelante, el modelo no lineal asumido para los pilares de puente es descrito, junto con los dos LPMs adoptados, i.e. los que en el documento se denominan como “*consistent*” y “*simplified*”.

La influencia en la computación de la respuesta sísmica de pilares de puentes cimentados sobre grupos de pilotes dependiendo del modelo asumido para el amortiguamiento material del suelo es presentada en el Capítulo 5. También, el tipo de LPM adoptado para reproducir el comportamiento dinámico complejo de las fuerzas de reacción de la cimentación, necesario para la ejecución de análisis en el dominio del tiempo, es estudiado en términos de la respuesta del pilar de puente. Un amplio estudio paramétrico implicando diferentes perfiles de suelo y superestructuras es llevado a cabo para estar en disposición de proporcionar conclusiones generales. Este análisis se realiza en un marco lineal elástico de forma que las conclusiones obtenidas de este estudio proporcionan un buen punto de partida para el estudio del caso no lineal.

Siguiendo las conclusiones generadas a través de los análisis en el rango lineal, el análisis de la respuesta no lineal de pilares de puente es mostrado en el Capítulo 6. Principalmente, los efectos beneficiosos del uso de pilotes inclinados en la cimentación, en términos de la reducción del daño sísmico producido a los pilares, son mostrados. Concretamente, los resultados se presentan en términos de la demanda dúctil y de la energía disipada por amortiguamiento o por plastificación. Una porción significativa del contenido de la Parte II ya ha sido publicada [97], o es parte de un artículo científico ya aceptado para su publicación [98].

Finalmente, un resumen de los logros más destacados y las conclusiones más importantes que se han obtenido gracias a este trabajo son presentados en el Capítulo 7. El documento termina discutiendo las posibles direcciones y desarrollos para investigaciones futuras que siguiesen este trabajo.

B.4 Trabajos publicados que se derivan de esta Tesis

El trabajo realizado a lo largo de esta tesis doctoral ha contribuido a varias publicaciones y comunicaciones a congresos. Los mismos se encuentran detallados a continuación.

B.4.1 Contribución a revistas JCR

- F González, LA Padrón, S Carbonari, M Morici, JJ Aznárez, F Dezi, and G Leoni. Seismic response of bridge piers on pile groups for different soil damping models and lumped parameter representations of the foundation. *Earthquake Engineering & Structural Dynamics*, 48(3):306–327, 2019. [97]
- F González, S Carbonari, LA Padrón, M Morici, JJ Aznárez, F Dezi, O Maeso, and G Leoni. Benefits of inclined pile foundations in earthquake resistant design of bridges. Enviado a *Engineering Structures*, aceptado. [98]
- F González, LA Padrón, JJ Aznárez and O Maeso. Equivalent linear model for the lateral dynamic analysis of pile foundations considering pile-soil interface degradation. Enviado a *Engineering Analysis with Boundary Elements*, en revisión. [96]

B.4.2 Contribución a conferencias

- F. González, L. A. Padrón, J. J. Aznárez, and O. Maeso. Implementation of the consistent lumped-parameter model for the computation of the seismic response of nonlinear piled structures. *En Actas de la 10ª Conferencia Internacional de Dinámica Estructural (EURODYN 2017)*. Roma, Italia, 10–13 septiembre 2017. [99]
- F. González, M. Morici, S. Carbonari, F. Dezi, M. C. Capatti, G. Leoni, L. A. Padrón, J. J. Aznárez, and O. Maeso. Lumped Parameter Models for time domain Soil-Structure Interaction analysis: consistent vs. simplified formulations and effects on the superstructure response. *En Actas del 5º Taller Internacional de Interacción Dinámica entre Suelo y Estructura (DISS_17)*. Roma, Italia, 19–20 octubre 2017. [100]

B.5 Resumen y conclusiones

Este documento propone nuevas ideas para el modelado de no linealidades en estructuras donde los fenómenos de SSI juegan un papel significativo. El documento, estando dividido en dos partes, es un fiel reflejo de como se ha llevado el proceso de investigación a lo largo de estos últimos años.

En la Parte I del documento, un modelo lineal equivalente para estimar la respuesta horizontal dinámica de pilotes considerando degradación del suelo a lo largo de la interfase pilote-suelo ha sido presentado, implementado y calibrado. La formulación propuesta incorpora la posibilidad de modelar una interfase pilote-suelo imperfecta o dañada en donde las condiciones de contacto no están garantizadas. Se ha utilizado un modelo BEM-FEM acoplado, que reúne las ventajas de ambos métodos: los pilotes son modelados con elementos finitos tipo viga, el suelo degradado en la interfase pilote-suelo es representado resortes y amortiguadores repartidos a lo largo de ella cuyas propiedades varían con la profundidad, y el suelo más allá de la interfaz degradada es modelado a través de elementos de contorno.

La formulación del modelo acoplado BEM-FEM no solo es computacionalmente más eficiente, sino que también es más versátil y requiere mucho menos tiempo en generar las mallas si lo comparamos con otros modelos existentes en la literatura. Esto permitirá ahora el estudio de problemas más complejos. La eficiencia del modelo permitirá también realizar análisis paramétricos o ser incorporado en procesos que requieran un gran número de evaluaciones, como ocurren en muchos problemas de optimización.

La Parte II estudia la respuesta sísmica de pilares de puente cimentados sobre grupos de pilotes. Para el modelado no lineal de pilares, es necesario simular la respuesta del sistema en el dominio del tiempo. Usualmente, el comportamiento del sistema suelo-cimentación tiene una marcada dependencia en frecuencia, cambiando su comportamiento dependiendo de la frecuencia de oscilación del puente. Esto entorpece el análisis dinámico en el dominio del tiempo. De entre las distintas alternativas que existen en la bibliografía para el análisis dinámico en el dominio del tiempo que tengan que hacer uso de fuerzas de reacción dependientes de la frecuencia, dos metodologías son ampliamente utilizadas, una de ellas consiste en hacer uso de la integral de convolución para estas reacciones, y la otra mediante el uso de modelos de elementos discretos equivalentes, también denominados LPM [130]. También existen metodologías híbridas que mezclan el dominio del tiempo con el dominio de la frecuencia. Aquí, dos alternativas de LPM han sido estudiadas e implementadas. Haciendo uso de un esquema de subestructuración, el sistema suelo-cimentación es sustituido por una combinación de masas, resortes y amortiguadores cuyos valores son independientes de la frecuencia y reproducen el comportamiento complejo de la cimentación. De esta forma, cuando ocurre un terremoto, la degradación en el puente puede ser evaluada dependiendo del diseño de la cimentación.

Ambos LPMs implementados han mostrado tener sus propias ventajas e inconvenientes. La implementación del aquí denominado como “*consistent*” es más complicada y laboriosa que el otro denominado como “*simplified*”, pero el *consistent* es capaz de ajustar curvas de impedancia de la cimentación con formas más intrincadas. Por otro lado, si únicamente es necesario el ajuste de un rango de frecuencias pequeño, como es el caso tratado en esta investigación, el *simplified* es una opción lo suficientemente precisa. Además, a través del estudio paramétrico realizado, se ha mostrado que existen otras suposiciones del modelado que tienen una influencia mayor en la respuesta sísmica del

sistema. Por ejemplo, el modelo histerético no causal, y por lo tanto no realista, que tradicionalmente se ha supuesto en la bibliografía para el amortiguamiento material del suelo, hace que se sobrestimen las fuerzas reactivas de la cimentación si es comparado con otro modelo para el amortiguamiento material del suelo como es el modelo causal de Biot. Se ha observado que las diferencias en la respuesta debidas al modelo de amortiguamiento utilizado son mayores que las debidas al LPM elegido. Sin embargo, vale la pena hacer notar que, en la presente investigación las superestructuras son modeladas utilizando un único grado de libertad, estando caracterizadas por su frecuencia fundamental. Para otros tipos de superestructuras, para las que es necesario considerar un sistema de múltiples grados de libertad, el más elaborado *consistent* LPM posiblemente sea el necesario para reproducir correctamente la contribución de los distintos modos de vibración, por lo que la opción simplificada probablemente no sea la adecuada.

Por otro lado, y también en la Parte II del documento, los efectos de SSI en el diseño sísmico, la respuesta y el daño de puentes cimentados sobre pilotes en suelos blandos han sido investigados atendiendo al papel que juega la inclinación de los pilotes. Los modelos de comportamiento no lineales de Takeda y bilineal han sido usados para representar las fisuras desarrolladas en la base de los pilares. A través del esquema de subestructuración, el LPM de bajo orden *simplified* adoptado muestra ser capaz de representar con suficiente precisión la dependencia en frecuencia de las funciones de impedancia de los distintos sistemas suelo-cimentación adoptados cuando es utilizado para computar la demanda dúctil y los balances de energía, incluso sabiendo que este tipo de LPM no es capaz de reproducir todas las formas intrincadas de las funciones de impedancia. En este sentido, también se ha visto que las funciones de impedancia y los factores de interacción cinemática computados tanto con el modelo tipo Winkler como con el modelo acoplado BEM-FEM dan lugar a idénticos resultados. También, para los casos estudiados aquí, se ha visto que se puede obtener una buena estimación de las demandas dúctiles de los pilares a través de simulaciones lineales equivalentes adoptando la regla de igual desplazamiento, mientras que una buena estimación de la demanda dúctil y la energía disipada por la plastificación puede ser obtenida a través de una simple ley de comportamiento bilineal.

Finalmente, en relación a la influencia de la inclinación de los pilotes en la respuesta sísmica de pilares, el comportamiento del sistema suelo-cimentación con pilotes inclinados afecta sensiblemente la respuesta del puente en todos los casos. Esto se produce aún habiendo unicamente un caso de todos los estudiados para el cual es obligatorio el análisis considerando SSI siguiendo los criterios definidos en el Eurocódigo 8. Además, la utilización de la metodología de diseño basada en desplazamiento para los puentes cimentados sobre pilotes inclinados en suelos blandos requiere que se defina una estrategia apropiada para tener en cuenta la flexibilidad y filtrado de la señal sísmica del sistema suelo-cimentación.

B.6 Líneas futuras de investigación

Respecto al modelo lineal equivalente expuesto en la Parte I para estimar la respuesta horizontal dinámica de pilotes considerando degradación del suelo a lo largo de la interfase pilote-suelo, algunos aspectos tienen que ser desarrollados todavía. Una vez que la formulación ha sido verificada para el análisis lateral de un pilote simple, ahora puede ser extendida al modelado de grupos de pilotes ya que el enfoque utilizado por medio de elementos de contorno para el modelado del suelo permite tener en cuenta de forma

rigurosa los efectos de interacción pilote-suelo-pilote. También puede ser calibrado para análisis longitudinales y generalizado a pilotes inclinados. El modelo puede ser usado para obtener resultados a través de análisis por subestructuración, o puede incorporar la superestructura y otros elementos para realizar análisis directos de sistemas completos suelo-cimentación-superestructura. Al mismo tiempo, la definición de las propiedades de la rigidez y amortiguamiento distribuidos a lo largo de la interfase podría incorporar también modelos más complejos de la degradación del suelo dependiendo, por ejemplo, de los niveles de deformación, como aquellos citados en la revisión bibliográfica (Sección 1.3.1).

Gracias a las curvas de degradación del suelo (mirar por ejemplo la Figura 2.1), se puede definir un módulo de rigidez del suelo en su dominio degradado dependiendo de los niveles inducidos de deformación a cortante. En este sentido, podría ser necesario adoptar un procedimiento iterativo para el cual en cada iteración se introduciría el módulo de rigidez que concuerda con el nivel de deformación en la iteración anterior para cada profundidad de la interfase. En el momento en el que no se obtenga variación en el módulo de rigidez, el proceso iterativo concluye. Al final, las fuerzas reactivas de la cimentación son obtenidas consecuentemente con los niveles de carga inducidos. Es posible que sea necesario analizar cuales serían las herramientas metodológicas necesarias para este caso particular.

El modelo ha sido verificado comparándolo contra resultados numéricos obtenidos por medio de un modelo más riguroso, pero debido a limitaciones de tiempo, todavía no ha sido validado contra resultados empíricos para los casos específicos de interés. Por esta misma razón, la comparación de resultados obtenidos con el modelo contra otros modelos no lineales para el computo de sistemas suelo-cimentación que tengan en cuenta no linealidades en la interfase todavía no se ha llevado a cabo. Existen resultados experimentales relacionados que podrían ser de gran interés, en los que se incluyen experimentos a escala real o por medio de máquina centrífuga. A continuación, como propuesta de líneas futuras de investigación, una visión conjunta de estos ensayos experimentales es comentada.

Los resultados experimentales presentados por Goit y Saitoh [14, 34], y por Goit et al. [32, 33, 35], son a priori, los más atractivos porque presentan los resultados en términos de funciones de impedancia y factores de interacción cinemática de pilotes y grupos de pilotes. A través de los análisis experimentales presentados en [14], se aprecia un comportamiento no lineal en las funciones de impedancia de pilotes simples inclinados. Son obtenidos distintos valores de las fuerzas reactivas cuando se cargan y se descargan los pilotes ya que se desarrollan distintos caminos en los huecos y fallos al contacto entre pilote y suelo debido a la inclinación de los pilotes. En [33], los efectos de la no linealidad del suelo en los cambios de la longitud activa de los pilotes son estudiados. Analizan el campo de desplazamientos del suelo en las proximidades al pilote para distintos niveles de carga, y como es la variación de la longitud activa de los pilotes. De forma similar a [14] para el caso de pilotes simples, en [34] el análisis de no linealidades de grupos de pilotes inclinados unidos por medio de un encepado rígido es mostrado. Los picos de resonancia que se aprecian en las funciones de impedancia aumentan a medida que la amplitud de la fuerza de excitación se incrementa, mostrando un fuerte carácter no lineal. En [35], los ensayos experimentales muestran no solo que existe un dominio degradado alrededor de cada pilote, sino que también podría aparecer un dominio de suelo degradado aún mayor que encierra a todo el grupo de pilotes en los caso en que los pilotes estén muy cerca unos de otros, o que la fuerza de excitación sea muy grande.

Los ensayos en máquina centrífuga, por otro lado, tienen un importante valor en geotecnia debido a la posibilidad de obtener en modelos a escala niveles de tensión equivalentes a aquellos que se pueden desarrollar en su correspondiente caso a escala real. Este aspecto es muy importante cuando las no linealidades en el problema pueden ser relevantes, como es el caso de cimentaciones pilotadas sometidas a fuertes excitaciones sísmicas que pueden generar respuestas no lineales del suelo o a lo largo de la interfase pilote-suelo. Por esta razón, comparar el modelo desarrollado contra resultados de la respuesta sísmica de cimentaciones pilotadas obtenidos a través de máquina centrífuga sería de gran interés para entender la validez de las suposiciones consideradas, calibrar el modelo, establecer los rangos de aplicabilidad o proponer modificaciones al modelo. Algunos artículos de interés relacionados con este tipo de pruebas experimentales son aquellos de Li et al. [37] y Hussien et al. [38]. Li et al. [37] utilizan una mesa de vibraciones dentro de una máquina centrífuga para el análisis de pilotes verticales e inclinados sometidos a excitaciones sísmicas. Por otro lado, Hussien et al. [38] realizan análisis de interacción cinemática e inercial de sistemas suelo-pilote-estructura haciendo uso de una caja de contornos rígidos. La reproducción de esos casos con el modelo desarrollado en esta tesis se espera que sea muy útil para continuar su desarrollo y calibración, incluso sabiendo que la tarea no se presupone que sea directa debido a la complejidad de la disposición y de las señales de entrada usadas por los autores.

También existe la alternativa de reproducir resultados obtenidos por medio de experimentos a escala real. Por ejemplo, El-Marsafawi et al. [146] obtuvieron, a través de experimentos de campo, la respuesta vertical armónica de dos grupos de pilotes variando la amplitud de la excitación. Luego, estos resultados fueron comparados contra los resultados publicados por Kaynia y Kausel [147] donde se asume un comportamiento lineal de todos los medios implicados. También fueron comparados contra los resultados obtenidos haciendo uso del programa DINA3 de Novak et al. [148] que incluye en su formulación la zona anular cilíndrica degradada primeramente propuesta por Novak and Sheta [53]. Investigaciones futuras podrían comparar nuevamente estos resultados experimentales pero contra esta nueva herramienta que se ha presentado en este documento. Algunas preocupaciones sobre estos resultados experimentales podrían aparecer puesto que, en muchos casos, para los niveles más bajos de la magnitud de la excitación no concuerdan con los proporcionados por el ampliamente extendido modelo de Kaynia y Kausel. Más recientemente, Banna y Bayda analizaron la vibración vertical de pilotes simples [29,149], y luego, Biswas et al. [31] su respuesta horizontal acoplada con la rotación. Los resultados experimentales obtenidos para las distintas magnitudes de la excitación son presentados, observándose un comportamiento no lineal evidente. Realizan una comparación contra análisis FEM donde se observan algunas discrepancias en algunos casos. También, el modelo lineal equivalente que incluye el dominio anular degradado de Novak y Sheta [53] es utilizado en algunos de esos estudios [29,31]. Este cilindro de suelo que rodea al pilote tiene un módulo de rigidez inferior y un amortiguamiento material superior a los del dominio exterior correspondiente al suelo no degradado.

Finalmente, el estudio de como variarían los momentos flectores y esfuerzos a cortante a lo largo de los pilotes a medida que el suelo se degrada es otro aspecto a explorar haciendo uso del modelo propuesto. También las variaciones en la envolventes sísmicas debidas a la degradación de la interfase pilote-suelo podrían ser analizadas.

Para el análisis de la respuesta sísmica de los pilares de puente abordados en la Parte II, las dos tipologías de LPM implementadas han permitido los análisis sobre el daño en los pilares incorporando los efectos de SSI. Estos LPM implementados pueden

ser usados ahora para estudiar la respuesta dinámica, en el dominio del tiempo, de otros tipos de estructuras. También, podría contemplarse la posibilidad de estudiar como sería incorporarlos en paquetes informáticos ampliamente utilizados y extendidos en la comunidad técnica y científica.

Por otro lado, algunas hipótesis simplificadoras han sido asumidas tanto en los análisis lineales como no lineales. Primero, un pilar intermedio ha sido considerado como representativo del comportamiento dinámico del viaducto completo. Esta consideración es válida únicamente para algunas situaciones donde todos los pilares tienen la misma altura. Segundo, el hecho de considerar únicamente la excitación transversal podría ser una limitación bastante fuerte. Y tercero, se ha considerado que un sistema de tres grados de libertad es suficiente para el modelado de la superestructura. Modelos más complejos que incluyan el viaducto completo mostrarán contribuciones de otros modos, no solo del modo fundamental. Otras tipologías de pilares pueden ser introducidas al modelo, en donde la plastificación no se produzca necesariamente en la base de los pilares, por lo tanto, la consideración en el modelo de que un resorte y un amortiguador en la base del pilar es representativa del comportamiento no lineal del mismo no sería válida. Si este fuera el caso, otros modelos serían necesarios para reproducir el comportamiento del pilar.

Ahora, todo el conocimiento recabado gracias a los análisis llevados a cabo en esta investigación puede ser utilizado para estudiar estructuras completas de puentes. Distintos mecanismos de daño aparecerán cuando se consideren otras tipologías de puentes y también considerando todo el sistema en las simulaciones. Las conclusiones que se derivan de esta tesis podrían no ser válidas en estos casos.

El estudio en base flexible de los pilares de puentes se ha centrado en la respuesta de la superestructura y en el daño producido a los pilares dependiendo de las consideraciones de diseño en la cimentación, como por ejemplo las distintas configuraciones de pilotes e inclinación de los mismos en los grupos de pilotes. Algunas de las consideraciones de diseño que han mostrado ser beneficiosas para la superestructura, podrían ser perjudiciales para el sistema suelo-cimentación. Las tensiones soportadas por los pilotes, por ejemplo en términos de momentos flectores y esfuerzos a cortante, y las cargas transmitidas al suelo, deberían ser exploradas en el futuro para poder dilucidar las posibles consecuencias que el uso de pilotes inclinados pueden tener en la cimentación.

En la Parte I de esta investigación, un modelo que considera degradación del suelo en la interfase entre pilote y suelo ha sido desarrollado; y en la Parte II, el daño en pilares de viaductos es evaluado teniendo en cuenta los efectos de SSI. Finalmente, los efectos de la degradación del suelo en la respuesta no lineal de pilares de puente pueden ser estudiados utilizando el modelo desarrollado en la Parte I y el esquema de subestructuración propuesto en la Parte II. Seguramente aparecerán muchos inconvenientes que imposibiliten estos análisis, es por lo que serán necesarias estrategias novedosas que solventen las distintas limitaciones. Por ejemplo, como las funciones de impedancia de las cimentaciones pilotadas dependen de la magnitud de la carga inducida, será necesario un desarrollo de los LPMs utilizados para que sean capaces de incluir la magnitud de la carga como parámetro.

Bibliography

- [1] National Geophysical Data Center / World Data Service (NGDC/WDS). *Global Significant Earthquake Database, 2150 BC to present*. National Oceanic and Atmospheric Administration (NOAA), 2015.
- [2] Pak RYS and Jennings PC. Elastodynamic response of pile under transverse excitations. *Journal of Engineering Mechanics*, 113(7):1101–1116, 1987.
- [3] Rajapakse RKND and Shah AH. On the lateral harmonic motion of an elastic bar embedded in an elastic half-space. *International Journal of Solids and Structures*, 23(2):287–303, 1987.
- [4] Abedzadeh F and Pak RYS. Continuum mechanics of lateral soil-pile interaction. *Journal of Engineering Mechanics*, 130(11):1309–1318, 2004.
- [5] Matlock H and Reese LC. Generalized solutions for laterally loaded piles. *Journal of the Soil Mechanics and Foundations Division*, 86(5):63–91, 1960.
- [6] Dobry R, Vicenti E, O’Rourke MJ, and Roesset JM. Horizontal stiffness and damping of single piles. *Journal of the Geotechnical Engineering Division*, 108(3):439–459, 1982.
- [7] Gazetas G, Fan K, Kaynia A, and Kausel E. Dynamic interaction factors for floating pile groups. *Journal of Geotechnical Engineering*, 117(10):1531–1548, 1991.
- [8] Mylonakis G and Gazetas G. Lateral vibration and internal forces of grouped piles in layered soil. *Journal of Geotechnical and Geoenvironmental Engineering*, 125(1):16–25, 1999.
- [9] Dezi F, Carbonari S, and Leoni G. A model for the 3D kinematic interaction analysis of pile groups in layered soils. *Earthquake Engineering & Structural Dynamics*, 38(11):1281–1305, 2009.
- [10] Anoyatis G and Lemnitzer A. Dynamic pile impedances for laterally-loaded piles using improved Tajimi and Winkler formulations. *Soil Dynamics and Earthquake Engineering*, 92:279–297, 2017.
- [11] Álamo GM, Bordón JDR, Aznárez JJ, and Maeso O. Relevance of soil-pile tangential tractions for the estimation of kinematic seismic forces: Formulation and setting of a Winkler approach. *Applied Mathematical Modelling*, 59:1–19, 2018.
- [12] Kuhlemeyer RL. Static and dynamic laterally loaded floating piles. *Journal of the Geotechnical Engineering Division*, 105(2):289–304, 1979.

- [13] Velez A, Gazetas G, and Krishnan R. Lateral dynamic response of constrained-head piles. *Journal of Geotechnical Engineering*, 109(8):1063–1081, 1983.
- [14] Goit CS and Saitoh M. Model tests and numerical analyses on horizontal impedance functions of inclined single piles embedded in cohesionless soil. *Earthquake Engineering and Engineering Vibration*, 12(1):143–154, 2013.
- [15] Kattis SE, Polyzos D, and Beskos DE. Vibration isolation by a row of piles using a 3-D frequency domain BEM. *International Journal for Numerical Methods in Engineering*, 46(5):713–728, 1999.
- [16] Kattis SE, Polyzos D, and Beskos DE. Modelling of pile wave barriers by effective trenches and their screening effectiveness. *Soil Dynamics and Earthquake Engineering*, 18(1):1–10, 1999.
- [17] Maeso O, Aznárez JJ, and García F. Dynamic impedances of piles and groups of piles in saturated soils. *Computers & Structures*, 83(10):769–782, 2005.
- [18] Kaynia AM. *Dynamic stiffness and seismic response of pile groups*. Research Report R83-03. Massachusetts Institute of Technology, Cambridge, MA, 1982.
- [19] Sen R, Davies TG, and Banerjee PK. Dynamic analysis of piles and pile groups embedded in homogeneous soils. *Earthquake Engineering & Structural Dynamics*, 13(1):53–65, 1985.
- [20] Mamoon SM, Kaynia AM, and Banerjee PK. Frequency domain dynamic analysis of piles and pile groups. *Journal of Engineering Mechanics*, 116(10):2237–2257, 1990.
- [21] Kaynia AM and Kausel E. Dynamics of piles and pile groups in layered soil media. *Soil Dynamics and Earthquake Engineering*, 10(8):386–401, 1991.
- [22] Guin J and Banerjee PK. Coupled soil-pile-structure interaction analysis under seismic excitation. *Journal of Structural Engineering*, 124(4):434–444, 1998.
- [23] Padrón LA, Aznárez JJ, and Maeso O. BEM-FEM coupling model for the dynamic analysis of piles and pile groups. *Engineering Analysis with Boundary Elements*, 31(6):473–484, 2007.
- [24] Ai ZY and Li ZX. Dynamic analysis of a laterally loaded pile in a transversely isotropic multilayered half-space. *Engineering Analysis with Boundary Elements*, 54:68–75, 2015.
- [25] Romero A and Galvín P. A BEM-FEM using layered half-space Green’s function in time domain for SSI analyses. *Engineering Analysis with Boundary Elements*, 55:93–103, 2015.
- [26] Álamo GM, Martínez-Castro AE, Padrón LA, Aznárez JJ, Gallego R, and Maeso O. Efficient numerical model for the computation of impedance functions of inclined pile groups in layered soils. *Engineering Structures*, 126:379–390, 2016.
- [27] El Shamouby B and Novak M. Dynamic experiments with group of piles. *Journal of Geotechnical Engineering*, 110(6):719–737, 1984.

- [28] El-Marsafawi H, Han YC, and Novak M. Dynamic experiments on two pile groups. *Journal of Geotechnical Engineering*, 118(4):576–592, 1992.
- [29] Manna B and Baidya DK. Dynamic nonlinear response of pile foundations under vertical vibration – Theory versus experiment. *Soil Dynamics and Earthquake Engineering*, 30(6):456–469, 2010.
- [30] Boominathan A, Krishna Kumar S, and Subramanian RM. Lateral dynamic response and effect of weakzone on the stiffness of full scale single piles. *Indian Geotechnical Journal*, 43(1):43–50, 2015.
- [31] Biswas S, Manna B, and Baidya DK. Experimental and theoretical study on the nonlinear response of full-scale single pile under coupled vibrations. *Soil Dynamics and Earthquake Engineering*, 94:109–115, 2017.
- [32] Goit CS, Saitoh M, Mylonakis G, Kawakami H, and Oikawa H. Model tests on horizontal pile-to-pile interaction incorporating local non-linearity and resonance effects. *Soil Dynamics and Earthquake Engineering*, 48:175–192, 2013.
- [33] Goit CS, Saitoh M, Oikawa H, and Kawakami H. Effects of soil nonlinearity on the active length of piles embedded in cohesionless soil: model studies. *Acta Geotechnica*, 9(3):455–467, 2014.
- [34] Goit CS and Saitoh M. Model tests on horizontal impedance functions of fixed-head inclined pile groups under soil nonlinearity. *Journal of Geotechnical and Geoenvironmental Engineering*, 140(6):04014023, 2014.
- [35] Goit CS, Saitoh M, and Mylonakis G. Principle of superposition for assessing horizontal dynamic response of pile groups encompassing soil nonlinearity. *Soil Dynamics and Earthquake Engineering*, 82:73–83, 2016.
- [36] Yu H, Zeng X, Li B, and Lian J. Centrifuge modeling of offshore wind foundations under earthquake loading. *Soil Dynamics and Earthquake Engineering*, 77:402–415, 2015.
- [37] Li Z, Escoffier S, and Kotronis P. Centrifuge modeling of batter pile foundations under earthquake excitation. *Soil Dynamics and Earthquake Engineering*, 88:176–190, 2016.
- [38] Hussien MN, Tobita T, Iai S, and Karray M. Soil-pile-structure kinematic and inertial interaction observed in geotechnical centrifuge experiments. *Soil Dynamics and Earthquake Engineering*, 89:75–84, 2016.
- [39] Taghavi A, Muraleetharan KK, and Miller GA. Nonlinear seismic behavior of pile groups in cement-improved soft clay. *Soil Dynamics and Earthquake Engineering*, 99:189–202, 2017.
- [40] Seong J-T and Kim D-s. Seismic evaluation of offshore wind turbine by geotechnical centrifuge test. *Wind Energy*, 22(8):1034–1042, 2019.
- [41] Boulanger RW, Curras CJ, Kutter BL, Wilson DW, and Abghari A. Seismic soil-pile-structure interaction experiments and analyses. *Journal of Geotechnical and Geoenvironmental Engineering*, 125(9):750–759, 1999.

- [42] El Naggar MH and Bentley KJ. Dynamic analysis for laterally loaded piles and dynamic p-y curves. *Canadian Geotechnical Journal*, 37(6):1166–1183, 2000.
- [43] Maheshwari BK and Watanabe H. Nonlinear dynamic behavior of pile foundations: effects of separation at the soil-pile interface. *Soils and Foundations*, 46(4):437–448, 2006.
- [44] Allotey N and El Naggar MH. A numerical study into lateral cyclic nonlinear soil-pile response. *Canadian Geotechnical Journal*, 45(9):1268–1281, 2008.
- [45] Soneji BB and Jangid RS. Influence of soil-structure interaction on the response of seismically isolated cable-stayed bridge. *Soil Dynamics and Earthquake Engineering*, 28(4):245–257, 2008.
- [46] Gerolymos N, Kassas K, Bouzoni E, and Brinkgreve RBJ. Dynamic analysis of piles subjected to axial and lateral loading with emphasis on soil and interface nonlinearities. *Numerical Methods in Geotechnical Engineering – Proceedings of the 8th European Conference on Numerical Methods in Geotechnical Engineering, NUMGE 2014*, 2:1117–1122, 2014.
- [47] Tombari A, El Naggar MH, and Dezi F. Impact of ground motion duration and soil non-linearity on the seismic performance of single piles. *Soil Dynamics and Earthquake Engineering*, 100:72–87, 2017.
- [48] Markou AA and Kaynia AM. Nonlinear soil-pile interaction for offshore wind turbines. *Wind Energy*, 21(7):558–574, 2018.
- [49] Rahmani A, Taiebat M, Liam Finn WD, and Ventura CE. Evaluation of p-y springs for nonlinear static and seismic soil-pile interaction analysis under lateral loading. *Soil Dynamics and Earthquake Engineering*, 115:438–447, 2018.
- [50] Angelides DC and Roesset JM. Non-linear lateral dynamic stiffness of piles. *Journal of the Geotechnical Engineering Division*, 107(11):1443–1460, 1981.
- [51] Bentley KJ and Naggar MHE. Numerical analysis of kinematic response of single piles. *Canadian Geotechnical Journal*, 37(6):1368–1382, 2000.
- [52] Bhowmik D, Baidya DK, and Dasgupta SP. A numerical and experimental study of hollow steel pile in layered soil subjected to lateral dynamic loading. *Soil Dynamics and Earthquake Engineering*, 53:119–129, 2013.
- [53] Novak M and Sheta M. Approximate approach to contact effects of piles. In *Proceedings of Session on Dynamic Response of Pile Foundations: Analytical Aspects, ASCE National Convention, Florida*, pages 53–79, 1980.
- [54] Veletsos AS and Dotson KW. Impedances of soil layer with disturbed boundary zone. *Journal of Geotechnical Engineering*, 112(3):363–368, 1986.
- [55] Novak M and Han YC. Impedances of soil layer with boundary zone. *Journal of Geotechnical Engineering*, 116(6):1008–1014, 1990.
- [56] Han YC and Sabin GCW. Impedances for radially inhomogeneous viscoelastic soil media. *Journal of Engineering Mechanics*, 121(9):939–947, 1995.

- [57] Luo C, Yang X, Zhan C, Jin X, and Ding Z. Nonlinear 3D finite element analysis of soil-pile-structure interaction system subjected to horizontal earthquake excitation. *Soil Dynamics and Earthquake Engineering*, 84:145–156, 2016.
- [58] Kausel E, Whitman RV, Morray JP, and Elsabee F. The spring method for embedded foundations. *Nuclear Engineering and Design*, 48(2):377–392, 1978.
- [59] Kausel E. Early history of soil-structure interaction. *Soil Dynamics and Earthquake Engineering*, 30(9):822–832, 2010.
- [60] Mylonakis G, Nikolaou A, and Gazetas G. Soil-pile-bridge seismic interaction: kinematic and inertial effects. Part I: soft soil. *Earthquake Engineering & Structural Dynamics*, 26(3):337–359, 1997.
- [61] Chaudhary MTA, Abé M, and Fujino Y. Identification of soil-structure interaction effect in base-isolated bridges from earthquake records. *Soil Dynamics and Earthquake Engineering*, 21(8):713–725, 2001.
- [62] Mylonakis G, Nikolaou S, and Gazetas G. Footings under seismic loading: analysis and design issues with emphasis on bridge foundations. *Soil Dynamics and Earthquake Engineering*, 26(9):824–853, 2006.
- [63] Carbonari S, Dezi F, and Leoni G. Seismic soil-structure interaction in multi-span bridges: application to a railway bridge. *Earthquake Engineering & Structural Dynamics*, 40(11):1219–1239, 2011.
- [64] Wolf JP and Somaini DR. Approximate dynamic model of embedded foundation in time domain. *Earthquake Engineering & Structural Dynamics*, 14(5):683–703, 1986.
- [65] Saitoh M. Simple model of frequency-dependent impedance functions in soil-structure interaction using frequency-independent elements. *Journal of Engineering Mechanics*, 133(10):1101–1114, 2007.
- [66] Lesgidis N, Kwon O-S, and Sextos A. A time-domain seismic SSI analysis method for inelastic bridge structures through the use of a frequency-dependent lumped parameter model. *Earthquake Engineering & Structural Dynamics*, 44(13):2137–2156, 2015.
- [67] Wolf JP. Consistent lumped-parameter models for unbounded soil: physical representation. *Earthquake Engineering & Structural Dynamics*, 20(1):11–32, 1991.
- [68] Wolf JP. Consistent lumped-parameter models for unbounded soil: frequency-independent stiffness, damping and mass matrices. *Earthquake Engineering & Structural Dynamics*, 20(1):33–41, 1991.
- [69] Meek JW and Veletsos AS. Simple models for foundations in lateral and rocking motion. *In Proceedings of the 5th World Conference on Earthquake Engineering*, 2:2610–2613, 1974.
- [70] De Barros FCP and Luco JE. Discrete models for vertical vibrations of surface and embedded foundations. *Earthquake Engineering & Structural Dynamics*, 19(2):289–303, 1990.

- [71] Jean W-Y, Lin T-W, and Penzien J. System parameters of soil foundations for time domain dynamic analysis. *Earthquake Engineering & Structural Dynamics*, 19(4):541–553, 1990.
- [72] EN1998-5. *Eurocode 8 – Design of structures for earthquake resistance. Part 5: foundations, retaining structures and geotechnical aspects*. CEN, 2004.
- [73] Bishop RED. The treatment of damping forces in vibration theory. *Journal of the Royal Aeronautical Society*, 59(539):738–742, 1955.
- [74] Chopra AK. *Dynamics of Structures. Theory and Applications to Earthquake Engineering. Third Edition*. Prentice-Hall, 2007.
- [75] Booij HC and Thoone GPJM. Generalization of Kramers-Kronig transforms and some approximations of relations between viscoelastic quantities. *Rheologica Acta*, 21(1):15–24, 1982.
- [76] Biot MA. Linear thermodynamics and the mechanics of solids. *In Proceedings of the 3rd U. S. National Congress of Applied Mechanics*, 1:1–18, 1958.
- [77] Makris N. Causal hysteretic element. *Journal of Engineering Mechanics*, 123(11):1209–1214, 1997.
- [78] Brito MB, Ishibashi H, and Akiyama M. Shaking table tests of a reinforced concrete bridge pier with a low-cost sliding pendulum system. *Earthquake Engineering & Structural Dynamics*, 48(3):366–386, 2019.
- [79] Xie Y and Zhang J. Design and optimization of seismic isolation and damping devices for highway bridges based on probabilistic repair cost ratio. *Journal of Structural Engineering*, 144(8):04018125, 2018.
- [80] Li Y and Conte JP. Probabilistic performance-based optimum design of seismic isolation for a California high-speed rail prototype bridge. *Earthquake Engineering & Structural Dynamics*, 47(2):497–514, 2018.
- [81] Okui Y, Nakamura K, Sato T, and Imai T. Seismic response of isolated bridge with high damping rubber bearings. *Steel Construction*, 12(1):2–9, 2019.
- [82] Liu C, Gao R, and Guo B. Seismic design method analyses of an innovative steel damping bearing for railway bridges. *Engineering Structures*, 167:518–532, 2018.
- [83] Bompa DV and Elghazouli AY. Inelastic cyclic behaviour of RC members incorporating threaded reinforcement couplers. *Engineering Structures*, 180:468–483, 2019.
- [84] Wang Z, Wang J-Q, Tang Y-C, Liu T-X, Gao Y-F, and Zhang J. Seismic behavior of precast segmental UHPC bridge columns with replaceable external cover plates and internal dissipaters. *Engineering Structures*, 177:540–555, 2018.
- [85] Zhao L, Bi K, Hao H, and Li X. Numerical studies on the seismic responses of bridge structures with precast segmental columns. *Engineering Structures*, 151:568–583, 2017.

- [86] Ghadban AA, Wehbe NI, and Pauly T. Seismic performance of self-consolidating concrete bridge columns. *Engineering Structures*, 160:461–472, 2018.
- [87] Ciampoli M and Pinto PE. Effects of soil-structure interaction on inelastic seismic response of bridge piers. *Journal of Structural Engineering*, 121(5):806–814, 1995.
- [88] Elnashai AS and McClure DC. Effect of modelling assumptions and input motion characteristics on seismic design parameters of RC bridge piers. *Earthquake Engineering & Structural Dynamics*, 25(5):435–463, 1996.
- [89] Mylonakis G and Gazetas G. Seismic soil-structure interaction: beneficial or detrimental? *Journal of Earthquake Engineering*, 4(3):277–301, 2000.
- [90] Jeremić B, Kunnath S, and Xiong F. Influence of soil-foundation-structure interaction on seismic response of the I-880 viaduct. *Engineering Structures*, 26(3):391–402, 2004.
- [91] Mylonakis G, Syngros C, Gazetas G, and Tazoh T. The role of soil in the collapse of 18 piers of Hanshin Expressway in the Kobe earthquake. *Earthquake Engineering & Structural Dynamics*, 35(5):547–575, 2006.
- [92] Medina C, Padrón LA, Aznárez JJ, Santana A, and Maeso O. Kinematic interaction factors of deep foundations with inclined piles. *Earthquake Engineering & Structural Dynamics*, 43(13):2035–2050, 2014.
- [93] Gerolymos N, Giannakou A, Anastasopoulos I, and Gazetas G. Evidence of beneficial role of inclined piles: observations and summary of numerical analyses. *Bulletin of Earthquake Engineering*, 6(4):705–722, 2008.
- [94] Medina C, Padrón LA, Aznárez JJ, and Maeso O. Influence of pile inclination angle on the dynamic properties and seismic response of piled structures. *Soil Dynamics and Earthquake Engineering*, 69:196–206, 2015.
- [95] Carbonari S, Morici M, Dezi F, Gara F, and Leoni G. Soil-structure interaction effects in single bridge piers founded on inclined pile groups. *Soil Dynamics and Earthquake Engineering*, 92:52–67, 2017.
- [96] González F, Padrón LA, Aznárez JJ, and Maeso O. Equivalent linear model for the lateral dynamic analysis of pile foundations considering pile-soil interface degradation. *Submitted to Engineering Analysis with Boundary Elements, under review.*
- [97] González F, Padrón LA, Carbonari S, Morici M, Aznárez JJ, Dezi F, and Leoni G. Seismic response of bridge piers on pile groups for different soil damping models and lumped parameter representations of the foundation. *Earthquake Engineering & Structural Dynamics*, 48(3):306–327, 2019.
- [98] González F, Carbonari S, Padrón LA, Morici M, Aznárez JJ, Dezi F, Maeso O, and Leoni G. Benefits of inclined pile foundations in earthquake resistant design of bridges. *Submitted to Engineering Structures, accepted.*
- [99] González F, Padrón LA, Aznárez JJ, and Maeso O. Implementation of the consistent lumped-parameter model for the computation of the seismic response of nonlinear piled structures. *In Proceedings of the 10th International Conference on Structural Dynamics, Procedia Engineering*, 199:2360–2365, 2017.

- [100] González F, Morici M, Carbonari S, Dezi F, Capatti MC, Leoni G, Padrón LA, Aznárez JJ, and Maeso O. Lumped Parameter Models for time domain Soil-Structure Interaction analysis: consistent vs. simplified formulations and effects on the superstructure response. *In Proceedings of the 5th International Workshop on Dynamic Interaction of Soil and Structure*, pages 181–204, 2017.
- [101] Seed HB and Idriss IM. *Soil moduli and damping factors for dynamic response analyses. REPORT NO. EERC 70-10*. Earthquake Engineering Research Center, University of California, Berkeley, 1970.
- [102] Vucetic M and Dobry R. Effect of soil plasticity on cyclic response. *Journal of Geotechnical Engineering*, 117(1):89–107, 1991.
- [103] Ishibashi I and Zhang X. Unified dynamic shear moduli and damping ratios of sand and clay. *Soils and Foundations*, 33(1):182–191, 1993.
- [104] Mendonça AV and Paiva JB. An elastostatic FEM/BEM analysis of vertically loaded raft and piled raft foundation. *Engineering Analysis with Boundary Elements*, 27(9):919–933, 2003.
- [105] Cruse TA and Rizzo FJ. A direct formulation and numerical solution of the general transient elastodynamic problem. I. *Journal of Mathematical Analysis and Applications*, 22(1):244–259, 1968.
- [106] Clough RW and Penzien J. *Dynamics of Structures. Second Edition*. McGraw-Hill, 1993.
- [107] Domínguez J. *Boundary Elements in Dynamics*. Computational Mechanics Publications, 1993.
- [108] Capatti MC, Tropeano G, Morici M, Carbonari S, Dezi F, Leoni G, and Silvestri F. Implications of non-synchronous excitation induced by nonlinear site amplification and of soil-structure interaction on the seismic response of multi-span bridges founded on piles. *Bulletin of Earthquake Engineering*, 15(11):4963–4995, 2017.
- [109] EN1998-1. *Eurocode 8 – Design of structures for earthquake resistance. Part 1: general rules, seismic actions and rules for buildings*. CEN, 2004.
- [110] Gazetas G, Fan K, Tazoh T, Shimizu K, Kavvadas M, and Makris N. Seismic pile-group-structure interaction. *Geotechnical special pulication, ASCE*, 34:56–93, 1992.
- [111] Priestley MJN, Calvi GM, and Kowalsky MJ. *Displacement-Based Seismic Design of Structures*. IUSS Press, 2007.
- [112] Takeda T, Sozen MA, and Nielsen NN. Reinforced concrete response to simulated earthquakes. *Journal of the Structural Division*, 96(12):2557–2573, 1970.
- [113] EN1998-2. *Eurocode 8 – Design of structures for earthquake resistance. Part 2: bridges*. CEN, 2005.
- [114] Montejo LA and Kowalsky MJ. *CUMBIA – Set of codes for the analysis of reinforced concrete members*. CFL Technical Rep. No. IS-07, 2007.

- [115] Mander JB, Priestley MJN, and Park R. Theoretical stress-strain model for confined concrete. *Journal of Structural Engineering*, 114(8):1804–1826, 1988.
- [116] King DJ, Priestley MJN, and Park R. *Computer Programs for Concrete Column Design. Research Report 86/12*. Department of Civil Engineering, University of Canterbury, 1986.
- [117] Aviram A, Mackie KR, and Stojadinović B. *Guidelines for Nonlinear Analysis of Bridge Structures in California. PEER Report 2008/03*. Pacific Earthquake Engineering Research Center, University of California, Berkeley, 2008.
- [118] Priestley MJN, Seible F, and Calvi GM. *Seismic Design and Retrofit of Bridges*. John Wiley & Sons, 1996.
- [119] Ambraseys NN, Smit P, Douglas J, Margaris B, Sigbjörnsson R, Ólafsson S, Suhadolc P, and Costa G. Internet site for European strong-motion data. *Bollettino di Geofisica Teorica ed Applicata*, 45(3):113–129, 2004.
- [120] Ancheta TD, Darragh RB, Stewart JP, Seyhan E, Silva WJ, Chiou BSJ, Wooddell KE, Graves RW, Kottke AR, Boore DM, Kishida T, and Donahue JL. *PEER NGA-West2 Database. PEER Report 2013/03*. Pacific Earthquake Engineering Research Center, University of California, Berkeley, 2013.
- [121] Goulet CA, Kishida T, Ancheta TD, Cramer CH, Darragh RB, Silva WJ, Hashash YMA, Harmon J, Stewart JP, Wooddell KE, and Youngs RR. *PEER NGA-East Database. PEER Report 2014/07*. Pacific Earthquake Engineering Research Center, University of California, Berkeley, 2014.
- [122] Smerzini C, Galasso C, Iervolino I, and Paolucci R. Ground motion record selection based on broadband spectral compatibility. *Earthquake Spectra*, 30(4):1427–1448, 2014.
- [123] Luzi L, Pacor F, and Puglia R. *Italian Accelerometric Archive v 2.2*. Istituto Nazionale di Geofisica e Vulcanologia, Dipartimento della Protezione Civile Nazionale, 2017.
- [124] NIED. *Internet site for the Kyoshin network (K-NET) and the Kiban Kyoshin network (KiK-net)*. National Research Institute for Earth Science and Disaster Resilience, 2019.
- [125] Boore DM and Bommer JJ. Processing of strong-motion accelerograms: needs, options and consequences. *Soil Dynamics and Earthquake Engineering*, 25(2):93–115, 2005.
- [126] Luco N and Bazzurro P. *Effects of earthquake record scaling on nonlinear structural response*. Report on PEER-LL Program Task 1G00 Addendum (Sub-Task 1 of 3), 2005.
- [127] Baker JW. Measuring bias in structural response caused by ground motion scaling. *In Proceedings of the 8th Pacific Conference on Earthquake Engineering. Paper Number 056*, 2007.

- [128] Katsanos EI, Sextos AG, and Manolis GD. Selection of earthquake ground motion records: A state-of-the-art review from a structural engineering perspective. *Soil Dynamics and Earthquake Engineering*, 30(4):157–169, 2010.
- [129] Kwong NS and Chopra AK. *Selection and Scaling of Ground Motions for Non-linear Response History Analysis of Buildings in Performance-Based Earthquake Engineering. PEER Report 2015/11*. Pacific Earthquake Engineering Research Center, University of California, Berkeley, 2015.
- [130] Wolf JP. *Soil-Structure Interaction Analysis in Time Domain*. Prentice-Hall, 1988.
- [131] Newmark NM. A method of computation for structural dynamics. *Journal of the Engineering Mechanics Division*, 85(3):67–94, 1959.
- [132] Wilson EL, Farhoomand I, and Bathe KJ. Nonlinear dynamic analysis of complex structures. *Earthquake Engineering & Structural Dynamics*, 1(3):241–252, 1972.
- [133] Carbonari S, Morici M, Dezi F, and Leoni G. A lumped parameter model for time-domain inertial soil-structure interaction analysis of structures on pile foundations. *Earthquake Engineering & Structural Dynamics*, 47(11):2147–2171, 2018.
- [134] Padrón LA, Aznárez JJ, and Maeso O. Dynamic analysis of piled foundations in stratified soils by a BEM-FEM model. *Soil Dynamics and Earthquake Engineering*, 28(5):333–346, 2008.
- [135] Padrón LA. *Numerical model for the dynamic analysis of pile foundations*. Ph.D. Thesis, Universidad de Las Palmas de Gran Canaria, 2009.
- [136] Padrón LA, Aznárez JJ, Maeso O, and Santana A. Dynamic stiffness of deep foundations with inclined piles. *Earthquake Engineering & Structural Dynamics*, 39(12):1343–1367, 2010.
- [137] Dezi F, Carbonari S, and Morici M. A numerical model for the dynamic analysis of inclined pile groups. *Earthquake Engineering & Structural Dynamics*, 45(1):45–68, 2016.
- [138] Kimball AL and Lovell DE. Internal friction in solids. *Physical Review*, 30(6):948–959, 1927.
- [139] Muravskii GB. On frequency independent damping. *Journal of Sound and Vibration*, 274(3-5):653–668, 2004.
- [140] Muravskii GB. Linear models with nearly frequency independent complex stiffness leading to causal behaviour in time domain. *Earthquake Engineering & Structural Dynamics*, 36(1):13–33, 2007.
- [141] Takewaki I. Closed-form sensitivity of earthquake input energy to soil-structure interaction system. *Journal of Engineering Mechanics*, 133(4):389–399, 2007.
- [142] Andersen L. *Linear Elastodynamic Analysis*. Department of Civil Engineering, Aalborg University, 2006.
- [143] Andersen L. Assessment of lumped-parameter models for rigid footings. *Computers & Structures*, 88(23-24):1333–1347, 2010.

- [144] Paronesso A and Wolf JP. Global lumped-parameter model with physical representation for unbounded medium. *Earthquake Engineering & Structural Dynamics*, 24(5):637–654, 1995.
- [145] Medina C, Aznárez JJ, Padrón LA, and Maeso O. Effects of soil-structure interaction on the dynamic properties and seismic response of piled structures. *Soil Dynamics and Earthquake Engineering*, 53:160–175, 2013.
- [146] El-Marsafawi H, Han YC, and Novak M. Dynamic experiments on two pile groups. *Journal of Geotechnical and Engineering*, 118(4):576–592, 1992.
- [147] Kaynia AM and Kausel E. Dynamic behaviour of pile groups. *2nd International Conference on Numerical Methods in Offshore Piling, Austin, Texas*, 1982.
- [148] Novak M, Sheta M, El Hifnawy L, El-Marsafawi H, and Ramadan O. *DYNA3 – A computer program for calculation of foundation response to dynamic loads. Report No. GEOP 90-02*. Geotechnical Research Centre, The University of Western Ontario, London, Ontario, Canada, 1990.
- [149] Manna B and Baidya DK. Vertical vibration of full-scale pile – Analytical and experimental study. *Journal of Geotechnical and Geoenvironmental Engineering*, 135(10):1452–1461, 2009.



INSTITUTO UNIVERSITARIO
SIANI
INGENIERIA COMPUTACIONAL

Edificio central del Parque Tecnológico
Campus Universitario de Tafira
35017 Las Palmas de Gran Canaria
e-mail: info@siani.es
www.siani.es



UNIVERSIDAD DE LAS PALMAS
DE GRAN CANARIA